DEVELOPMENT OF SMOOTH PARTICLE HYDRODYNAMICS FOR THE MODELLING OF STRESSES AROUND JACK-IN PILE

by

PERPETUA AANIYA CYRIL

Thesis submitted to the University of Nottingham for the degree of Doctor of Philosophy

March 2019

Declaration of Authorship

I, Perpetua Aaniya Cyril, hereby declare that the work presented in this thesis is solely mine and it has not been submitted elsewhere for any other degree at this University or any other institution. To the best of my knowledge, the thesis contains no materials from previously published work other than those been cited and acknowledged.

Perpetua Aaniya Cyril

20th MARCH 2019

Abstract

Jack-in pile installation generates large deformations in the surrounding soil. These deformations cause significant changes to the soil stress levels. Such variations in stresses greatly influence the pile bearing capacity. Therefore, prediction of stresses in soil during the installation phase is crucial. However, over the past, limited knowledge has been gained on soil stress field during jack-in pile installation. The experimental techniques available for obtaining soil stress measurements involve a great level of complexity. Accurate simulation of the stress field necessitates pile to be modelled as an elastic or elastic-perfectly plastic material from the soil surface considering soil-pile interaction. However, most of the numerical models in the literature based on mesh-based or mesh-free methods have adopted various simplified assumptions in modelling the phenomenon. The models have provided limited knowledge regarding the progress of soil stress distribution with pile penetration. Furthermore, Smooth Particle Hydrodynamics (SPH), a renowned and a promising numerical approach for large deformation applications is yet unexplored in this field of research. Therefore, with mounting demand in SPH, current dissertation presents the development of SPH model for simulating soil stress field around jack-in pile. Unlike the numerical models in the literature, the SPH model is introduced with minimised simplified assumptions and increased

capabilities for delivering precise estimation and comprehensive understanding of the soil stress field.

For achieving the goal of this thesis, the study initially presents the development of von-Mises and Drucker-Prager constitutive models in two-dimensional (2D) SPH framework for plane stress condition. SPH models are developed comprising each of these constitutive models for examining the stresses and strains of materials under uniaxial compression. The models provide great insight into the behaviour of stresses in materials under loading. During simulation, stresses are experienced outside the yield surface. For eliminating this problem, two-dimensional tension cracking treatment and stress scaling back pressure are introduced for both criteria. Numerical results achieved utilizing the proposed SPH models establish good correlation with analytical solutions. It is found that the developed constitutive models function as fundamental computational frameworks for researchers for analysing stresses and strains in 2D plane stress materials.

Following similar approach, the dissertation further presents von-Mises and Drucker-Prager constitutive models in a complete two-dimensional SPH framework for the investigation of stresses and strains in plane strain applications. SPH models with the proposed plane strain constitutive models are applied for modelling in-plane stresses and strains in materials under uniaxial compression. Numerical results achieved through the proposed plane strain models correlate well with analytical solutions proving the effectiveness of the proposed plane strain

constitutive models in simulating the stresses and strains in plane strain applications.

The thesis finally presents the development of SPH model for simulating jack-in pile installation. The model simulates pile and soil by the proposed von-Mises and Drucker-Prager constitutive models for plane strain condition. In addition to soil stress estimation, the model generates visual representation of both horizontal and vertical soil stress distribution at various pile penetration depths. Such ability of the model provides great insight into the progress of soil stress distribution with pile penetration. Furthermore, the SPH model is proposed to contain the combined ability of simulating pile as an elastic-perfectly plastic material from the soil surface to the end of pile penetration with consideration of soil-pile interaction. This minimises the simplified assumptions made in most of the numerical models in literature. Numerical results achieved with the proposed approach establish good correlation with formerly published experimental solutions. Furthermore, results published using material point method (MPM) are compared. The SPH model successfully simulates the complex phenomenon with reduced simplified assumptions providing reliable estimations and in-depth knowledge of soil stress distribution throughout the installation process. Thus, the proposed model is considered to be a promising numerical approach.

List of publications

1. P. A. Cyril, S. T. Kok, M. K. Song, A. Chan, J.-Y. Wong, and W. K. Choong, "Smooth particle hydrodynamics for the analysis of stresses in soil around Jack-in Pile," *Eur. J. Environ. Civ. Eng.*, vol. 0, no. 0, pp. 1–27, 2019 (In Press).

2. P. A. Cyril, S.-T. Kok, M.-K. Song, A. Chan, J.-Y. Wong and W.-K. Choong. Development of Smooth Particle Hydrodynamics for the Analysis of Stresses and Strains under Plane Stress Condition, Mechanics of Advanced Materials and Structures. (Under Review)

Acknowledgements

First and foremost, I would like to thank God the almighty for providing me the ability, strength and knowledge for successfully completing my research. Without his blessings, this would have been impossible. Secondly, I would like to offer my sincere gratitude to my principal supervisor, Dr. Sien Ti Kok for providing continuous support and motivation throughout my research at the University. It is with her patience and knowledge, I was given the freedom and space for successfully conducting the research. Her experience and knowledge provided immense support to my research. Followingly, I would like to thank my supervisor Dr. Myung Kyu Song. It is an honour to be his first PhD student. I am very grateful for his tremendous support during both uphill and downhill of my project. Even though his presence was not physical after first year of my PhD, the support he provided in the time of need is remarkable. His experience and expertise greatly supported my research.

Help and support from Dr. Choong Wee Kang and Dr. Jing-Ying Wong at the University of Nottingham, Malaysia are highly appreciated. I thank Prof. Andy Chan for the support and insightful discussions on my annual review.

I would like to thank Fundamental Research Grant Scheme Malaysia (FRGS) and the University of Nottingham, Malaysia for the funding of this project.

Finally, I thank my friends for sharing love and support throughout the journey of my research. Without their support, this journey wouldn't be pleasant. A special gratitude to each and every one who in one way or another shared love and support for completing my dissertation.

Contents

Declaration of Authorship ..... **i**

Abstract ..... **ii**

List of publications ..... **v**

Acknowledgements ..... **vi**

List of Figures ..... **xiv**

List of Tables ..... **xxii**

Chapter 1 Introduction **1**

1.1 Background of the study 1

1.2 Statement of the problem 4

1.3 Purpose of the study 8

1.4 Objectives of the study 9

1.5 Summary of original contributions 9

1.6 Significance of the study 11

1.7 Organisation of the study 12

Chapter 2 Literature review **15**

2.1 Importance of piling 15

2.2 Problem with closed-end steel piles 16

2.3 Installation methods for closed-end steel piles 18

2.4 Problem with jack-in installation of closed-end steel piles 20

2.4.1 Experimental investigations on soil stress field around closed-end steel piles 21

2.4.2 Numerical investigations on soil stress field around closed-end steel piles 25

2.5 Numerical Methods adopted for jack-in pile installation 30

2.5.1 Finite Element Method (FEM) 31

2.5.2 Material Point Method (MPM) 33

2.5.3 Discrete Element Method (DEM) 35

2.6 Smooth particle hydrodynamics and its application in geomechanics 37

2.7 Summary of literature review 39

Chapter 3 Methodology 42

3.1 Introduction 42

3.2 Basic formulation of SPH 43

3.2.1 Integral representation of a function 44

3.2.2 Integral representation for the derivative of a function 46

3.2.3 Particle approximation of a function 47

3.2.4 Particle approximation of a derivative of a function 49

3.2.5 Smoothing functions 49

3.3 Governing equations in SPH 51

3.3.1 Derivation of governing equations in Lagrangian form 52

3.3.2 Particle approximation for governing equations in Lagrangian form 57

3.4 Total stress tensor ($\sigma\alpha\beta$) 60

3.5 Constitutive model 63

3.5.1 Elastic-perfectly plastic model 64

3.5.2 Elastic strain rate tensor 65
3.5.3 Plastic strain rate tensor 68
3.6 Failure criterion 70
3.6.1 Tresca criterion 71
3.6.2 Von-Mises criterion 72
3.6.3 Mohr-Coulomb criterion 73
3.6.4 Drucker-Prager criterion 74
3.7 Summary 76

Chapter 4 Development of smooth particle hydrodynamics models for plane stress condition 79
4.1 Introduction 79
4.2 Geometrical setup for uniaxial compression 84
4.3 Development of elastic-perfectly plastic constitutive models for 2D plane stress condition 85
4.3.1 Development of elastic-perfectly plastic constitutive equation for plane stress condition using von-Mises yield criterion 89
4.3.2 Development of elastic-perfectly plastic constitutive equation for plane stress condition using Drucker-Prager yield criterion 92
4.3.2.1 Derivation of 2D-plane stress constitutive model for Drucker-Prager yield criterion with non-associated flow rule 93
4.3.2.2 Derivation of 2D-plane stress constitutive model for Drucker-Prager yield criterion with associated flow rule . 94
4.4 SPH governing equations for 2D compression 96
4.5 Problems in SPH and solving techniques 98

4.5.1 Artificial viscosity 98

4.5.2 Development of tension cracking treatment and stress scaling backpressure for plane stress condition 100

4.5.2.1 Development of treatments for von-Mises yield criterion 100

4.5.2.2 Development of treatments for Drucker-Prager yield criterion 103

4.6 Boundary conditions 105

4.7 Time integration 108

4.8 Flow chart for uniaxial compression 109

4.9 Results 111

4.9.1 Results obtained using von-Mises constitutive model 114

4.9.2 Results obtained using Drucker-Prager constitutive model with non-associated flow rule 121

4.9.3 Results obtained using Drucker-Prager constitutive model with associated flow rule 127

4.9.4 Comparison between results obtained from associated and non-associated flow rule for Drucker-Prager constitutive model 133

4.10 Discussion 134

4.11 Conclusion 137

Chapter 5 Development of smooth particle hydrodynamics for the analysis of stresses and strains in 2D-plane strain structures 139

5.1 Introduction 139

5.2 Development of elastic-perfectly plastic constitutive models for 2D-plane strain condition 141

5.2.1 Development of von-Mises elastic-perfectly plastic constitutive model for 2D-plane strain condition 144

5.2.2 Development of Drucker-Prager constitutive models for 2D-plane strain condition 146

5.2.2.1 Derivation of 2D-plane strain Drucker-Prager constitutive model with non-associated flow rule in SPH framework 147

5.2.2.2 Derivation of 2D-plane strain Drucker-Prager constitutive model with associated flow rule in SPH framework 148

5.3 Numerical application 149

5.4 SPH governing equations for 2D compression 151

5.5 Results 152

5.5.1 Results obtained using von-Mises constitutive model 154

5.5.2 Results obtained using Drucker-Prager constitutive model with non-associated flow rule 159

5.5.3 Results obtained using Drucker-Prager constitutive model with associated flow rule 166

5.5.4 Comparison between Drucker-Prager non-associated and associated flow rule 173

5.6 Discussion 174

5.7 Conclusion 177

Chapter 6 Development of smooth particle hydrodynamics for the analysis of stresses around jack-in-pile 179

6.1 Introduction 179

6.2 Experimental set up of jack-in pile installation 180

6.3 Numerical model for jack-in pile installation 184

6.4 Development of SPH model to simulate jack-in pile installation 188
6.4.1 Problem during simulation and solving techniques 189
6.4.1.1 Artificial viscosity and treatments 190
6.4.1.2 Artificial stress method 190
6.4.1.3 Soil-pile interaction 193
6.4.2 Method of stress computation 194
6.4.3 Boundary condition 194
6.4.4 Time integration 196
6.5 Results and discussion 196
6.6 Conclusion 212
Chapter 7 Conclusion and future work 214
7.1 Conclusions 214
7.1.1 Development and validation of plane stress von-Mises and Drucker-Prager SPH constitutive models 214
7.1.2 Development and validation of plane strain von-Mises and Drucker-Prager SPH constitutive models 215
7.1.3 Development and validation of SPH numerical model with reduced simplified assumptions for modelling jack-in pile installation 216
7.2 Future work 216

Bibliography 219

List of Figures

Figure 2.1: Shallow foundations and Deep foundations. 16

Figure 2.2 : (a) Soil displacement [71]; (b) Pile bearing capacity [7]..... 17

Figure 2.3 : (a) Horizontal stress at final penetration depth, (b) Vertical stress at final penetration depth. [17]. 22

Figure 2.4 : In centrifuge [25]: (a) Radial stress; (b) Vertical stress. In-situ test [23] : (c) Radial stress ; (d) Vertical stress. 25

Figure 2.5 : Discretization of a 2D structure in FEM with triangular elements and nodal points. 32

Figure 2.6 : Discretization of problem domain in MPM: (a) Subdomain for each particle; (b) Fixed Eulerian grid. 34

Figure 2.7 : Particle approximation for particle i within the support domain defined by smoothing function. 37

Figure 3.1: Flow chart of research methodology 43

Figure 3.2: Dirac Delta function when (a) $\boldsymbol{x}' = \mathbf{0}$ (b) $\boldsymbol{x}' = \mathbf{2}$. 45

Figure 3.3: (a) Lagrangian control volume; (b) Change in control volume [77]. 52

Figure 3.4: Infinitesimal fluid cell [79]. 53

Figure 3.5: Forces acting on an infinitesimal fluid cell in x direction [77]. 56

Figure 3.6: (a) Stress vector at point P_0; (b) Stress vector along each plane [98]. 60
Figure 3.7: Stress-Strain relationship for elastic-perfectly plastic model [106]. 64
Figure 3.8: (a) $\boldsymbol{d\sigma\alpha\beta}$ for elastic-perfectly plastic model; (b) Plastic flow for elastic-perfectly plastic model [100]. 70
Figure 3.9: Tresca yield criterial in 2D space [110]. 71
Figure 3.10: Von-Mises yield criterion in 2D space [110]. 72
Figure 3.11: Mohr-Coulomb criterion [110]. 73
Figure 3.12: Drucker-Prager failure criterion in 2D space [111]. 76
Figure 3.13: Methodology in flow chart. 77
Figure 4.1: Geometrical setup for uniaxial compression. 84
Figure 4.2: Tension cracking treatment and Stress-scaling back pressure for von-Mises yield criterion. 101
Figure 4.3: Tension cracking treatment and Stress-scaling back pressure for von-Mises yield criterion. 103
Figure 4.4: Boundary particles: (a) solid boundary; (b) moving solid boundary. 107
Figure 4.5: SPH algorithm for uniaxial compression. 110
Figure 4.6: Average vertical stress-strain curve from simulation for case 1. 114
Figure 4.7: Verification of stress-strain curve from simulation with analytical result for case 1. 115

Figure 4.8: Vertical stress distribution during simulation at different time-steps for case1. 116
Figure 4.9: Average vertical stress-strain curve from simulation for case 2. 116
Figure 4.10: Verification of stress-strain curve from simulation with analytical result for case 2. 117
Figure 4.11: Vertical stress distribution during simulation at different time-steps for case 2. 118
Figure 4.12: Average vertical stress-strain curve from simulation for case 3. 118
Figure 4.13: Verification of stress-strain curve from simulation with analytical result for case 3. 119
Figure 4.14: Vertical stress distribution during simulation at different time-steps for case 3. 120
Figure 4.15: Average vertical stress-strain curve from simulation for case 4. 121
Figure 4.16: Verification of stress-strain curve from simulation with analytical result for case 4. 121
Figure 4.17: Vertical stress distribution during simulation at different time-steps for case 4. 122
Figure 4.18: Average vertical stress-strain curve from simulation for case 5. 123
Figure 4.19: Verification of stress-strain curve from simulation with analytical result for case 5. 123

Figure 4.20: Vertical stress distribution during simulation at different time-steps for case 5. 124
Figure 4.21: Average vertical stress-strain curve from simulation for case 6. 125
Figure 4.22: Verification of stress-strain curve from simulation with analytical results for case 6. 125
Figure 4.23: Average vertical stress-strain curve from simulation for case 7. 127
Figure 4.24: Verification of stress-strain curve from simulation with analytical result for case 7. 127
Figure 4.25: Vertical stress distribution during simulation at different time-steps for case 7. 128
Figure 4.26: Average vertical stress-strain curve from simulation for case 8. 129
Figure 4.27: Verification of stress-strain curve from simulation with analytical result for case 8. 129
Figure 4.28: Vertical stress distribution during simulation at different time-steps for case 8. 130
Figure 4.29: Average vertical stress-strain curve from simulation for case 9. 131
Figure 4.30: Verification of stress-strain curve from simulation with analytical results for case 9. 131
Figure 4.31: Vertical stress distribution during simulation at different time-steps for case 9. 132

Figure 4.32: Stress-Strain from simulation for soil with E=120MPa. ... 133
Figure 4.33: Stress-Strain from simulation for soil with E=207MPa. ... 133
Figure 4.34: Stress-Strain from simulation for soil with E=144MPa. ... 134
Figure 5.1: Vertical stress distribution at various time-steps for case 10. 155
Figure 5.2: Comparison of plane strain and plane stress stress-strain curve for Beryllium alloy..... 155
Figure 5.3: Comparison of plane strain and plane stress stress-strain curve for Aluminium alloy. 155
Figure 5.4: Vertical stress distribution at various time-steps for case 11. 157
Figure 5.5: Comparison of plane strain and plane stress stress-strain curve for Lead alloy. 157
Figure 5.6: Vertical stress distribution at various time-steps for case 12. 158
Figure 5.7: Average vertical stress-strain curve from simulation for case 13. 159
Figure 5.8: Verification of simulation result with analytical result for case 13. 159
Figure 5.9: Comparison of plane strain and plane strain results for Soil with E=120MPa. 159
Figure 5.10: Vertical stress distribution at various time-steps for case 13. 161

Figure 5.11: Average vertical stress-strain curve from simulation for case 14. 161
Figure 5.12: Verification of simulation result with analytical result for case 14. 161
Figure 5.13: Comparison of plane strain and plane stress results for Soil with E=207MPa. 162
Figure 5.14: Vertical stress distribution at various time-steps for case 14. 163
Figure 5.15: Average vertical stress-strain curve from simulation for case 15. 163
Figure 5.16: Verification of simulation result analytical results for case 15. 164
Figure 5.17: Comparison of plane strain and plane stress results for Soil with E=144MPa. 164
Figure 5.18: Vertical stress distribution at various time-steps for case 15. 165
Figure 5.19: Average vertical stress-strain curve from simulation for case 16. 166
Figure 5.20: Verification of simulation result with analytical result for case 16. 166
Figure 5.21: Comparison of plane strain and plane stress results for soil with E=120MPa. 166
Figure 5.22: Vertical stress distribution at various time-steps for case 16. 168

Figure 5.23: Average vertical stress-strain curve from simulation for case 17. 168
Figure 5.24: Verification of simulation result with analytical results for case 17. 168
Figure 5.25: Comparison of plane strain and plane stress results for Soil with E=207MPa. 169
Figure 5.26: Vertical stress distribution at various time-steps for case 17. 170
Figure 5.27: Average vertical stress-strain curve from simulation for case 18. 170
Figure 5.28: Verification of simulation result with analytical result for case 18. 171
Figure 5.29: Comparison of plane strain and plane stress results for Soil with E=144MPa. 171
Figure 5.30: Vertical stress distribution at various time-steps for case 18. 172
Figure 5.31: Comparison between associated and non-associated flow for soil with E=120MPa. 173
Figure 5.32: Comparison between associated and non-associated flow for soil with E=207MPa. 173
Figure 5.33: Comparison between associated and non-associated flow for soil with E=144MPa. 174
Figure 6.1: Experimental setup for measuring stresses in soil [15]..... 180

Figure 6.2: Radial stress at point 55cm depth and 3.6cm radial distance from the pile axis [15]..... 181
Figure 6.3: Vertical stress at end of: (a) push; (b) pause [18]..... 182
Figure 6.4: Radial stress at end of: (a) push; (b) pause [18]. 182
Figure 6.5: (a)-(c) horizontal stress; (d)-(e) vertical stress during jack-in pile installation [29]. 183
Figure 6.6: SPH particle arrangement for Jack-in pile installation. 185
Figure 6.7: SPH algorithm for modelling jack-in pile installation..... 187
Figure 6.8: Tensile instability during jack-in pile installation. 191
Figure 6.9: Soil particle penetrating through pile particle..... 194
Figure 6.10: Solid boundary particles..... 195
Figure 6.11: Radial stress during jack-in pile installation at the end of each: (a) push; (b) push; (c) pause; (d) pause..... 199
Figure 6.12: Vertical stress at the end of each: (a) push; (b) pause. 201
Figure 6.13: Horizontal stress distribution..... 205
Figure 6.14: Vertical stress distribution. 210
Figure 6.15: SPH results with measured and MPM solutions. 211

List of Tables

Table 4.1: Material Parameters. 85

Table 4.2: Accuracy of von-Mises constitutive model..... 135

Table 4.3: Accuracy of Drucker-Prager constitutive model. 137

Table 5.1: Material Parameters. 150

Table 5.2: Accuracy for plane strain models. 175

Table 6.1: Material parameters for jack-in pile simulation..... 186

Table 6.2: Comparison between experiment and SPH results. 197

Table 6.3: Comparison between experiment and MPM results..... 206

Chapter 1
Introduction

1.1 Background of the study

Piles are the most important and widely used type of deep foundation. They are slender and relatively long structural members which transfer overlying structural loads to deeper firm layers of soil. Since primitive years, piles have been extensively employed for supporting overlying structures built in unfavourable soil conditions for shallow foundations.

For designing purposes, piles have been categorized as end bearing piles and friction piles. End bearing piles support the overlying structure through its end bearing capacity by resting on a relatively incompressible stratum. On the other hand, friction piles sustain the overlying loads through the built in skin friction achieved during the installation [1]. However, the load bearing capacity of a pile depends on both end resistance and skin friction after installation. This is because, the dynamic response of soil due to soil-pile interaction resulting from the installation process greatly influence the designed values of end resistance and skin friction. This in result alters the designed pile bearing capacity. Thus, the method of pile installation plays a pivotal role in determining the pile bearing capacity.

The methods of pile installation vary from bored to driven piles. During installation, bored piles known as non-displacement piles cause little or no change to the displacements of surrounding soil. Instead, the piles are formed in or placed within the pre-bored holes in the soil stratum. Therefore, bored piles cause minimum variations in the soil stress levels [2]. As such, bored piles retain the designed values of pile bearing capacity. Conversely, driven piles identified as displacement piles generate extreme deformations in the surrounding soil during installation.

Displacement piles are closed-end steel / timber / concrete piles driven with means of hammer / vibration / jacking mechanism [3]. Hammer driven piles are installed by means of hammer impacts. The hammer is dropped from a certain height for installing the pile and the motion is repeated until the final depth of penetration. Alternatively, piles could be driven with means of vibrations. Based on this method, the pile is driven into the ground using an appropriate level of vibration to overcome the skin friction. On the other hand, hydraulic jacks could be also employed for installing piles. According to this mechanism, piles are jacked into the ground at constant speed involving continuous cycles of loading and unloading.

However, among the installation methods, hammer driven piles and piles driven through vibrations inherit several drawbacks. These methods generate impacts or vibrations on the piles. Such vibrations transfer from pile to the surrounding soil due to soil-pile interaction. Subsequently, these vibrations propagate from soil to neighbouring structures and may lead to

severe damages in adjacent structures. In addition, these installation methods cause great disturbance to surrounding occupants [4]. Hence, both the installation methods are inappropriate for urban environment. On the other hand, jacking mechanism is proven to minimise such impacts on the environment. The method causes reduced noise contributing to minimised disturbance to the surrounding occupants. As such, the installation method is most preferred in the urban environment [5], [6]. Therefore, jacking mechanism is the most promising installation technique in comparison to the conventional driven methods.

Even though jack-in pile installation is most preferred and contains greater benefits, similar to other displacement piles, the method generates large amount of soil displacement around the pile's vicinity [7], [8]. Such large deformations in soil significantly varies the soil stress levels contributing to changes in the estimated pile bearing capacity [9]–[11]. In addition, such changes in stresses not only affect the pile's performance but also affect the stresses exerted on adjacent sub-structures [12]. Insufficient knowledge in the magnitude of stress changes cause great difficulty for engineers to understand the soil behaviour near the pile during installation. Therefore, it is significantly important for obtaining an in-depth understanding of the soil stress response during the installation of a jack-in pile.

1.2 Statement of the problem

Stresses in soil around jack-in pile is an intensely researched sector due to the increased complexity in understanding the soil response during installation [9], [10], [13], [14]. This phenomenon has been widely explored via several empirical methods. In these approaches, soil stress measurements have been increasingly performed through the placement of stress sensors [15]–[20] or null gauges [12] in the soil mass. However, great difficulties have been encountered in acquiring the soil stress measurements during the installation phase. Extreme deformations cause movements in the locations of sensors making it extremely troublesome for obtaining accurate stress measurements near the pile shaft. Furthermore, achievement of a detailed stress field demands large number of sensor placement in the soil. [15], [16]. In addition, sensors and cables tend to reinforce the surrounding soil resulting in considerable increment to local stress values. As such, it has become vitally important to record local stress values during the installation [14], [18].

In midst of the above experimental difficulties in obtaining precise soil stress measurements, it is essential to establish accurate measurement of soil stress field for complete understanding of soil-structure interaction, load-displacement response and time-dependent behaviour of the phenomenon. An accurate numerical model contains the potential in providing the powerful insights. However, for accurate simulation, the numerical model should be capable of incorporating the

modelling of extreme stresses, large deformations, moving boundaries, pile-soil interaction, load cycling and particle breakage. Nevertheless, consideration of all these factors inflict great modelling difficulties [11], [12], [14]. As a result of such complications, stresses in soil around jack-in pile has been modelled with various simplified assumptions.

Finite element method (FEM) has been primarily employed in modelling the scenario. The grid-based models either considered the pile as a rigid material [21]–[23] and / or performed the simulation on a pre-embedded pile [24], [25] or modelled the pile as an elastic material [26]. Such simplified assumptions have been adopted for minimising the difficulties and complications involved in the simulation.

Apart from grid based methods, stresses in soil around jack-in pile has been numerically attempted by a few meshless methods such as material point method (MPM) and discrete element method (DEM) [11], [27]–[29]. Even though the few attempts of employing meshless methods were able to handle large deformations with simplicity, most of the studies contained various simplified assumptions as the grid-based methods. The pile has been pre-embedded and / or modelled as a rigid material [27], [28]. Even though, Esposito et al. [11] avoided the above simplified assumptions, the study achieved only qualitative agreement with the empirical soil stress measurements.

Furthermore, it should be emphasized that soil-pile interaction is an important feature to be considered when modelling the stresses in soil during installation. Stresses generated by jack-in motion is transferred

from the pile to surrounding soil through soil-pile interaction. Hence, neglecting soil-pile interaction contributes to reduced accuracy in soil stress estimation. However, soil-pile interaction has been seldom considered in the numerical studies of jack-in pile installation [11], [23], [26].

Moreover, there is lack of clear visualisation of soil stress contour plots during the installation. Experimental and numerical soil stress distributions have mostly been presented at the final depth of penetration [14], [18], [23], [26], [30]. Nevertheless, it should be highlighted, presentation of visual images of soil stress distributions at various penetration depths will certainly contribute to greater understanding of the soil behaviour throughout the installation.

It is obvious from above, none of the numerical models in the literature contained the combined ability of modelling the pile as an elastic-perfectly plastic material from the soil surface with consideration of soil-pile interaction and to provide graphical representation of the system behaviour throughout the installation.

Apart from above, as mentioned earlier, FEM has been primarily employed to model stresses in soil around jacked pile. However, the traditional grid-dependent method is not well suited for large deformation applications involving excessive mesh distortions. Pile installation comprises large deformations in soil around the pile's vicinity. Hence, the method fails to capture such deformations due to its grid-based system [28]. Its discontinuous property makes the approach unreliable for stress

computation. In addition, mesh generation is time consuming. As such, major costs are incurred. Therefore, grid-based methods may lead to serious computational difficulties and inaccuracies in modelling the jack-in pile installation [31]–[33].

In comparison to grid-based methods, meshless methods are more appropriate to simulate stresses in soil around jacked pile. This is because the methods not only contain the capability of handling large deformations, but also contribute to minimised computational difficulties and inaccuracies due to the absence of mesh distortions [31]–[33]. Based on literature, meshless methods MPM and DEM have been employed to model the phenomenon. Even though these numerical models can easily handle large deformation scenarios, the models either adopted several assumptions to simulate the scenario or provided qualitative agreement with the experimental solutions or delivered lack of knowledge in the soil stress distribution. Nevertheless, due to the advanced nature of meshless methods for large deformation applications, it is worth considering the development of a mesh-free method to analyse stresses in soil around jack-in pile.

Among the mesh-free methods, Smooth Particle Hydrodynamics (SPH), an ancient mesh-free method introduced in 1977 [34], [35] is yet unexplored in this field of research. SPH possess several advantages over grid-based methods. It well simulates material interfaces, free surfaces and moving boundaries. Most importantly, SPH holds the capability of modelling extremely large deformations. Thus, the method has been

extensively employed in many engineering and science applications. SPH method has been developed and applied to various problems in hydraulics [36]–[40], failure of solids [41], free-surface and multiphase flows [42]–[44], fluid-structure, soil-water interaction [45], [46], heat transfer [47], dynamic responses of materials [48], [49] and many more. In addition, the enduring success of the method steered its development for many geotechnical applications [50]–[57]. The above studies prove the capability of SPH in successfully simulating multidisciplinary applications with extreme deformations. As such, due to the advanced nature and success of the method, it is worth considering the development of a SPH model to simulate jack-in pile installation with the lacking combined capabilities from the numerical models in the literature.

1.3 Purpose of the study

The aim of this research is to develop SPH model for providing increased understanding and reliable estimation of soil stress field around jack-in pile. As such, unlike previous numerical models, the study focuses on developing the numerical model with unique combined ability to model pile as an elastic-perfectly plastic material from the soil surface with consideration of soil-pile interaction and to present graphical images of soil stress distributions at various pile penetration depths.

1.4 Objectives of the study

1. To develop plane stress von-Mises and Drucker-Prager constitutive models in two-dimensional SPH framework.
2. To validate plane stress constitutive models with analytical solutions.
3. To develop plane strain von-Mises and Drucker-Prager constitutive models in two-dimensional SPH framework.
4. To validate plane strain constitutive models with analytical results.
5. To develop SPH numerical model to analyse stress fields in soil around jack-in pile with minimised simplified assumptions.
6. To validate SPH model with previously published experimental and numerical results.

1.5 Summary of original contributions

The novelty of this work is to expand the knowledge on soil stress fields around jack-in pile through the development of a plane strain SPH model with reduced simplified assumptions. Perseverance to this, the study initially presents von-Mises and Drucker-Prager elastic-perfectly plastic constitutive models in a complete two-dimensional SPH framework for plane stress condition. For the derivations of these constitutive models, the study introduces second invariant of deviatoric stress tensor in terms of hydrostatic stress rate tensor and deviatoric stress rate tensor. In addition,

two-dimensional tension cracking treatment and stress scaling back pressure are proposed for both criteria for eliminating the numerical error in stress computation. A method has been introduced for the stress computation at the solid boundary particles. Finally, SPH models comprising the above developments are proposed in present dissertation for examining the internal stresses and strains in 2D-plane stress materials under uniaxial compression. Analytical solutions are presented for the verification of the proposed numerical models.

Once the developed models were capable of accurately simulating the stresses and strains in 2D plane stress materials, utilizing similar approach, the study presents the development of von-Mises and Drucker-Prager constitutive models on *xy* space for plane strain condition. SPH models comprising these plane strain constitutive models are applied to simulate stresses and strains on *xy* space in plane strain materials under uniaxial compression. The study presents analytical results for verifying the numerical results.

Subsequently, the thesis presents the development of the SPH model comprising the proposed plane strain constitutive models and treatments for both Drucker-Prager and von-Mises yield criterion including the proposed methodology of stress computation at the solid boundary for modelling the complex phenomenon. Results acquired using the developed SPH model are verified through previously published experimental results by Richard et al. [15], [18] and numerically simulated results by Lorenzo et al. [28].

The SPH models presented in this thesis are constructed with means of C++ language, OpenGL and OpenCL. OpenGL is employed to produce graphical images of system behaviour throughout the simulation and OpenCL is adopted to parallelize the programme code for minimizing the computational period.

1.6 Significance of the study

The thesis presents the development of general smooth particle hydrodynamics (SPH) constitutive models to solve plane stress (2D) elastic-perfectly plastic problems. These developed models function as a fundamental computational framework for researchers to analyse stresses and strains in 2D-plane stress structures. Similarly, developed plane strain elastic-perfectly plastic constitutive models on *xy* space could be utilized in plane strain applications to analyse stresses and strains under applied loads. Therefore, the developed general constitutive models for both plane stress and plane strain conditions in SPH framework are promising and significantly important platforms for the modelling of respective structures in engineering applications.

In addition to above, none of the numerical models in the literature existed with the combined ability to model the pile as an elastic-perfectly plastic material from the soil surface along with the consideration of soil-pile interaction and to provide graphical images of the model behaviour at various depths of pile penetration. Therefore, through the outcome of this

thesis, smooth particle hydrodynamics is not only developed for the first time in literature to simulate stresses in soil around jacked pile but is also developed with the lacking combined features in previous numerical models. Large deformations were simulated with reduced difficulty, facilitating concurrent precise measurements of horizontal and vertical stresses in soil. Pile was modelled with ease from the soil surface due to the method's mesh-free nature. Furthermore, generation of visual images provided greater insight into the progress of stress distribution which has not been performed well in the past. Hence this thesis not only developed general platforms to simulate plane stress and plane strain problems, but also developed SPH to handle a complex scenario and to study the stresses in the vicinity of the pile with minimised simplified assumptions. The acquaintance in stresses developed around jacked piles are essential as bearing capacity and skin friction are dependent on it. Therefore, present research enhances the knowledge in such complex phenomenon and contributes to engineers for establishing safe and economical installation.

1.7 Organisation of the study

Chapter 2 presents the literature review on current state of knowledge of pile foundations and its installation methods. The importance of soil stress measurements during the installation of a closed-end steel pile through jack-in mechanism is highlighted in this chapter. A comprehensive review is conducted on both experimental and numerical studies focusing on the

investigation of soil stress measurements around jack-in pile. In addition, the chapter comprises a brief discussion on the numerical methods which have been previously employed. Finally, the importance of adopting SPH method is emphasized and a review on the numerical method is included in this chapter.

Chapter 3 presents the literature survey on SPH basic formulations. Additionally, for completing these basic formulations, detailed comprehension on total stress tensor, constitutive models and various types of failure criterion are included. Through this, the selected SPH basic formulations employed in the development of the SPH models are highlighted in this chapter.

Chapter 4 introduces von-Mises and Drucker-Prager constitutive models in SPH framework for plane stress condition. For achieving these formulations, the chapter introduces second invariant of deviatoric stress tensor in terms of hydrostatic stress rate tensor and deviatoric stress rate tensor. The chapter comprises the development of two-dimensional tension cracking treatment and stress scaling back pressure for both criteria. A stress computation method at the model boundaries is proposed in this chapter. Comprising the above, an SPH algorithm is introduced for analysing the stresses and strains in 2D plane stress materials under uniaxial compression. Analytical solutions are further included in this chapter for validating the proposed numerical models.

Chapter 5 presents the development of von-Mises and Drucker-Prager constitutive equations in two-dimensional SPH framework for plane strain condition. Utilizing the proposed SPH algorithm in chapter 4, SPH models are constructed with the proposed plane strain constitutive models in current chapter for the investigation of stresses and strains in 2D plane strain materials under uniaxial compression. Analytical solutions are obtained and presented in this chapter for the validation of the numerical results.

Chapter 6 introduces the SPH model with the combined ability for the investigation of soil stress fields around jack-in pile. Detail description of the SPH algorithm employed for the enhancement of the SPH model for current analysis is presented in this chapter. The numerical results are validated through previously published experimental and numerical solutions.

Chapter 7 concludes this thesis with the summary of findings and recommendations for future work.

Chapter 2
Literature review

2.1 Importance of piling

Factors such as soil condition, weight and height of superstructure determines the type of foundation necessary for supporting the overlying structure. Foundations could be either built in shallow depths, widely known as shallow foundations or be driven or casted into deeper soil stratum which are under the category of deep foundations. As illustrated in Figure 2.1, structures comprising reduced weight and containing good soil conditions are generally supported by shallow foundations such as pad footing / raft foundation / strip footing. Alternatively, taller and heavier structures with multiple stores and / or containing poor soil conditions are commonly supported by pile foundations. As such, piling is an essential type of foundation as structures are able to be constructed at various locations despite its heavy weight, multi-storeyed structure and deprived soil condition.

The demand for pile foundations have inclined over the years due to significant increase in number of multi-storey buildings. Heavy and multiple floored structures are being built due to increased population and limited space [58], [59]. Multi-storeyed structures require transferring of

loads to deeper firm stratum for acquiring sufficient bearing capacity. Hence, the demand for pile foundations have increased. As such, due to diverse soil conditions and design requirements various types of piles and pile installation methods have been introduced.

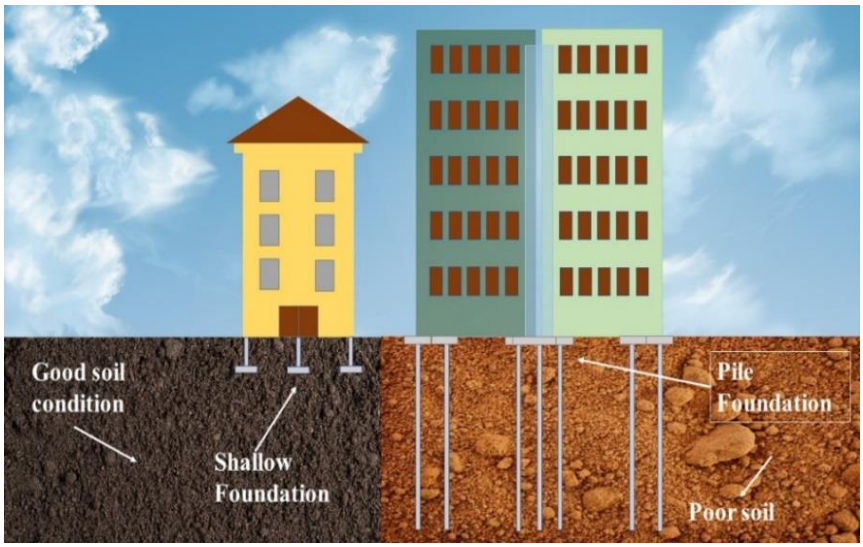
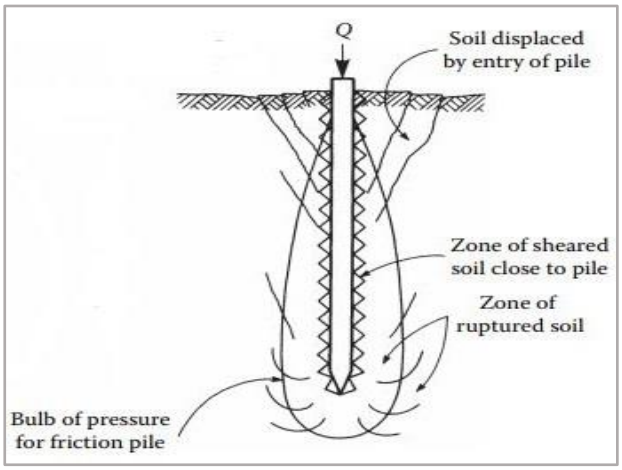


Figure 2.1: Shallow foundations and Deep foundations.

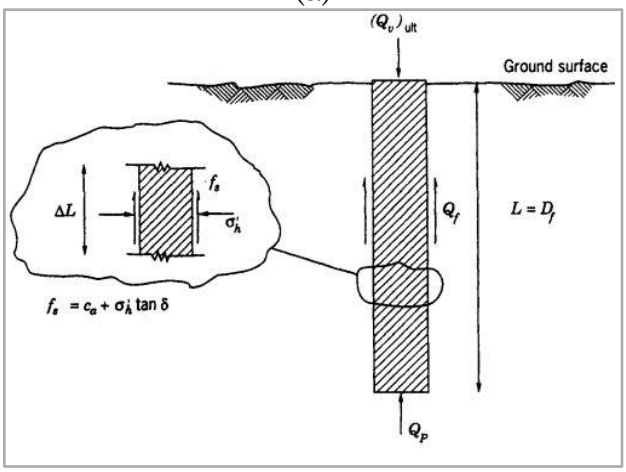
2.2 Problem with closed-end steel piles

Even though steel piles are of high demand, during the installation of a closed-end steel pile, the soil is pushed away resulting in large deformations around the pile as shown in Figure 2.2a. Such deformations lead to changes of stress levels in the surrounding soil. The evolution of such changes in the stress field continues as the pile further penetrates the ground. Consequently, the disturbed soil results in a new stress state with new strength properties. It is well known that the load bearing

capacity $(Q_v)_{ult}$ of a pile depends on the surrounding soil from which the pile gains its support through the skin friction (Q_f) and end-bearing capacity (Q_P) as illustrated in Figure 2.2b [7]. Therefore, since the skin friction and end bearing capacity depend on the final soil properties, the designed pile bearing capacity becomes inconstant with the in-situ pile bearing capacity [60], [61]. This problem exists for closed-end steel piles despite the differences in its installation methods.



(a)



(b)

Figure 2.2 : (a) Soil displacement [71]; (b) Pile bearing capacity [7].

2.3 Installation methods for closed-end steel piles

Pile installation methods such as hammer, vibration, jacking have been adopted for the installation of closed-end steel piles [62], [63]. Among the methods, hammers are used to drive the piles into the ground by means of hammer impacts. A variety of hammers such as drop hammers, hydraulic hammers, single-acting vapour, double-acting vapour and diesel hammers have been employed in the industry. These categories differ based on the energy of the hammer in a single blow and on the rate of blow per unit time. A drop hammer is a steel block weighing half to two times the weight of pile which is dropped from a height onto the pile head and elevated back with means of pulley. The motion of releasing the hammer and lifting it to required height is repeated until the pile has reached its sufficient depth into the soil mass [63]. Similarly, in hydraulic hammers, hydraulic fluid is used instead of pulley. The mechanism includes fluid transportation from high pressure to low pressure chambers for lifting and dropping of the hammer. The cycle is repeated until the pile is driven into the final penetration depth [64]. On the other hand, vapour is used as a key factor in functioning both single-acting and double-acting vapour hammers. For single-acting vapour hammers, inflow of vapour is utilized to lift the hammer. Ones the inflow is terminated, the hammer strikes the pile. Having similar technique, double-acting vapour hammers further provide a second source of steam from the top during the release of the hammer. This facilitates rapid fall of the hammer onto the pile head [7].

Furthermore, explosion of diesel in combustion chamber contributes to the function of diesel hammers. During the downward motion of hammer, diesel is injected into the combustion chamber filled with compressed air. Ones the hammer impacts the pile, explosion is induced for elevating the hammer. This process is repeated until the pile achieved its final depth [64].

Apart from above, piles are also driven with means of vibration. This is performed by providing stationary heavy weight and vibration in perpendicular direction to the pile length. Such method is generally efficient for open-end than closed-end steel piles. Moreover, the method is limited to softer and unconsolidated soil, whereas impact hammers contain the capability of driving piles into wide range of soil conditions. The method further demands impact from drop hammer at the end of pile installation to ensure the achievement of final bearing capacity as the driving method does not involve a force to install the pile. Hence, in comparison, hammers are mostly employed to install closed-end steel piles than vibration method [65]. However, both driving methods generate significant disturbance to the surrounding habitat and nearby structures [60], [62].

On the other hand, pile jacking is a quiet alternative approach. The method uses static load unlike the dynamic installation methods which results in reduced impact to the environment. Pile jacking is performed with means of pile jacking rig. The process is initiated by the installation of rig at a point of pile penetration. The pile is held in a vertical position at

the point by a clamping mechanism. Ones the pile is positioned, hydraulic jack presses the pile into the ground with means of a jacking force up to a standard length. As it reached, the pile is released, and the jacking mechanism is lifted to repeat the cycle. This is continued until the final penetration depth [66]. The press-in mechanism involved in jack-in pile installation reduces vibrations in the ground by an order of magnitude in comparison to dynamic piling methods such as hammers and vibrators. Hence, the method is well appropriate for the installation of piles in urban environment. Therefore, it is apparent, among the piling methods for closed-end steel piles, jacking method is most preferred due to its reduced generation of vibration and noise to the surroundings. Furthermore, due to such benefits the method has become increasingly valuable and has gained significant demand in construction industry [67]–[70].

2.4 Problem with jack-in installation of closed-end steel piles

Even though jack-in mechanism is the most popular and preferred method of pile installation for closed-end steel piles, the method inherits a major drawback similar to other installation methods. The installation approach displaces large amount of soil around the pile's vicinity [12], [71]. As discussed in Section 2.2, the extreme deformations result in significant changes to the soil stress levels considerably affecting the pile bearing capacity [9], [10], [24]. In addition, such variations in stresses affect the

stresses exerted on adjacent sub-structures [12]. As such, it is significantly important for understanding the soil stress response during the installation. This will contribute to engineers for providing safe and economical designs of pile foundations. Therefore, a wide range of studies have been conducted in the past for well understanding this phenomenon.

2.4.1 Experimental investigations on soil stress field around closed-end steel piles

Experimental investigation of soil stresses requires the placement of stress sensors at various locations within the soil mass. Many considerations should be accounted when adopting these measuring devices. However, a complete attention is not often provided. Placement of sensors itself alters the in-situ stress states contributing to imprecise readings. Stress sensors replacing sand materials should contain identical material properties which is impossible to obtain. This further demands the understanding of the interaction between soil and stress sensors. Based on these understandings authors have adopted correction factors for acquiring the field stresses from the measured values [61]. Therefore, it is apparent that understanding the stress levels in soil through experiments is of great complexity. In midst of such increased difficulty few researchers have performed experimental investigations on the analysis of soil stress field during the installation of jack-in pile.

Dijkstra et al. [14] made an attempt to empirically acquire soil stress field during the jacking of a steel model pile in a photoelastic material. The development of stresses and strains were quantified using the photoelastic method. This alternative approach has been adopted for avoiding the problems associated in measuring the stresses with means of transducers. The study managed to quantify horizontal stresses at various points in the soil mass. However, it should be emphasized that the experiment was performed on glass particles instead of soil and stress contour plots were not presented in the study.

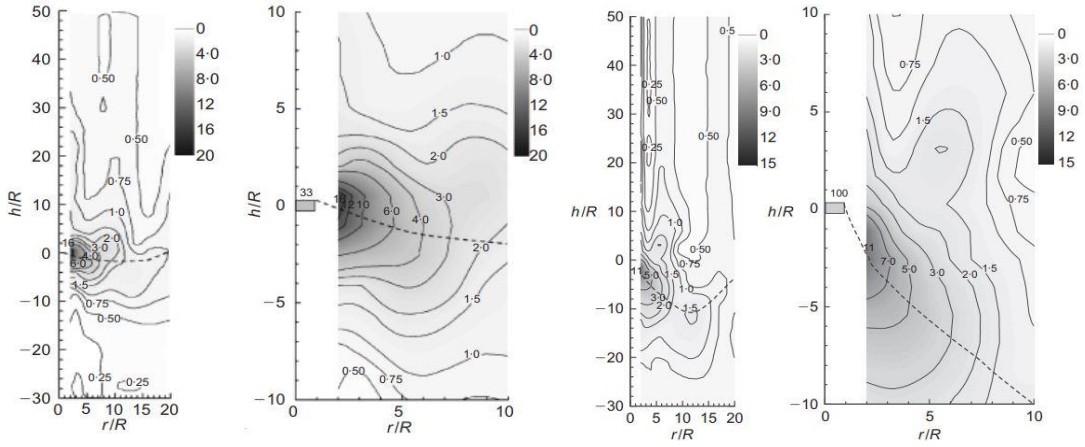


Figure 2.3 : (a) Horizontal stress at final penetration depth, (b) Vertical stress at final penetration depth. [17].

Thereafter, Jardine et al. [15] and Zhu et al. [16] proposed an experimental arrangement for jack-in installation of a closed-end steel pile in a calibration chamber. The method was introduced for obtaining reliable stress measurements in the soil. Jardine et al. [15] placed 12 diaphragm cells in the soil mass for measuring stresses in locations between 2R and 20R distance from the pile axis, where R is considered to be the radius of

the pile. Similarly, Zhu et al. [16] measured stresses in soil at 40 locations within the calibration chamber. Locations were selected to be within the range 1-10 pile diameters from the pile axis. However, the authors provided horizontal stress values only at 0.55m depth and 2R distance from the pile axis throughout the installation process. The authors faced great difficulty during the measurement of soil stresses near the pile shaft due to extreme load fluctuations. Extreme loads varied the positions of sensors making it extremely troublesome for obtaining accurate stress measurements. Furthermore, the authors stated that, multiple number of sensors are necessary for acquiring reliable trends of soil stress distribution. As such, it is obvious that the process of obtaining reliable soil stress field during the installation is extremely complicated.

Subsequently, employing similar experimental setup as Jardine et al. [15], Jardine et al. [18] provided both horizontal and vertical stresses for two additional points in the soil mass at 3R and 8R distances from pile axis at 0.7m depth. Even though the measurements were acquired, great difficulty was encountered by the authors during stress measurements. Some instrument cables parted during the installation process and several devices were overloaded. Furthermore, cells and cables had a tendency to reinforce the surrounding soil causing rise to the local stress value by 15-17%. This further demanded the measurement of local stress values during the installation.

Moreover, utilising similar experimental setup as Jardine et al. [18], Jardine et al. [17] provided horizontal and vertical stress contour plots in

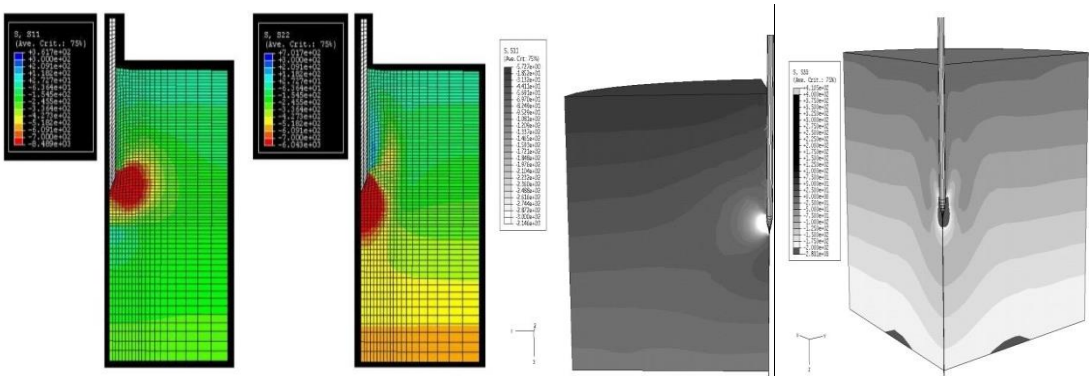
the soil mass. This is shown in Figure 2.3. The plots have been experimentally achieved for the first time in the literature. The plots were obtained with means of sensor array placement at various levels within the soil mass. However, the authors faced great difficulty in establishing vertical stress trends near the pile shaft as the sensors and connecting cables tend to move apart due to steep radial and vertical soil movements.

Subsequently, instead of employing stress sensors, Burali et al. [12] measured soil stresses through the placement of null-gauges embedded in adjacent pile and in surrounding soil. The study provided comprehension of soil stresses for piles jacked in adjacent to existing piles. However, the presence of adjacent pile disturbs the actual soil stress distribution from the jack-in of a closed-end steel pile. Thus, the approach prevents from achieving a complete understanding of the soil stress response during the installation of a jack-in pile.

Furthermore, Wang and Zhang. [19] developed an experimental setup for exploring the behaviour of friction fatigue by soil stress variation around jack-in pile. The variations in soil stresses were empirically obtained with means of pressure sensors. Similarly, the study performed by Lu et al. [20] involved the investigation of horizontal soil stress field through the placement of pressure sensors at various locations within the soil mass. However, the employment of stress sensors in above studies are known to generate great level of complexity in achieving accurate stress measurements.

Therefore, it is apparent from above literature, obtaining accurate soil stress measurements through experiments is an extremely challenging process. It can be observed that, large soil deformations occurring around the pile shaft is the main contributing factor for such increased complexity.

2.4.2 Numerical investigations on soil stress field around closed-end steel piles



(a) (b) (c) (d)

Figure 2.4 : In centrifuge [25]: (a) Radial stress; (b) Vertical stress. In-situ test [23] : (c) Radial stress ; (d) Vertical stress.

In midst of the difficulty in acquiring empirical soil stress measurements, the phenomenon has been widely explored via several numerical approaches. Sheng at al. [23] used a numerical approach using FEM for modelling jack-in installation of a closed-end steel pile in a centrifuge with dry sand. The study simulated soil-pile interaction using a Lagrangian multiplier method. The approach allowed the authors to simulate pile penetration from the soil surface to the desired depth. The study assumed the pile to be rigid and modelled soil using modified Cam Clay model. The

study quantified the stresses at three points in the soil mass and presented both horizontal and vertical soil stress distributions at the final depth as shown in Figure. 2.4 (a and b) respectively.

Continuing the research by Sheng at al. [23], Sheng at al. [26] modelled the scenario with consideration to frictional contact at the soil-pile interface. Instead of considering the pile as a rigid material, the pile was modelled as an elastic material. Even-though the research was focused on frictional contact between the pile and soil, the study provided both vertical and horizontal soil stress distribution at the final depth of penetration. However, stresses were not analysed at various points in the soil mass during the installation. The authors stated that severe mesh distortions resulting from the installation is yet a major challenge to be confronted by the numerical model.

Similarly, Henke and Grabe. [21] introduced a three-dimensional finite element method for the investigation of pile installation process and its influence on adjacent structures. The pile was modelled as a rigid material and the behaviour of soil was investigated using a hypo-plasticity constitutive model. The study presented both horizontal and vertical in-situ soil stress contour plots at the end of penetration of a jack-in pile as illustrated in Figure 2.4c and d. However, the work was not focused on the quantification of stresses at various points within the soil mass throughout the installation. Furthermore, it should be emphasized that a three-dimensional model consumes greater computational cost than a 2D model.

Dijkstra et al. [30] modelled jack-in installation of a closed-end steel pile using Eularian code. The study employed Mohr-Coulomb constitutive model for representing the soil material. Two approaches were carried out for the simulation of the installation process. In the first approach, pile was pre-embedded within the soil mass for avoiding large mesh distortions during the installation. The method involved the movement of soil while maintaining the pile fixed. On the other hand, the second approach moved the pile geometry while maintaining the mesh fixed. However, the force achieved on the pile base from each of these methods deviated from the experimental solutions. In addition, the study presented horizontal and vertical soil stress distributions for both approaches at 5 meters of pile penetration.

Moreover, Qiu et al. [25] numerically simulated jacking pile installation process using Coupled Eulerian-Lagrangian (CEL) method. The method adopted hypo-plastic constitutive model for representing the soil material. Stress states in surrounding soil were analysed during the installation phase along the radial distance from the pile axis at 2.0m depth. The results were compared with classical FEM approach. In addition, horizontal stress contour plots were provided at 5m of pile penetration. Even though the model proved its success in simulating the stresses in soil around jack-in pile, the pile was modelled as a rigid material. The authors simulated the pile penetration from the top to the final depth of pile penetration which is an extremely challenging phenomenon to model. However, the pile was pre-embedded to an initial

depth of 40cm above the soil surface for avoiding large deformations at the beginning of the installation. This led to additional mesh generation above the soil surface. Moreover, such modelling procedure fails to replicate the actual loosening and uplift of the soil at the surface.

Phuong et al. [27] numerically simulated the installation of a pushed in steel pile in a centrifuge using Material Point Method (MPM). Soil was modelled with means of an elasto-plastic Mohr-Coulomb constitutive model. The model considered the pile as a rigid material and the pile was pre-embedded to a depth of 1.13cm prior to installation. Visual image of horizontal stress distribution was only provided at the end of pile penetration.

Zhang et al. [22] predicted stresses in soil around a jack-in steel pile using the FEM approach proposed by Zhang et al. [72] involving the breakage mechanics. The authors compared the numerically simulated stress results with experimental solutions published by Jardine et al. [15], [17]. However, the approach simulated the pile as a rigid material and the pile was only modelled for 4m of penetration within the soil mass. Furthermore, stress contour plots were not provided for in-depth understanding of the stress development during the pile installation. Thereafter, Liu and Wang. [29] developed a two-dimensional discrete element model to exploit development of stresses in soil during pile installation. Stresses at various locations within the soil mass were quantified. However, graphical representations of stress distributions were not presented at various pile penetration depths.

Subsequently, Lorenzo et al. [28] employed MPM for simulating the scenario featuring radial stresses in soil surrounding the jack-in installation of a steel pile. Nevertheless, pile was considered to be rigid and modelled with means of a moving boundary condition. Modified Cam Clay and Subloading Cam Clay constitutive models were employed for simulating the soil behaviour. The authors compared simulated results with measured values published by Jardine et al. [17] and Yang et al. [73]. Even though the simulated curves plotted for horizontal stresses comprised similar trend to the measured plots, the results were far from the experimental solutions. In addition, the numerical model failed to provide vertical or horizontal stress contour plots in the soil during the penetration process.

Thereafter, Esposito et al. [11] numerically simulated stresses at two points within the soil using discrete element method (DEM) including the particle rotation during jack-in pile installation. The results were compared with previously published experimental results by Jardine et al. [17] and Yang et al. [73]. Even though the numerical model was capable on providing qualitative agreement with experimental solutions, stress contour plots were not presented. Moreover, an up to date summary on both experimental and numerical studies on soil stress fields during pile jacking are included in the study performed by Jardine and Yang. [74].

According to literature, numerical methods based on FEM, DEM and MPM have been employed to model the phenomenon. However, both mesh-based and mesh-free methods have adopted various simplified

assumptions in simulating the scenario. The models either considered the pile as a rigid / elastic material and / or performed the simulation on a pre-embedded pile. In most of the previous studies, pile has been assumed to be pre-embedded or rigid for minimising the difficulty and complications involved in the simulation. However, such assumptions fail to characterize the actual soil stress response due to soil-pile interaction. Even though certain authors managed to avoid these assumptions, the models provided only qualitative agreement with experimental results and lacked visual understanding of the soil stress response throughout the installation contributing to insufficient knowledge of the phenomenon. Thus, it is obvious, there is no reliable numerical tool in the literature with minimised simplified assumptions and ability to provide graphical images of the soil stress distribution throughout the installation for delivering comprehensive understanding of the soil stress response during the jack-in installation of a closed-end steel pile.

2.5 Numerical Methods adopted for jack-in pile installation

As discussed in Section 2.4.2, numerical methods such as FEM, MPM and DEM have been primarily attempted for exploring the soil stress fields around jack-in installation of closed-end steel piles. As such, these methods are discussed in brief as follows:

2.5.1 Finite Element Method (FEM)

The fundamental feature of finite element method is that the method uses 'finite elements' to model the problem domain (structures / solids). The method discretizes the structural system into multiple number of elements and connects each element through nodal points for assembling the desired structure. As an illustration, Figure 2.5 is included where a 2D rectangular structure is build-up by multiple number of triangular elements and nodal points.

During modelling, FEM provides solution for the structure by combining the field variables (velocity / displacement / pressure / potential / temperature) of each element. Variation in any of these properties within an element is computed by approximating functions in-terms of the values of the field variable at its nodal points. Thus, it is apparent that the value of a field variable of an element depends on the field variable's value at the nodes of an element. Thus, the number and size of the elements through which the structure is discretized plays a pivotal role in determining the accuracy level of solutions. Greater the number and lesser the size of elements, the higher would be the level of accuracy. However, this significantly increases the computational cost of the numerical model [33], [75].

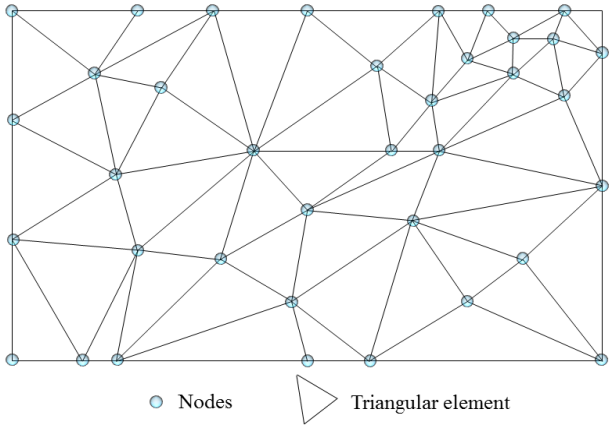


Figure 2.5 : Discretization of a 2D structure in FEM with triangular elements and nodal points.

FEM method has been widely employed for modelling many engineering applications. This has been due to its increased benefits such as its applicability to vast range of problems in fluids and solids involving elastic / non-elastic / linear / non-linear / plastic behaviours and crack propagations. The method further contains the ability for easily discretizing irregular shaped support domains. Since the grid is Lagrangian based, it allows to acquire time history of the field variables. Free surfaces, material interfaces and moving boundaries are easily achievable through the movement of the nodal points at the boundaries. Furthermore, the grid is restricted to the problem domain and there are no additional elements required outside the problem domain. This makes the approach computationally effective. Even though the method contains the above significant benefits, the conventional approach is very difficult to be applied for large deformation scenarios due to extreme mesh distortions. This is because, FEM formulations are based on grids and therefore extremely deformed mesh greatly affects the accuracy of the formulations,

resulting in imprecise solutions. For managing this problem, mesh should be rezoned. This is performed by overlaying the new mesh on the deformed mesh for the continuation of the computation. The properties of the new mesh are copied from the old mesh. However, this process of rezoning is extremely time consuming. Moreover, there is high possibility of losing material history during this process. Hence, great numerical difficulties are encountered by the grid-based method in accurately simulating large deformation applications such as penetration, fragmentation, impact, explosions, and fluid-structure interaction problems [76], [77]. According to literature in Section 2.4.2, FEM method has been significantly employed for the investigation of stresses in soil around jack-in pile. However, since the application comprises large deformations, for the prevention of excessive mesh distortions during simulation, various assumptions have been adopted for simplifying the problem.

2.5.2 Material Point Method (MPM)

MPM is a particle-based approach which discretizes the problem domain into discrete number of particles as illustrated in Figure 2.6. Each particle in the problem domain occupies a subdomain as shown in Figure 2.6a which contains its own set of variables such as velocity, stress tensor, density, mass, etc. In-addition to the particles, the method further involves a fixed Eulerian grid as presented in Figure 2.6b.

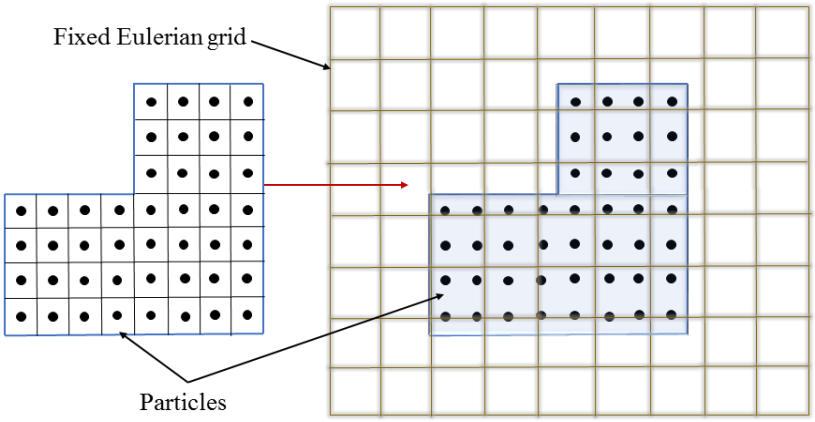


Figure 2.6 : Discretization of problem domain in MPM: (a) Subdomain for each particle; (b) Fixed Eulerian grid.

During computation, particles in the domain deform with the grid following the Lagrangian finite element approach. Thereafter, conservation of momentum is solved at the deformed grids instead of particles using the standard FEM formulation. Subsequently, the grid is reset to initial position while the particles are undisturbed from their deformed configurations. This cycle is repeated at every time-step of the modelling process. It should be emphasized that in MPM all the material properties are carried by the particles and not by the grid. The grid is solely employed for the computation of conservation of momentum and is reset at every time-step. Hence, unlike in FEM, this feature in MPM makes it prevalent for avoiding the problem related to heavy mesh distortions. Furthermore, the particle approach in MPM facilitates accurate flow of material properties and prevents tangling of meshes during simulation [78]. Thus, due to its increased benefits and its capability in handling large deformations, the method has been widely explored in the investigations of large deformation scenarios [79]–[81].

As discussed in Section 2.4.2, the method has been adopted for the analysis of soil stress fields around jack-in pile. Even-though the method has proven its success in many engineering applications involving large deformations, the soil stress field obtained through MPM around jack-in pile showed a considerable deviation from the experimental solutions. This may have been due to the employment of increased number of simplified assumptions.

2.5.3 Discrete Element Method (DEM)

Discrete element method is a popular numerical approach in many engineering applications where the evaluation of a system is based on the motion and behaviour of particles. Therefore, due to its great potential in providing the dynamic behaviour of discrete particles, the method has been predominantly employed in geotechnical, solid, and fluid problems. The method begins the simulation by the detection of interaction points between particles. Thereafter, by utilizing the force-displacement law, the method computes the interaction force for each particle by its point of interaction and overlapping distance. This computed value of interaction force is applied to cause particle movement. Subsequently, by utilizing Newton's second law of motion and the value of interaction force, the properties of each particle such as velocity, acceleration and displacement are updated at every time-step of the simulation. This cycle is repeated until the final step of the simulation.

Although DEM is a powerful numerical tool, there are several challenges being encountered. The method tracks the movement and interaction of every particle in the system. This technique increases the computational cost of the approach. Thus, greater number of particles cause significant increase in the computational time. Moreover, particle shapes and the models used for obtaining contact forces affect the computational time. Apart from above limitations, it is extremely difficult to validate DEM results as experimental measurements are difficult to obtain or cost prohibitive [82], [83]. Having the above difficulties, the method has been adopted for the investigation of soil stress field around jack-in pile as discussed in Section 2.4.2. The models achieved qualitative agreement with the experimental solution and / or lacked the ability to provide in-depth understanding of the soil stress field for the duration of the installation process.

Sections 2.5.1-2.5.3 included the summary about the numerical methods in the literature. Both advantages and disadvantages of each method have been discussed. Even-though the numerical methods such as FEM, DEM and MPM have been attempted for the analysis of stresses in soil around jack-in pile, it could be identified that the most popular and successful meshless method, Smooth Particle Hydrodynamics is still unexplored in this field of research.

2.6 Smooth particle hydrodynamics and its application in geomechanics

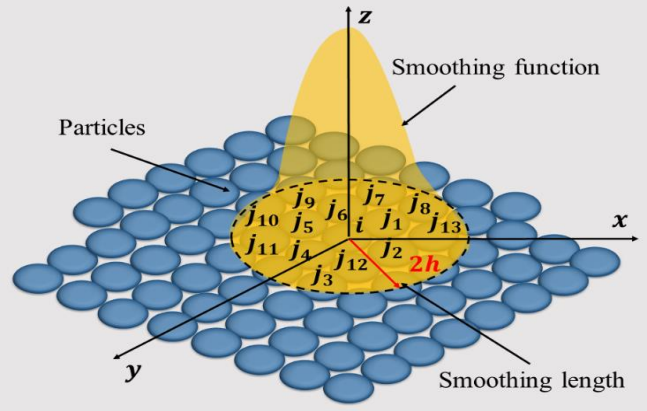


Figure 2.7 : Particle approximation for particle *i* within the support domain defined by smoothing function.

Smooth particle hydrodynamics (SPH) is a mesh-free Lagrangian approach which functions on particles instead of grids. In this approach, the problem domain is represented by particles and each particle contains its own set of variables such as mass, velocity, density, energy etc. During computation, as illustrated in Figure 2.7, variables of each particle (i) are updated by approximating from the variables from the surrounding particles (j) in the neighbourhood defined by the smoothing distance $2h$ where h is the smoothing length in the simulation [77].

SPH was originally invented by Lucy. [35] and Gingold and Monaghan. [34] for simulating astrophysical problems. Due to its success, the method was further extended for macroscopic continuum problems in fluid and solid dynamics as well as for atomistic scale simulations. Furthermore, its ability in handling complex scenarios in three-dimension

and its application in astrophysics led to its development for simulating steller collisions and binary stars [84], collapse and formation of galaxies [85] and many more. Thereafter, the method was extensively employed to solve complex problems in fluid and solid mechanics due to its ability in incorporating complicated physical properties into its formulation [77]. The enduring success of the method further steered its development for many geo-mechanical applications.

Bui et al. [50] developed a numerical model in SPH framework for simulating the collapse of dry soil and soil erosion in response to water flow. The approach not only proved to overcome the problem of grid distortion in traditional FEM method, but also contributed for reasonable solutions. This confirmed the ability of the approach in simply handling large deformation scenarios. The authors further introduced SPH method to simulate soil-water interaction [86]. Numerical results revealed that the SPH method successfully modelled the gross discontinuities involved in the phenomenon. Bui et al. [51] proposed SPH method for simulating large deformation and post failures of geomaterials. The results illustrated good correlation with existing methods. Due to its success, the method was further developed or applied to simulate several geotechnical applications involving extreme deformations such as seismic slope failures, large deformation and post failure behaviour of soils [56], [57], [87], [88], geo disasters [89], soil and solid structure interaction [87]. In addition, Peng et al. [52] introduced a hypoplastic constitutive model in SPH framework for simulating large deformation problems. The developed SPH model

reasonably captured the large deformations involved during the simulation of soil collapse between two plates and the failure of the soil slope. An et al. [53] extended Bui et al. [51]'s method to three-dimension for numerically simulating the deformation and failure of granular slopes. Good agreement with previously simulated results and experimental observations demonstrated that the developed model successfully simulated large deformations of the slope failure. Most recently, SPH models have been developed for simulating soil-water-structure interaction [54], quasi-static and dynamic collapse of sand columns [55] and explosions within the soil mass [90].

It is apparent from above, SPH well simulated numerous large deformation applications in the field of geomechanics. Therefore, adoption of SPH method in current study is believed to contribute for reliable solutions.

2.7 Summary of literature review

The literature review is initiated with a detail discussion on piles. Piling methods for closed-end steel piles have been focused and the problems related to its installation methods have been discussed. Among the installation methods, jack-in pile installation is emphasised due to its increased benefits over the remaining methods. Although it is the most preferred method of pile installation for closed-end steel piles, the method displaces large amount of soil resulting in significant changes to the soil

stress levels. Understanding these stress levels is significantly important due to its influence on pile bearing capacity. Therefore, this has been the subject of many researches.

Thus, a comprehensive review has been included on past experimental and numerical works comprising the investigations on soil stress field around jack-in installation of a closed-end steel pile. The review confirmed that it was not only complicated to achieve experimental measurements of soil stresses, but it was also a major challenge for the grid based numerical models to precisely simulate large deformations involved in the phenomenon. Hence, many assumptions have been adopted in these models. In addition, only very few meshless methods such as MPM and DEM have been attempted for solving the problems related to large deformations. However, these mesh-free methods considered the pile as a rigid material or lacked capability in providing visual representation of the soil stress field throughout the installation.

A gap is identified from the literature where the most popular and successful meshless method, Smooth Particle Hydrodynamics is still unattended for the analysis of stresses in soil around jack-in pile. Moreover, it should be emphasized that none of the numerical models in the literature possessed the combined ability of modelling the pile as an elastic-perfectly plastic material from the soil surface to the final penetration depth considering soil-pile interaction and to provide visual representation of both horizontal and vertical soil stress distributions at various penetration depths. Therefore, due to the advanced nature and

success of the method, it is worth considering the development of a SPH model with aforementioned capabilities for providing a reliable numerical tool for the analysis of soil stress field around jack-in pile.

Chapter 3
Methodology

3.1 Introduction

As the goal of the thesis is to develop SPH model to simulate stresses in soil around jack-in pile, present chapter focuses in providing a detail information about the research methodology adopted as an initiation for achieving the final goal of the thesis. On this basis, as shown in Figure 3.1, the chapter initially presents the basic formulation of SPH. This comprises a detail information about the integral representation and particle approximation of field functions through which the SPH formulations are formed. Followingly, a comprehensive review / understanding is provided on the derivation of SPH governing equations based on conservation of mass and conservation of momentum for describing motion. For completing the total stress tensor of these governing equations, constitutive models incorporating failure criteria are adopted. Thus, as shown in Figure 3.1, the key segments such as total stress tensor, constitutive models and failure criteria which require an in-depth knowledge are discussed prior to the development of constitutive models and SPH models for achieving the final goal of the thesis.

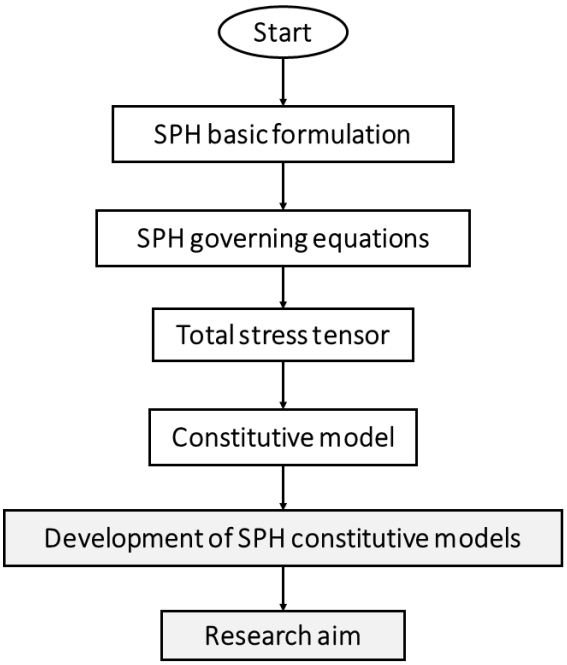


Figure 3.1: Flow chart of research methodology

3.2 Basic formulation of SPH

Physical phenomena in SPH are described by the governing equations which are in the form of partial differential equations (PDE). These PDE equations are of field variables such as velocity, density, energy etc. In SPH, the problem domain is divided into discrete number of particles and PDE equations are solved for every particle in the problem domain. Such complex computation requires computer aided solutions.

Subsequent to the discretization of the problem domain, a computational framework is formed for the numerical approximation. Values for the field variables and their derivatives are generally

approximated using integral representation method. However, in SPH, the integral representation of a function is transformed into particle approximation where the integral sign is converted into summation sign over the neighbouring particles. These particle approximation formulas are ordinary differential equations with respect to time and are solved at every time step for each particle by the standard integration method. Hence, the values for field variables are computed at every time step and are dependent on the current local distribution of particles [77]. SPH Formulation based on 'particle approximation' begins from the derivation of 'integral representation' of field functions. Hence the following involves the detail understanding about the origination of SPH formulas.

3.2.1 Integral representation of a function

Integral representation, known as kernel approximation of a function is derived using the direc delta function. Direc delta function is a function which is used to model physical systems involving a rapid peak behaviour where it becomes infinitely strong and continues to be zero elsewhere. As illustrated in Figure 3.2a, if direc delta function is considered to vanish elsewhere except for $x' = 0$, the equation for direc delta function is expressed as [91]:

$$\int_{-\infty}^{\infty} \delta(x')dx' = 1 \tag{3.1}$$

where $\delta(x')$ is the direc delta function and its integral is equal to 1. The function reaches infinity when $x' = 0$.

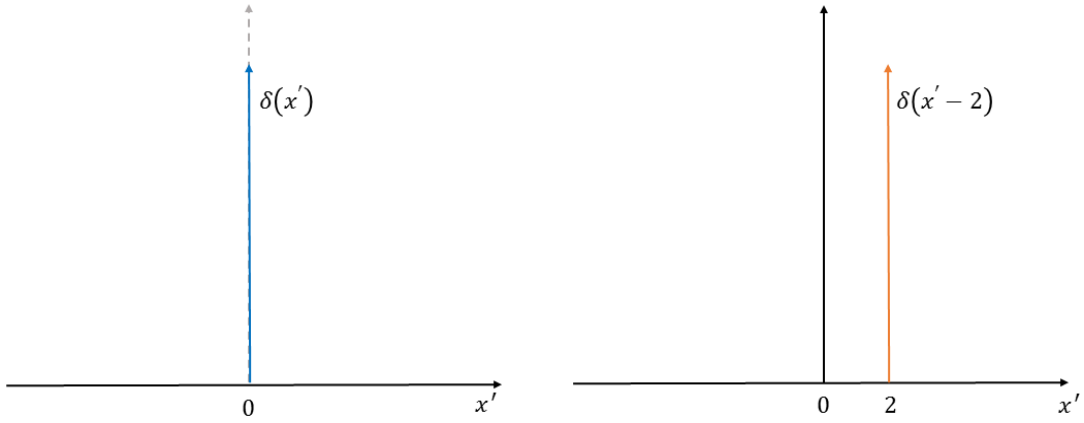


Figure 3.2: Dirac Delta function when (a) $\boldsymbol{x' = 0}$ (b) $\boldsymbol{x' = 2}$.

Similarly, if direc delta function occurs when $x' = 2$, the plot is shifted from 0 to 2 as shown in Figure 3.2b. Hence Eq. (3.1) becomes:

$$\int_{-\infty}^{\infty} \delta(x' - 2)dx' = 1 \tag{3.2}$$

Multiplying a field function $f(x')$ by a dirac delta function leads to:

$$f(x) = \int_{-\infty}^{\infty} f(x')\, \delta(x' - x)dx' \tag{3.3}$$

where $f(x)$ represents a function of three-dimensional position vector x. As mentioned earlier, direc delta function achieves the peak at position vector x and becomes zero elsewhere. Therefore, multiplication of the field function by the direct delta function computes $f(x)$ at position vector x. As such, by employing Eq. (3.3), the value of a function is computed at a given position. This enables the modelling of a physical system.

In SPH, by restricting the limits to problem domain (Ω) and by replacing delta function by the smoothing function ($W(x-x',h)$), Eq. (3.3) is rewritten as:

$$f(x) \doteq \int_{\Omega} f(x')\, W(x-x',h)dx' \tag{3.4}$$

where h is the smoothing length. $W(x-x',h)$ is not a direc delta function. As such, the integral representation expressed in equation (3.4) is only an approximation of a function. This is how the integral representation of a function is originated in SPH and is expressed as:

$$< f(x) >= \int_{\Omega} f(x')\, W(x-x',h)dx' \tag{3.5}$$

3.2.2 Integral representation for the derivative of a function

Derivative of a function measures the rate of change of a function. Therefore, Eq. (3.5) is written as:

$$< \nabla.f(x) > = \int_{\Omega} [\nabla.f(x')]\, W(x-x',h)dx' \tag{3.6}$$

Using partial derivations, Eq. (3.6) is expressed as:

$$\nabla.[f(x')\, W(x-x',h)] = [\nabla.f(x')]W(x-x',h) + f(x')\, \nabla W(x-x',h) \tag{3.7}$$

By substituting Eq. (3.7) in Eq. (3.6), leads to:

$$< \nabla . f(x) > = \int_{\Omega} \nabla . [f(x')\, W(x - x', h)] dx' \qquad (3.8)$$

$$- \int_{\Omega} f(x')\, \nabla W(x - x', h) dx'$$

According to divergence theorem [92]:

$$\iint_{S} \mathrm{F} . n \, d\mathrm{S} = \iiint_{E} div \, \mathrm{F} \, dV \qquad (3.9)$$

where, S and E represent the surface integral and volume integral respectively. By employing this theorem, Eq. (3.8) becomes:

$$< \nabla . f(x) > = \int_{\mathrm{S}} f(x')\, W(x - x', h)\, n \, dx' - \int_{\Omega} f(x')\, \nabla W(x - x', h) dx' \qquad (3.10)$$

It is essential for the support domain to lie within the problem domain. As such, the surface integral in equation (3.10) is considered zero. Therefore, integral representation for the derivative of a function in SPH is expressed as:

$$< \nabla . f(x) > = - \int_{\Omega} f(x')\, \nabla W(x - x', h) dx' \qquad (3.11)$$

3.2.3 Particle approximation of a function

As mentioned in the beginning of Section 3.2, the problem domain in SPH is represented by particles. Therefore, integral representation of a function should be converted into the form of particle approximation.

Considering particle i in Figure 2.7. The variable of particle i is found by summing the respective variable over the neighbouring particles within its support domain. Therefore Eq. (3.5) is expressed in particle form as:

$$< f(x) >= \sum_{j=1}^{N} f(x_j)\ W(x - x_j, h)dx \tag{3.12}$$

where j ranges from 1, 2, 3…N number of particles and W is the smoothing function. If particle j occupies a finite volume ΔVj, mass of the particle is considered as:

$$m_j = \Delta V_j \rho_j \tag{3.13}$$

where ρ is the density of particle j. Therefore, by replacing dx by ΔV_j, Eq. (3.12) is re-written as:

$$< f(x) >= \sum_{j=1}^{N} f(x_j)\ W(x - x_j, h)\Delta V_j \tag{3.14}$$

By substituting Eq. (3.13) in Eq. (3.14), particle approximation of a function is presented as:

$$< f(x) > = \sum_{j=1}^{N} \frac{m_j}{\rho_j}\ f(x_j)\ W(x - x_j, h) \tag{3.15}$$

3.2.4 Particle approximation of a derivative of a function

Similar to Section 3.2.2, particle approximation of a derivative of a function is expressed as:

$$< \nabla . f(x) > = -\sum_{j=1}^{N} \frac{m_j}{\rho_j} \; f(x_j) . \nabla W(x - x_j, h) \tag{3.16}$$

This is re-written to the final form as:

$$\frac{\partial f(x_i)}{\partial x} = \sum_{j=1}^{N} \frac{m_j}{\rho_j} \; f(x_j) . \frac{\partial W_{ij}}{\partial x_i} \tag{3.17}$$

where, $W_{ij} = W(x_i - x_j \; , h)$.

3.2.5 Smoothing functions

Smoothing function (W) plays a pivotal role in SPH approximation. As illustrated in Figure 2.7, it determines the pattern of function approximation and defines the dimension of the support domain. Hence, the accuracy of particle approximation is governed by the smoothing function [93]. Smoothing functions should satisfy three main conditions for describing a physical phenomenon:

Normalization condition:

$$\int_{\Omega} W(x - x', h) dx' = 1 \tag{3.18}$$

Delta function property: when $h \longrightarrow 0$, W becomes δ function.

$$\lim_{h\to 0} W(x-x',h) = \delta(x-x') \tag{3.19}$$

Compact condition:

$$W(x-x',h) = 0 \; when \; |x-x'| > kh \tag{3.20}$$

Several smoothing functions have been introduced in the literature. Among them, the commonly employed types include bell-shaped, gaussian and cubic-spline are discussed in present study [77]. Bell-shaped smoothing function is defined as:

$$W(x-x',h) = W(R,h) = \alpha_d \begin{cases} (1+3R)(1-R)^3 & R \le 1 \\ 0 & R > 1 \end{cases} \tag{3.21}$$

$$R = \frac{r}{h} = \frac{|x-x'|}{h}$$

where α_d is $5/4h$, $5/\pi h^2$ and $105/16\pi h^3$ for 1D, 2D, and 3D respectively. r is the distance and R is the relative distance between the interacting pairs. On the other hand, gaussian smoothing function is expressed as:

$$W(R,h) = \alpha_d e^{-R^2} \tag{3.22}$$

where α_d is $1/\pi^{1/2}h$, $1/\pi h^2$ and $1/\pi^{3/2}\, h^3$ for 1D, 2D, and 3D respectively. Monaghan [84] stated that the employment of gaussian is better than bell-shaped smoothing function for obtaining physical interpretation of SPH formulations. However, the method inherits several drawbacks. For satisfying the compact condition expressed in Eq. (3.20), R in Eq. (3.22) should approach infinity. As such, gaussian smoothing function is not very compact. In addition, the function requires longer duration for approaching zero. Thus, is computationally expensive and results in larger support

domain. As an alternative, cubic-spline smoothing function has been introduced as:

$$W(R,h) = \alpha_d \times \begin{cases} \frac{2}{3} - R^2 + \frac{1}{2}R^3 & 0 \le R < 1 \\ \frac{1}{6}(2-R)^3 & 1 \le R < 2 \\ 0 & R \ge 2 \end{cases} \tag{3.23}$$

where α_d: $1/h$, $15/7\pi h^2$ and $3/2\pi h^3$ for one, two, and three-dimension respectively. Resembling gaussian, cubic-spline smoothing function comprises a narrower compact support. Therefore, among the widely known smoothing functions cubic-spline has been significantly applied [94]–[96]. Thus, it is adopted in present study.

3.3 Governing equations in SPH

A set of basic governing equations are used to describe the motion of a system. The equations are well known as Navier-Strokes equations and are based on conservation laws such as conservation of mass, momentum and energy. Conservation of energy is not considered in present study. As such, in current section, the derivation of SPH equations of motion obtained through the incorporation of particle approximation into the Largrangian form of conservation of mass and momentum equations are presented [77].

3.3.1 Derivation of governing equations in Lagrangian form

Governing equations in Lagrangian form can be achieved either through the adoption of Lagrangian control volume which derives the governing equations in integral form or via the employment of infinitesimal fluid cell through which the governing equations are expressed in the form of partial differential equations.

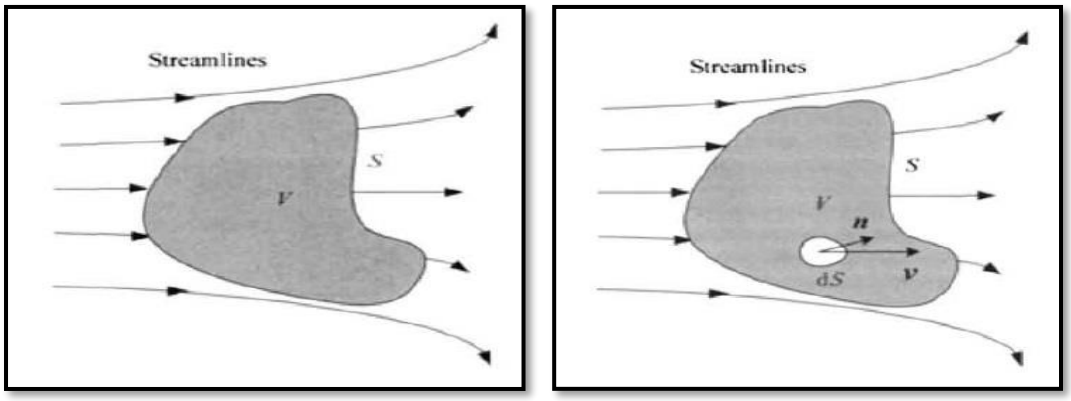


Figure 3.3: (a) Lagrangian control volume; (b) Change in control volume [77].

In view of the first approach, as illustrated in Figure 3.3, Lagrangian control volume in a fluid flow is defined by a closed control volume V with a control surface S. The mass within the control volume is kept unchanged even under the action of forces such as compression / expansion / deformation. Using this approach, the conservation laws are directly applied to the fluid within the control volume. However, movement of fluid within the control volume causes changes in the control surface.

This in result varies the control volume. Such variation in the control volume (ΔV) over time Δt is expressed as:

$$\Delta V = v\Delta t \cdot ndS \tag{3.24}$$

where dS is the change in control surface, v is the velocity vector and n is the unit vector normal to the surface as shown in Figure 3.3b. From this, the total volume change for the entire Lagrangian control volume is expressed as:

$$\Delta V = \int_S v\Delta t \cdot ndS \tag{3.25}$$

where S is the control surface. Thereafter, by dividing Eq. (3.25) by Δt and using divergence theorem, the governing equation in integral form is expressed as:

$$\frac{\Delta V}{\Delta t} = \int_V \nabla \cdot v \, dV \tag{3.26}$$

where $\nabla \cdot v$ is the divergence of velocity vector and V is the control volume.

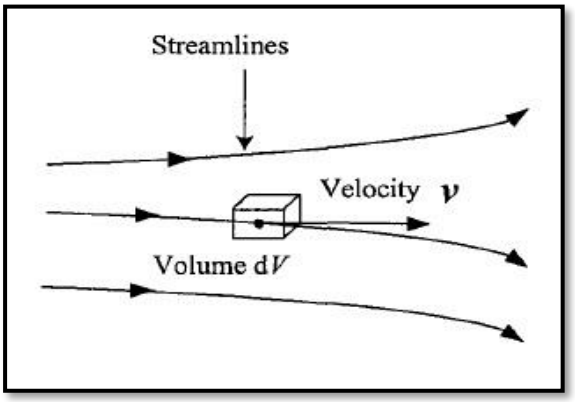


Figure 3.4: Infinitesimal fluid cell [79].

On the other hand, infinitesimal fluid cell approach is performed by considering an infinitesimal fluid cell which moves along a streamline with velocity vector $v = (v_x, v_y, v_z)$ as indicated in Figure 3.4. It consists of a very small control volume δV and control surface δS which consists of clumped particles. The field property within the cell is assumed to be identical throughout the entire cell.

Applying conservation laws to the infinitesimal fluid cell, equation (3.26) becomes:

$$\frac{\Delta(\delta V)}{\Delta t} = \int_V \nabla \cdot v \, d(\delta V) \tag{3.27}$$

By simplifying, governing equation in partial differential form is obtained as:

$$\frac{\Delta(\delta V)}{\Delta t} = \nabla \cdot v \int_V d(\delta V)$$

$$\frac{\Delta(\delta V)}{\Delta t} = (\nabla \cdot v)\, \delta V$$

$$\frac{1}{\delta V}\frac{D(\delta V)}{Dt} = (\nabla \cdot v) \tag{3.28}$$

Governing equations in SPH are in the form of partial differential equations. As such, the derivation of governing equation based on conservation of mass is achieved from the expression in Eq. (3.28) as follows:

Using the relationship $\frac{D(\delta m)}{Dt} = 0$, the mass of infinitesimal fluid cell is expressed as:

$$\frac{\rho}{\delta V}\frac{D(\delta V)}{Dt} + \frac{D\rho}{Dt} = 0 \tag{3.29}$$

where ρ is the density. By substituting Eq. (3.28) in Eq. (3.29), the mass conservation equation in Lagrangian form (continuity equation) is expressed as:

$$\frac{D\rho}{Dt} = -\rho\nabla \cdot v \tag{3.30}$$

$$\frac{D\rho}{Dt} = -\rho\frac{\partial v^{\beta}}{\partial x^{\beta}} \tag{3.31}$$

where β denotes x, y, z cartesian coordinates. Similarly, derivation of conservation of momentum equation is based on Newton's second law of motion. Newton's second law of motion states that the rate of change of momentum of an object is equal to sum of forces (body and surface forces) acting on it [97]. Therefore, by applying Newton's second law of motion to the infinitesimal fluid cell illustrated in Figure 3.5, conservation of momentum equation in Lagrangian form is obtained for all three dimensions as follows:

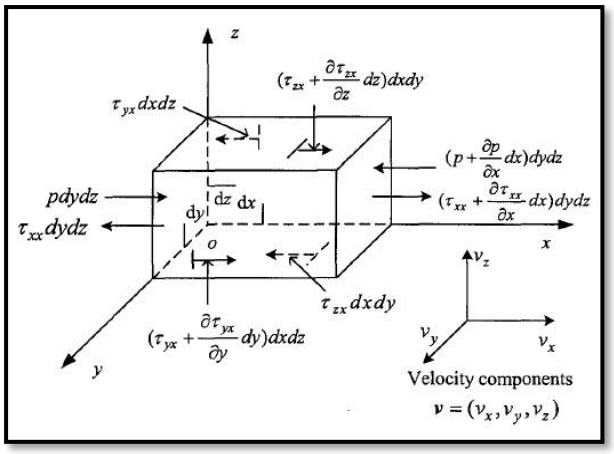


Figure 3.5: Forces acting on an infinitesimal fluid cell in x direction [77].

Considering the forces along x direction in Figure 3.5, Newton's second law of motion is expressed as:

$$\frac{\partial \tau_{zx}}{\partial z}dxdydz+\frac{\partial \tau_{yx}}{\partial y}dxdydz+\frac{\partial \tau_{xx}}{\partial x}dxdydz-\frac{\partial p}{\partial x}dxdydz \tag{3.32}$$

$$+F_x\rho dxdydz=\rho dxdydz\,a$$

where F_x is body force per unit volume in the x axis. Once simplified, momentum equation along the x direction becomes:

$$\rho F_x+\frac{\partial \tau_{zx}}{\partial z}+\frac{\partial \tau_{yx}}{\partial y}+\frac{\partial \tau_{xx}}{\partial x}-\frac{\partial p}{\partial x}=\rho\frac{Dv_x}{Dt} \tag{3.33}$$

Similarly, momentum equations along y and z directions are expressed by Eqs. (3.34) and (3.35) respectively.

$$\rho F_y+\frac{\partial \tau_{zy}}{\partial z}+\frac{\partial \tau_{yy}}{\partial y}+\frac{\partial \tau_{xy}}{\partial x}-\frac{\partial p}{\partial y}=\rho\frac{Dv_y}{Dt} \tag{3.34}$$

$$\rho F_z+\frac{\partial \tau_{zz}}{\partial z}+\frac{\partial \tau_{yz}}{\partial y}+\frac{\partial \tau_{xz}}{\partial x}-\frac{\partial p}{\partial z}=\rho\frac{Dv_z}{Dt} \tag{3.35}$$

Hence, from above, momentum conservation equation in Lagrangian form is expressed as:

$$\frac{Dv^{\alpha}}{Dt} = \frac{1}{\rho}\frac{\partial \sigma^{\alpha\beta}}{\partial x^{\beta}} + F^{\alpha} \tag{3.36}$$

where $\sigma^{\alpha\beta}$ is the total stress tensor, superscripts α and β denote coordinate directions x, y and z.

3.3.2 Particle approximation for governing equations in Lagrangian form

SPH is based on particle approximation. Therefore, the governing equations represented by Eqs. (3.31) and (3.36) should be expressed in terms of particle approximation. The method of arriving at these formulations in SPH framework are presented as follows:

Density could be approximated with aid of the conservation of mass in Eq. (3.31). By using Eq. (3.17), $(\partial v_i\hat{}\beta)/(\partial x\hat{}\beta\ )$ in Eq. (3.31) is expressed as:

$$\frac{\partial v_i^{\beta}}{\partial x^{\beta}} = \sum_{j=1}^{N} \frac{m_j}{\rho_j}\ v_j^{\beta} . \frac{\partial W_{ij}}{\partial x_i^{\beta}} \tag{3.37}$$

where v_j and m_j are the velocity and mass of particle j respectively. Substituting Eq. (3.37) in Eq. (3.31) leads to:

$$\frac{D\rho_i}{Dt} = -\rho \sum_{j=1}^{N} \frac{m_j}{\rho_j}\ v_j^{\beta} . \frac{\partial W_{ij}}{\partial x_i^{\beta}} \tag{3.38}$$

In practice it is more accurate to include velocity difference between the two interacting pairs. This is achieved by multiplying the gradient of unity expressed in Eq. (3.39) by $\rho_i v_i$. This is conveyed by Eq. (3.40).

$$\nabla 1 = \sum_{j=1}^{N} \frac{m_j}{\rho_j} \frac{\partial W_{ij}}{\partial x_i^\beta} = 0 \tag{3.39}$$

$$\rho_i \sum_{j=1}^{N} \frac{m_j}{\rho_j} v_i^\beta . \frac{\partial W_{ij}}{\partial x_i^\beta} = 0 \tag{3.40}$$

Addition of Eqs. (3.40) and (3.38) leads to:

$$\frac{D\rho_i}{Dt} = \rho_i \sum_{j=1}^{N} \frac{m_j}{\rho_j} (v_i^\beta - v_j^\beta) \frac{\partial W_{ij}}{\partial x_i^\beta} \tag{3.41}$$

$$\frac{D\rho_i}{Dt} = \rho_i \sum_{j=1}^{N} \frac{m_j}{\rho_j} v_{ij}^\beta \frac{\partial W_{ij}}{\partial x_i^\beta} \tag{3.42}$$

where $v_{ij}^\beta = (v_i^\beta - v_j^\beta)$. Various transformations result in various forms of density equations. However, the derivation procedure of the most commonly used type of density equation in SPH literature is presented as follows.

$$-\rho \frac{\partial v^\beta}{\partial x^\beta} = -v^\beta \frac{\partial \rho}{\partial x^\beta} - \frac{\partial (\rho v^\beta)}{\partial x^\beta} \tag{3.43}$$

By using particle approximation, Eq. (3.43) is re-written as:

$$\frac{D\rho_i}{Dt} = \sum_{j=1}^{N} m_j v_i^\beta \frac{\partial W_{ij}}{\partial x_i^\beta} - \sum_{j=1}^{N} m_j v_j^\beta \frac{\partial W_{ij}}{\partial x_i^\beta} \tag{3.44}$$

Finally, re-arranging Eq. (3.44) leads to the most commonly used mass conservation equation in SPH framework as:

$$\frac{D\rho_i}{Dt} = \sum_{j=1}^{N} m_j (v_i^\beta - v_j^\beta) \frac{\partial W_{ij}}{\partial x_i^\beta} \tag{3.45}$$

Apart from above, using the relationship in Eq. (3.46), the momentum equation in Eq. (3.36) could be re-written as expressed in Eq. (3.47).

$$\frac{1}{\rho}\left(\frac{\partial \sigma^{\alpha\beta}}{\partial x^\beta}\right) = \frac{\partial}{\partial x}\left(\frac{\sigma^{\alpha\beta}}{\rho}\right) + \frac{\sigma^{\alpha\beta}}{\rho^2}\frac{\partial \rho}{\partial x^\beta} \tag{3.46}$$

$$\frac{Dv^\alpha}{Dt} = \frac{\partial}{\partial x}\left(\frac{\sigma^{\alpha\beta}}{\rho}\right) + \frac{\sigma^{\alpha\beta}}{\rho^2}\frac{\partial \rho}{\partial x^\beta} + F^\alpha \tag{3.47}$$

Thereafter, by using particle approximation, Eq. (3.47) is expressed as:

$$\frac{Dv^\alpha}{Dt} = \sum_{j=1}^{N} \frac{m_j}{\rho_j} \frac{\sigma_j^{\alpha\beta}}{\rho_j} \frac{\partial W_{ij}}{\partial x_i^\beta} + \sum_{j=1}^{N} m_j \frac{\sigma_i^{\alpha\beta}}{\rho_i^2} \frac{\partial W_{ij}}{\partial x_i^\beta} + F^\alpha \tag{3.48}$$

Finally, by further simplifying Eq. (3.48), the most popular form of SPH approximation for momentum equation is obtained as [77]:

$$\frac{Dv^\alpha}{Dt} = \sum_{j=1}^{N} m_j \left(\frac{\sigma_j^{\alpha\beta}}{\rho_j^2} + \frac{\sigma_i^{\alpha\beta}}{\rho_i^2}\right) \frac{\partial W_{ij}}{\partial x_i^\beta} + F^\alpha \tag{3.49}$$

To close down the above governing equations, constitutive models are employed for the total stress tensor ($\sigma^{\alpha\beta}$) as proposed by Bui et al. [51].

3.4 Total stress tensor ($\sigma^{\alpha\beta}$)

Stress at a point is defined by the internal forces acting in-between the particles of a body across the imaginary planes. For instance, if a cut plane of an area ΔA with a unit vector n normal to its surface is considered to pass through a point P_0 as shown in Figure 3.6a and if the resultant force is considered to be F_n, then the stress vector T_n at point P_0 is obtained as $T_n = F_n/\Delta A$.

Infinite number of cut planes passes through a single point. Therefore, there are infinite number of values of T_n. These infinite number of values provide the stress state at a point. However, it is not necessary to obtain all the stress vectors passing though the point. Instead, if three mutually perpendicular stress vectors are known, it becomes possible for obtaining the stress vector acting on any plane passing through that point [98].

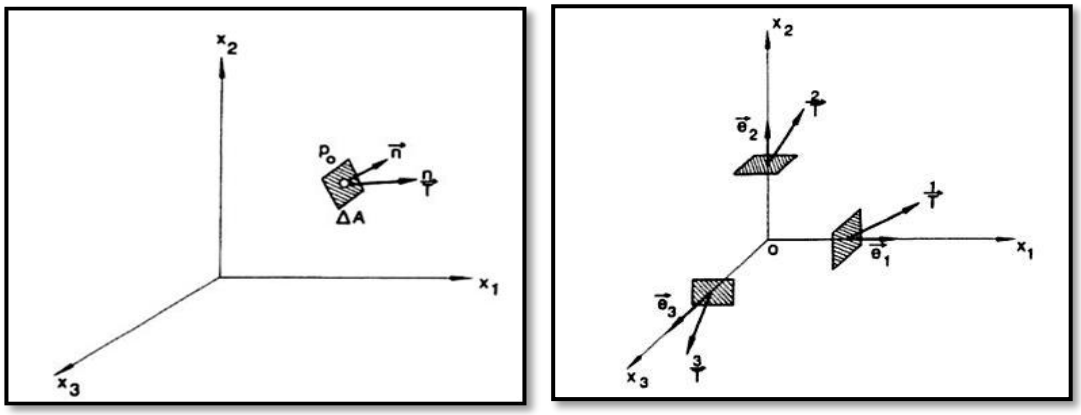


Figure 3.6: (a) Stress vector at point P_0; (b) Stress vector along each plane [98].

As illustrated in Figure 3.6b, consider three mutually perpendicular planes x, y and z with stress vectors T_1, T_2 and T_3 respectively. Each of these stress vectors contain three components by resolving into a normal and two shear components. For instance, stress vector T_1 could be resolved as σ_{11} in normal and σ_{12}, σ_{13} in parallel to its plane. Therefore, in summation, the stress vectors contain nine components. These nine components which are written to define stress vectors are the total components of a stress tensor. This is expressed in matrix form as:

$$\sigma_{\alpha\beta} = \begin{bmatrix} T_1 \\ T_2 \\ T_3 \end{bmatrix} = \begin{bmatrix} \sigma_{11} & \sigma_{12} & \sigma_{13} \\ \sigma_{21} & \sigma_{22} & \sigma_{23} \\ \sigma_{31} & \sigma_{32} & \sigma_{33} \end{bmatrix} \tag{3.50}$$

Present study focuses on the development of SPH numerical model in two-dimension (2D). Therefore, the stress tensor in 2D should be considered instead of a 3D stress tensor. Stress vector in 2D are restricted to lie on two mutually perpendicular planes along x and y directions. Each stress vector is resolved into one normal component and one shear component [99]. Therefore, the stress tensor in 2D contains four components. This is expresses as:

$$\sigma_{\alpha\beta} = \begin{bmatrix} T_1 \\ T_2 \end{bmatrix} = \begin{bmatrix} \sigma_{11} & \sigma_{12} \\ \sigma_{21} & \sigma_{22} \end{bmatrix} \tag{3.51}$$

Furthermore, in SPH formulation, total stress tensor is generally divided into deviatoric stress tensor and hydrostatic stress tensor. This is expressed in 3D as [98]:

$$\begin{bmatrix}\sigma_{11} & \sigma_{12} & \sigma_{13}\\ \sigma_{21} & \sigma_{22} & \sigma_{23}\\ \sigma_{31} & \sigma_{32} & \sigma_{33}\end{bmatrix}=\begin{bmatrix}\sigma_{11}-p & \sigma_{12} & \sigma_{13}\\ \sigma_{21} & \sigma_{22}-p & \sigma_{23}\\ \sigma_{31} & \sigma_{32} & \sigma_{33}-p\end{bmatrix}+\begin{bmatrix}p & 0 & 0\\ 0 & p & 0\\ 0 & 0 & p\end{bmatrix} \quad (3.52)$$

And similarly Eq. (3.52) is presented in 2D as [100]:

$$\begin{bmatrix}\sigma_{11} & \sigma_{12}\\ \sigma_{21} & \sigma_{22}\end{bmatrix}=\begin{bmatrix}\sigma_{11}-p & \sigma_{12}\\ \sigma_{21} & \sigma_{22}-p\end{bmatrix}+\begin{bmatrix}p & 0\\ 0 & p\end{bmatrix} \quad (3.53)$$

Moreover, the Eqs. (3.52) and (3.53) could be expressed in equation form as:

$$\sigma^{\alpha\beta}=s^{\alpha\beta}+p\delta^{\alpha\beta} \quad (3.54)$$

where $s^{\alpha\beta}$ is the deviatoric stress tensor and p is the hydrostatic stress tensor. α and β indicates cartesian coordinates depending on the number of dimensions. $\delta^{\alpha\beta}$ is the Kronecker's delta where $\delta^{\alpha\beta}=1$ if $\alpha=\beta$ or $\delta^{\alpha\beta}=0$ if $\alpha\neq\beta$.

Eqs. (3.52) to (3.54) demonstrate the relationship between hydrostatic stress tensor and deviatoric stress tensor. Hydrostatic stress is a state of stress at which the principle stresses are equal and shear stresses are zero. These stresses are responsible for the volume change in a material. If the principal stresses are not equal, in that case the mean value of the stresses are considered as hydrostatic stresses. Hence, considering compression as positive the equation for hydrostatic stress is written for 3D as [99]:

$$p=\frac{\sigma^{xx}+\sigma^{yy}+\sigma^{zz}}{3}=\frac{\sigma^{\gamma\gamma}}{3} \quad (3.55)$$

where γ denotes (x, y, z) directions. Similarly in 2D, only x and y directions are considered [100], [101]. Hence Eq. (3.55) is expressed as:

$$p = \frac{\sigma^{xx} + \sigma^{yy}}{2} = \frac{\sigma^{\gamma\gamma}}{2} \tag{3.56}$$

On the other hand, the part of the stress tensor, which is remaining after subtracting hydrostatic stress tensor as presented in Eq. (3.52) and (3.53) is known as the deviatoric stress tensor. These are the stresses which are responsible for the shape change in a material [102]. All-in-all stress tensor presented for 2D will be employed in the development of the SPH constitutive models.

3.5 Constitutive model

In solid mechanics, constitutive models are used to describe the stress-strain behaviour of a phenomenon [103]. Various types of constitutive models such as elastic, elastic-perfectly plastic, elasto-viscoplastic constitutive models are available and are adopted based on its suitability for modelling the application. The aim of this research is to analyse the development of stresses in soil during jack-in-pile installation. In this application, pile is considered as stainless steel which does not consider the effect of hydrostatic pressure. On the other hand, soil is a material which involves both volumetric and shear deformations. As such, for numerically simulating this complex phenomenon, both pile and soil

should be modelled with appropriate constitutive models suitable for describing the respective behaviour.

It is more realistic to employ elasto-plastic and elasto-viscoplastic models for simulating the behaviour. As an initiation to this, present study employs elastic-perfectly plastic theory for the development of the 2D constitutive models in SPH framework for modelling the complex phenomenon.

3.5.1 Elastic-perfectly plastic model

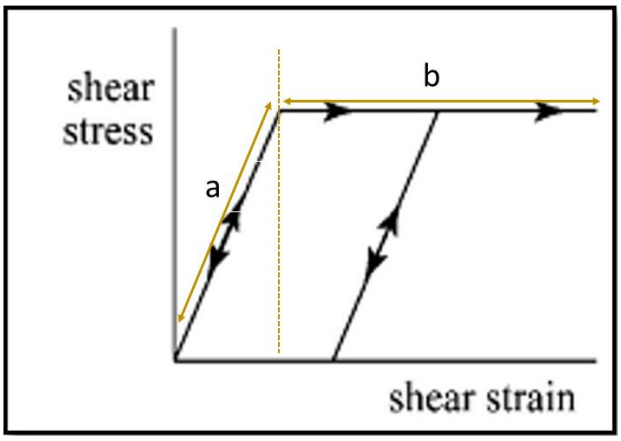


Figure 3.7: Stress-Strain relationship for elastic-perfectly plastic model [106].

Stress against strain response for an elastic-perfectly plastic model is of two sections such as a linear elastic part and a perfectly plastic part as illustrated by 'a' and 'b' in Figure 3.7 respectively [104]. The linear elastic section ('a') satisfies the linear stress-strain relationship by Hook's law where the stress is proportional to strain and perfectly plastic section ('b') is indicated by a horizontal line signifying that the deformation beyond the

yield point occurs under constant stress level. It is apparent from Figure 3.7 that the total strain rate tensor is the summation of elastic strain rate tensor and plastic strain rate tensor which is expressed as:

$$\dot{\varepsilon}^{\alpha\beta} = \dot{\varepsilon}_e^{\alpha\beta} + \dot{\varepsilon}_p^{\alpha\beta} \tag{3.57}$$

where $\dot{\varepsilon}_e^{\alpha\beta}$ is the elastic strain rate tensor and $\dot{\varepsilon}_p^{\alpha\beta}$ is the plastic strain rate tensor.

3.5.2 Elastic strain rate tensor

Present study introduces the development of elastic-perfectly plastic constitutive models for both plane stress and plane strain condition in two-dimensional SPH framework. The elastic strain rate tensor of these constitutive models is derived using plane stress Hooke's law and plane strain Hooke's law in index notation. As such, for achieving an in-depth knowledge prior to the constitutive model developments in chapter 4 and 5, current section presents the derivation of Hooke's law in index notation for both plane stress and plane strain condition.

Hooke's Law for plane stress condition and its derivation into an index form:

According to Hooke, the stress-strain relationship for 2D-plane stress condition in matrix form is expressed as [105]:

$$\begin{bmatrix}\sigma_{xx}\\ \sigma_{yy}\\ \sigma_{xy}\end{bmatrix}=\frac{E}{1-v^2}\begin{bmatrix}1 & v & 0\\ v & 1 & 0\\ 0 & 0 & 1-v\end{bmatrix}\begin{bmatrix}\varepsilon_{xx}\\ \varepsilon_{yy}\\ \varepsilon_{xy}\end{bmatrix} \tag{3.58}$$

where E is the Young's modulus and v is the Poisson's ratio. By inversing the matrix in Eq. (3.58), the plane stress compliance matrix is obtained as:

$$\begin{bmatrix}\varepsilon_{xx}\\ \varepsilon_{yy}\\ \varepsilon_{xy}\end{bmatrix}=\frac{1}{E}\begin{bmatrix}1 & -v & 0\\ -v & 1 & 0\\ 0 & 0 & 1+v\end{bmatrix}\begin{bmatrix}\sigma_{xx}\\ \sigma_{yy}\\ \sigma_{xy}\end{bmatrix} \tag{3.59}$$

From the compliance matrix, strain equations on mutually perpendicular planes can be formed as:

$$\varepsilon_{xx}=\frac{1}{E}\left(\sigma_{xx}-v\sigma_{yy}\right) \tag{3.60}$$

$$\varepsilon_{yy}=\frac{1}{E}\left(\sigma_{yy}-v\sigma_{xx}\right)$$

Adding the term $v\sigma_{xx}$ into Eq. (3.60) leads to:

$$\varepsilon_{xx}=\frac{1}{E}\left((1+v)\sigma_{xx}-v(\sigma_{xx}+\sigma_{yy})\right) \tag{3.61}$$

$$\varepsilon_{yy}=\frac{1}{E}\left((1+v)\sigma_{yy}-v(\sigma_{xx}+\sigma_{yy})\right)$$

Rearranging Eq. (3.61) derives into:

$$\sigma_{xx}=\frac{E}{1+v}\varepsilon_{xx}+\frac{v}{1+v}\left(\sigma_{xx}+\sigma_{yy}\right) \tag{3.62}$$

$$\sigma_{yy}=\frac{E}{1+v}\varepsilon_{yy}+\frac{v}{1+v}\left(\sigma_{xx}+\sigma_{yy}\right)$$

Addition of equations presented in Eq. (3.62) leads to:

$$(\sigma_{xx}+\sigma_{yy})=\frac{E}{1-v}(\varepsilon_{xx}+\varepsilon_{yy}) \tag{3.63}$$

Substituting Eq. (3.63) in Eq. (3.62) derives into:

$$\sigma_{xx} = \frac{E}{1+v}\varepsilon_{xx} + \frac{v}{1+v}\left(\frac{E}{1-v}(\varepsilon_{xx} + \varepsilon_{yy})\right) \tag{3.64}$$

$$\sigma_{yy} = \frac{E}{1+v}\varepsilon_{yy} + \frac{v}{1+v}\left(\frac{E}{1-v}(\varepsilon_{xx} + \varepsilon_{yy})\right)$$

Finally, Hooke's Law for plane stress condition could be represented in index form as:

$$\sigma^{\alpha\beta} = \frac{E}{1+v}\varepsilon^{\alpha\beta} + \frac{vE}{(1+v)(1-v)}\varepsilon^{\gamma\gamma}\delta^{\alpha\beta} \tag{3.65}$$

Hooke's Law for plane strain condition and its derivation into an index form:

Stress-strain relationship for plane strain condition is provided by Hooke in matrix form as [106]:

$$\begin{bmatrix}\sigma_{xx}\\ \sigma_{yy}\\ \sigma_{xy}\end{bmatrix} = \frac{E}{(1+v)(1-2v)}\begin{bmatrix}1-v & v & 0\\ v & v & 0\\ 0 & 0 & \frac{1-2v}{2}\end{bmatrix}\begin{bmatrix}\varepsilon_{xx}\\ \varepsilon_{yy}\\ 2\varepsilon_{xy}\end{bmatrix} \tag{3.66}$$

This is expressed in compliance matrix form as:

$$\begin{bmatrix}\varepsilon_{xx}\\ \varepsilon_{yy}\\ 2\varepsilon_{xy}\end{bmatrix} = \frac{1+v}{E}\begin{bmatrix}1-v & -v & 0\\ -v & 1-v & 0\\ 0 & 0 & 1\end{bmatrix}\begin{bmatrix}\sigma_{xx}\\ \sigma_{yy}\\ \sigma_{xy}\end{bmatrix} \tag{3.67}$$

Considering strain along mutually perpendicular directions, following equations can be obtained from the compliance matrix in Eq. (3.67):

$$\varepsilon_{xx} = \frac{1-v^2}{E}\left(\sigma_{xx} - \frac{v}{1-v}\sigma_{yy}\right) \tag{3.68}$$

$$\varepsilon_{yy} = \frac{1-v^2}{E}\left(\sigma_{yy} - \frac{v}{1-v}\sigma_{xx}\right)$$

Adding $\frac{v\sigma_{xx}}{(1-v)}$ and rearranging the formulas in Eq. (3.68) leads to:

$$\sigma_{xx} = \frac{E}{1+v}\varepsilon_{xx} + v\left(\sigma_{xx} + \sigma_{yy}\right) \tag{3.69}$$

$$\sigma_{yy} = \frac{E}{1+v}\varepsilon_{yy} + v\left(\sigma_{xx} + \sigma_{yy}\right)$$

Adding σ_{xx} and σ_{yy} derives into:

$$(\sigma_{xx} + \sigma_{yy}) = \frac{E}{(1+v)(1-2v)}(\varepsilon_{xx} + \varepsilon_{yy}) \tag{3.70}$$

Substituting Eq. (3.70) in Eq. (3.69) leads to:

$$\sigma_{xx} = \frac{E}{1+v}\varepsilon_{xx} + \frac{vE}{(1+v)(1-2v)}(\varepsilon_{xx} + \varepsilon_{yy}) \tag{3.71}$$

$$\sigma_{yy} = \frac{E}{1+v}\varepsilon_{yy} + \frac{vE}{(1+v)(1-2v)}(\varepsilon_{xx} + \varepsilon_{yy})$$

Finally, plane strain Hooke's law could be expressed in index form as:

$$\sigma^{\alpha\beta} = \frac{E}{1+v}\varepsilon^{\alpha\beta} + \frac{vE}{(1+v)(1-2v)}\varepsilon^{\gamma\gamma}\delta^{\alpha\beta} \tag{3.72}$$

where α and β denote x and y coordinate directions and $\varepsilon^{\gamma\gamma} = \varepsilon_{xx} + \varepsilon_{yy}$.

3.5.3 Plastic strain rate tensor

Material's elastic limit under all possible combinations of stresses defines the yield function. Geometrical representation of a yield function determines the yield surface. For an elastic-perfectly plastic material, the plastic deformation occurs when the stress state of the material is on the

yield surface. The plastic deformation (plastic flow) continues as the state of stress continues to be on the yield surface. Instead, if the stress state drops below the yield surface, all incremental deformations are considered as elastic. These states of stresses occur during the loading and unloading process of the material.

For instance, if consider the stress of a material at plastic state is $\sigma^{\alpha\beta}$ and an infinitesimal increment in the stress level (additional loading) is $d\sigma^{\alpha\beta}$. As illustrated in Figure 3.8a, this additional loading for an elastic-perfectly plastic material should not move beyond the yield surface, instead it should travel along the tangential direction to cause plastic flow [98]. As the stress level does not exist beyond the yield surface, change in yield function is considered to be zero. Thus, the condition is provided as:

$$df = \frac{\partial f}{\partial \sigma^{\alpha\beta}} d\sigma^{\alpha\beta} = 0 \tag{3.73}$$

On the other hand, the plastic strain is obtained from the plastic flow rule. Plastic flow rule is derived by differentiating the plastic potential function $\mathrm{g}(\sigma^{\alpha\beta})$ with respect to stress $(\sigma^{\alpha\beta})$ as shown in Figure 3.8b. Hence, the expression for plastic flow is:

$$d\varepsilon_p^{\alpha\beta} = d\lambda \frac{\partial \mathrm{g}}{\partial \sigma^{\alpha\beta}} \tag{3.74}$$

From Eq. (3.74), the plastic strain rate tensor is defined as:

$$\dot{\varepsilon}_p^{\alpha\beta} = \dot{\lambda} \frac{\partial \mathrm{g}}{\partial \sigma^{\alpha\beta}} \tag{3.75}$$

where $\dot{\lambda}$ is the rate of change of plastic multiplier which is solved utilizing the relationship in Eq. (3.73).

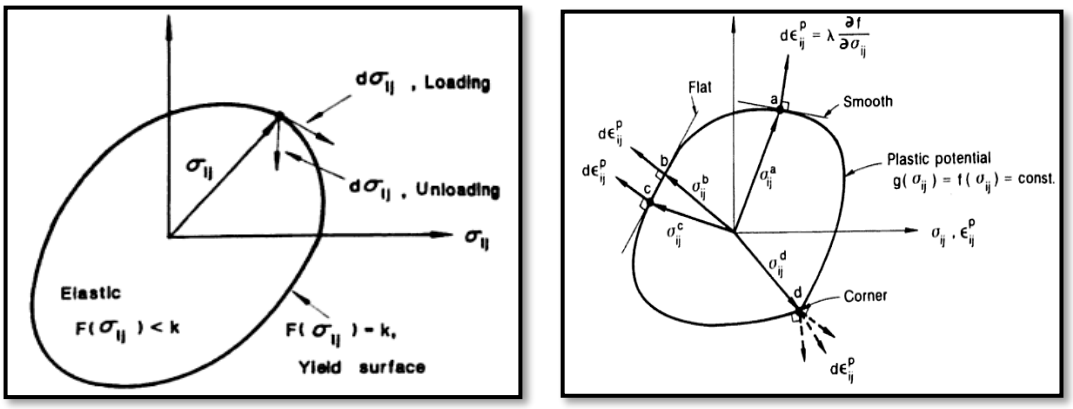


Figure 3.8: (a) $d\sigma^{\alpha\beta}$ for elastic-perfectly plastic model; (b) Plastic flow for elastic-perfectly plastic model [100].

3.6 Failure criterion

The shear stress on failure plane at which the material fails is defined as the shear strength of the material. However, identifying the plane at which the failure occurs is of question. Doubt arises to determine whether is it the plane at which the maximum stress takes place or is it the plane at which the ratio of shear stress to normal stress reaches maximum. Hence, in order to provide solutions to these problems, several failure criterion have been introduced for materials [107]. Some of the mainly used failure criteria are Tresca criterion, von-Mises yield criterion, Drucker-Prager and Mohr-Coulomb criterion.

3.6.1 Tresca criterion

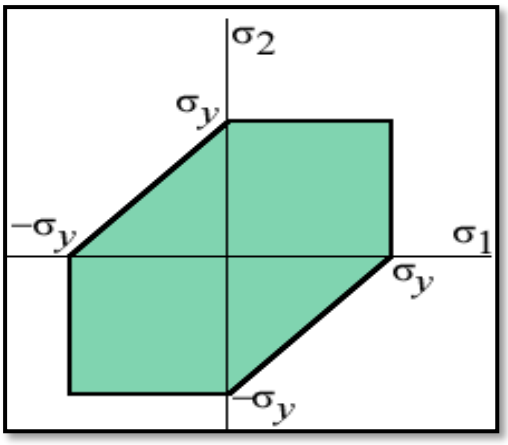


Figure 3.9: Tresca yield criterial in 2D space [110].

Tresca failure criterion was introduced by Tresca in the year 1864. It was the first failure criterion which was introduced for combined state of stress for metals. The hypothesis of this criterion is that the failure occurs when the maximum shear stress reaches the critical value of k. Hence, Tresca criterion is given by the expression [108]:

$$\tau_{max}\left[\left|\frac{\sigma_1-\sigma_2}{2}\right|,\left|\frac{\sigma_2-\sigma_3}{2}\right|,\left|\frac{\sigma_3-\sigma_1}{2}\right|\right]=\frac{\sigma_y}{2}=k \tag{3.76}$$

where σ_y is the yield stress in simple tension. Tresca criterion is plotted in 2D space by considering $\sigma_3 = 0$ as illustrated in Figure 3.9. However, the criterion inherits several drawbacks which prevent its application to soil material. The method ignores the effect of hydrostatic pressure in computing the shear strength. It predicts similar values of stresses at failure under both tension and compression. This is in contradiction to the soil behaviour as the material contains a lower tensile

strength than its compressive strength [109]. Furthermore, the criterion disregards the effect of intermediate principal stress σ_2 which makes it unreliable for metal applications [108].

3.6.2 Von-Mises criterion

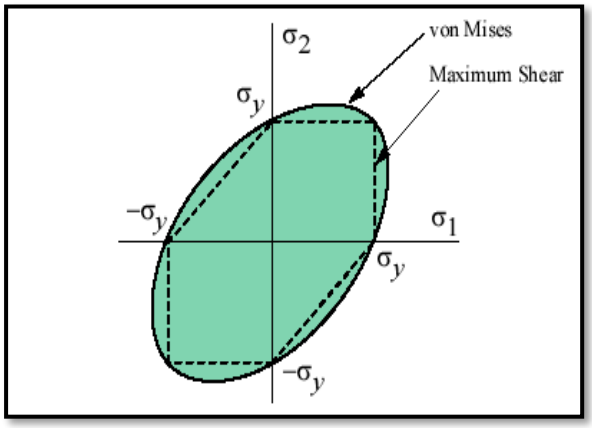


Figure 3.10: Von-Mises yield criterion in 2D space [110].

Von-Mises yield criterion assumes that failure occurs when the square root of second invariant of deviatoric stress tensor J_2 becomes equivalent to a critical value of k. The mathematical relationship for von-Mises yield criterion is defined as:

$$\sqrt{J_2} = \frac{\sigma_y}{\sqrt{3}} = k \tag{3.77}$$

where σ_y is the yield stress in simple tension. von-Mises failure criterion can be plotted in 2D space by considering $\sigma_3 = 0$ as illustrated in Figure 3.10. Similar to Tresca criterion, von-Mises failure criterion does not consider the effect of hydrostatic pressure. Therefore, the criterion is

only applicable for materials which are pressure insensitive such as metals. Furthermore, unlike Tresca criterion, von-Mises considers the effect of intermediate principal stress σ_2. As such, due to its advantages over Tresca criterion, von-Mises yield criterion is selected in present study for simulating the behaviour of metals.

Tresca and von-Mises yield criterion are not applicable to simulate pressure dependent materials such as soil due to its nature in ignoring the effect of hydrostatic pressure. As such, other widely known failure criterion considering the effect of hydrostatic pressure such as Mohr-Coulomb criterion and Drucker-Prager yield criterion are discussed below.

3.6.3 Mohr-Coulomb criterion

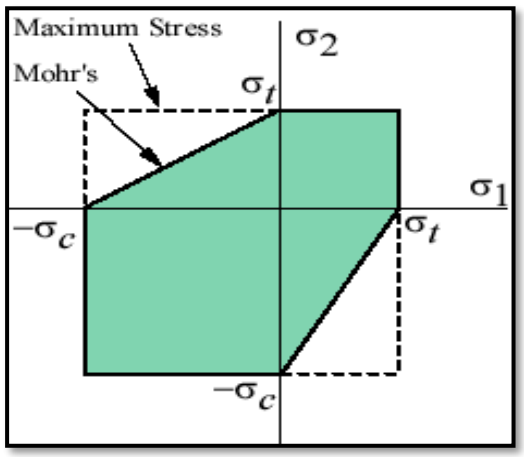


Figure 3.11: Mohr-Coulomb criterion [110].

Mohr Coulomb failure criterion is the extended version of Tresca criterion [109]. This criterion suggests that the failure of material occurs when the

limiting value of shear stress reaches the failure envelope. The failure envelop is defined by:

$$\tau_{ff} = \sigma_{ff} tan\phi + c \tag{3.78}$$

where σ is the normal stress, τ is the shear strength and subscripts ff refers to the 'failure plane' and 'at failure' respectively. c is the intercept at which failure envelope intersects τ axis. This is known as cohesion and ϕ (angle of friction) is the slope of failure envelope [110]. Furthermore, Figure 3.11 illustrates Mohr-Coulomb failure criterion in 2D space.

Mohr-Coulomb failure criterion is a frequently employed criterion for soil mechanics [107]. However, its failure surface consists sharp edges as shown in Figure 3.11. This feature causes numerical inconvenience and complications when the side of the hexagon to be employed is unknown or when each point fails to contain a set of fixed principal directions [111]. In addition, the criterion assumes that there is negligible effect of intermediate stress on failure. Nevertheless, these shortfalls are overcome in the extended version of von-Mises, which is known as Drucker-Prager failure criterion [109].

3.6.4 Drucker-Prager criterion

Drucker-Prager failure criterion is the most often used criterion in practical applications [109]. It is not only the extended version of von-Mises

but also a smoothed version of Mohr-Coulomb criterion. The mathematical representation of the criterion is expressed as:

$$\sqrt{J_2} + \alpha_\phi I_1 = k \tag{3.79}$$

where J_2 is the second invariant of deviatoric stress tensor, I_1 is the first invariant of stress tensor, α_ϕ and k are material constants which are related to ϕ and c. The relationship of material constants to shear strength parameters vary in many ways. For instance, if Mohr-Coulomb hexagon surface is considered to coincide with Drucker-Prager cone surface along the compression meridian (0^0, point A in Figure 3.12), the material constants are expressed as:

$$\alpha_\phi = \frac{2\sin\phi}{\sqrt{3}(3-\sin\phi)} \; and \; k = \frac{6c\cos\phi}{\sqrt{3}(3-\sin\phi)} \tag{3.80}$$

On the other hand, if Mohr-Coulomb hexagon surface coincides with smaller Drucker-Prager cone surface along tension meridian (60^0, point B in Figure 3.12), then the material constants are expressed as:

$$\alpha_\phi = \frac{2\sin\phi}{\sqrt{3}(3+\sin\phi)} \; and \; k = \frac{6c\cos\phi}{\sqrt{3}(3+\sin\phi)} \tag{3.81}$$

Drucker-Prager failure criterion consists of a smooth surface instead of sharp edges as Mohr-Coulomb yield criterion. This feature makes it convenient to acquire numerical solutions. Its material constants can be easily determined using conventional tri-axial tests. Furthermore, the criterion considers the effect of hydrostatic pressure in determining the soil strength [109]. Hence, the criterion has been widely applied in geotechnical applications [112]. As such, Drucker-Prager yield criterion is selected in

the development of SPH constitutive model to simulate the soil material in current study.

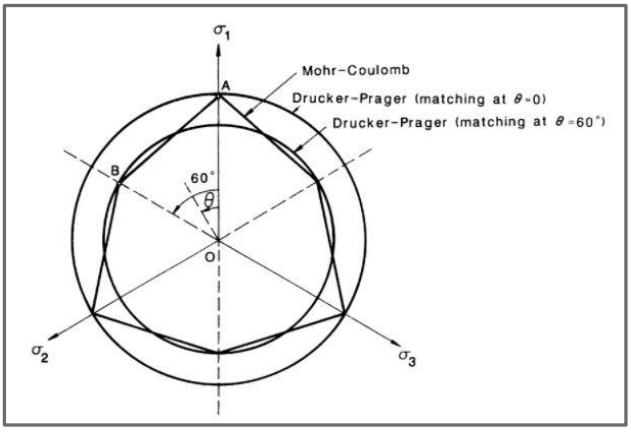


Figure 3.12: Drucker-Prager failure criterion in 2D space [111].

3.7 Summary

Zone 1 and 2 in Figure 3.13 present the summary of current chapter in the form of a flow chart. This is shown by the main categories of 'SPH basic formulation', 'total stress tensor' and 'failure criterion'. 'SPH basic formulation' comprised the complete derivation process of SPH formulations. This contributed for an in-depth knowledge of the formulations for further improvement. Moreover, according to SPH formulations, there are various types of smoothing functions. However, subsequently to the study on three types of smoothing functions, Cubic-Spline is selected as shown in Figure 3.13. Thereafter, for completing the SPH governing equations in two-dimension, 2D stress tensor is selected as shown under the category of 'total stress tensor' in Figure 3.13.

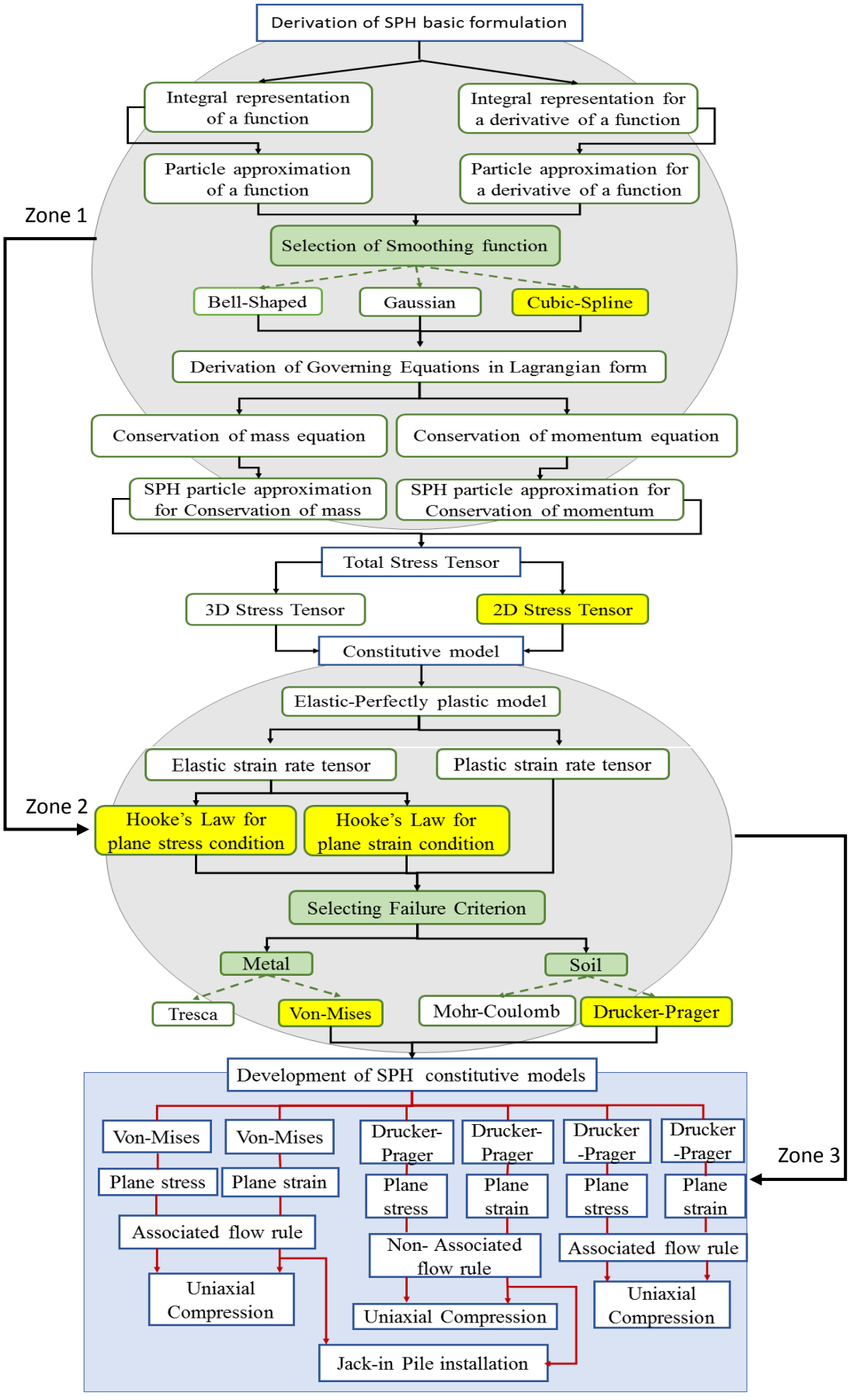


Figure 3.13: Methodology in flow chart.

The chapter further involves an explanation on the selection of elastic-perfectly plastic constitutive model. This is shown in Zone 2 of Figure 3.13. The derivation of Hook's law for both plane stress and plane strain conditions are mainly focused as these are the key to derive the elastic sections of the SPH constitutive models. Moreover, the study involves a review on failure criterion. Among the failure criterion, von-Mises and Drucker-Prager yield criterion are selected as illustrated in Figure 3.13.

All-in-all using the above segments, current study presents the development of six SPH constitutive models as shown by Zone 3 in Figure 3.13. These developed constitutive models are initially examined on simulating the stress-strain behaviour of materials under uniaxial compression prior to its application to the complex scenario as indicated in Figure 3.13. Hence, the development of SPH constitutive models for plane stress and plane strain condition and their application to simulate stresses and strains in 2D materials under uniaxial compression are presented in chapter 4 and 5 respectively. Subsequently, SPH model development incorporating the proposed constitutive models to analyse stresses around jack-in pile is introduced in chapter 6.

Chapter 4
Development of smooth particle hydrodynamics models for plane stress condition

4.1 Introduction

Multitude of engineering applications such as bars under compression or tension, beams, aircraft wing panels, various components of vehicles, machines and thin plates are de-graded from three-dimensional to two-dimensional (2D) problems and are assumed to be of plane stress condition [113]–[116]. Designing of such structures necessitate a complete comprehension of its stress and strain response including emphasis to plastic behaviour under plane stress condition to external stimuli. This is significantly important to create safe engineering structural designs [114], [117]. Therefore, constitutive equations under this condition plays a pivotal role in providing an in-depth knowledge on stress-strain relationship of such desired structures. This is an intensely researched sector due to the importance of precise constitutive models for applications in solids and structures [103], [118].

Constitutive models for plane stress problems are of complex mathematical formulations and are predominantly solved using finite

element method (FEM) in solid mechanics [119]. Marcal and King. [120] developed constitutive equation based on FEM applicable for elastic-perfectly plastic materials for both plane stress and plane strain conditions obeying von-Mises yield criterion. Yoshida et al. [121] performed numerical simulation using FEM for the development of elastic-perfectly plastic constitutive model to study the in-plane stresses and strains for two types of steel sheets. Furthermore, Feng et al. [122] derived Drucker-Prager yield criterion constitutive relation based on mechanism-based gradient-dependent plasticity to study the behaviour of pressure-sensitive materials. Thereafter, Dharan et al. [123] extended elastic, elastic-plastic and fully plastic constitutive equations based on plane stress condition to predict fracture in flat plates. Having the above proof, FEM being a grid-based method has efficiently solved constitutive models in solid mechanics.

Despite its success, the method inherits several drawbacks. The grid-based system limits its application from many complex scenarios due to substantial difficulties in simulating certain aspects of the scenarios. It has become impossible for the method to accurately simulate free surfaces, moving interface, deformable boundaries and excessive deformations. Most importantly, stress computation under this method are of reduced accuracy due to the presence of their discontinuous property [31], [32], [124].

Alternatively, SPH possesses several advantages over the conventional grid-based method. The Lagrangian nature of the method allows to acquire the time history of the particles. Unlike the Eulerian

method, the approach naturally simulates material interfaces, free surfaces and moving boundaries through suitable arrangement of particles. In addition, it innates the potential of dealing with extreme deformations. The application of SPH in solid mechanics was initially introduced by Libersky and Petscheck. [48]. The authors presented von-Mises elastic-perfectly plastic constitutive equation in SPH framework to model deformation of iron rod under plane strain condition. Subsequently, Libersky et al. [49] extended the above 2D elastic-perfectly plastic constitutive model to 3D to simulate solid dynamics. Benz and Asphaug. [41] implemented fracture into this 3D model to simulate fracture of brittle solids. Thereafter, Randles and Libersky. [125] modelled deformation, fracture and fragmentation in both 2D and 3D structures utilizing 2D plane strain and 3D elastic-perfectly plastic constitutive models respectively. Subsequently, utilizing the elastic SPH model, Gray et al. [126] studied the dynamic response of 2D elastic solids. Later, the elastic-perfectly plastic constitutive model introduced by Libersky and Petschek. [48] for plane strain condition was modified by Gray and Monaghan. [127] by incorporating damage model to simulate fracture around magma chambers. Das and Cleary. [128] extended Gray et al. [126] elastic SPH model to predict the dynamic fracture in rock under impact. Patiño et al. [129] analysed deformations of 2D structures utilizing a visco-plastic model and an elastic-perfectly plastic constitutive model under plane strain condition. Thereafter, by coupling Drucker-Prager and Grady-Kipp constitutive models, Thomas et al. [130] examined fracture in rock

materials under plane strain condition. Subsequently, the authors simulated fracture in rock by utilizing 2D and 3D elastic SPH models [131].

Several constitutive models have been introduced in general SPH framework over the years. These models have been developed to analyse deformation, fracture and fragmentation of 2D and 3D structures [41], [48], [49], [125]–[131]. However, according to literature, constitutive equations incorporating plasticity for 2D structures have been mainly developed under plane strain condition [48], [125], [127], [129], [130]. Thus, it is apparent, the constitutive models involving plasticity are yet to be developed under plane stress condition in general SPH framework. Furthermore, utilizing these constitutive models incorporating plasticity, the standard SPH formulation has not been developed to analyse materials' and structures' stress-strain behaviour. Hence, due to the advanced nature and success of SPH method, it is worth considering the development of these constitutive models in general SPH framework for the investigation of stress-strain response of 2D structures under plane stress condition.

Therefore, aim of this chapter is to introduce a SPH framework for plane stress applications involving plasticity and to deliver an efficient numerical tool for structural and mechanical engineers. Perseverance to this, it is essential to extend SPH with constitutive models containing elasto-plastic, elasto-viscous plastic flow rules. As an initiation to this, the chapter presents the development of three constitutive models in SPH framework under plane stress conditions. This includes the development

of von-Mises elastic-perfectly plastic constitutive model with associated flow rule and Drucker-Prager elastic-perfectly plastic constitutive model with associated and non-associated flow rule. SPH models are proposed comprising these constitutive models for simulating stresses and strains in materials under uniaxial compression. The models are constructed by developing the SPH programme code using C++ language. In addition, OpenGL is incorporated within the programme for providing continuous graphical representation of stress distribution in the materials. The results are validated with analytical solutions. However, during simulation stresses were experienced outside the yield surface. Hence, for eliminating the problem further contribution has been made by proposing tension cracking treatment and stress-scaling back pressure for both models under 2D plane stress condition. Furthermore, stress computation is proposed at the solid boundary. Materials selected for uniaxial compression are within a wider range of Poisson's ratio. Drucker-Prager model involves the hydrostatic component which facilitates its application in pressure sensitive dilatant materials. On the other hand, von-Mises is applicable for pressure-independent materials. Thus, the proposed constitutive models are applied to analyse the stress-strain behaviour of various materials within a wide range of Poisson's ratio allowing us to examine the proposed models' capability for numerous plane stress applications.

4.2 Geometrical setup for uniaxial compression

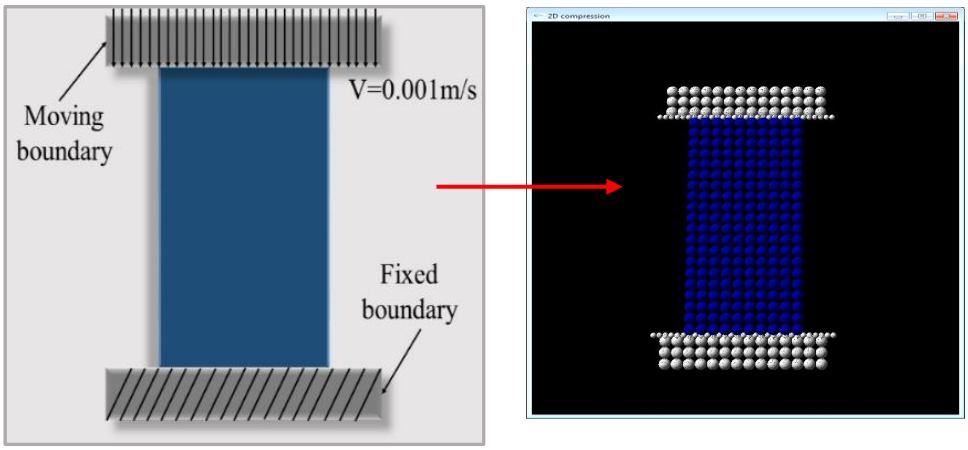


Figure 4.1: Geometrical setup for uniaxial compression.

The geometry of the system considered for the analysis is presented in Figure 4.1. The dimensions are 0.038 m and 0.076 m in width and height respectively. The model is generated with 200 real particles (10 particles along x direction and 20 along y direction) and 84 boundary particles to represent the upper and lower solid boundaries. Smoothing length h is chosen to be 0.004 m. The material is loaded by the upper boundary with constant velocity 0.001m/s.

The chapter presents nine computational cases, three cases for each proposed constitutive model. The analysis is performed by varying the parameters while maintaining the system unchanged as shown in Figure. 4.1. Parameters considered for each case are listed in Table 4.1. Results obtained for each case includes stress-strain response of the system under loading. Apart from that, the modelling further comprises presentation of

graphical images. This provides the benefit of clear visualisation of vertical stress distribution in particles during uniaxial compression.

Table 4.1: Material Parameters.

	von-Mises plane stress Constitutive model			Drucker-Prager plane stress Constitutive model for both non-associated and associated flow rule		
	Case 1: Berylliu m alloy	Case 2: Aluminium alloy	Case 3: Lead alloy	Case 4, 7: Soil 1	Case 5, 8: Soil 2	Case 6, 9: Soil 3
Bulk modulus (K)	139.21 GPa	53.04GPa	14.55 GPa	70.59 MPa	147.86 MPa	93.51 MPa
Shear modulus (G)	109.38 GPa	25.54GPa	5.52 GPa	52.17 MPa	79.62 MPa	58.54 MPa
Young's modulus (E)	245 GPa	68.95GPa	16GPa	120MPa	207 MPa	144MPa
Yield stress (MPa)	360	500	33	-	-	-
Poisson's ratio	0.12	0.35	0.45	0.15	0.3	0.23
Friction angle (ϕ)	-	-	-	30	30	30
Cohesion (c)	-	-	-	69kPa	69kPa	69kPa
density	2900	2700	11100	1380	1850	1430

4.3 Development of elastic-perfectly plastic constitutive models for 2D plane stress condition

In this section, the development of both Drucker-Prager and von-Mises constitutive models for 2D plane stress condition are presented. Initially, the derivation of the general elastic-perfectly plastic constitutive equation is introduced. Thereafter, the development of these equations with the

incorporation of von-Mises and Drucker-Prager yield criterion are included in Sections 4.3.1 and 4.3.2 respectively.

Derivation of the general elastic-perfectly plastic constitutive equation for 2D plane stress condition:

The derivation is initiated by substituting Eq. (3.51) in Eq. (3.65) for obtaining the following expression for total stress tensor:

$$s^{\alpha\beta} = \frac{E}{1+v}\varepsilon^{\alpha\beta} + \frac{vE}{(1+v)(1-v)}\varepsilon^{\gamma\gamma}\delta^{\alpha\beta} - P\delta^{\alpha\beta} \tag{4.1}$$

where $\varepsilon^{\alpha\beta}$ and $s^{\alpha\beta}$ are the total strain tensor and deviatoric shear stress tensor respectively. By using the expressions in Eq. (4.2) for 2D plane stress condition [132], Eq. (4.1) is rearranged as shown in Eq. (4.3):

$$K = \frac{E}{2(1-v)};\ G = \frac{E}{2(1+v)}\ ;P = K\varepsilon^{\gamma\gamma} \tag{4.2}$$

$$s^{\alpha\beta} = \frac{E}{1+v}\varepsilon^{\alpha\beta} + \frac{vE}{(1+v)(1-v)}\varepsilon^{\gamma\gamma}\delta^{\alpha\beta} - \frac{E}{2(1-v)}\varepsilon^{\gamma\gamma}\delta^{\alpha\beta} \tag{4.3}$$

where K and G are bulk and Shear modulus for plane stress condition. Furthermore, $\varepsilon^{\alpha\beta}$ is the summation of deviatoric shear strain tensor ($e^{\alpha\beta}$) and volumetric strain tensor ($\varepsilon^{\gamma\gamma}$). This is expressed for 2D as [133]:

$$\varepsilon^{\alpha\beta} = e^{\alpha\beta} + \frac{1}{2}\varepsilon^{\gamma\gamma}\delta^{\alpha\beta} \tag{4.4}$$

Substituting Eq. (4.4) in Eq. (4.3) leads to:

$$s^{\alpha\beta} = \frac{E}{1+v} e^{\alpha\beta} + \frac{(E - Ev + 2Ev - E - Ev)}{2(1+v)(1-v)} \varepsilon^{\gamma\gamma} \delta^{\alpha\beta} \tag{4.5}$$

which simplifies into the expression for deviatoric shear strain tensor as:

$$e^{\alpha\beta} = \frac{s^{\alpha\beta}}{2G} \tag{4.6}$$

On the other hand, by substituting the relationship $\varepsilon^{\gamma\gamma} = \frac{p}{K} = \frac{\sigma^{\gamma\gamma}}{2K}$ and Eq. (4.2) in Eq. (4.4), the volumetric strain tensor is derived as:

$$\frac{1}{2} \varepsilon^{\gamma\gamma} \delta^{\alpha\beta} = \frac{(1-v)}{2E} \sigma^{\gamma\gamma} \delta^{\alpha\beta} \tag{4.7}$$

Finally, by substituting Eq. (4.6) and Eq. (4.7) in Eq. (4.4), the elastic strain rate tensor for 2D plane stress condition is obtained as:

$$\dot{\varepsilon}_e^{\alpha\beta} = \frac{\dot{s}^{\alpha\beta}}{2G} + \frac{(1-v)}{2E} \dot{\sigma}^{\gamma\gamma} \delta^{\alpha\beta} \tag{4.8}$$

Thereafter, substituting Eq. (4.8) and Eq. (3.75) in Eq. (3.57) derives the total strain rate tensor as:

$$\dot{\varepsilon}^{\alpha\beta} = \frac{\dot{s}^{\alpha\beta}}{2G} + \frac{(1-v)}{2E} \dot{\sigma}^{\gamma\gamma} \delta^{\alpha\beta} + \dot{\lambda} \frac{\partial \mathrm{g}}{\partial \sigma^{\alpha\beta}} \tag{4.9}$$

Using the relationships in Eqs. (3.54), (4.2) and (4.4), Eq. (4.9) is re-written as:

$$\dot{\varepsilon}^{\alpha\beta} = \frac{\dot{s}^{\alpha\beta}}{2G} + \frac{\dot{\varepsilon}^{\gamma\gamma}}{2} \delta^{\alpha\beta} + \dot{\lambda} \frac{\partial \mathrm{g}}{\partial \sigma^{\alpha\beta}} \tag{4.10}$$

Multiplying Eq. (4.10) by $2G$ leads to:

$$2G\dot{\varepsilon}^{\alpha\beta} = \dot{s}^{\alpha\beta} + \dot{G}\varepsilon^{\gamma\gamma} \delta^{\alpha\beta} + 2G\dot{\lambda} \frac{\partial \mathrm{g}}{\partial \sigma^{\alpha\beta}} \tag{4.11}$$

Substituting Eqs. (4.4) and (3.54) into Eq. (4.11) derives the general elastic-perfectly plastic constitutive equation for 2D-plane stress condition as:

$$\dot{\sigma}^{\alpha\beta} = 2G\dot{e}^{\alpha\beta} + K\dot{\varepsilon}^{\gamma\gamma}\delta^{\alpha\beta} - \dot{\lambda}\left[2G\frac{\partial \mathrm{g}}{\partial \sigma^{\alpha\beta}}\right] \tag{4.12}$$

The general form of rate of change of plastic multiplier $\dot{\lambda}$ is derived using the relationship in Eq. (3.73) as:

$$\dot{\lambda} = \frac{2G\dot{\varepsilon}^{\alpha\beta}\frac{\partial f}{\partial \sigma^{\alpha\beta}} + (K-G)\dot{\varepsilon}^{\gamma\gamma}\frac{\partial f}{\partial \sigma^{\alpha\beta}}\delta^{\alpha\beta}}{2G\frac{\partial f}{\partial \sigma^{\alpha\beta}}\frac{\partial \mathrm{g}}{\partial \sigma^{\alpha\beta}}} \tag{4.13}$$

where f and g are the yield function and plastic potential function respectively. Furthermore, for stress-strain relations, it is necessary to employ the rate of stress which is invariant with respect to the rotation of the solid body. As such, Jaumann stress rate is adopted in this study, which is expressed as [126]:

$$\hat{\dot{\sigma}}^{\alpha\beta} = \dot{\sigma}^{\alpha\beta} - \sigma^{\alpha\gamma}\dot{\omega}^{\beta\gamma} - \sigma^{\gamma\beta}\dot{\omega}^{\alpha\gamma} \tag{4.14}$$

where $\dot{\omega}^{\alpha\beta}$ is the spin rate tensor and is defined as:

$$\dot{\omega}^{\alpha\beta} = \frac{1}{2}\left(\frac{\partial v^{\alpha}}{\partial x^{\beta}} - \frac{\partial v^{\beta}}{\partial x^{\alpha}}\right) \tag{4.15}$$

Finally, by substituting Eq. (4.14) in Eq. (4.12) the final form of general elastic-perfectly plastic constitutive equation for 2D plane stress condition is proposed in this study as:

$$\dot{\sigma}^{\alpha\beta} = \sigma^{\alpha\gamma}\dot{\omega}^{\beta\gamma} + \sigma^{\gamma\beta}\dot{\omega}^{\alpha\gamma} + 2G\dot{e}^{\alpha\beta} + K\dot{\varepsilon}^{\gamma\gamma}\delta^{\alpha\beta} - \dot{\lambda}\left[2G\frac{\partial \mathrm{g}}{\partial \sigma^{\alpha\beta}}\right] \tag{4.16}$$

where $\dot{\lambda}$ is defined by Eq. (4.13).

4.3.1 Development of elastic-perfectly plastic constitutive equation for plane stress condition using von-Mises yield criterion

Eq. (4.16) provides the general form of constitutive equation for 2D plane stress condition. It is now essential to develop it to suit the yield criterion. Therefore, this section proposes the development of the constitutive model for von-Mises yield criterion with associated flow rule.

$$f = \sqrt{J_2} - \frac{\sigma_y}{\sqrt{3}} \tag{4.17}$$

$$J_2 = \frac{1}{3}[\sigma_{11}^2 - \sigma_{11}\sigma_{22} + \sigma_{22}^2] + \sigma_{12}^2 \tag{4.18}$$

Von-Mises yield criterion is defined by Eq. (4.17). In the expression, σ_y is the yield stress, and J_2 is the second invariant of deviatoric stress tensor. For plane stress condition, J_2 is generally expressed by Eq. (4.18) [134]. However, the development of von-Mises constitutive model necessitates Eq. (4.18) in terms of $s^{\alpha\beta}$ and $\sigma^{\gamma\gamma}$. Therefore, current study introduces J_2 in terms of $s^{\alpha\beta}$ and $\sigma^{\gamma\gamma}$ for two-dimension. The derivation is presented as follows:

Stress tensor in 2D space could be divided into deviatoric stress tensor and hydrostatic stress tensor as expressed by Eq. (3.53). This could be written in an alternative form as:

$$\begin{bmatrix}\sigma_{11} & \sigma_{12}\\ \sigma_{12} & \sigma_{22}\end{bmatrix} = \begin{bmatrix}s_{11} & s_{12}\\ s_{12} & s_{22}\end{bmatrix} + \begin{bmatrix}\sigma_m & 0\\ 0 & \sigma_m\end{bmatrix} \tag{4.19}$$

where mean stress $\sigma_m = \frac{\sigma_{11}+\sigma_{22}}{2}$

Using the above formulation, Eq. (4.18) is re-written as:

$$J_2 = \frac{1}{3}[(s_{11} + \sigma_m)^2 - (s_{11} + \sigma_m)(s_{22} + \sigma_m) + (s_{22} + \sigma_m)^2] + s_{12}^2 \quad (4.19)$$

$$J_2 = \frac{1}{3}[(s_{11})^2 + (s_{22})^2 + (\sigma_m)^2 + (s_{11}\sigma_m) + (s_{22}\sigma_m) - (s_{11}s_{22})] + s_{12}^2 \quad (4.19)$$

Simplifying the relationship $(s_{11} + s_{22})^2 = 0$ leads to:

$$(s_{11})^2 + (s_{22})^2 = -2s_{11}s_{22} \quad (4.20)$$

Substituting Eq. (4.20) in Eq. (4.19) derives:

$$J_2 = \frac{1}{2}[(s_{11})^2 + (s_{22})^2] + \frac{1}{3}[(\sigma_m)^2 + (s_{11}\sigma_m) + (s_{22}\sigma_m)] + s_{12}^2 \quad (4.21)$$

Using expression $(s_{11} + s_{22}) = 0$ [135], Eq. (4.21) is derived as:

$$J_2 = \frac{1}{2}[(s_{11})^2 + (s_{22})^2 + 2s_{12}^2] + \frac{(\sigma_m)^2}{3} \quad (4.22)$$

Finally, the study introduces Eq. (4.22) in terms of deviatoric stress tensor $(s^{\alpha\beta})$ and hydrostatic stress tensor $(\sigma^{\gamma\gamma})$ as:

$$J_2 = \frac{1}{2}s^{\alpha\beta}s^{\alpha\beta} + \frac{1}{12}\left(\sigma_{\gamma\gamma}\right)^2 \quad (4.23)$$

where $\sigma_{\gamma\gamma} = \sigma_{11} + \sigma_{22}$, and α and β denote x and y coordinate directions.

In addition to above, for the completion of stress-strain relationship, it is essential to define the plastic potential function. Von-Mises plastic potential function for associated flow rule is equivalent to its yield function. This is expressed as:

$$g = \sqrt{J_2} - \frac{\sigma_y}{\sqrt{3}} \tag{4.24}$$

$\frac{\partial f}{\partial \sigma^{\alpha\beta}}$ and $\frac{\partial g}{\partial \sigma^{\alpha\beta}}$ for von-Mises yield criterion is:

$$\frac{\partial f}{\partial \sigma^{\alpha\beta}} = s^{\alpha\beta};\ \frac{\partial g}{\partial \sigma^{\alpha\beta}} = s^{\alpha\beta} \tag{4.25}$$

In present study, by substituting Eq. (4.25) in Eq. (4.16), von-Mises constitutive equation with associated flow rule is derived under plane stress condition as:

$$\dot{\sigma}^{\alpha\beta} = \sigma^{\alpha\gamma}\dot{\omega}^{\beta\gamma} + \sigma^{\gamma\beta}\dot{\omega}^{\alpha\gamma} + 2G\dot{e}^{\alpha\beta} + K\dot{\varepsilon}^{\gamma\gamma}\delta^{\alpha\beta} - \dot{\lambda}\left[2Gs^{\alpha\beta}\right] \tag{4.26}$$

Furthermore, by substituting Eq. (4.25) in Eq. (4.13), $\dot{\lambda}$ is obtained as:

$$\dot{\lambda} = \frac{2G\dot{e}^{\alpha\beta}s^{\alpha\beta} + K\dot{\varepsilon}^{\gamma\gamma}\delta^{\alpha\beta}s^{\alpha\beta}}{2Gs^{\alpha\beta}s^{\alpha\beta}} \tag{4.27}$$

Thereafter, by using the relationship $s^{\alpha\beta}\delta^{\alpha\beta} = 0$ and Eq. (4.23) in Eq. (4.27), $\dot{\lambda}$ is derived as:

$$\dot{\lambda} = \frac{\dot{e}^{\alpha\beta}s^{\alpha\beta}}{2\left(\frac{\sigma_y^2}{3} - \frac{1}{12}(\sigma^{\gamma\gamma})^2\right)} \tag{4.28}$$

Finally, the ultimate form of von-Mises constitutive equation for plane stress condition is proposed in SPH framework as:

$$\frac{D\sigma_i^{\alpha\beta}}{Dt} = \sigma^{\alpha\gamma}\dot{\omega}^{\beta\gamma} + \sigma^{\gamma\beta}\dot{\omega}^{\alpha\gamma} + 2G\dot{e}^{\alpha\beta} + K\dot{\varepsilon}^{\gamma\gamma}\delta^{\alpha\beta} - \dot{\lambda}\left[Gs^{\alpha\beta}\right] \tag{4.29}$$

$$\dot{\lambda} = \frac{\dot{e}^{\alpha\beta}s^{\alpha\beta}}{\left(\frac{\sigma_y^2}{3} - \frac{1}{12}(\sigma^{\gamma\gamma})^2\right)}$$

Von-Mises failure criterion ignores the effect of hydrostatic pressure [108]. Hence, the developed model is applicable for pressure insensitive materials. Furthermore, pressure insensitive materials such as metals and metal structures are more suitable to be modelled using associated flow rule [136]. Therefore, the proposed constitutive model is applicable for modelling plane stress pressure independent materials such as metals and metal structures. Most importantly, the developed model could be utilized for clear understanding of their internal stresses and strains under applied loads.

4.3.2 Development of elastic-perfectly plastic constitutive equation for plane stress condition using Drucker-Prager yield criterion

In this section, Eqs. (4.16) and (4.13) are further derived incorporating Drucker-Prager yield criterion under plane stress condition for both non-associated and associated flow rule. To begin with, the mathematical representation of the yield criterion is expressed as:

$$f = \sqrt{J_2} + \alpha_\phi I_1 - k \tag{4.30}$$

where J_2 is the second invariant of deviatoric stress tensor expressed by Eq. (4.23) and I_1 is the first invariant of two-dimensional stress tensor, which is defined as:

$$I_1 = \sigma^{xx} + \sigma^{yy} \tag{4.31}$$

α_ϕ and k are Drucker-Prager constants expressed by Eq. (3.80) [111]:

4.3.2.1 Derivation of 2D-plane stress constitutive model for Drucker-Prager yield criterion with non-associated flow rule

The plastic potential function for non-associated flow rule varies from its yield function as:

$$g = \sqrt{J_2} + 3I_1 sin\psi \tag{4.32}$$

where ψ is the dilatancy angle, which is considered to be zero. This specifies that there will be absence of plastic volumetric deformations. Furthermore, for completing Eqs. (4.16) and (4.13), $\frac{\partial f}{\partial \sigma^{\alpha\beta}}$ and $\frac{\partial g}{\partial \sigma^{\alpha\beta}}$ for Drucker-Prager yield criterion with non-associated flow rule are defined as:

$$\frac{\partial f}{\partial \sigma^{\alpha\beta}} = \alpha_\phi \delta^{\alpha\beta} + \frac{s^{\alpha\beta}}{2\sqrt{J_2}};\ and\ \frac{\partial g}{\partial \sigma^{\alpha\beta}} = 3sin\psi\delta^{\alpha\beta} + \frac{s^{\alpha\beta}}{2\sqrt{J_2}} \tag{4.33}$$

In present study, by substituting Eq. (4.33) in Eq. (4.16), Drucker-Prager stress-strain relationship for plane stress condition with non-associated flow rule is derived as:

$$\begin{aligned}\dot{\sigma}^{\alpha\beta} &= \sigma^{\alpha\gamma}\dot{\omega}^{\beta\gamma} + \sigma^{\gamma\beta}\dot{\omega}^{\alpha\gamma} + 2G\dot{e}^{\alpha\beta} + K\dot{\varepsilon}^{\gamma\gamma}\delta^{\alpha\beta} \\ &- \dot{\lambda}\left[6Gsin\psi\delta^{\alpha\beta} + \frac{G}{\sqrt{J_2}}s^{\alpha\beta}\right]\end{aligned} \tag{4.34}$$

Similarly, by substituting Eq. (4.33) in Eq. (4.13), $\dot{\lambda}$ is obtained as:

$$\dot{\lambda} = \frac{2G\dot{e}^{\alpha\beta}\left(\alpha_\phi\delta^{\alpha\beta} + \frac{s^{\alpha\beta}}{2\sqrt{J_2}}\right) + K\dot{\varepsilon}^{\gamma\gamma}\delta^{\alpha\beta}\left(\alpha_\phi\delta^{\alpha\beta} + \frac{s^{\alpha\beta}}{2\sqrt{J_2}}\right)}{2G\left(\alpha_\phi\delta^{\alpha\beta} + \frac{s^{\alpha\beta}}{2\sqrt{J_2}}\right)\left(3sin\psi\delta^{\alpha\beta} + \frac{s^{\alpha\beta}}{2\sqrt{J_2}}\right)} \tag{4.35}$$

Thereafter, by utilizing the expressions $s^{\alpha\beta}\delta^{\alpha\beta}= 0$, $\delta^{\alpha\beta}\delta^{\alpha\beta} = 2$ and Eq. (4.23), Eq. (4.35) is simplified as:

$$\dot{\lambda} = \frac{2\alpha_\phi K\dot{\varepsilon}^{\gamma\gamma} + \frac{G}{\sqrt{J_2}}s^{\alpha\beta}\dot{\varepsilon}^{\alpha\beta}}{12G\alpha_\phi sin\psi + G\left(\frac{\left[J_2 - \frac{(I_1)^2}{12}\right]}{J_2}\right)} \tag{4.36}$$

Finally, the ultimate form of Drucker-Prager constitutive equation with non-associated flow rule for plane stress condition is proposed in SPH framework as:

$$\frac{D\sigma_i^{\alpha\beta}}{Dt} = \sigma^{\alpha\gamma}\dot{\omega}^{\beta\gamma} + \sigma^{\gamma\beta}\dot{\omega}^{\alpha\gamma} + 2G\dot{e}^{\alpha\beta} + K\dot{\varepsilon}^{\gamma\gamma}\delta^{\alpha\beta} - \dot{\lambda}\left[6Gsin\psi\delta^{\alpha\beta} + \frac{G}{\sqrt{J_2}}s^{\alpha\beta}\right] \tag{4.37}$$

$$\dot{\lambda} = \frac{2\alpha_\phi K\dot{\varepsilon}^{\gamma\gamma} + \frac{G}{\sqrt{J_2}}s^{\alpha\beta}\dot{\varepsilon}^{\alpha\beta}}{12G\alpha_\phi sin\psi + G\left(\frac{\left[J_2 - \frac{(I_1)^2}{12}\right]}{J_2}\right)}$$

4.3.2.2 Derivation of 2D-plane stress constitutive model for Drucker-Prager yield criterion with associated flow rule

The plastic potential function for associated flow rule is identical to the yield function of the criterion which is expressed as:

$$g = \sqrt{J_2} + \alpha_\phi I_1 - k \tag{4.38}$$

For completing Eqs. (4.16) and (4.13), $\frac{\partial f}{\partial \sigma^{\alpha\beta}}$ and $\frac{\partial g}{\partial \sigma^{\alpha\beta}}$ for Drucker-Prager yield criterion with associated flow rule are defined as:

$$\frac{\partial f}{\partial \sigma^{\alpha\beta}} = \alpha_\phi \delta^{\alpha\beta} + \frac{s^{\alpha\beta}}{2\sqrt{J_2}};\ and\ \frac{\partial g}{\partial \sigma^{\alpha\beta}} = \alpha_\phi \delta^{\alpha\beta} + \frac{s^{\alpha\beta}}{2\sqrt{J_2}} \tag{4.39}$$

By substituting Eq. (4.39) in Eq. (4.16), the stress-strain relationship for Drucker-Prager elastic-perfectly plastic model with associated flow rule is obtained as:

$$\dot{\sigma}^{\alpha\beta} = \sigma^{\alpha\gamma}\dot{\omega}^{\beta\gamma} + \sigma^{\gamma\beta}\dot{\omega}^{\alpha\gamma} + 2G\dot{e}^{\alpha\beta} + K\dot{\varepsilon}^{\gamma\gamma}\delta^{\alpha\beta} - \dot{\lambda}\left[2G\alpha_\phi\delta^{\alpha\beta} + \frac{G}{\sqrt{J_2}}s^{\alpha\beta}\right] \tag{4.40}$$

Substituting Eq. (4.39) in Eq. (4.13) derives $\dot{\lambda}$ as:

$$\dot{\lambda} = \frac{2G\dot{e}^{\alpha\beta}\left(\alpha_\phi\delta^{\alpha\beta} + \frac{s^{\alpha\beta}}{2\sqrt{J_2}}\right) + K\dot{\varepsilon}^{\gamma\gamma}\delta^{\alpha\beta}\left(\alpha_\phi\delta^{\alpha\beta} + \frac{s^{\alpha\beta}}{2\sqrt{J_2}}\right)}{2G\left(\alpha_\phi\delta^{\alpha\beta} + \frac{s^{\alpha\beta}}{2\sqrt{J_2}}\right)\left(\alpha_\phi\delta^{\alpha\beta} + \frac{s^{\alpha\beta}}{2\sqrt{J_2}}\right)} \tag{4.41}$$

Using the expressions $s^{pa}\delta^{pa} = 0$, $\delta^{pa}\delta^{pa} = 2$ and Eq. (4.23), $\dot{\lambda}$ is simplified as:

$$\dot{\lambda} = \frac{2\alpha_\phi K\dot{\varepsilon}^{\gamma\gamma} + \frac{G}{\sqrt{J_2}}s^{\alpha\beta}\dot{\varepsilon}^{\alpha\beta}}{4G{\alpha_\phi}^2 + G\left(\frac{\left[J_2 - \frac{(I_1)^2}{12}\right]}{J_2}\right)} \tag{4.42}$$

Finally, the ultimate form of Drucker-Prager constitutive equation with associated flow rule for plane stress condition is proposed in SPH framework as:

$$\frac{D\sigma_i^{\alpha\beta}}{Dt} = \sigma^{\alpha\gamma}\dot{\omega}^{\beta\gamma} + \sigma^{\gamma\beta}\dot{\omega}^{\alpha\gamma} + 2G\dot{e}^{\alpha\beta} + K\dot{\varepsilon}^{\gamma\gamma}\delta^{\alpha\beta} - \dot{\lambda}\left[2G\alpha_\phi\delta^{\alpha\beta} + \frac{G}{\sqrt{J_2}}s^{\alpha\beta}\right] \tag{4.43}$$

$$\dot{\lambda} = \frac{2\alpha_\phi K\dot{\varepsilon}^{\gamma\gamma} + \frac{G}{\sqrt{J_2}}s^{\alpha\beta}\dot{\varepsilon}^{\alpha\beta}}{4G{\alpha_\phi}^2 + G\left(\frac{\left[J_2 - \frac{(I_1)^2}{12}\right]}{J_2}\right)}$$

Drucker-Prager yield criterion comprises hydrostatic pressure. Hence is appropriate for pressure dependent dilatant materials. Therefore, the developed stress-strain relationships in SPH framework for both associated and non-associated flow rules are applicable for investigating the behaviour of pressure sensitive dilatant plane stress materials and structures.

4.4 SPH governing equations for 2D compression

The continuity equation and momentum equation presented by Eqs. (3.45) and (3.49) are employed in this study. In addition, for completing these governing equations, the proposed constitutive models presented in section 4.3 are adopted and are summarized as follows:

von-Mises constitutive equation with associated flow rule:

$$\frac{D\sigma_i^{\alpha\beta}}{Dt} = \sigma^{\alpha\gamma}\dot{\omega}^{\beta\gamma} + \sigma^{\gamma\beta}\dot{\omega}^{\alpha\gamma} + 2G\dot{e}^{\alpha\beta} + K\dot{\varepsilon}^{\gamma\gamma}\delta^{\alpha\beta} - \dot{\lambda}\left[Gs^{\alpha\beta}\right] \tag{4.44}$$

$$\dot{\lambda} = \frac{\dot{e}^{\alpha\beta}s^{\alpha\beta}}{\left(\frac{\sigma_y^2}{3} - \frac{1}{12}(\sigma^{\gamma\gamma})^2\right)}$$

Drucker-Prager constitutive equation with non-associated flow rule:

$$\frac{D\sigma_i^{\alpha\beta}}{Dt} = \sigma^{\alpha\gamma}\dot{\omega}^{\beta\gamma} + \sigma^{\gamma\beta}\dot{\omega}^{\alpha\gamma} + 2G\dot{e}^{\alpha\beta} + K\dot{\varepsilon}^{\gamma\gamma}\delta^{\alpha\beta} - \dot{\lambda}\left[6G sin\psi\delta^{\alpha\beta} + \frac{G}{\sqrt{J_2}}s^{\alpha\beta}\right] \tag{4.45}$$

$$\dot{\lambda} = \frac{2\alpha_\phi K\dot{\varepsilon}^{\gamma\gamma} + \frac{G}{\sqrt{J_2}}s^{\alpha\beta}\dot{\varepsilon}^{\alpha\beta}}{12G\alpha_\phi sin\psi + G\left(\frac{\left[J_2 - \frac{(I_1)^2}{12}\right]}{J_2}\right)}$$

Drucker-Prager constitutive equation with associated flow rule:

$$\frac{D\sigma_i^{\alpha\beta}}{Dt} = \sigma^{\alpha\gamma}\dot{\omega}^{\beta\gamma} + \sigma^{\gamma\beta}\dot{\omega}^{\alpha\gamma} + 2G\dot{e}^{\alpha\beta} + K\dot{\varepsilon}^{\gamma\gamma}\delta^{\alpha\beta} - \dot{\lambda}\left[2G\alpha_\phi\delta^{\alpha\beta} + \frac{G}{\sqrt{J_2}}s^{\alpha\beta}\right] \tag{4.46}$$

$$\dot{\lambda} = \frac{2\alpha_\phi K\dot{\varepsilon}^{\gamma\gamma} + \frac{G}{\sqrt{J_2}}s^{\alpha\beta}\dot{\varepsilon}^{\alpha\beta}}{4G{\alpha_\phi}^2 + G\left(\frac{\left[J_2 - \frac{(I_1)^2}{12}\right]}{J_2}\right)}$$

Furthermore, to complete the above equations, strain and spin rate tensors in SPH framework are as follows [125]:

$$\dot{\varepsilon}^{\alpha\beta} = \frac{1}{2}\left(\frac{\partial v^\alpha}{\partial x^\beta} + \frac{\partial v^\beta}{\partial x^\alpha}\right) = \frac{1}{2}\left[\sum_{j=1}^{N}\frac{m_j}{\rho_j}\left(v_j^\alpha - v_i^\alpha\right)\frac{\partial W_{ij}}{\partial x_i^\beta} + \sum_{j=1}^{N}\frac{m_j}{\rho_j}\left(v_j^\beta - v_i^\beta\right)\frac{\partial W_{ij}}{\partial x_i^\alpha}\right] \tag{4.47}$$

$$\dot{\omega}^{\alpha\beta} = \frac{1}{2}\left(\frac{\partial v^\alpha}{\partial x^\beta} - \frac{\partial v^\beta}{\partial x^\alpha}\right) = \frac{1}{2}\left[\sum_{j=1}^{N}\frac{m_j}{\rho_j}\left(v_j^\alpha - v_i^\alpha\right)\frac{\partial W_{ij}}{\partial x_i^\beta} - \sum_{j=1}^{N}\frac{m_j}{\rho_j}\left(v_j^\beta - v_i^\beta\right)\frac{\partial W_{ij}}{\partial x_i^\alpha}\right] \tag{4.48}$$

4.5 Problems in SPH and solving techniques

Even though SPH is an accurate and successful numerical method it inherits problems such as unphysical oscillation, clumping of particles and tensile instability. Several authors have introduced various methods to overcome such issues during the simulation. Similarly, problems such as unphysical oscillations and stresses outside the yield function were encountered during the modelling of uniaxial compression using the developed models. However, the problem of unphysical oscillation was solved by adopting artificial viscosity. In addition, present study proposes tension cracking treatment and stress-scaling back pressure for plane stress condition. This treatment is employed for preventing stresses outside the yield surface.

Hence, in addition to artificial viscosity current section presents the development of tension cracking treatment for both von-Mises and Drucker-Prager yield criterion for 2D-plane stress condition.

4.5.1 Artificial viscosity

Artificial viscosity was initially discovered by VonNeumann and Richtmyer. [137] for simulating shockwaves. Thereafter, Monaghan and Gingold. [138], Monaghan and Pongracic. [139] developed an alternative approach of artificial viscosity. Subsequently, many have been researching and introducing new methods of artificial viscosity [140], [141]. However,

among them the most widely used method, Monaghan's artificial viscosity is employed in this study [138], [139]. There were unphysical oscillations in the numerical simulation. This occurs due to failure in smearing the shocks on a length scale greater than the discretization region. Such problem is eliminated by introducing artificial viscosity into the momentum equation as [138]:

$$\frac{Dv^{\alpha}}{Dt} = \sum_{j=1}^{N} m_j \left(\frac{\sigma_j^{\alpha\beta}}{\rho_j^2} + \frac{\sigma_i^{\alpha\beta}}{\rho_i^2} - \Pi_{ij}\delta^{\alpha\beta} \right) \frac{\partial W_{ij}}{\partial x_i^{\beta}} + F^{\alpha} \tag{4.49}$$

where (Π_{ij}) is artificial viscosity and is defined as:

$$\Pi_{ij} = \begin{cases} \dfrac{-\alpha_{\Pi} c_{ij} \phi_{ij} + \beta_{\Pi} \phi^2}{\rho_{ij}} & if \ \Big((v_j - v_i) \cdot (x_j - x_i) \Big) < 0 \\ 0 & if \ \Big((v_j - v_i) \cdot (x_j - x_i) \Big) \geq 0 \end{cases}$$

$$\phi_{ij} = \frac{h_{ij} \Big((v_j - v_i) \cdot (x_j - x_i) \Big)}{|x_{ij}|^2 + 0.01 {h_{ij}}^2}, \quad h_{ij} = \frac{h_i + h_j}{2},$$

$$\rho_{ij} = \frac{\rho_i + \rho_j}{2}, \qquad c_{ij} = \frac{c_i + c_j}{2}$$

where α_{Π} and β_{Π} are constants related to bulk viscosity and von-Newman-Richtmyer artificial viscosity. Libersky et al. [49] proposed 2.5 for both constants for modelling solids. Alternatively, Monaghan. [84] employed $\alpha_{\Pi} = 1$ and $\beta_{\Pi} = 2$ and suggested values closer to 1 for best solutions. As such, in present study $\alpha_{\Pi} = \beta_{\Pi} = 1.0$ is employed. c is the speed of sound in the material. The values of c considered for beryllium alloy, aluminium alloy, lead alloy and soil are considered to be 13000 m/s, 5100 m/s, 1260 m/s and 600 m/s respectively.

4.5.2 Development of tension cracking treatment and stress scaling backpressure for plane stress condition

It is necessary to ensure elastic-perfectly plastic response when both constitutive models are employed for current plane stress application. To elaborate further, the stress state should not exceed the yield surface during the plastic deformation. The problem existed for both constitutive models during simulation. Such instability is solvable using tension cracking treatment and stress scaling back pressure [142]. For instance, point A in Figure 4.2 indicates a point beyond $-2\sigma_y$ of the yield surface. The process of re-allocating it to point B is identified as tension cracking treatment. Furthermore, point C in Figure 4.2 shows the point which is beyond the yield surface along $\sqrt{J_2}$ direction. The process of re-allocating it to point D is recognized as stress scaling back pressure. Hence, in this study both tension cracking treatment and stress scaling back pressure for plane stress condition is introduced for both von-Mises and Drucker-Prager models as follows:

4.5.2.1 Development of treatments for von-Mises yield criterion

Using Eq. (4.23), Eq. (4.17) is expressed for plane stress as:

$$\sqrt{\frac{1}{2}(s^{\alpha\beta}s^{\alpha\beta}) + \frac{1}{12}(\sigma^{\gamma\gamma})^2} = \frac{\sigma_y}{\sqrt{3}} \tag{4.50}$$

Using $I_1 = \sigma^{xx} + \sigma^{yy} = \sigma^{\gamma\gamma}$, Eq. (4.50) is re-written as:

$$\sqrt{\frac{1}{2}(s^{\alpha\beta}s^{\alpha\beta}) + \frac{1}{12}{I_1}^2} = \frac{\sigma_y}{\sqrt{3}} \tag{4.51}$$

To obtain $\sqrt{J_2}$ against I_1 plot as presented in Figure 4.2, considering $J_2 = \frac{1}{2}(s^{\alpha\beta}s^{\alpha\beta})$, Eq. (4.51) is expressed as:

$$\sqrt{J_2} = \sqrt{-\frac{1}{12}{I_1}^2 + \frac{{\sigma_y}^2}{3}} \tag{4.52}$$

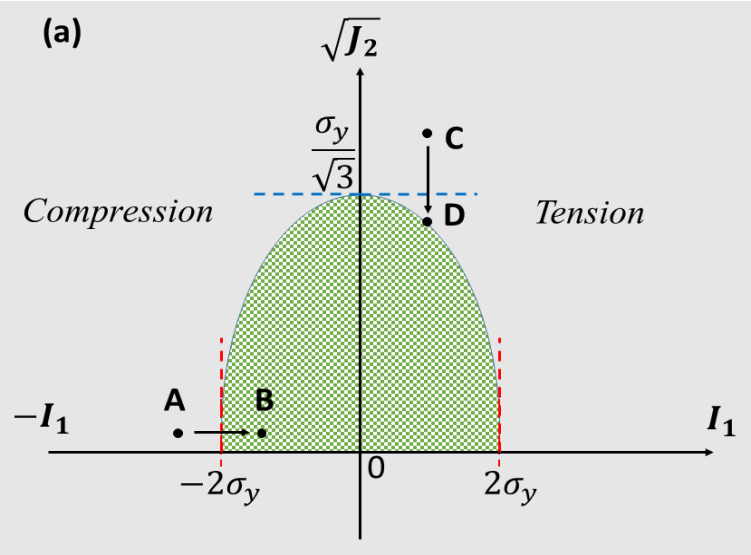


Figure 4.2: Tension cracking treatment and Stress-scaling back pressure for von-Mises yield criterion.

Point A in Figure 4.2 satisfies the condition ($I_1^t < -2\sigma_y$) under compression at time-step t. In such situation, normal stresses in x and y directions require to be adjusted to lie within the yield surface which is indicated by point B in Figure 4.2. This is achieved via adopting expressions (4.53) and (4.54) in the simulation.

$$\widetilde{\sigma_t^{xx}} = \sigma_t^{xx} - \frac{1}{2}\left(I_1^t - \left(-2\sigma_y\right)\right) \tag{4.53}$$

$$\widetilde{\sigma_t^{yy}} = \sigma_t^{yy} - \frac{1}{2}\left(I_1^t - \left(-2\sigma_y\right)\right) \tag{4.54}$$

On the other hand, if point A satisfies the condition $\left(I_1^t > 2\sigma_y\right)$ under tension at time-step t, then instead of using expressions (4.53) and (4.54), (4.55) and (4.56) are employed.

$$\widetilde{\sigma_t^{xx}} = \sigma_t^{xx} - \frac{1}{2}\left(I_1^t - 2\sigma_y\right) \tag{4.55}$$

$$\widetilde{\sigma_t^{yy}} = \sigma_t^{yy} - \frac{1}{2}\left(I_1^t - 2\sigma_y\right) \tag{4.56}$$

Furthermore, if a stress state similar to point C as indicated in Figure 4.2 occurs satisfying the condition described in Eq. (4.57), stress scaling back pressure should be adopted, which is for plane stress (2D) is proposed from Eq. (4.58) to (4.61).

$$\sqrt{J_2^t} > \sqrt{-\frac{1}{12}\left(I_1^t\right)^2 + \frac{{\sigma_y}^2}{3}} \tag{4.57}$$

To transfer point from C to D, scaling factor at time-step t: sf_{vm}^t is employed, which is described as:

$$sf_{vm}^t = \frac{\sqrt{-\frac{1}{12}\left(I_1^t\right)^2 + \frac{{\sigma_y}^2}{3}}}{\sqrt{J_2^t}} \tag{4.58}$$

By reducing the deviatoric stress component in proportion to sf_{vm}^t, point C is re-allocated to point D along $\sqrt{J_2}$ direction. This is expressed as follows:

$$\widetilde{\sigma_t^{xx}} = sf_{vm}^t s_t^{xx} + \frac{1}{2} I_1^t \tag{4.59}$$

$$\widetilde{\sigma_t^{yy}} = sf_{vm}^t s_t^{yy} + \frac{1}{2} I_1^t \tag{4.60}$$

$$\widetilde{\sigma_t^{xy}} = sf_{vm}^t s_t^{xy} \tag{4.61}$$

where $I_1^t = \sigma_t^{xx} + \sigma_t^{yy}$

4.5.2.2 Development of treatments for Drucker-Prager yield criterion

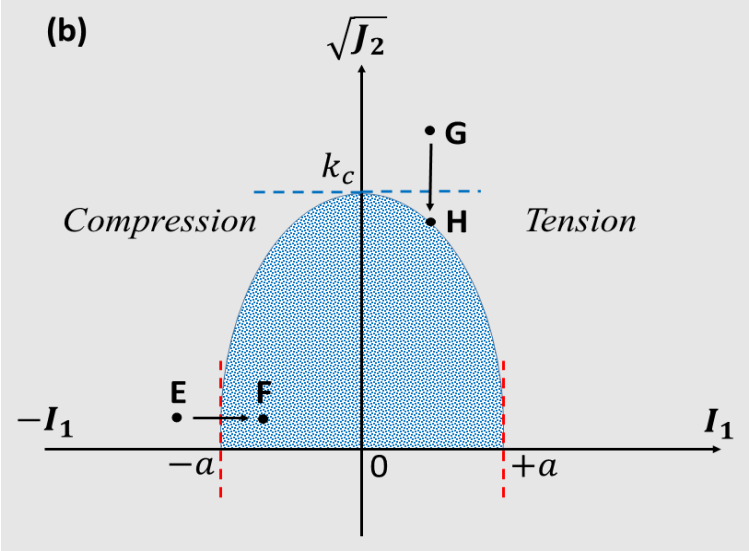


Figure 4.3: Tension cracking treatment and Stress-scaling back pressure for von-Mises yield criterion.

Using Eq. (4.23) and expression $I_1 = \sigma^{xx} + \sigma^{yy} = \sigma^{\gamma\gamma}$, Eq. (4.30) is written for plane stress as:

$$\sqrt{\frac{1}{2}(s^{\alpha\beta}s^{\alpha\beta}) + \frac{1}{12} {I_1}^2} = -\alpha_\phi I_1 + k_c \tag{4.62}$$

In order to achieve $\sqrt{J_2}$ against I_1 plot as shown in Figure 4.3, using expression $J_2 = \frac{1}{2}\left(s^{\alpha\beta}s^{\alpha\beta}\right)$, Eq. (4.62) is expressed as:

$$\sqrt{J_2} = \sqrt{\left(\alpha^2 - \frac{1}{12}\right) {I_1}^2 - (2\alpha k_c)\, I_1 + {k_c}^2} \tag{4.63}$$

where expressions for a in Figure 4.3 are as follows:

$$a_1 = \frac{k_c\left(2\sqrt{3}\alpha + 1\right)}{2\sqrt{3}\left(\alpha^2 - \frac{1}{12}\right)}, \qquad a_2 = \frac{k_c\left(2\sqrt{3}\alpha - 1\right)}{2\sqrt{3}\left(\alpha^2 - \frac{1}{12}\right)} \tag{4.64}$$

If $a_1 > 0, a_1 = +a$ else $a_1 = -a$ and if $a_2 > 0, a_2 = +a$ else $a_2 = -a$. Hence, a_1 and a_2 whether it is positive or negative depends on the value of α, and α depends on friction angle of the material. If point E in Figure 4.3 satisfies the condition $(I_1^t < -a)$ under compression at time-step t, point E should be moved to point F within the yield surface. Therefore, similar to von-Mises, this is achieved via following expressions:

$$\widetilde{\sigma_t^{xx}} = \sigma_t^{xx} - \frac{1}{2}\left(I_1^t - (-a)\right) \tag{4.65}$$

$$\widetilde{\sigma_t^{yy}} = \sigma_t^{yy} - \frac{1}{2}\left(I_1^t - (-a)\right) \tag{4.66}$$

Likewise, if point E satisfies condition $(I_1^t > a)$ under tension at time-step t, then Eqs. (4.67) and (4.68) are employed instead of Eqs. (4.65) and (4.66).

$$\widetilde{\sigma_t^{xx}} = \sigma_t^{xx} - \frac{1}{2}(I_1^t - a) \tag{4.67}$$

$$\widetilde{\sigma_t^{yy}} = \sigma_t^{yy} - \frac{1}{2}(I_1^t - a) \tag{4.68}$$

Furthermore, if a stress state similar to G in Figure. 3.3 befalls satisfying the condition in Eq. (4.69), stress scaling back pressure should be employed to transfer the point from G to H as presented in Figure 4.3. This is achieved through scaling factor sf_{dp}^{t} at time-step t which is for plane stress (2D) is proposed in Eq. (4.70).

$$\sqrt{J_2^t} > \sqrt{\left(\propto^2 - \frac{1}{12}\right)(I_1^t)^2 - (2\alpha k_c)I_1^t + {k_c}^2} \tag{4.69}$$

$$sf_{dp}^{t} = \frac{\sqrt{\left(\propto^2 - \frac{1}{12}\right)(I_1^t)^2 - (2\alpha k_c)I_1^t + {k_c}^2}}{\sqrt{J_2^t}} \tag{4.70}$$

By reducing the deviatoric stress component in proportion to sf_{dp}^{t} at time-step t, point G is reduced to point H along $\sqrt{J_2}$ direction. This is achieved by adopting Eqs. (4.59) to (4.61) by replacing sf_{vm}^{t} by sf_{dp}^{t}.

4.6 Boundary conditions

Particles at the solid boundary lack neighbouring particles. SPH particle's material properties rely cardinally over the neighbourhood. Therefore, approximation of variables for these particles near the solid boundary becomes inaccurate leading to imprecise solutions. Thus, it is crucial to utilize an approach which minimises such errors in the physical behaviour [143]. Several methods have been introduced in the past and are commonly solved using virtual particles [144]–[146]. As such, virtual particles are adopted in current study for the solid boundaries.

For current application, two types of solid boundaries are employed which are fixed boundary and moving solid boundary. Both boundaries are generated using three rows of virtual particles at the upper and lower boundaries. Green particles in Figures 4.4a and 4.4b represent the fixed solid boundary at the lower end and moving solid boundary at the top end respectively. Each particle at the solid boundary is spaced similar to that of real particle and contains the same density as real particle. As stated by Morris et al. [145], boundary particles contribute to the computation of stress and velocity gradients. However, density of boundary particles is not evolved in current study. Morris et al. [145] proposed a method for no-slip boundary condition. This is adopted for fixed solid boundary particles. Under this approach, for every real particle R as shown in Figure 4.4a, normal distance dr is calculated from the solid wall. Similarly, normal distance dv is computed for imaginary boundary particles. Finally, artificial velocity of virtual particle V is computed using the following expression, assuming zero velocity on the plane:

$$v_V = -\left(\frac{dv}{dr}\right) v_R \tag{4.71}$$

where v_R is the velocity of real particle. Velocity v_V contributes to the calculation of velocity gradient of real particles on or near the solid boundary. These boundary particles' positions are not updated as they are assumed to be fixed. However, relative velocity between the real and imaginary particle is defined by:

$$v_{RV} = \beta(v_R) \tag{4.72}$$

where

$$\beta = \min\left(\beta_{max}, 1 + \frac{dv}{dr}\right) \tag{4.73}$$

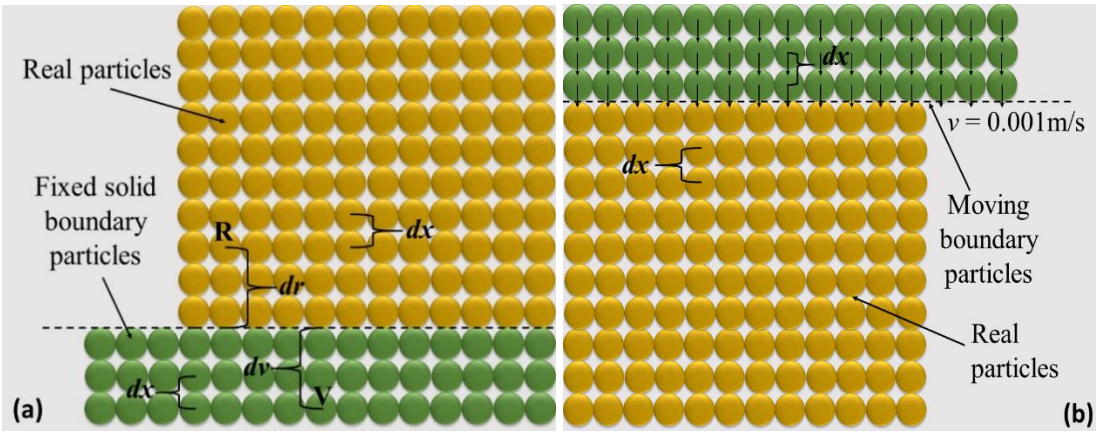


Figure 4.4: Boundary particles: (a) solid boundary; (b) moving solid boundary.

As proposed by Morris et al. [145] β_{max} is adopted to be 1.5. Furthermore, for moving solid boundary, loading velocity of 0.001m/s is assigned for every imaginary particle. Positions of these particles are updated at every time-step according to the constant loading velocity in the simulation. This velocity of moving solid boundary particles contribute to the computation of velocity gradient of real particles.

Furthermore, Morris et al. [145] treatment alone was insufficient for handling the boundary condition for current application. During simulation, penetration of particles was observed through the solid boundaries. Moreover, it is also essential to assign stress to solid boundary particles for the estimation of stress on real particles. As such, Eq. (4.74)

is proposed in this study based on the assumption of opposing the real particle movement through the boundary by the assignment of stress to solid boundary particles. The way of assigning stress on boundary particle (V) is explained as follows. Firstly, for a boundary particle (V) stresses on its neighbouring real particles (R) are summed. Dividing this summed value by *niac* (total number of neighbouring real particles within the support domain) provides the average stress of real particles. Finally, the negative value of this averaged stress is assigned to the boundary particle (V). Through this formulation each particle at the solid boundary opposes the stresses from its nearing real particles.

$$\sigma_V^{\alpha\beta} = -\frac{\sum_{R=1}^{N} \sigma_R^{\alpha\beta}}{niac} \tag{4.74}$$

where $\sigma_R^{\alpha\beta}$ is the stress on real particle and $\sigma_V^{\alpha\beta}$ is the stress on boundary particle. In addition, XSPH correction term introduced by Monaghan. [147] is adopted with $\varepsilon = 0.5$ to minimise the unphysical penetration of particles.

4.7 Time integration

To solve the SPH governing equations the most popular scheme Leap-Frog (LF) method is employed to integrate the field variables such as density, velocity, stress and particle position for every particle in the system [77]. Based on this method the field variables are updated at every time-step according to the following relationships:

$$\rho_{t+\left(\frac{1}{2}\right)} = \rho_{t-\left(\frac{1}{2}\right)} + \Delta t \left(\frac{D\rho}{Dt}\right)_t \tag{4.75}$$

$$v_{t+\left(\frac{1}{2}\right)} = v_{t-\left(\frac{1}{2}\right)} + \Delta t \left(\frac{Dv}{Dt}\right)_t \tag{4.76}$$

$$x_{t+1} = x_t + \Delta t v_{t+\left(\frac{1}{2}\right)} \tag{4.77}$$

$$\sigma_{t+\left(\frac{1}{2}\right)} = \sigma_{t-\left(\frac{1}{2}\right)} + \Delta t \left(\frac{D\sigma^{\alpha\beta}}{Dt}\right)_t \tag{4.78}$$

Furthermore, under this method to determine the value of Δt, Courant-Friedrichs-Levy condition is employed, which is defined by the following expression:

$$\Delta t \leq C_{cour} \frac{h}{c} \tag{4.79}$$

where h is the smoothing legth, c is the speed of sound through the media and C_{cour} is considered to be 0.2. Speed of sound through solids are large which results in extremely small value of time-step (Δt). This consequently steered to capture clear details of changes in stresses and strains in the system.

4.8 Flow chart for uniaxial compression

SPH model is developed comprising each constitutive model for analysing stresses and strains in materials under uniaxial compression. The SPH algorithm proposed for each numerical model is similar except for the constitutive model employed. Therefore, the algorithm adopted in present

chapter for the development of SPH models for simulating uniaxial compression is presented by Figure 4.5.

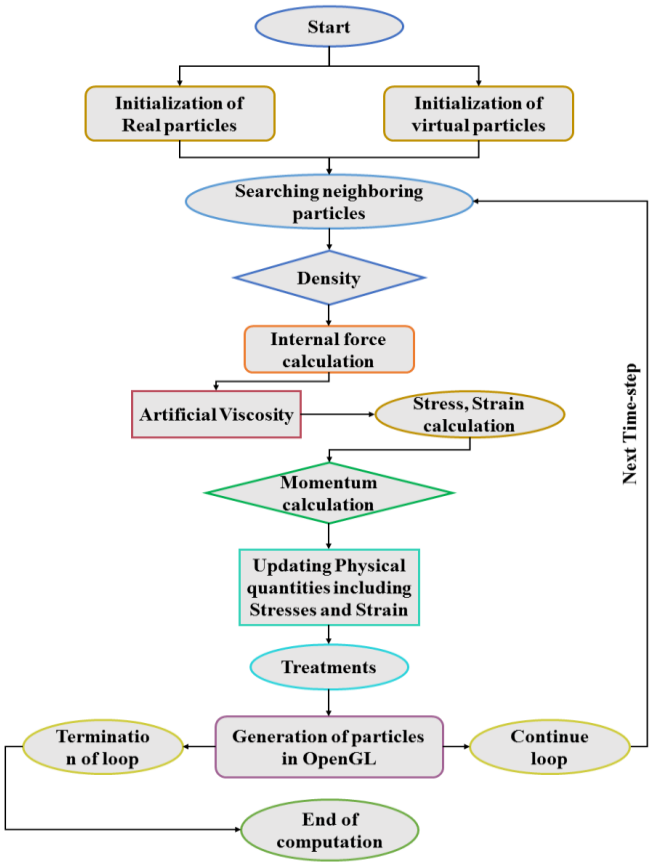


Figure 4.5: SPH algorithm for uniaxial compression.

As shown in Figure 4.5, the algorithm begins with the initialization of particles' physical properties and positions. Subsequently, particles in the system searches its neighbouring pairs. This is followed by the computation of field variables such as density and internal forces. Subsequently to the adoption of artificial viscosity, stress and strain of every particle are calculated with means of the proposed constitutive models. Thereafter, following the momentum calculation, physical properties are updated. If the updated values of stresses fall beyond the

yield surface the proposed treatments for plane stress condition are activated for eliminating the incorrect modelling of the physics. Finally, the updated particle positions and vertical stress distribution are not only stored on data files but also made visually available at every time-step using OpenGL. As illustrated in Figure 4.5, this loop is repeated until the final step of the programme is achieved.

The programme is written in C++ language incorporating appropriate programme commands to create an OpenGL window. The complete programme is executed using command prompt (DOS) in Windows Operating System.

4.9 Results

Numerical simulation is conducted on six types of materials as shown in Table 4.1. The developed SPH model with von-Mises constitutive equation is used to simulate stresses and strains in three types of pressure insensitive materials such as aluminium, beryllium alloy and lead alloy. Poisson's ratio of these materials are within the range 0 to 0.45. On the other hand, numerical models developed with Drucker-Prager constitutive equation for associated and non-associated flow rule are employed to model stresses and strains in three types of pressure sensitive materials such as soil with various parameters as presented in Table 4.1. Poisson's ratio of these materials are selected within the range 0 to 0.3.

Thus, it is apparent that nine computational cases are analysed in present chapter. Parameters for cases 4 to 6 which are modelled with means of Drucker-Prager constitutive model with non-associated flow rule are common for cases 7 to 9 modelled using Drucker-Prager constitutive model with associated flow rule.

Sections 4.9.1, 4.9.2 and 4.9.3 present internal stress against internal strain response obtained from modelling cases 1-3, 4-6 and 7-9 respectively. These numerical stress-strain response for each material is plotted by averaging the summation of internal vertical stresses against internal vertical strains over the total number of particles in the system.

Numerical stress-strain curves achieved for cases 1-9 are verified with analytical stress-strain plots. The following explains the method of obtaining these analytical plots. In general, stress-strain curve through uniaxial compression represent the material properties [148]. Therefore, the elastic and perfectly plastic stress-strain graph achieved through the model characterises the material properties: Young's modulus and yield stress respectively. If these properties are known in the numerical model, the elastic-perfectly plastic sections could be directly validated via these material properties. In von-Mises SPH model, Young's modulus and yield stress are used as input parameters. Therefore, if the algorithm is successful, the elastic and perfectly plastic sections of the stress-strain graph achieved via the numerical simulation for cases 1-3 should define the same input material properties: Young's modulus and yield stress respectively. This theory is used to obtain the analytical stress-strain plots.

For von-Mises SPH model for cases 1-3, the gradient of the elastic section of analytical stress-strain curve should satisfy the Young's modulus of the material. Therefore, by utilizing the simulated strain values of every particle, analytical stresses during the elastic behaviour are computed using the general linear relationship which is stress is equivalent to strain multiplied by Young's modulus. These computed values of stresses are summed and averaged over the total number of particles. This averaged value of analytical stresses is plotted against averaged value of strains until the yield stress of the material. This is represented as 'E' in Figures. 4.7, 4.10 and 4.13 for cases 1-3 respectively. Furthermore, according to theory, the perfectly plastic section begins at the yield stress of the material. As such, subsequent to the elastic deformation, analytical stresses become constant at the yield stress of the material. This continues for the remaining values of plastic strains in the material and is plotted as 'Y' in Figures. 4.7, 4.10 and 4.13 for cases 1-3 respectively. These analytical stress-strain solutions represented by 'E' and 'Y' are used to verify the simulated stress-strain responses.

Similarly, in Drucker-Prager SPH models for cases 4 to 9, Young's modulus, friction angle and cohesion are used as input material parameters. The method of obtaining analytical stress-strain curve for these materials is similar as of cases 1-3 except for the perfectly plastic section, where constant k is used instead of yield stress of the material. According to Drucker-Prager yield criterion, at plasticity, k from simulation should become equivalent to constant k which is made up of

material input parameters: friction angle and cohesion. This is computed by Eq. (3.80) and is shown in Figures 4.16, 4.19, 4.22, 4.24, 4.28 and 4.32 for cases 4-9 by the plot $k = 82800$. On the other hand, the curve 'k from simulation' shown in these figures are obtained through Eq. (4.80). For each particle, left side of Eq. (4.80) is computed utilizing the simulated stress components. Thereafter, the average of these k values is plotted against strain as 'k from simulation' in Figures 4.16, 4.19, 4.22, 4.24, 4.28 and 4.32 for cases 4-9 respectively. Finally, 'k from simulation' is compared with '$k = 82800$' for validating the perfectly plastic section of the stress-strain curves.

$$\alpha(\sigma^{xx}+\sigma^{yy}) + \sqrt{\frac{1}{3}((\sigma^{xx})^2 - (\sigma^{xx}\sigma^{yy}) + (\sigma^{yy})^2 + (3(\sigma^{xy})^2))} = k \tag{4.80}$$

4.9.1 Results obtained using von-Mises constitutive model

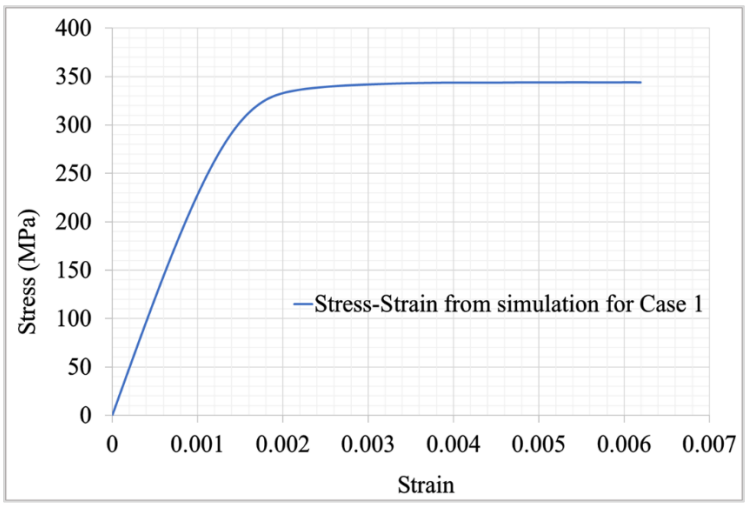


Figure 4.6: Average vertical stress-strain curve from simulation for case 1.

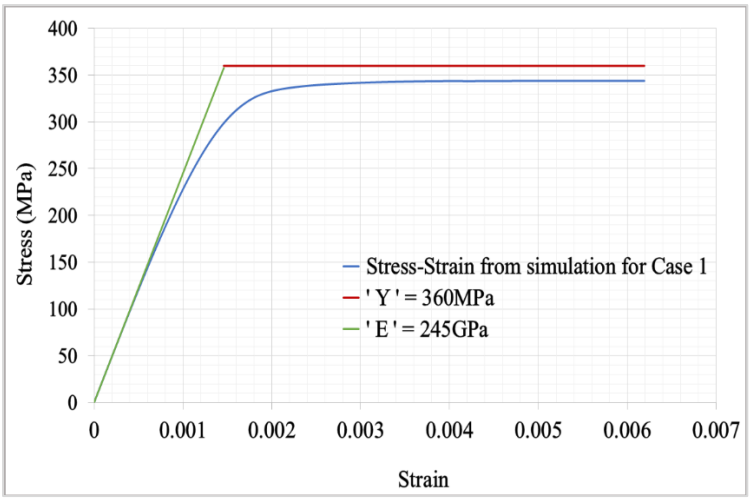
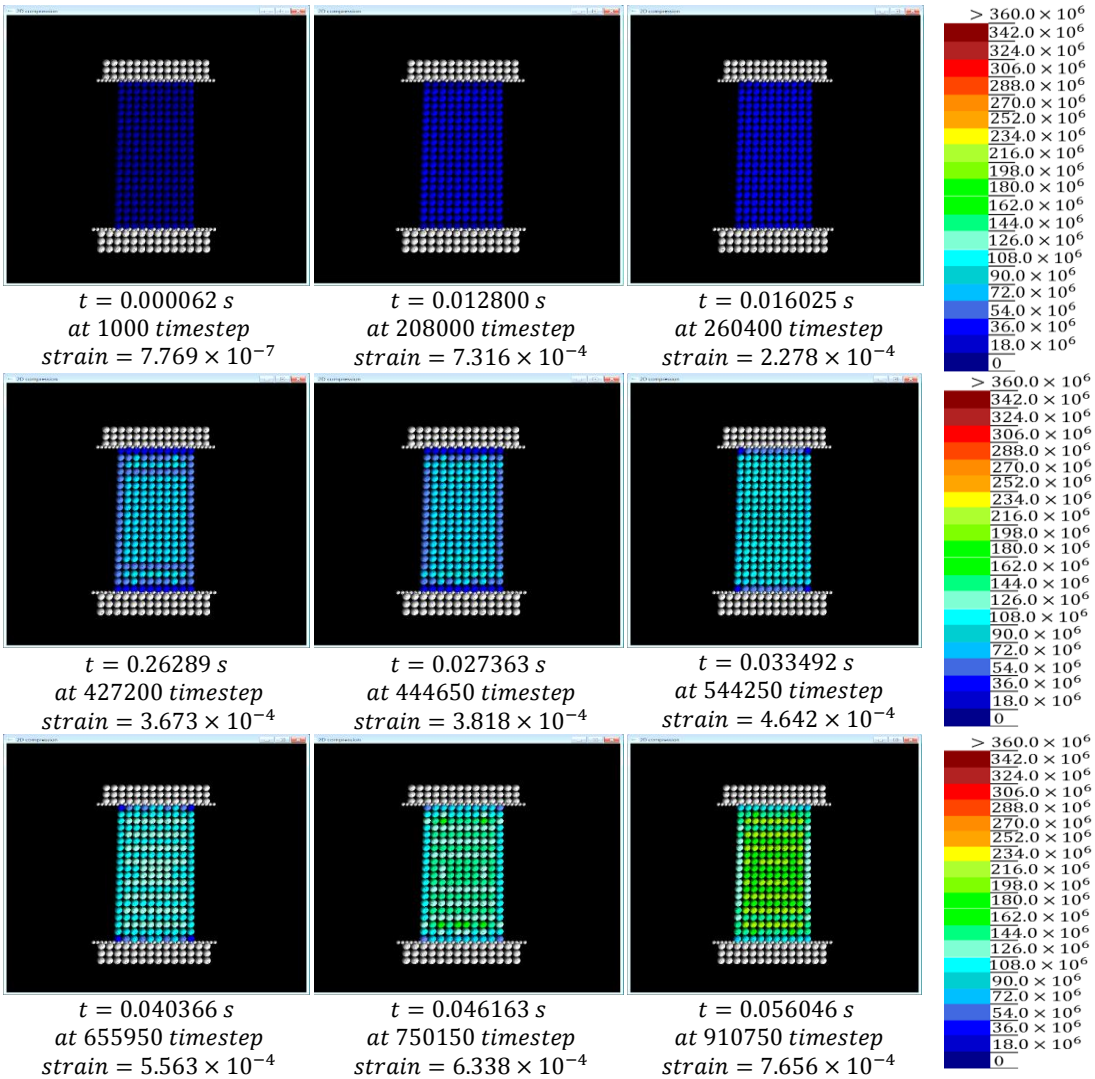


Figure 4.7: Verification of stress-strain curve from simulation with analytical result for case 1.



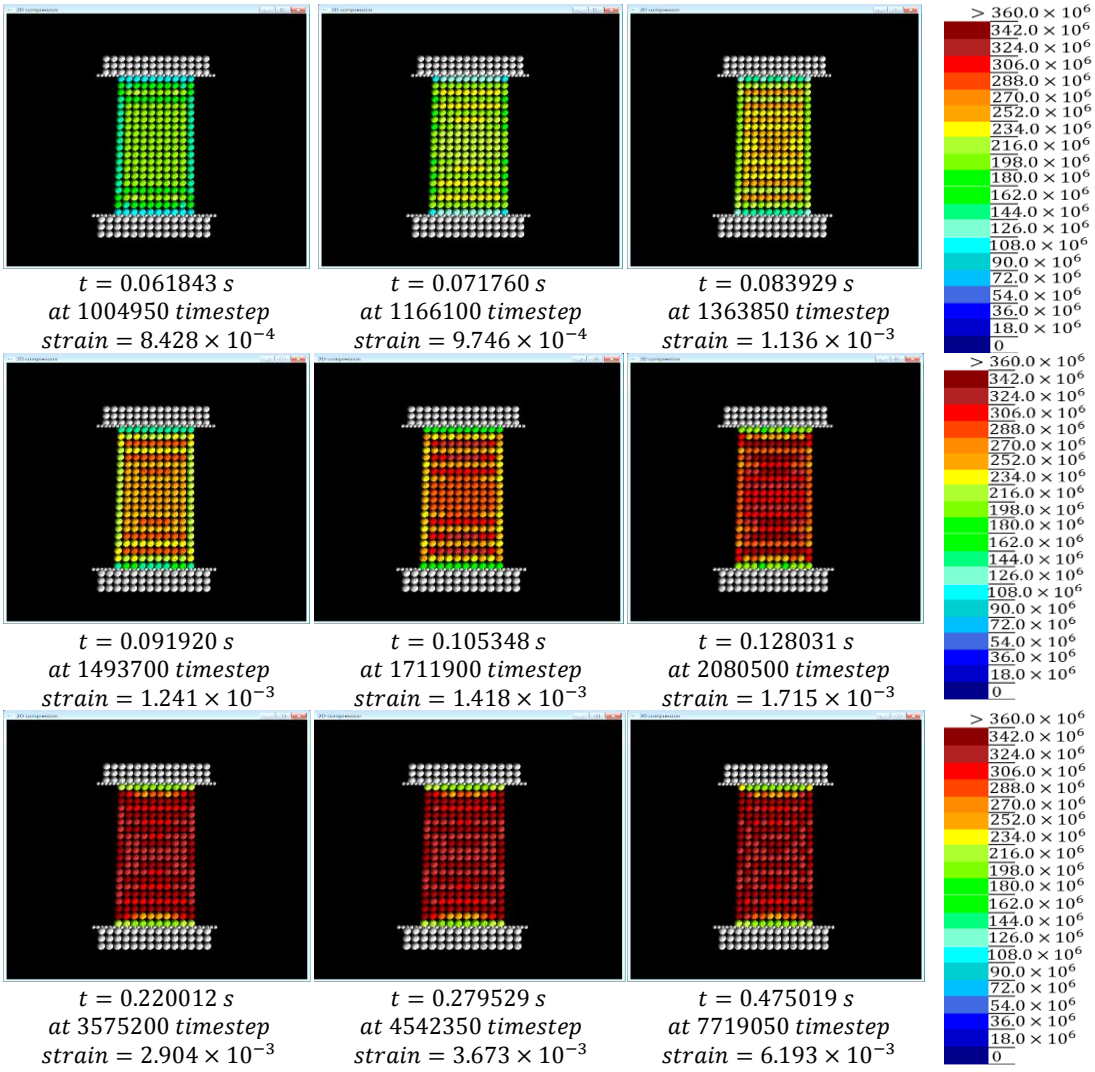


Figure 4.8: Vertical stress distribution during simulation at different time-steps for case1.

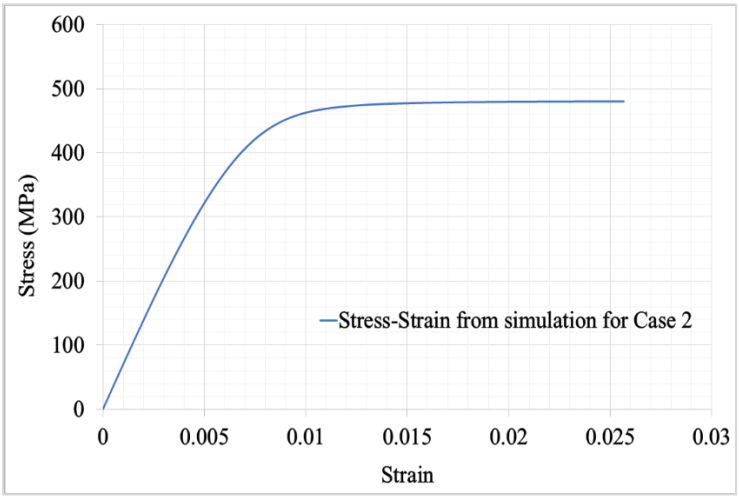


Figure 4.9: Average vertical stress-strain curve from simulation for case 2.

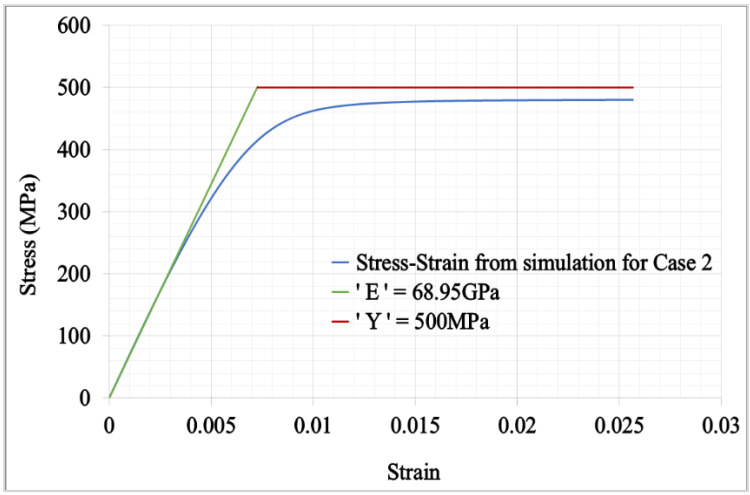
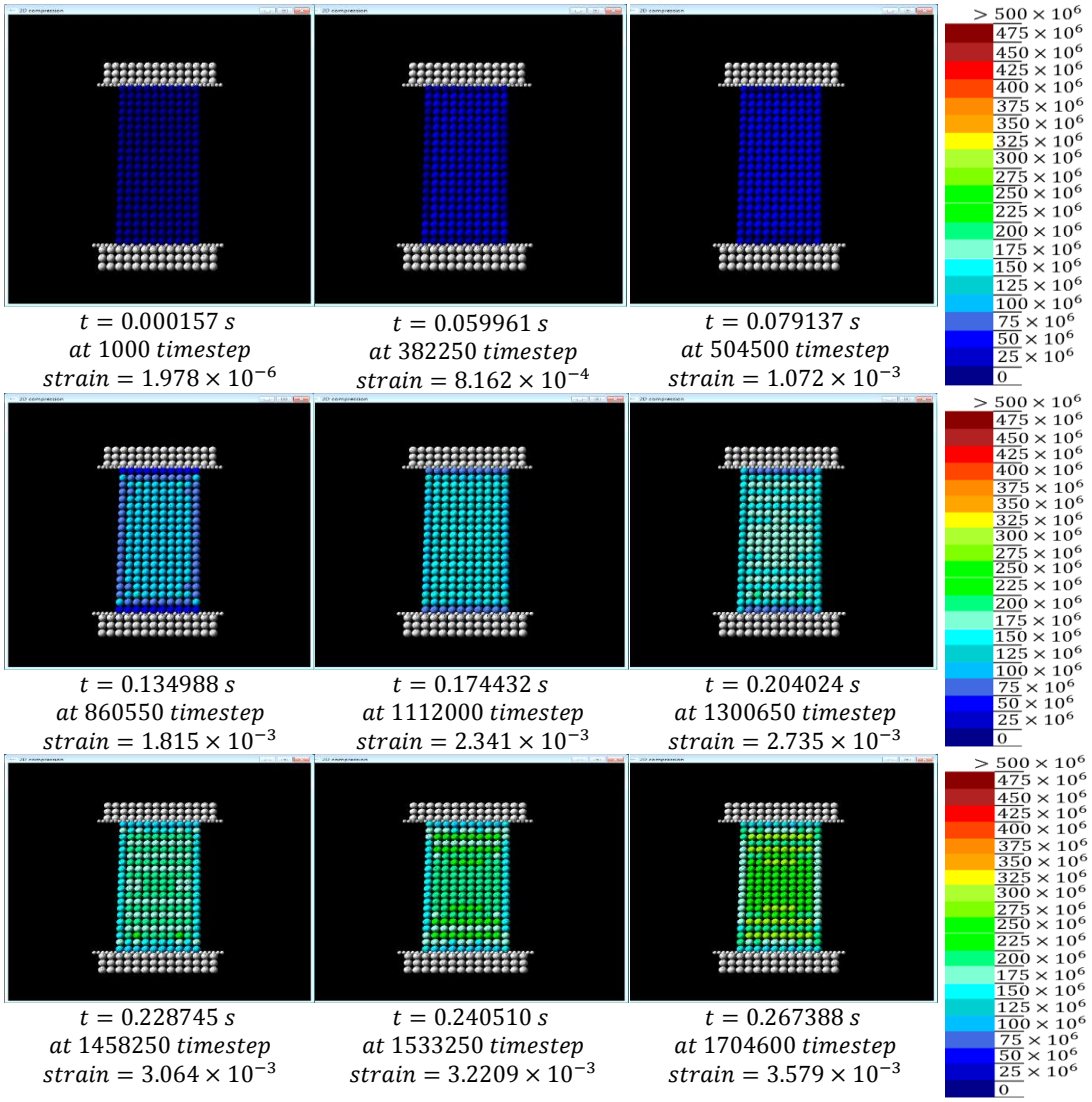


Figure 4.10: Verification of stress-strain curve from simulation with analytical result for case 2.



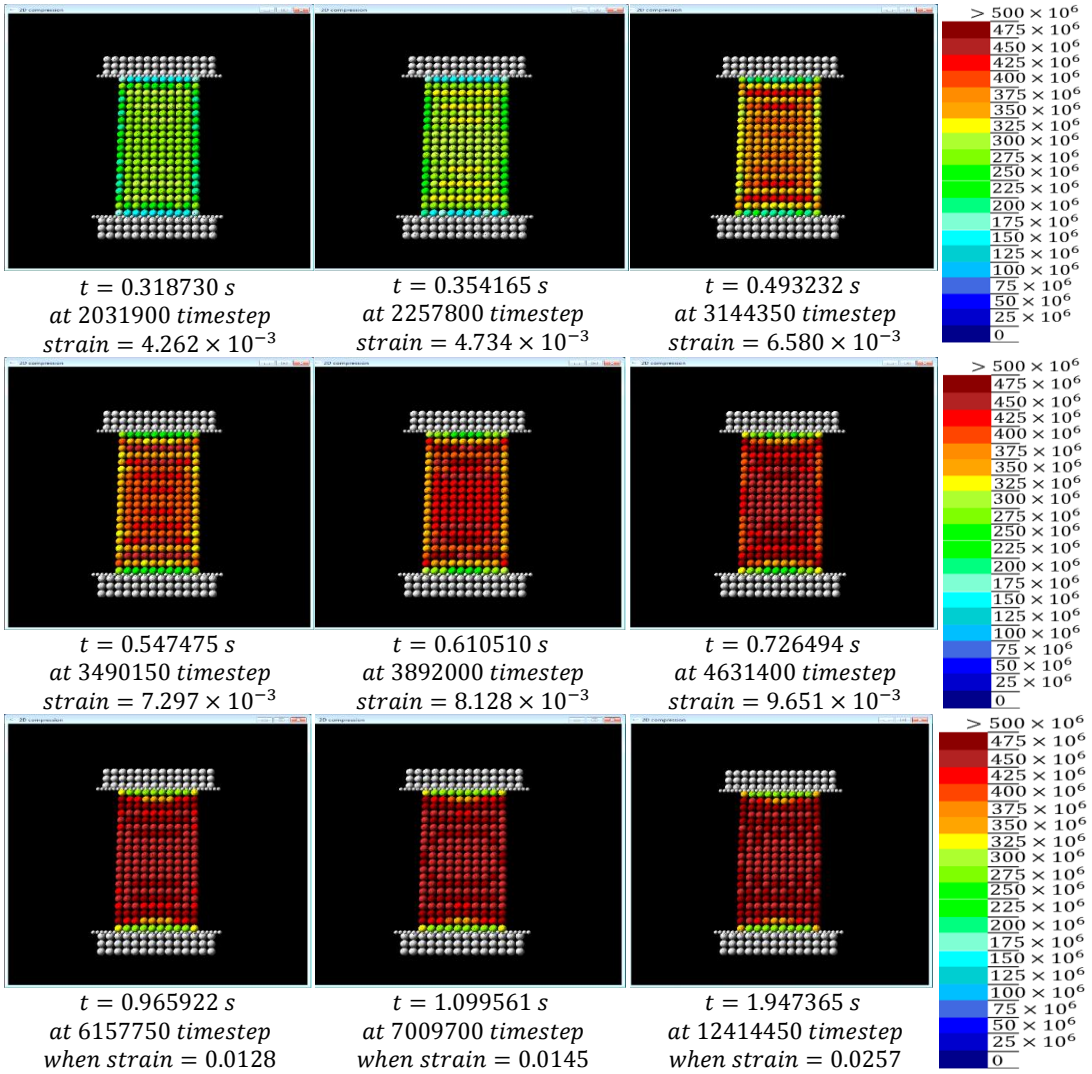


Figure 4.11: Vertical stress distribution during simulation at different time-steps for case 2.

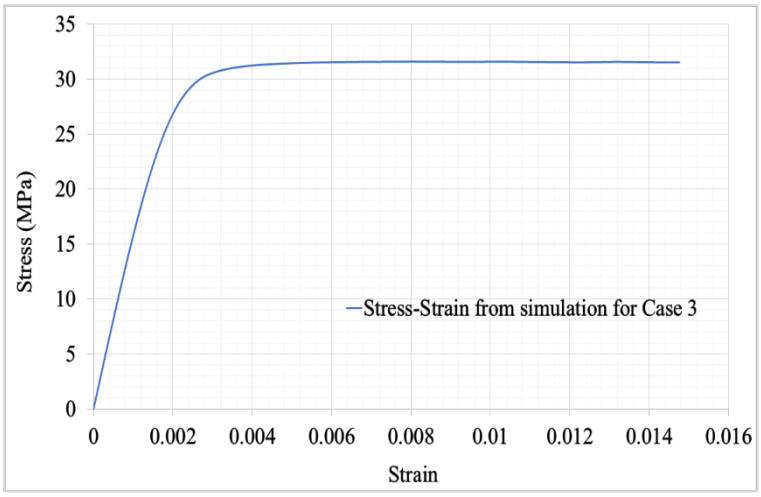


Figure 4.12: Average vertical stress-strain curve from simulation for case 3.

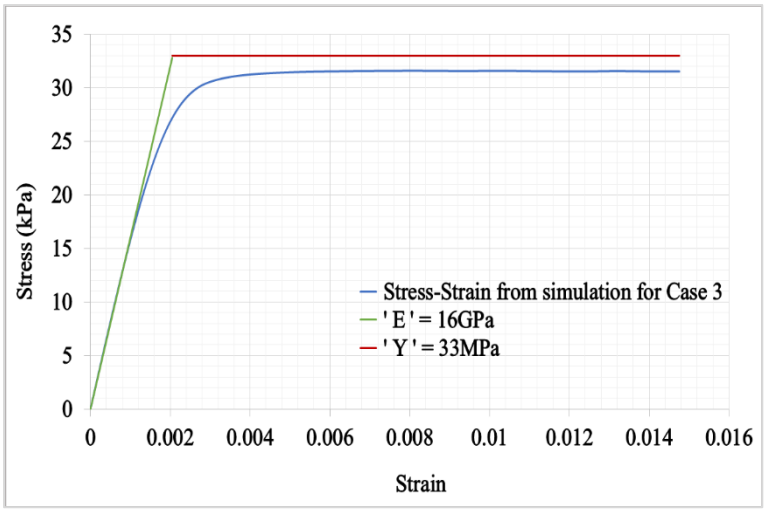
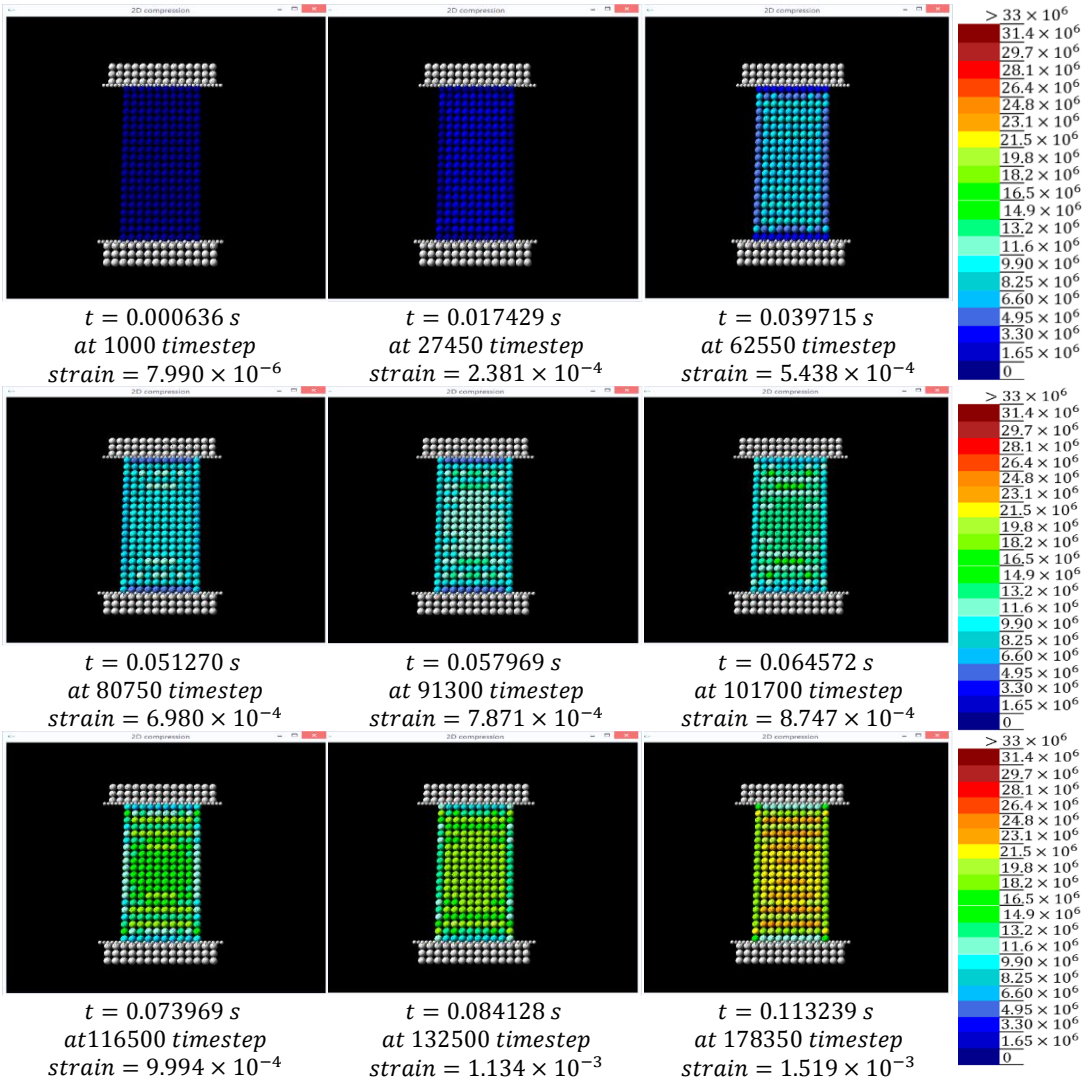


Figure 4.13: Verification of stress-strain curve from simulation with analytical result for case 3.



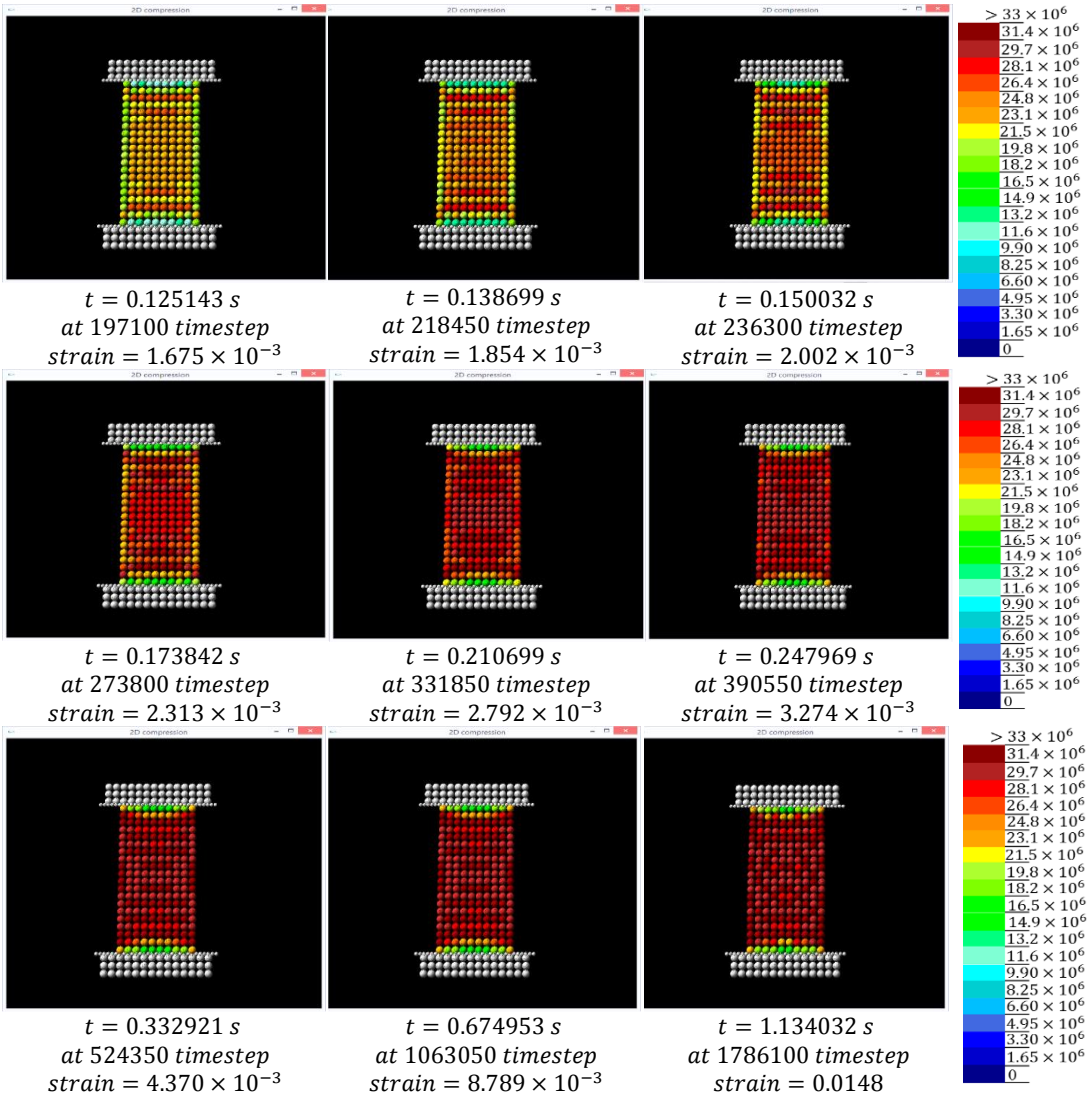


Figure 4.14: Vertical stress distribution during simulation at different time-steps for case 3.

4.9.2 Results obtained using Drucker-Prager constitutive model with non-associated flow rule

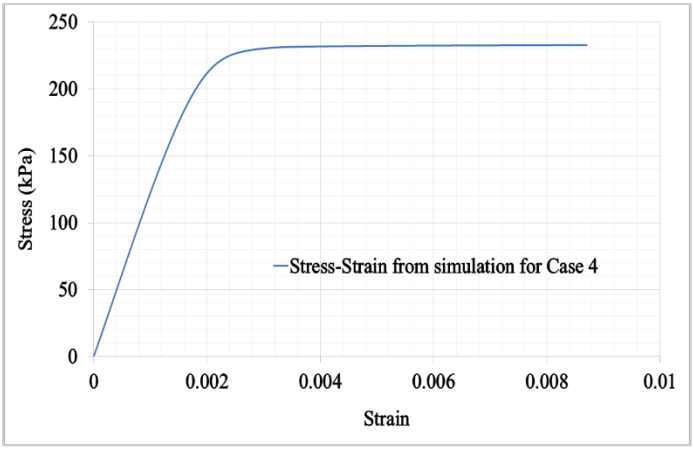


Figure 4.15: Average vertical stress-strain curve from simulation for case 4.

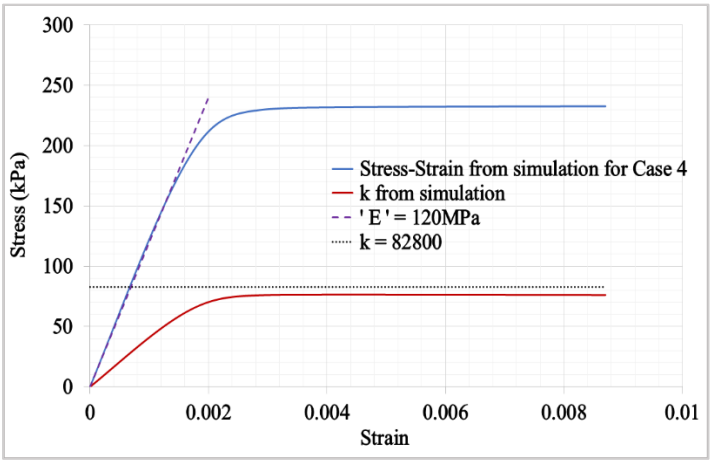
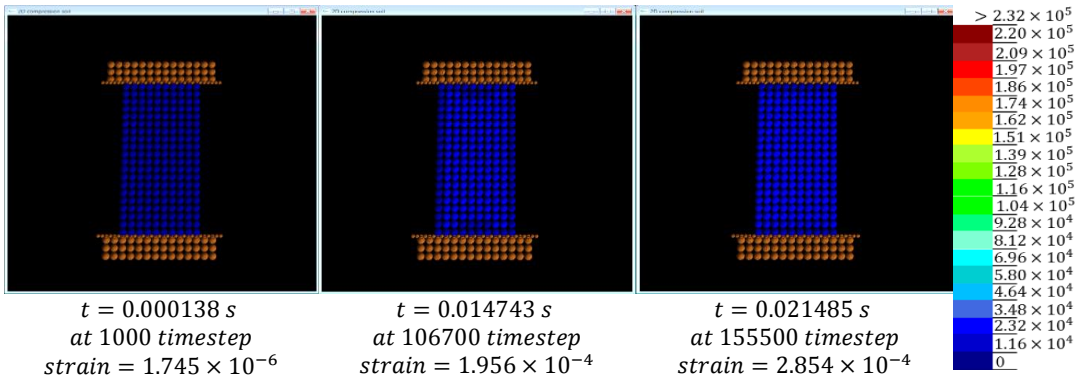


Figure 4.16: Verification of stress-strain curve from simulation with analytical result for case 4.



$t = 0.000138\ s$ *at* 1000 *timestep* $strain = 1.745 \times 10^{-6}$

$t = 0.014743\ s$ *at* 106700 *timestep* $strain = 1.956 \times 10^{-4}$

$t = 0.021485\ s$ *at* 155500 *timestep* $strain = 2.854 \times 10^{-4}$

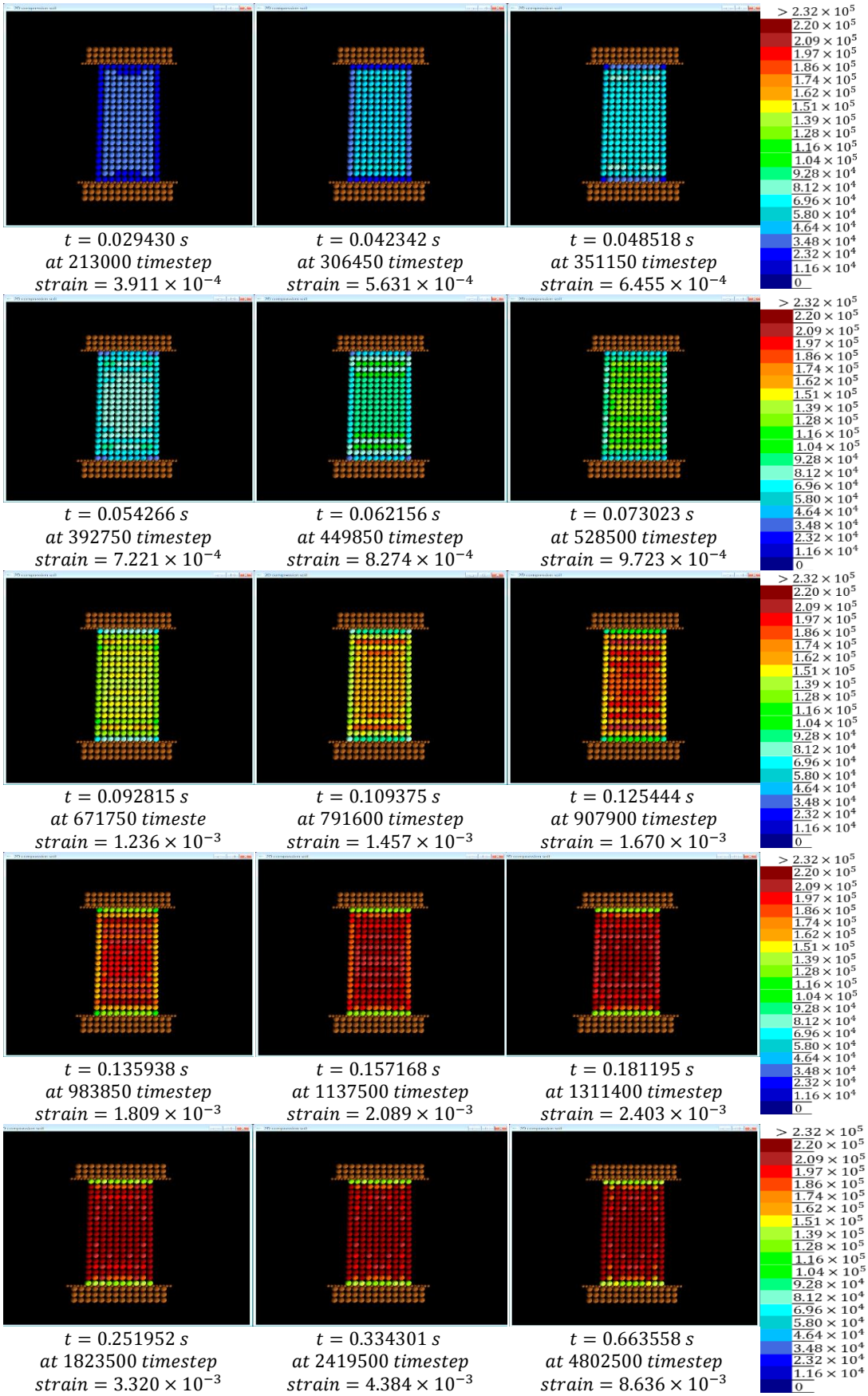


Figure 4.17: Vertical stress distribution during simulation at different time-steps for case 4.

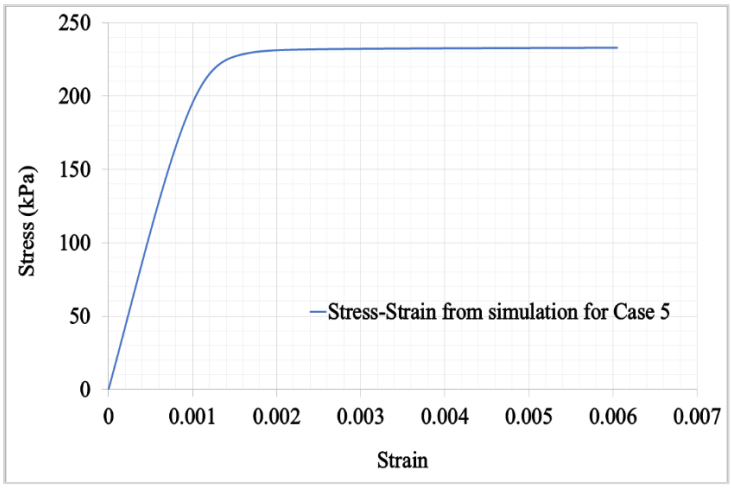


Figure 4.18: Average vertical stress-strain curve from simulation for case 5.

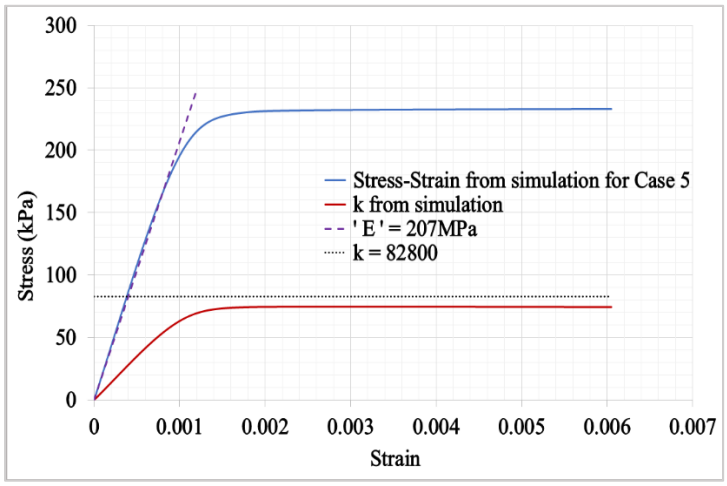
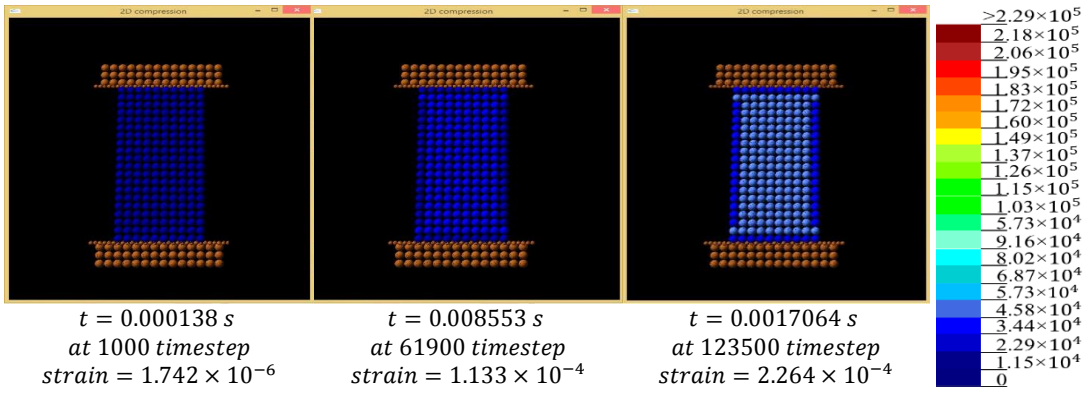


Figure 4.19: Verification of stress-strain curve from simulation with analytical result for case 5.



$t = 0.000138\ s$ *at* 1000 *timestep* $strain = 1.742 \times 10^{-6}$

$t = 0.008553\ s$ *at* 61900 *timestep* $strain = 1.133 \times 10^{-4}$

$t = 0.0017064\ s$ *at* 123500 *timestep* $strain = 2.264 \times 10^{-4}$

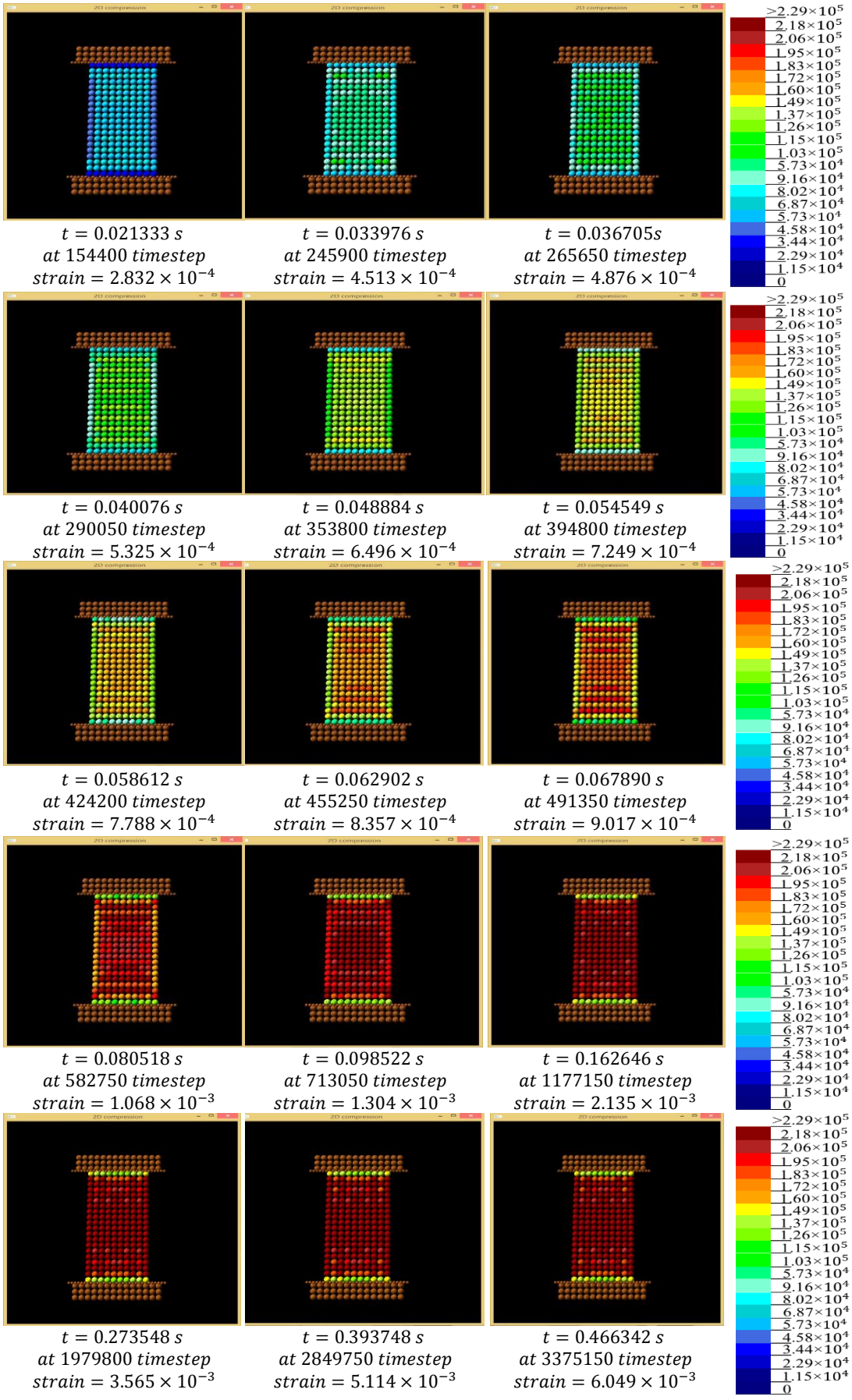


Figure 4.20: Vertical stress distribution during simulation at different time-steps for case 5.

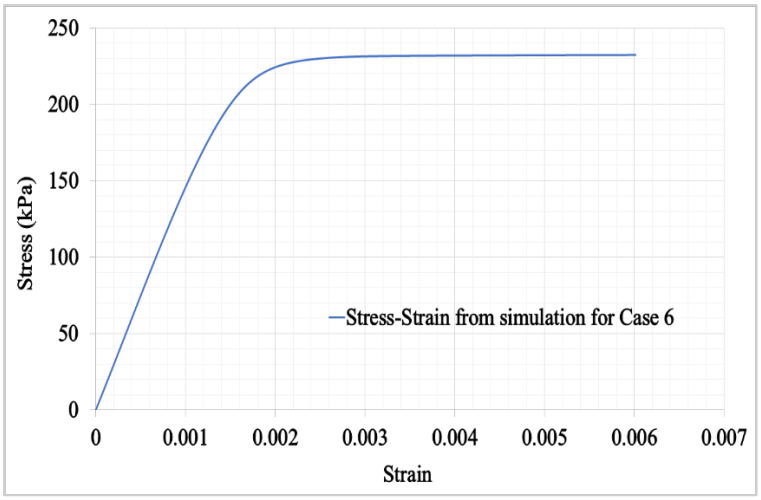


Figure 4.21: Average vertical stress-strain curve from simulation for case 6.

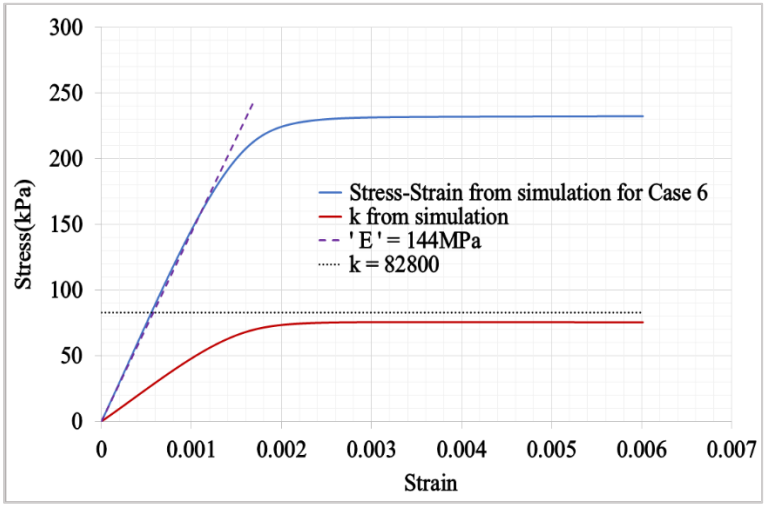
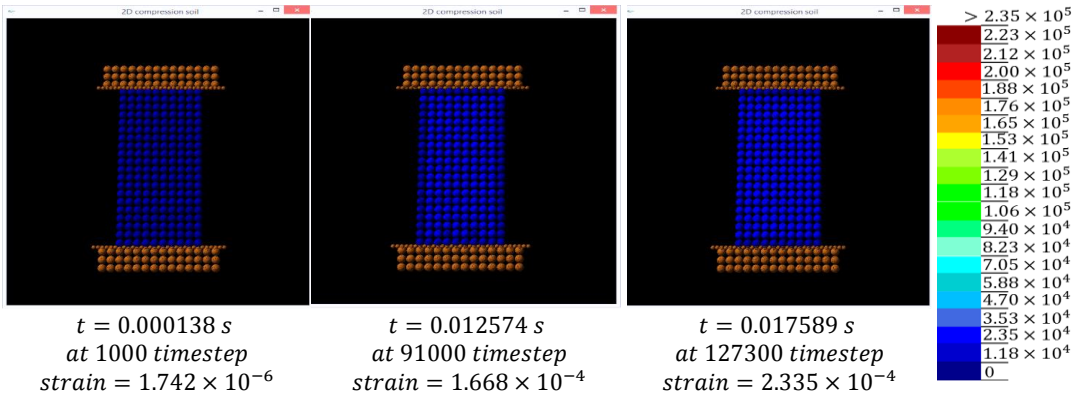


Figure 4.22: Verification of stress-strain curve from simulation with analytical results for case 6.



$t = 0.000138\ s$ $at\ 1000\ timestep$ $strain = 1.742 \times 10^{-6}$

$t = 0.012574\ s$ $at\ 91000\ timestep$ $strain = 1.668 \times 10^{-4}$

$t = 0.017589\ s$ $at\ 127300\ timestep$ $strain = 2.335 \times 10^{-4}$

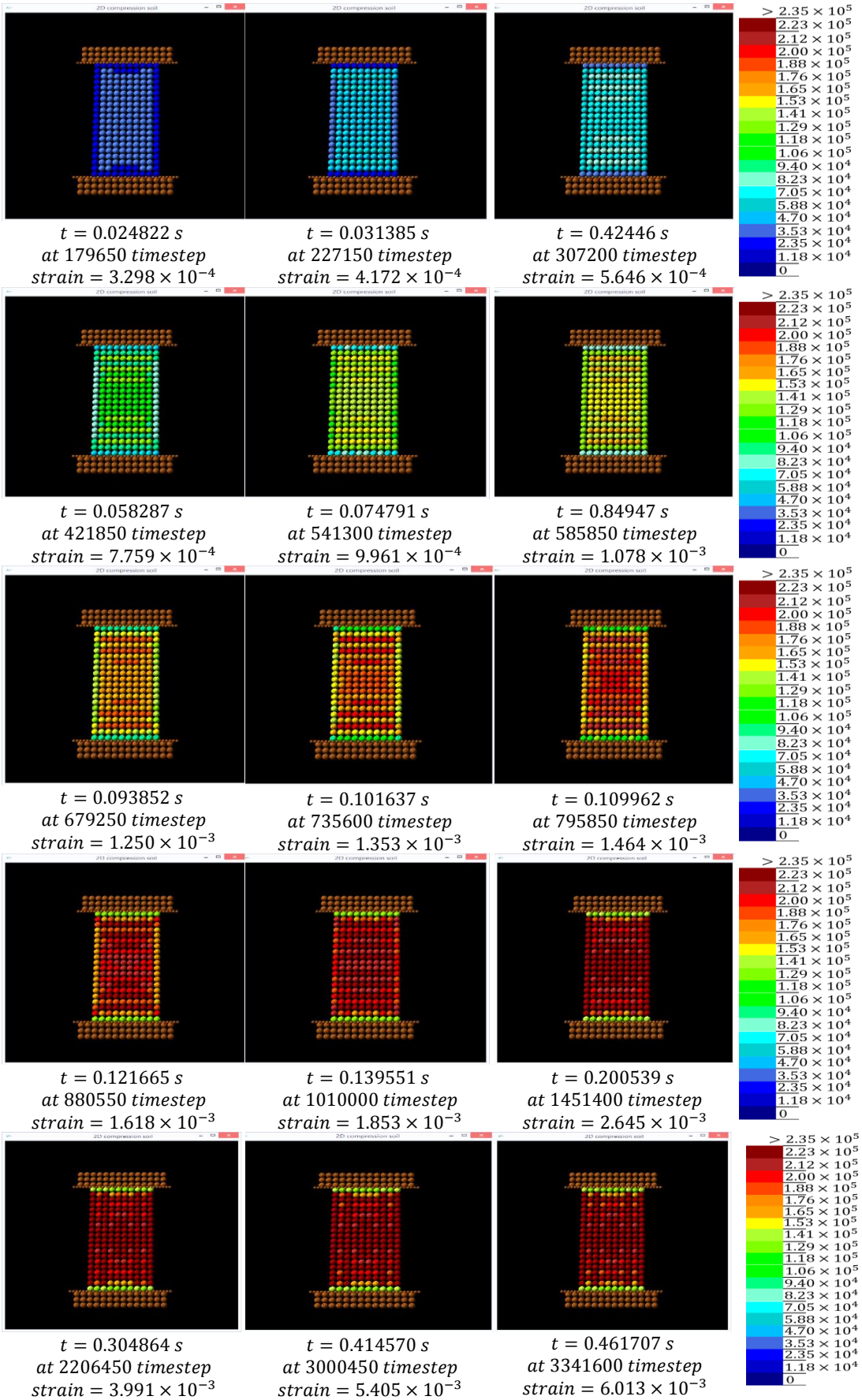


Figure 4. 1: Vertical stress distribution during simulation at different time-steps for case 6.

4.9.3 Results obtained using Drucker-Prager constitutive model with associated flow rule

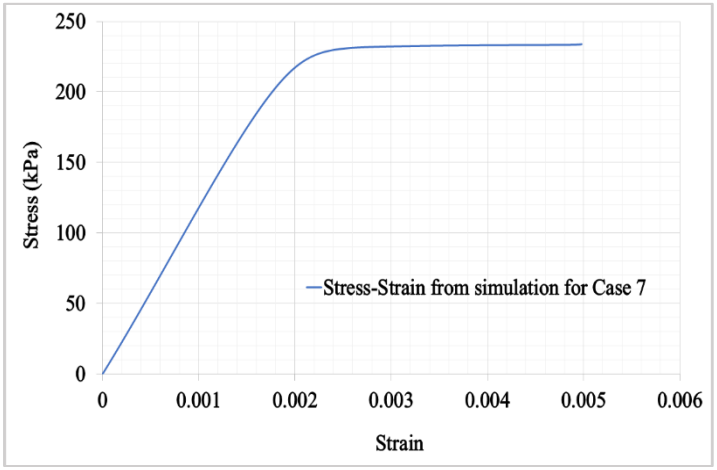


Figure 4.23: Average vertical stress-strain curve from simulation for case 7.

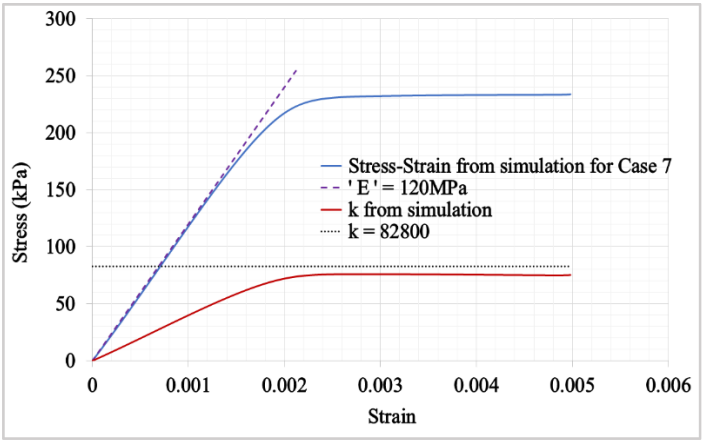
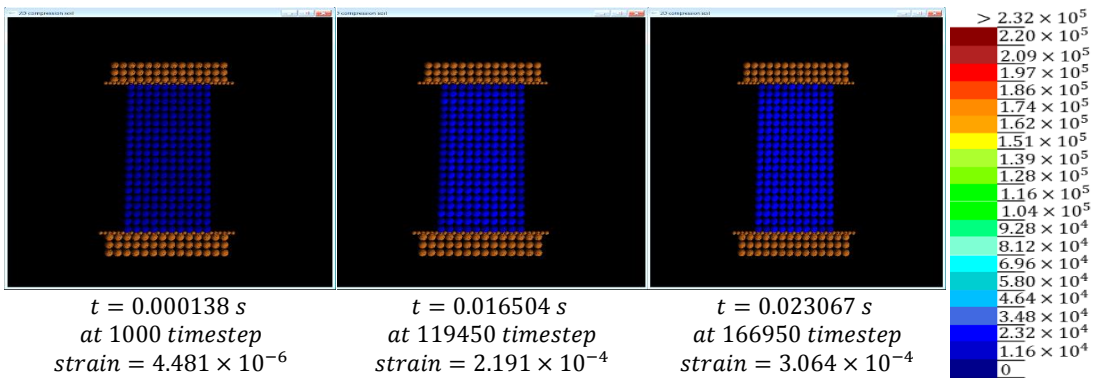


Figure 4.24: Verification of stress-strain curve from simulation with analytical result for case 7.



$t = 0.000138\ s$ at 1000 *timestep* $strain = 4.481 \times 10^{-6}$

$t = 0.016504\ s$ at 119450 *timestep* $strain = 2.191 \times 10^{-4}$

$t = 0.023067\ s$ at 166950 *timestep* $strain = 3.064 \times 10^{-4}$

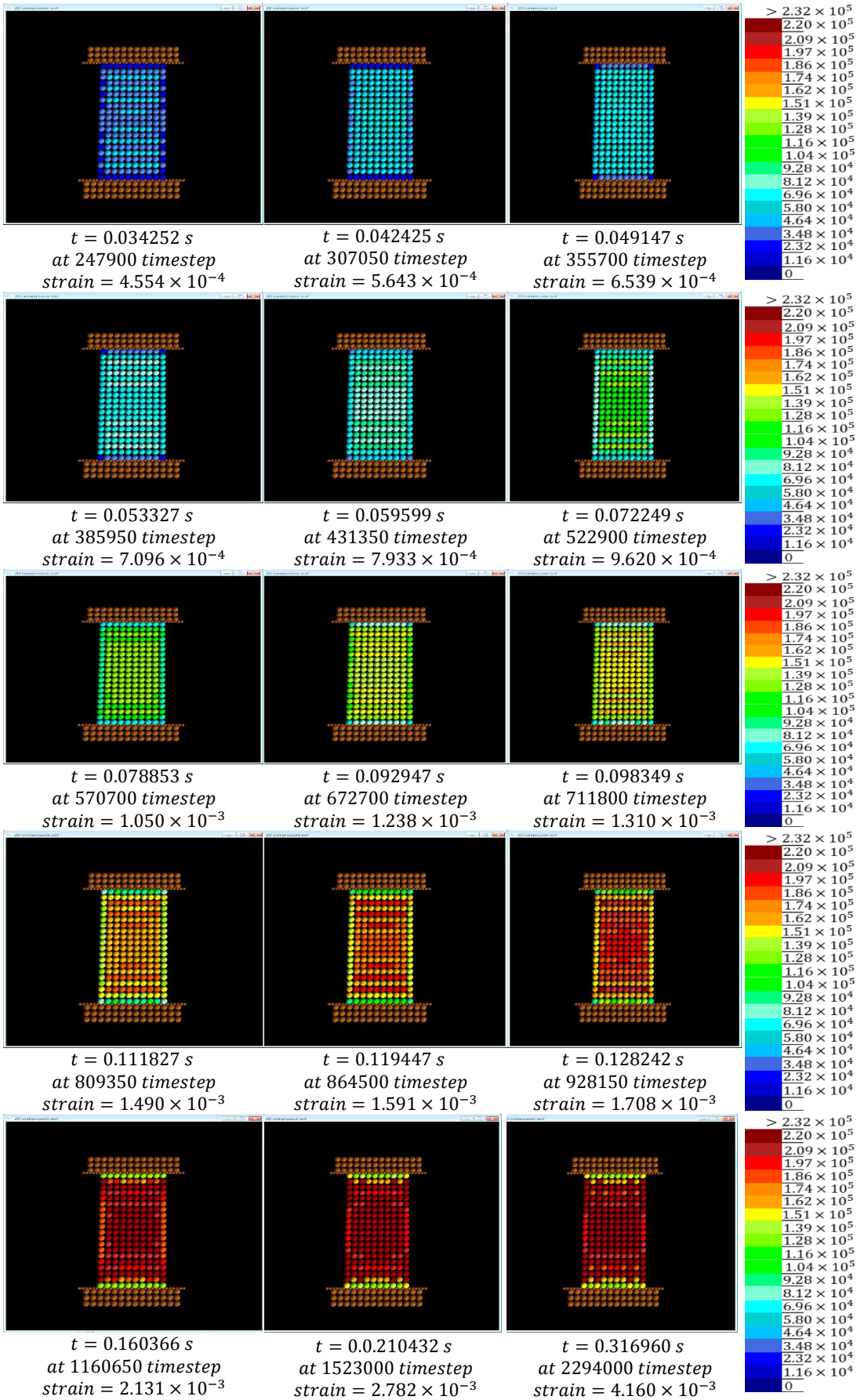


Figure 4.25: Vertical stress distribution during simulation at different time-steps for case 7.

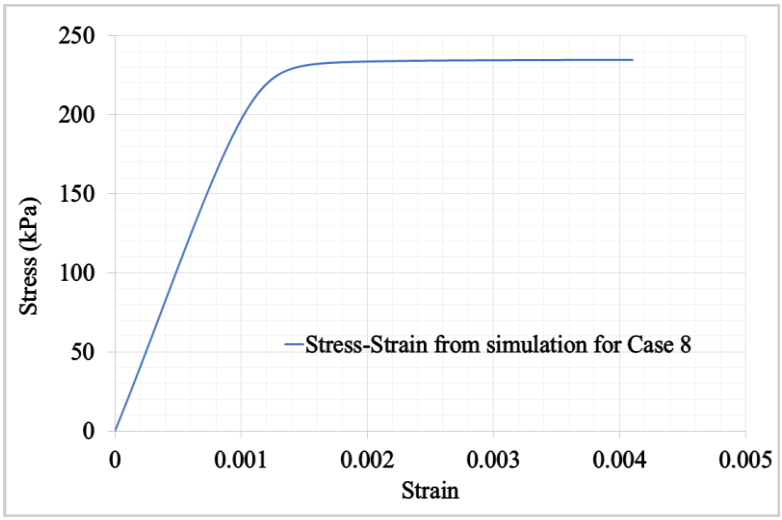


Figure 4.26: Average vertical stress-strain curve from simulation for case 8.

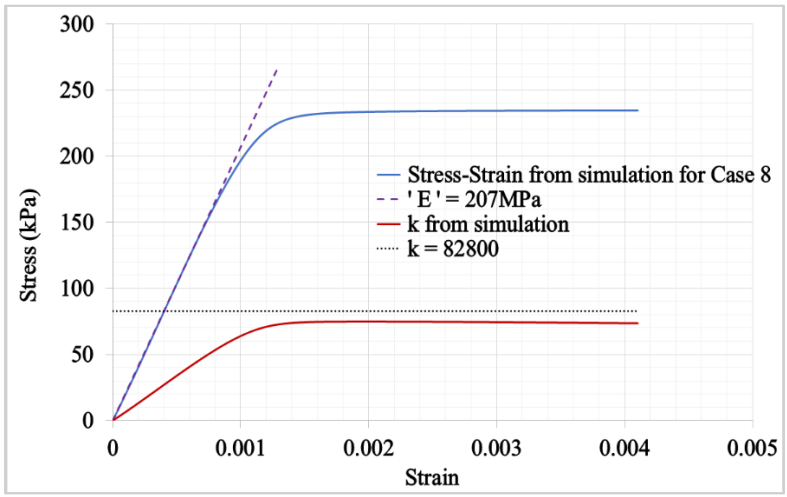
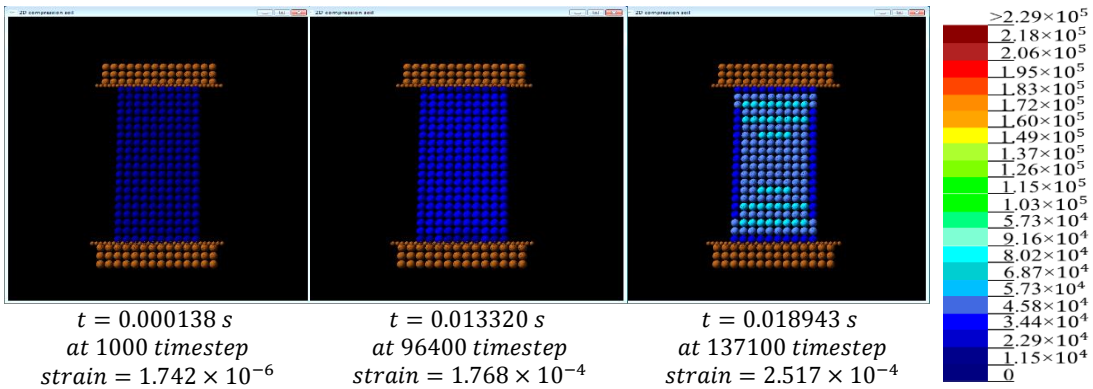


Figure 4.27: Verification of stress-strain curve from simulation with analytical result for case 8.



$t = 0.000138\ s$ *at* 1000 *timestep* $strain = 1.742 \times 10^{-6}$

$t = 0.013320\ s$ *at* 96400 *timestep* $strain = 1.768 \times 10^{-4}$

$t = 0.018943\ s$ *at* 137100 *timestep* $strain = 2.517 \times 10^{-4}$

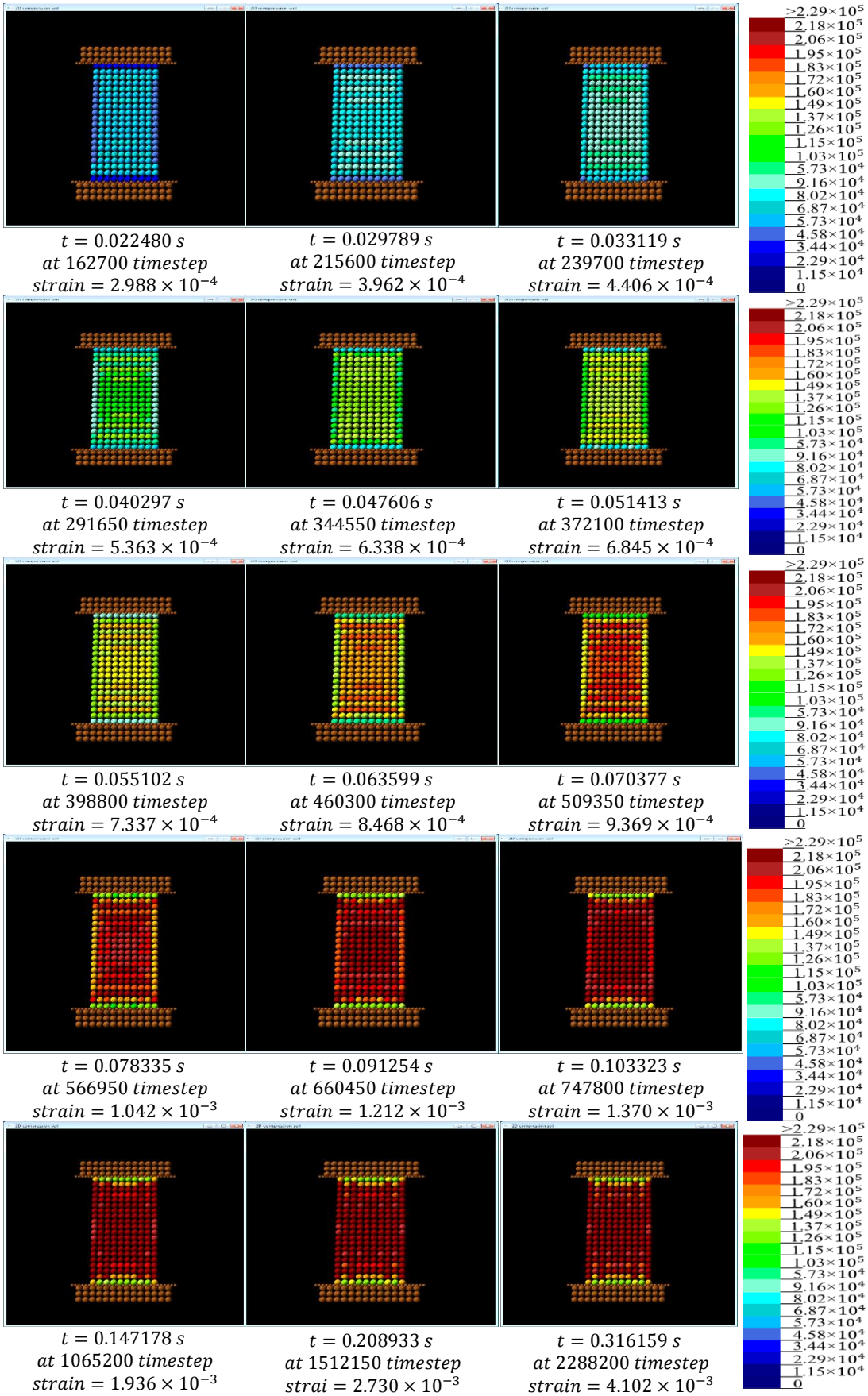


Figure 4.28: Vertical stress distribution during simulation at different time-steps for case 8.

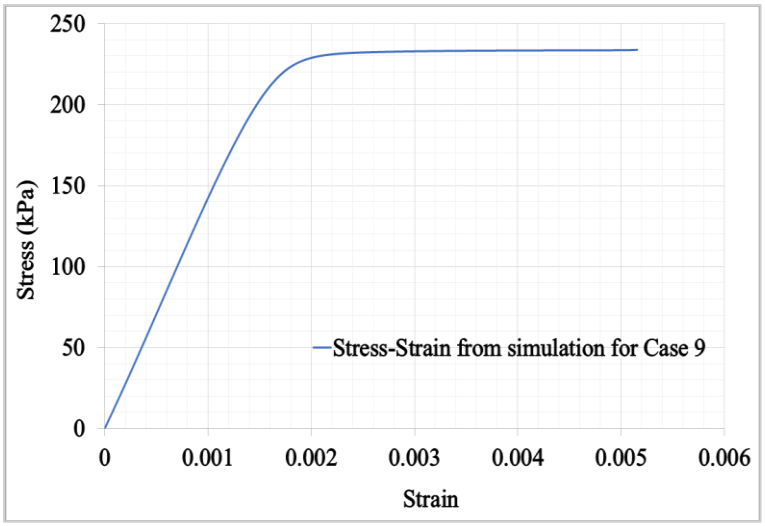


Figure 4.29: Average vertical stress-strain curve from simulation for case 9.

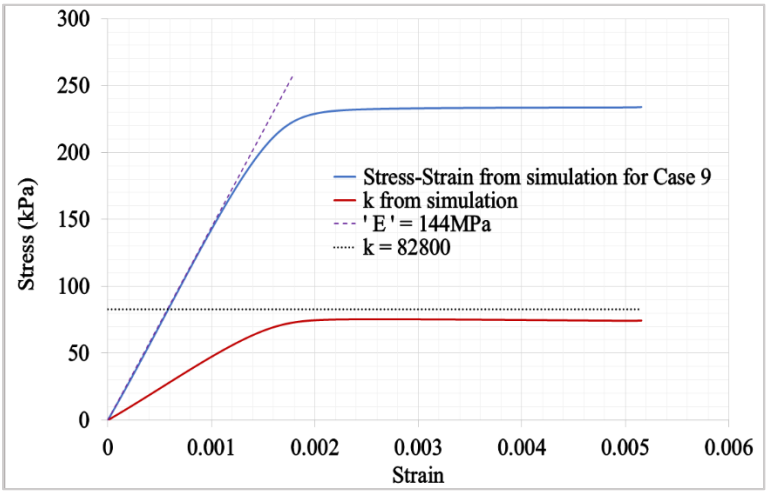
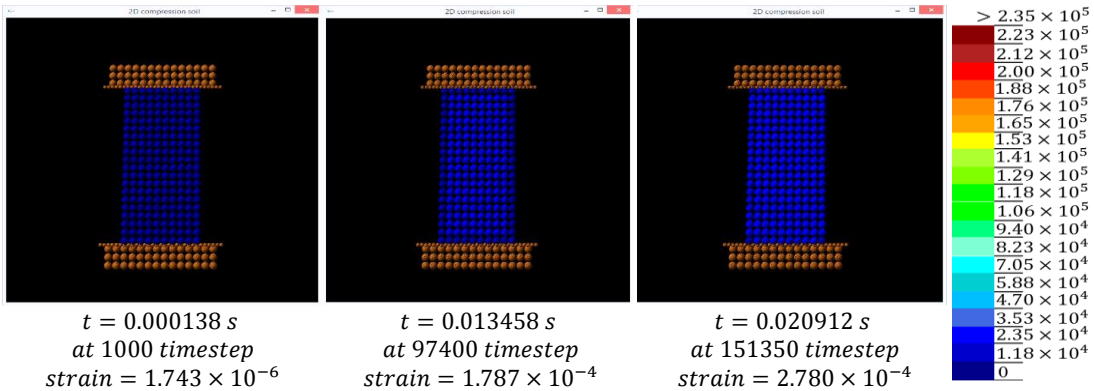


Figure 4.30: Verification of stress-strain curve from simulation with analytical results for case 9.



$t = 0.000138\ s$
$at\ 1000\ timestep$
$strain = 1.743 \times 10^{-6}$

$t = 0.013458\ s$
$at\ 97400\ timestep$
$strain = 1.787 \times 10^{-4}$

$t = 0.020912\ s$
$at\ 151350\ timestep$
$strain = 2.780 \times 10^{-4}$

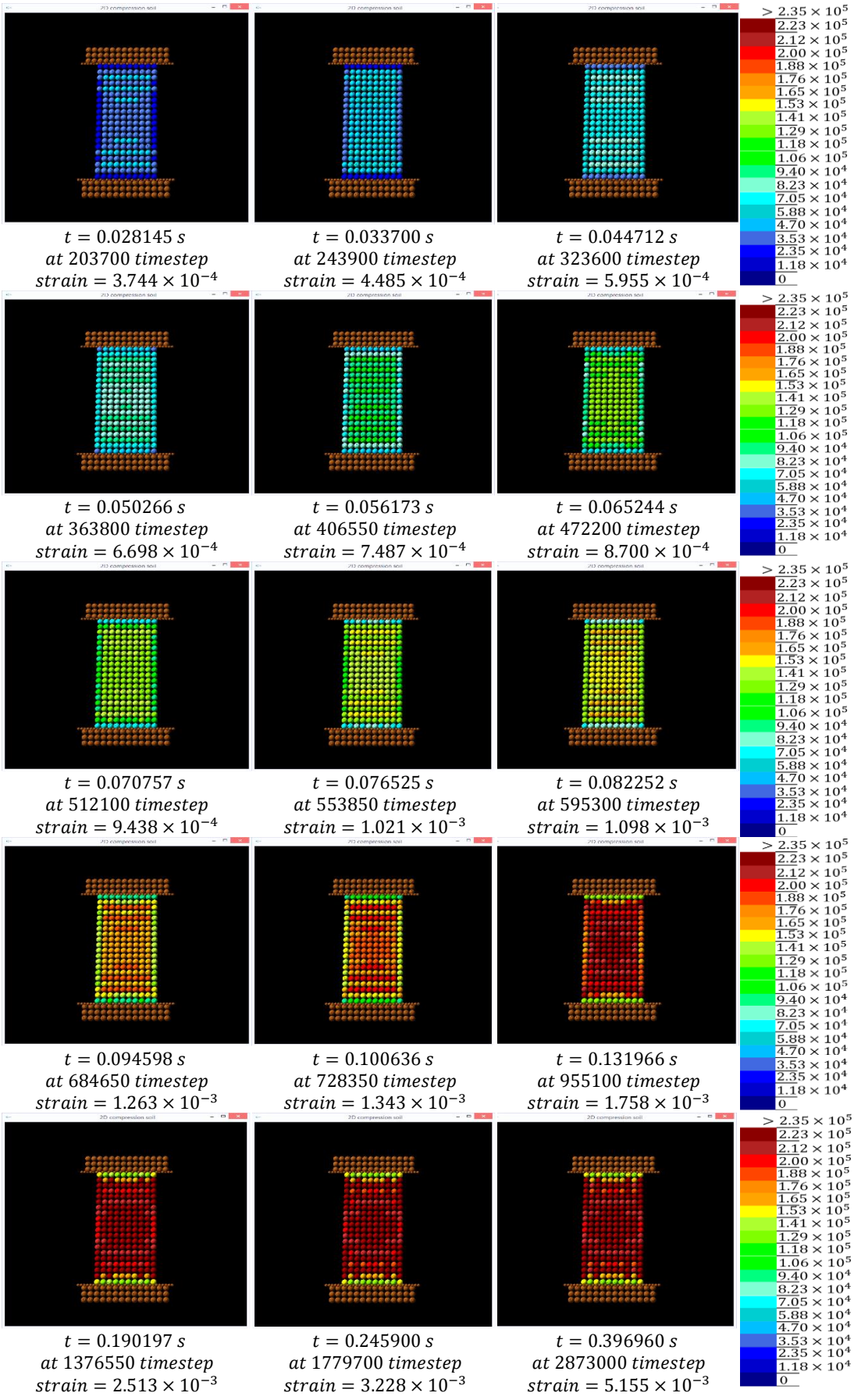


Figure 4.31: Vertical stress distribution during simulation at different time-steps for case 9.

4.9.4 Comparison between results obtained from associated and non- associated flow rule for Drucker-Prager constitutive model

In this section, stress-strain responses achieved through Drucker-Prager constitutive model with associated flow rule are compared with the Drucker-Prager constitutive model with non-associated flow rule. As such, the comparison between cases 4 and 7, 5 and 8, 6 and 9 are presented as follows:

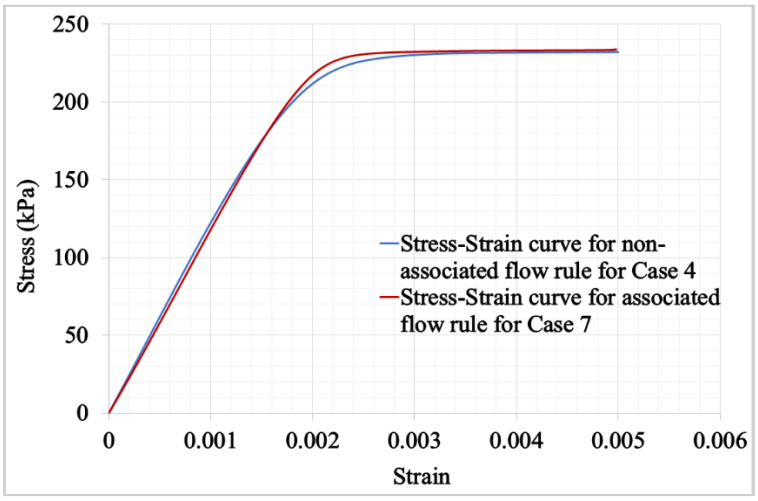


Figure 4.32: Stress-Strain from simulation for soil with E=120MPa.

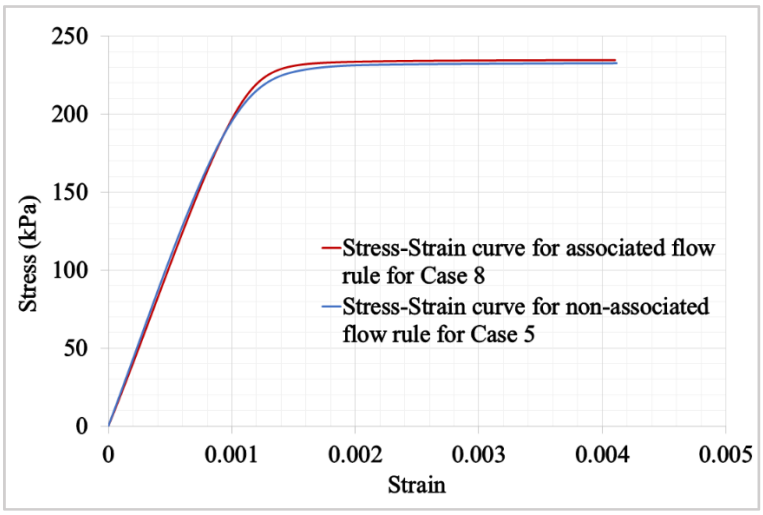


Figure 4.33: Stress-Strain from simulation for soil with E=207MPa.

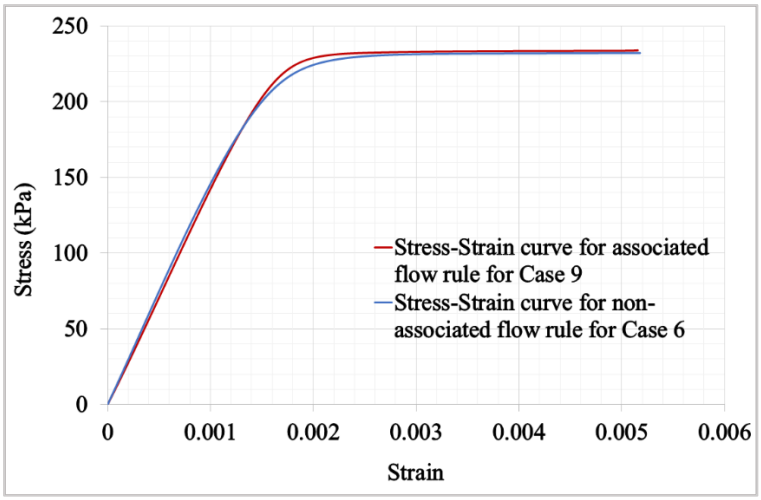


Figure 4.34: Stress-Strain from simulation for soil with E=144MPa.

4.10 Discussion

From Figures 4.7, 4.10 and 4.13, it is apparent that 'E' and 'Y' for cases 1-3 agree well with the elastic and plastic sections of the simulated curves. As presented in Table 4.2, an accuracy greater than 98% and 95% is maintained by the developed von-Mises model in simulating the elastic and perfectly plastic response of various metals. As such, the proposed von-Mises SPH model successfully simulates the stress-strain behaviour of metals such as beryllium alloy, aluminium alloy and lead alloy with Poisson's ratio within the range 0 to 0.45.

Figures. 4.16, 4.19, 4.22, 4.24, 4.27 and 4.30 show the comparison between simulated results and analytical solutions for cases 4-9 respectively. As indicated in Table 4.3, the elastic section of the simulated curve correlates well with analytical curve 'E' proving greater than 97% accuracy. Furthermore, at plasticity, k from simulation agree well with

input value of k with accuracy greater than 90% as shown in Table 4.3. It is also apparent from these figures that when k becomes constant, stress becomes constant. This satisfies the condition in Eq. (4.80). Therefore, it is obvious from above cases that both the developed Drucker-Prager SPH models with associated and non-associated flow rules effectively simulates the stress-strain behaviour of soil materials within Poisson's ratio range 0-0.3.

Table 4.2: Accuracy of von-Mises constitutive model.

Case Number	Figure Number	Accuracy to elastic section with 'E'	Accuracy to plastic section with 'Y'
1	4.7	98.663%	95.512%
2	4.10	99.832%	95.729%
3	4.13	98.873%	95.636%

Moreover, graphical representation of vertical stress distribution obtained during the simulation are presented in Figures. 4.8, 4.11, 4.14, 4.17, 4.20, 4.24, 4.25, 4.28, and 4.31 for cases 1-9 respectively. Each figure includes several visual images of vertical stress distribution in the system obtained at various time-steps during the simulation. These individual images in Figures. 4.8, 4.11, 4.14, 4.17, 4.20, 4.24, 4.25, 4.28, and 4.31 could be matched according to the corresponding values of strain with the stress-strain curves shown in Figures. 4.6, 4.9, 4.12, 4.15, 4.18, 4.21, 4.23, 4.26, and 4.29 respectively. This provides greater insight of the system behaviour at different points of the curve. Particles' position is also

updated at every time-step of the simulation. It could be clearly observed from the final set of images presented in Figures. 4.8, 4.11, 4.14, 4.17, 4.20, 4.24, 4.25, 4.28, and 4.31 that the vertical stresses in particles remain unchanged for extensive period satisfying the plastic section of the stress-strain plots.

Furthermore, the comparison between associated and non-associated flow rule for Drucker-Prager constitutive model from Figures 4.32, 4.33, 4.34 and Table 4.3 prove that even though the flow rules are similar in predicting the elastic behaviour, the associated flow rule (cases 7,8,9) better predicted the plastic behaviour of pressure sensitive cohesive materials by 1.11%, 2.2% and 0.8% than the non-associated flow rule (cases 4,5,6).

Therefore, acquired simulation results and graphical images verify that the developed von-Mises and Drucker-Prager SPH models possess the capability of effectively simulating the internal stresses and strains of selected materials. As such, the proposed von-Mises SPH algorithm could be utilized for clear understanding of stress and strain response of 2D pressure independent materials such as metals and metal structures under compression. This is applicable for structures with Poisson's ratio within the ranger 0-0.45. On the other hand, Drucker-Prager SPH algorithm for both associated and non-associated flow rule is suitable for modelling plane stress pressure sensitive dilatant materials and structures under compression. For effective simulation, these materials' Poisson's ratio should be maintained within the range 0-0.3.

Table 4.3: Accuracy of Drucker-Prager constitutive model.

Case Number	Flow rule	Figure Number	Accuracy to elastic section with 'E'	Accuracy of 'k from simulation' to $k = 82800$
4	non-associated	4.16	97.335%	92.347%
5	non-associated	4.19	98.488%	90.229%
6	non-associated	4.22	97.693%	91.233%
7	associated	4.24	98.774%	93.452%
8	associated	4.27	98.773%	92.423%
9	associated	4.30	99.112%	92.023%

4.11 Conclusion

The chapter has introduced Drucker-Prager and von-Mises elastic-perfectly plastic constitutive models in general SPH framework under plane stress condition. In addition, the study has proposed tension cracking treatment and stress-scaling backpressure for both criteria to eliminate the stress instability during the modelling process. A stress computation method at the solid boundary has also been proposed. Comprising the above developments, von-Mises and Drucker-Prager SPH models are further presented in this chapter for analysing stress and strain response of 2D structures.

Utilizing the proposed SPH models, stress and strain behaviour of various materials were analysed under uniaxial compression. Pressure independent materials with Poisson's ratio 0.12, 0.35, 0.45 and pressure

dependent dilatant materials with Poisson's ratio 0.15, 0.3, 0.23 were simulated using the developed von-Mises and Drucker-Prager SPH models respectively.

The results attained for considered materials agreed well with analytical solutions with greater than 90% of accuracy. As such, from the selected values of Poisson's ratio, it could be predicted that the proposed von-Mises SPH model is capable of accurately simulating internal stress and strain of pressure in-sensitive materials within the Poisson's ratio 0-0.45. Similarly, Drucker-Prager SPH models with associated and non-associated flow rule are capable of modelling pressure sensitive dilatant materials within the Poisson's ratio 0-0.3. This verifies that the developed SPH models contain a wider application range. Furthermore, the results achieved have highlighted the effectiveness of the proposed constitutive models in accurately simulating the plane stress problems. Therefore, the developed models are promising tools for engineers to investigate stress and strain response of elastic-perfectly plastic plane stress structures.

Chapter 5
Development of smooth particle hydrodynamics for the analysis of stresses and strains in 2D-plane strain structures

5.1 Introduction

2D-plane strain condition is equally important as of 2D-plane stress condition. The condition aids three-dimensional structures (3D) containing greater thickness along the Z direction to be modelled in two-dimension. This causes significant reduction in the number of SPH particles and corresponding computational time [149], [150]. Multitude of geotechnical structures such as strip footing, retaining walls, dams, tunnels, embankments are modelled as plane strain structures [151]–[156]. Therefore, similar to plane stress constitutive models, plane strain constitutive models in SPH framework are of equal importance for modelling the stress-strain behaviour of plane strain structures in engineering applications.

Elastic-perfectly plastic constitutive model was firstly introduced by Libersky and Petschek. [48] in SPH framework for 2D applications in solid mechanics. Subsequently, Libersky et al. [49] extended the model to 3D for

numerically simulating solid dynamics. However, when the method was applied in solid mechanics, particles formed clumps. Such instability has been studied in detail by Swegle et al. [157] and several methods have been introduced for eliminating the problem for improving the numerical model [125], [126]. Apart from that, the hydrostatic pressure in SPH formulation are generally computed by an equation of state which is a function of density change. As such, Libersky and Petschek. [48] and Libersky et al. [49] calculated the hydrostatic pressure with means of Gruneisen equation of state to complete the elastic-perfectly plastic SPH models. On the other hand, Bui et al. [51], [87] used an alternative approach, which is constitutive equation to calculate the hydrostatic pressure. Using this, the authors proposed a plane strain elastic-perfectly plastic constitutive model in SPH framework for geotechnical applications. The study employed generalized Hooke's law and plane strain formulation of yield criterion for the development of the constitutive models. As an alternative approach, current chapter introduces both Drucker-Prager and von Mises constitutive models for plane strain condition on xy space using Hooke's law for plane strain condition and two-dimensional formulas focusing on in-plane stresses and strains.

Therefore, the aim of this chapter is to develop a general two-dimensional SPH framework for analysing in-plane stresses and strains of plane strain structures. Thus, similar to chapter 4, present chapter introduces the development of three elastic-perfectly plastic constitutive models on xy space for plane strain condition. The constitutive models are

developed for von Mises yield criterion, Drucker-Prager yield criterion for both associated and non-associated flow rules. SPH models comprising the proposed constitutive models are applied to simulate stresses and strains in various materials under uniaxial compression. This is performed for verifying the developed models' accuracy and applicability range prior to its development to a complex problem which is to simulate the soil stress field around jack-in pile.

5.2 Development of elastic-perfectly plastic constitutive models for 2D-plane strain condition

Current section introduces the general constitutive models for both von-Mises and Drucker-Prager yield criterion on xy space under plane strain condition.

To begin with, total strain rate tensor defined by Eq. (3.57) is adopted. α and β in Eq. (3.57) denote x and y coordinate directions. This is because, for plane strain condition, the components of the total strain rate tensor along the z direction are zero.

In present study, $\dot{\varepsilon}_e^{\alpha\beta}$ is computed using the Hooke's Law for plane strain condition [158]. Based on this formulation, it can be observed that the elastic stress and strain components on xy plane are independent of the non-zero stress component along the z direction (σ^{zz}). As such, z coordinate can be eliminated and the plane strain formulation can be reduced to xy space as exemplified by Lee. [159]. Thus, $\dot{\varepsilon}_e^{\alpha\beta}$ is obtained from

the matrix formulation of Hooke's law for plane strain condition expressed in Eq. (3.72) which describes the elastic stress-strain relationship on xy plane. Substituting Eq. (3.54) in Eq. (3.72) leads to:

$$s^{\alpha\beta} = \frac{E}{1+v}\varepsilon^{\alpha\beta} + \frac{vE}{(1+v)(1-2v)}\varepsilon^{\gamma\gamma}\delta^{\alpha\beta} - P\delta^{\alpha\beta} \tag{5.1}$$

Using the expressions in Eq. (5.2), Eq. (5.1) is re-arranged as presented in Eq. (5.3)

$$K_{2\mathrm{D}} = \frac{E}{2(1+v)(1-2v)};\ G = \frac{E}{2(1+v)};\ P = K_{2\mathrm{D}}\varepsilon^{\gamma\gamma}; K_{2D} = \frac{3K_{3D}}{2(1+v)} \tag{5.2}$$

$$s^{\alpha\beta} = \frac{E}{1+v}\varepsilon^{\alpha\beta} + \frac{vE}{(1+v)(1-2v)}\varepsilon^{\gamma\gamma}\delta^{\alpha\beta} - \frac{E}{2(1+v)(1-2v)}\varepsilon^{\gamma\gamma}\delta^{\alpha\beta} \tag{5.3}$$

where K_{3D} is the bulk modulus for 3D, $K_{2\mathrm{D}}$ and G are bulk and shear modulus for 2D plane strain condition respectively [160], [161].

Substituting Eq. (4.4) in Eq. (5.3) leads to:

$$s^{\alpha\beta} = \frac{E}{1+v}e^{\alpha\beta} + \frac{(E - 2Ev + 2Ev - E)}{2(1+v)(1-2v)}\varepsilon^{\gamma\gamma}\delta^{\alpha\beta} \tag{5.4}$$

This simplifies into the expression for deviatoric shear strain tensor as:

$$e^{\alpha\beta} = \frac{s^{\alpha\beta}}{2G} \tag{5.5}$$

On the other hand, by substituting the relationship $\varepsilon^{\gamma\gamma} = \frac{p}{K_{2\mathrm{D}}} = \frac{\sigma^{\gamma\gamma}}{2K_{2\mathrm{D}}}$ and Eq. (5.2) in the volumetric part of Eq. (4.4), the volumetric strain tensor is derived as:

$$\frac{1}{2}\varepsilon^{\gamma\gamma}\delta^{\alpha\beta} = \frac{(1+v)(1-2v)}{2E}\sigma^{\gamma\gamma}\,\delta^{\alpha\beta} \tag{5.6}$$

Finally, by substituting Eq. (5.5) and Eq. (5.6) in Eq. (4.4), $\dot{\varepsilon}_e^{\alpha\beta}$ is derived for plane strain condition on xy plane as:

$$\dot{\varepsilon}_e^{\alpha\beta} = \frac{\dot{s}^{\alpha\beta}}{2G} + \frac{(1+v)(1-2v)}{2E}\dot{\sigma}^{\gamma\gamma}\,\delta^{\alpha\beta} \tag{5.7}$$

where $\dot{\sigma}^{\gamma\gamma} = \dot{\sigma}^{xx} + \dot{\sigma}^{yy}$, $\dot{\varepsilon}_p^{\alpha\beta}$ in Eq. (3.57) is obtained utilizing the plastic flow rule. As such, by substituting the plastic flow rule for $\dot{\varepsilon}_p^{\alpha\beta}$ and Eq. (5.7) for $\dot{\varepsilon}_e^{\alpha\beta}$ in Eq. (3.57), the total strain rate tensor is expressed for plane strain condition on xy space as:

$$\dot{\varepsilon}^{\alpha\beta} = \frac{\dot{s}^{\alpha\beta}}{2G} + \frac{(1+v)(1-2v)}{2E}\dot{\sigma}^{\gamma\gamma}\,\delta^{\alpha\beta} + \dot{\lambda}\frac{\partial \mathrm{g}}{\partial \sigma^{\alpha\beta}} \tag{5.8}$$

Using the relationships in Eqs. (3.54), (5.2) and (4.4), Eq. (5.8) is simplified as:

$$\dot{\varepsilon}^{\alpha\beta} = \frac{\dot{s}^{\alpha\beta}}{2G} + \frac{\dot{\varepsilon}^{\gamma\gamma}}{2}\delta^{\alpha\beta} + \dot{\lambda}\frac{\partial \mathrm{g}}{\partial \sigma^{\alpha\beta}} \tag{5.9}$$

Multiplying Eq. (5.9) by $2G$ leads to:

$$2G\dot{\varepsilon}^{\alpha\beta} = \dot{s}^{\alpha\beta} + \dot{G}\varepsilon^{\gamma\gamma}\delta^{\alpha\beta} + 2G\dot{\lambda}\frac{\partial \mathrm{g}}{\partial \sigma^{\alpha\beta}} \tag{5.10}$$

Thereafter, by substituting Eqs. (4.4), (3.54) and (5.2) in Eq. (5.10), the general elastic-perfectly plastic constitutive equation is derived for plane strain condition on xy space as:

$$\dot{\sigma}^{\alpha\beta} = 2G\dot{e}^{\alpha\beta} + \frac{3K_{3D}}{2(1+v)}\dot{\varepsilon}^{\gamma\gamma}\delta^{\alpha\beta} - \dot{\lambda}\left[2G\frac{\partial \mathrm{g}}{\partial \sigma^{\alpha\beta}}\right] \tag{5.11}$$

Finally, by employing Jaumann stress rate tensor in Eq. (5.11), the general constitutive relationship for plane strain condition is proposed on xy space as:

$$\dot{\sigma}^{\alpha\beta} = \sigma^{\alpha\gamma}\dot{\omega}^{\beta\gamma} + \sigma^{\gamma\beta}\dot{\omega}^{\alpha\gamma} + 2G\dot{e}^{\alpha\beta} + \frac{3K_{3D}}{2(1+v)}\dot{\varepsilon}^{\gamma\gamma}\delta^{\alpha\beta} - \dot{\lambda}\left[2G\frac{\partial \mathrm{g}}{\partial\sigma^{\alpha\beta}}\right] \quad (5.12)$$

where $\dot{\lambda}$ is derived using Eq. (3.73) as:

$$\dot{\lambda} = \frac{2G\dot{\varepsilon}^{\alpha\beta}\frac{\partial f}{\partial\sigma^{\alpha\beta}} + \left(\frac{3K_{3D}}{2(1+v)} - G\right)\dot{\varepsilon}^{\gamma\gamma}\frac{\partial f}{\partial\sigma^{\alpha\beta}}\delta^{\alpha\beta}}{2G\frac{\partial f}{\partial\sigma^{\alpha\beta}}\frac{\partial \mathrm{g}}{\partial\sigma^{\alpha\beta}}} \quad (5.13)$$

Even though σ^{zz} does not affect the computation of elastic stress-strain response on xy plane, it could be observed from Eqs. (5.12) and (5.13), the value of σ^{zz} in the formulation of $\frac{\partial f}{\partial\sigma^{\alpha\beta}}$ and $\frac{\partial \mathrm{g}}{\partial\sigma^{\alpha\beta}}$ of the yield criterion for plane strain condition would contribute to the computation of plastic stress-strain response on xy plane. However, for maintaining the plane strain formulation on xy space, σ^{zz} is avoided in the computation of plastic stress-strain response. As such, the plane strain formulations of yield criterion on xy space are employed in this approach.

5.2.1 Development of von-Mises elastic-perfectly plastic constitutive model for 2D-plane strain condition

In current section, von-Mises yield criterion with associated flow rule is incorporated into Eqs. (5.12) and (5.13) as follows:

As σ^{zz} is avoided from the plane strain formulation of the yield criterion, the expression of von Mises yield criterion employed in the derivation is similar to that of plane stress condition. Therefore, by substituting Eq. (4.25) in Eq. (5.12), von-Mises stress-strain relationship for plane strain

condition is derived on xy space as:

$$\dot{\sigma}^{\alpha\beta} = \sigma^{\alpha\gamma}\dot{\omega}^{\beta\gamma} + \sigma^{\gamma\beta}\dot{\omega}^{\alpha\gamma} + 2G\dot{e}^{\alpha\beta} + \frac{3K_{3D}}{2(1+v)}\dot{\varepsilon}^{\gamma\gamma}\delta^{\alpha\beta} - \dot{\lambda}\left[2Gs^{\alpha\beta}\right] \tag{5.14}$$

Similarly, by substituting Eqs. (4.25) and (4.4) in Eq. (5.13), $\dot{\lambda}$ is obtained as:

$$\dot{\lambda} = \frac{2G\dot{e}^{\alpha\beta}s^{\alpha\beta} + \frac{3K_{3D}}{2(1+v)}\dot{\varepsilon}^{\gamma\gamma}\delta^{\alpha\beta}s^{\alpha\beta}}{2Gs^{\alpha\beta}s^{\alpha\beta}} \tag{5.15}$$

Thereafter, by using the relationship $s^{\alpha\beta}\delta^{\alpha\beta}= 0$ and Eq. (4.23), Eq. (5.15) is simplified as:

$$\dot{\lambda} = \frac{\dot{e}^{\alpha\beta}s^{\alpha\beta}}{2\left(\frac{\sigma_y^2}{3} - \frac{1}{12}(\sigma^{\gamma\gamma})^2\right)} \tag{5.16}$$

Finally, the ultimate form of von-Mises constitutive equation for plane strain condition is proposed on xy space in SPH framework as:

$$\frac{D\sigma_i^{\alpha\beta}}{Dt} = \sigma^{\alpha\gamma}\dot{\omega}^{\beta\gamma} + \sigma^{\gamma\beta}\dot{\omega}^{\alpha\gamma} + 2G\dot{e}^{\alpha\beta} + \frac{3K_{3D}}{2(1+v)}\dot{\varepsilon}^{\gamma\gamma}\delta^{\alpha\beta} - \dot{\lambda}\left[Gs^{\alpha\beta}\right] \tag{5.17}$$

$$\dot{\lambda} = \frac{\dot{e}^{\alpha\beta}s^{\alpha\beta}}{\left(\frac{\sigma_y^2}{3} - \frac{1}{12}(\sigma^{\gamma\gamma})^2\right)}$$

The proposed constitutive model is applicable for the modelling of 2D-plane strain pressure independent materials such as metals and metal structures which contains greater thickness along its z direction. Most importantly, the developed model could be utilized for clear understanding of their internal stresses and strains under applied loads.

5.2.2 Development of Drucker-Prager constitutive models for 2D-plane strain condition

In this section, Eqs. (5.12) and (5.13) are developed incorporating Drucker-Prager yield criterion for both non-associated and associated flow rule. The development of these constitutive models is presented in Sections 5.2.2.1 and 5.2.2.2 respectively.

The mathematical representation of Drucker-Prager yield criterion presented by Eq. (4.30) is employed for the derivation of both plane strain constitutive models. As σ^{zz} is avoided from the plane strain formulation of the yield criterion, the mathematical representation of Drucker-Prager yield criterion is similar to that of plane stress condition except for Drucker-Prager constants. This is because, the constants α_ϕ and k for plane strain condition varies from that of plane stress condition [111]. As such, the constants for plane strain condition are employed as:

$$\alpha_\phi = \frac{\tan\phi}{\sqrt{9 + 12tan^2\phi}} \; and \; k = \frac{3c}{\sqrt{9 + 12tan^2\phi}} \tag{5.18}$$

where ϕ is the friction angle and c is the cohesion of material.

5.2.2.1 Derivation of 2D-plane strain Drucker-Prager constitutive model with non-associated flow rule in SPH framework

By substituting Eq. (4.33) in Eq. (5.12), Drucker-Prager elastic-perfectly plastic constitutive model with non-associated flow rule for plane strain condition is derived on xy space as:

$$\dot{\sigma}^{\alpha\beta} = \sigma^{\alpha\gamma}\dot{\omega}^{\beta\gamma} + \sigma^{\gamma\beta}\dot{\omega}^{\alpha\gamma} + 2G\dot{e}^{\alpha\beta} + \frac{3K_{3D}}{2(1+v)}\dot{\varepsilon}^{\gamma\gamma}\delta^{\alpha\beta} - \dot{\lambda}\left[6Gsin\psi\delta^{\alpha\beta} + \frac{G}{\sqrt{J_2}}s^{\alpha\beta}\right] \tag{5.19}$$

Similarly, by substituting Eq. (4.33) in Eq. (5.13), $\dot{\lambda}$ is derived as:

$$\dot{\lambda} = \frac{2G\dot{e}^{\alpha\beta}\left(\alpha_\phi\delta^{\alpha\beta} + \frac{s^{\alpha\beta}}{2\sqrt{J_2}}\right) + \frac{3K_{3D}}{2(1+v)}\dot{\varepsilon}^{\gamma\gamma}\delta^{\alpha\beta}\left(\alpha_\phi\delta^{\alpha\beta} + \frac{s^{\alpha\beta}}{2\sqrt{J_2}}\right)}{2G\left(\alpha_\phi\delta^{\alpha\beta} + \frac{s^{\alpha\beta}}{2\sqrt{J_2}}\right)\left(3sin\psi\delta^{\alpha\beta} + \frac{s^{\alpha\beta}}{2\sqrt{J_2}}\right)} \tag{5.20}$$

Thereafter, by utilizing the expressions $s^{pa}\delta^{pa} = 0$, $\delta^{pa}\delta^{pa} = 2$ and Eq. (4.23), Eq. (5.20) is simplified as:

$$\dot{\lambda} = \frac{2\alpha_\phi\frac{3K_{3D}}{2(1+v)}\dot{\varepsilon}^{\gamma\gamma} + \frac{G}{\sqrt{J_2}}s^{\alpha\beta}\dot{\varepsilon}^{\alpha\beta}}{12G\alpha_\phi sin\psi + G\left(\frac{\left[J_2 - \frac{(I_1)^2}{12}\right]}{J_2}\right)} \tag{5.21}$$

Finally, the ultimate form of Drucker-Prager constitutive equation with non-associated flow rule for plane strain condition is introduced on xy space in SPH framework as:

$$\frac{D\sigma_i^{\alpha\beta}}{Dt} = \sigma^{\alpha\gamma}\dot{\omega}^{\beta\gamma} + \sigma^{\gamma\beta}\dot{\omega}^{\alpha\gamma} + 2G\dot{e}^{\alpha\beta} + \frac{3K_{3D}}{2(1+v)}\dot{\varepsilon}^{\gamma\gamma}\delta^{\alpha\beta} - \dot{\lambda}\left[6Gsin\psi\delta^{\alpha\beta} + \frac{G}{\sqrt{J_2}}s^{\alpha\beta}\right] \tag{5.22}$$

where $\dot{\lambda}$ is defined by Eq. (5.21).

5.2.2.2 Derivation of 2D-plane strain Drucker-Prager constitutive model with associated flow rule in SPH framework

$\frac{\partial f}{\partial \sigma^{\alpha\beta}}$ and $\frac{\partial g}{\partial \sigma^{\alpha\beta}}$ for Drucker-Prager yield criterion with associated flow rule are defined by Eq. (4.40). Hence, by substituting Eq. (4.40) in Eq. (5.12) leads to:

$$\dot{\sigma}^{\alpha\beta} = \sigma^{\alpha\gamma}\dot{\omega}^{\beta\gamma} + \sigma^{\gamma\beta}\dot{\omega}^{\alpha\gamma} + 2G\dot{e}^{\alpha\beta} + \frac{3K_{3D}}{2(1+v)}\dot{\varepsilon}^{\gamma\gamma}\delta^{\alpha\beta} - \dot{\lambda}\left[2G\alpha_\phi\delta^{\alpha\beta} + \frac{G}{\sqrt{J_2}}s^{\alpha\beta}\right] \tag{5.23}$$

Similarly, by substituting Eq. (4.40) in Eq. (5.13) derives $\dot{\lambda}$ as:

$$\dot{\lambda} = \frac{2G\dot{e}^{\alpha\beta}\left(\alpha_\phi\delta^{\alpha\beta} + \frac{s^{\alpha\beta}}{2\sqrt{J_2}}\right) + \frac{3K_{3D}}{2(1+v)}\dot{\varepsilon}^{\gamma\gamma}\delta^{\alpha\beta}\left(\alpha_\phi\delta^{\alpha\beta} + \frac{s^{\alpha\beta}}{2\sqrt{J_2}}\right)}{2G\left(\alpha_\phi\delta^{\alpha\beta} + \frac{s^{\alpha\beta}}{2\sqrt{J_2}}\right)\left(\alpha_\phi\delta^{\alpha\beta} + \frac{s^{\alpha\beta}}{2\sqrt{J_2}}\right)} \tag{5.24}$$

Utilizing expressions $s^{pa}\delta^{pa} = 0$, $\delta^{pa}\delta^{pa} = 2$ and Eq. (4.23), Eq. (5.24) is simplified as:

$$\dot{\lambda} = \frac{2\alpha_\phi\frac{3K_{3D}}{2(1+v)}\dot{\varepsilon}^{\gamma\gamma} + \frac{G}{\sqrt{J_2}}s^{\alpha\beta}\dot{\varepsilon}^{\alpha\beta}}{4G\alpha_\phi{}^2 + G\left(\frac{\left[J_2 - \frac{(I_1)^2}{12}\right]}{J_2}\right)} \tag{5.25}$$

Finally, the ultimate form of Drucker-Prager constitutive equation with associated flow rule for plane strain condition is proposed on xy space in SPH framework as:

$$\frac{D\sigma_i^{\alpha\beta}}{Dt} = \sigma^{\alpha\gamma}\dot{\omega}^{\beta\gamma} + \sigma^{\gamma\beta}\dot{\omega}^{\alpha\gamma} + 2G\dot{e}^{\alpha\beta} + \frac{3K_{3D}}{2(1+v)}\dot{\varepsilon}^{\gamma\gamma}\delta^{\alpha\beta} - \dot{\lambda}\left[2G\alpha_\phi\delta^{\alpha\beta} + \frac{G}{\sqrt{J_2}}s^{\alpha\beta}\right] \tag{5.26}$$

As discussed in chapter 4, Drucker-Prager yield criterion comprises hydrostatic pressure which makes it reliable for pressure dependent dilatant materials. As such, the proposed stress-strain relationships in SPH framework for both associated and non-associated flow rule are applicable for modelling pressure sensitive materials and structures for plane strain condition. As such, the proposed plane strain constitutive models are suitable for geotechnical applications.

5.3 Numerical application

For examining the application range and success of proposed von-Mises and Drucker-Prager constitutive models with associated and non-associated flow rules for plane strain condition, SPH models are constructed for each constitutive model to analyse stresses and strains in materials under uniaxial compression. The SPH algorithm used for von-Mises and Drucker-Prager SPH models with associated and non-associated flow rules for plane strain condition is similar to the algorithm proposed in Section 4.8 except for the constitutive models. Section 4.8

introduced SPH models for analysing stresses and strains in materials under uniaxial compression for plane stress condition. In this section, this algorithm is adopted by replacing the plane stress constitutive models with the proposed plane strain constitutive models on *xy* space for examining the in-plane stresses and strains in materials under plane strain condition. For more details on the algorithm and geometry of the system please refer to chapter 4.

Table 5.1: Material Parameters.

	von-Mises plane strain Constitutive model			Drucker-Prager plane strain Constitutive model for non-associated and associated flow rules		
	Case 10: Beryllium alloy	Case 11: Aluminium alloy	Case 12: Lead alloy	Case 13, 16: Soil 1	Case 14, 17: Soil 2	Case 15, 18: Soil 3
Bulk modulus (K_{3D})	107.46GPa	76.61GPa	53.33 GPa	57.14 MPa	172.5 MPa	88.89 MPa
Shear modulus (G)	109.38GPa	25.54GPa	5.52GPa	52.17 MPa	79.62 MPa	58.54 MPa
Young's modulus (E)	245GPa	68.95GPa	16GPa	120 MPa	207 MPa	144 MPa
Yield stress	360MPa	500MPa	33MPa	-	-	-
Poisson's ratio	0.12	0.35	0.45	0.15	0.3	0.23
Friction angle (ϕ)	-	-	-	30	30	30
Cohesion (c)	-	-	-	69kPa	69kPa	69kPa
Density	2900	2700	11100	1380	1850	1430

Similar to Table 4.1, Numerical simulation is conducted on six types of materials as shown in Table 5.1. SPH model with von-Mises constitutive equation is adopted to simulate stresses and strains in three types of metals such as aluminium alloy, beryllium alloy and lead alloy (cases 10-12). Poisson's ratio of these materials are within the range 0-0.45. On the other hand, Drucker-Prager SPH model with non-associated flow rule is employed to model stresses and strains in three categories of soil (cases 13-15) with various parameters as presented in Table 5.1. Poisson's ratio of these materials are within the range 0-0.3. Comprising similar parameters of materials from cases 13-15, cases 16-18 are modelled utilizing Drucker-Prager SPH model with associated flow rule.

5.4 SPH governing equations for 2D compression

The governing equations employed for modelling uniaxial compression for plane strain condition is identical to the governing equations presented in Section 4.4 apart from the constitutive models. As such, instead of Eqs. (4.44) to (4.46) the constitutive models proposed for plane strain condition are adopted as follows:

von-Mises constitutive model with associated flow rule in SPH framework:

$$\frac{D\sigma_i^{\alpha\beta}}{Dt} = \sigma^{\alpha\gamma}\dot{\omega}^{\beta\gamma} + \sigma^{\gamma\beta}\dot{\omega}^{\alpha\gamma} + 2G\dot{e}^{\alpha\beta} + \frac{3K_{3D}}{2(1+v)}\dot{\varepsilon}^{\gamma\gamma}\delta^{\alpha\beta} - \dot{\lambda}\left[Gs^{\alpha\beta}\right] \tag{5.27}$$

$$\dot{\lambda} = \frac{\dot{e}^{\alpha\beta}s^{\alpha\beta}}{\left(\frac{\sigma_y^2}{3} - \frac{1}{12}(\sigma^{\gamma\gamma})^2\right)}$$

Drucker-Prager constitutive model with non-associated flow rule in SPH framework:

$$\frac{D\sigma_i^{\alpha\beta}}{Dt} = \sigma^{\alpha\gamma}\dot{\omega}^{\beta\gamma} + \sigma^{\gamma\beta}\dot{\omega}^{\alpha\gamma} + 2G\dot{e}^{\alpha\beta} + \frac{3K_{3D}}{2(1+v)}\dot{\varepsilon}^{\gamma\gamma}\delta^{\alpha\beta} - \dot{\lambda}\left[6G sin\psi\,\delta^{\alpha\beta} + \frac{G}{\sqrt{J_2}}s^{\alpha\beta}\right] \tag{5.28}$$

$$\dot{\lambda} = \frac{2\alpha_\phi \frac{3K_{3D}}{2(1+v)}\dot{\varepsilon}^{\gamma\gamma} + \frac{G}{\sqrt{J_2}}s^{\alpha\beta}\dot{\varepsilon}^{\alpha\beta}}{12G\alpha_\phi sin\psi + G\left(\frac{\left[J_2 - \frac{(I_1)^2}{12}\right]}{J_2}\right)}$$

Drucker-Prager constitutive model with associated flow rule in SPH framework:

$$\frac{D\sigma_i^{\alpha\beta}}{Dt} = \sigma^{\alpha\gamma}\dot{\omega}^{\beta\gamma} + \sigma^{\gamma\beta}\dot{\omega}^{\alpha\gamma} + 2G\dot{e}^{\alpha\beta} + \frac{3K_{3D}}{2(1+v)}\dot{\varepsilon}^{\gamma\gamma}\delta^{\alpha\beta} - \dot{\lambda}\left[2G\alpha_\phi\,\delta^{\alpha\beta} + \frac{G}{\sqrt{J_2}}s^{\alpha\beta}\right] \tag{5.29}$$

$$\dot{\lambda} = \frac{2\alpha_\phi \frac{3K_{3D}}{2(1+v)}\dot{\varepsilon}^{\gamma\gamma} + \frac{G}{\sqrt{J_2}}s^{\alpha\beta}\dot{\varepsilon}^{\alpha\beta}}{4G{\alpha_\phi}^2 + G\left(\frac{\left[J_2 - \frac{(I_1)^2}{12}\right]}{J_2}\right)}$$

5.5 Results

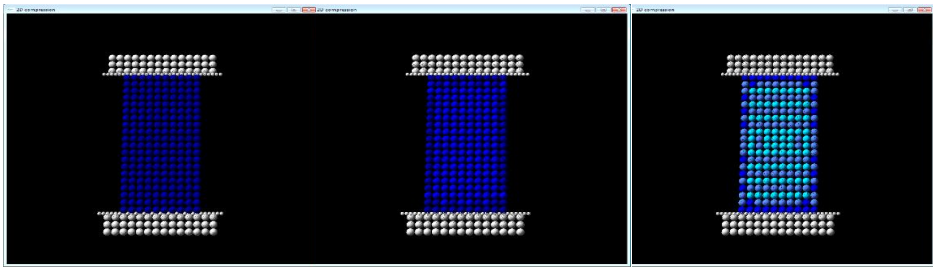
Similar to the SPH models in chapter 4, von-Mises and Drucker-Prager SPH models for plane strain condition deliver the materials' stress-strain behaviour and graphical representation of vertical stress distribution at

every time-step of the simulation. Stress-strain response for each material is plotted by averaging the summation of internal vertical stresses against internal vertical strains over the total number of particles in the system (200 particles).

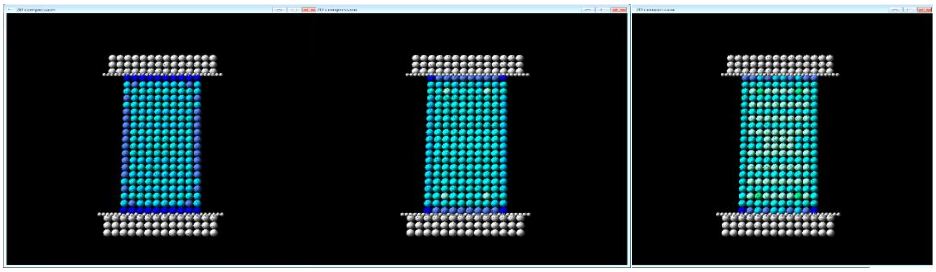
Sections 5.5.1, 5.5.2 and 5.5.3 present the results obtained from modelling cases 10-12, 13-15 and 16-18 respectively. Numerically achieved stress-strain plot for cases 10-18 are shown in Figures 5.2, 5.3, 5.5, 5.7, 5.11, 5.15, 5.19, 5.23 and 5.27 respectively. These results clearly demonstrate the achievement of elastic-perfectly plastic response of the materials.

The validation method of these numerical results is identical to the method explained for plane stress condition in Section 4.9 for both von-Mises and Drucker-Prager yield criterion except for the value of k used for cases 13-18. This is because, the expression of k for plane stress condition is dissimilar from plane strain condition as defined by Eqs. (3.80) and (5.18) respectively. Hence, the input value of k from Eq. (5.18) varies from Eq. (3.80). As such, 'k from simulation' for cases 13-18 are verified with the input value of k = 57411.47031 from Eq. (5.18). Furthermore, the plane stress stress-strain plots achieved for cases 1-9 are compared with the plane strain stress-strain plots of cases 10-18 as shown in Figures. 5.2, 5.3, 5.5, 5.9, 5.13, 5.17, 5.21, 5.25, 5.29 respectively. In addition, the stress-strain curves achieved through Drucker-Prager SPH model with non-associated flow rule (cases 13-15) are compared with the associated flow rule (cases 16-18) in Section 5.5.4.

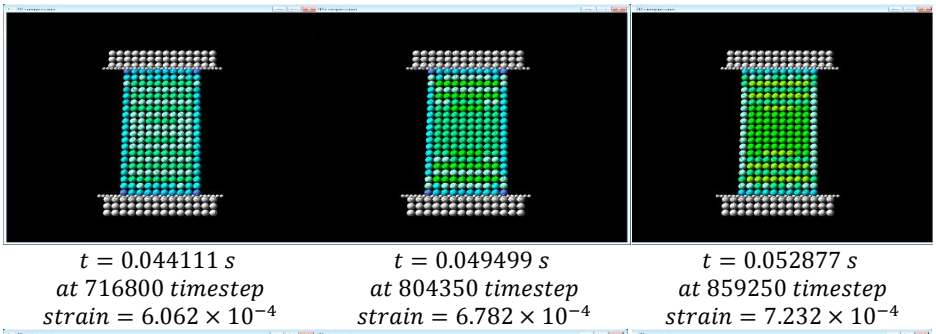
5.5.1 Results obtained using von-Mises constitutive model



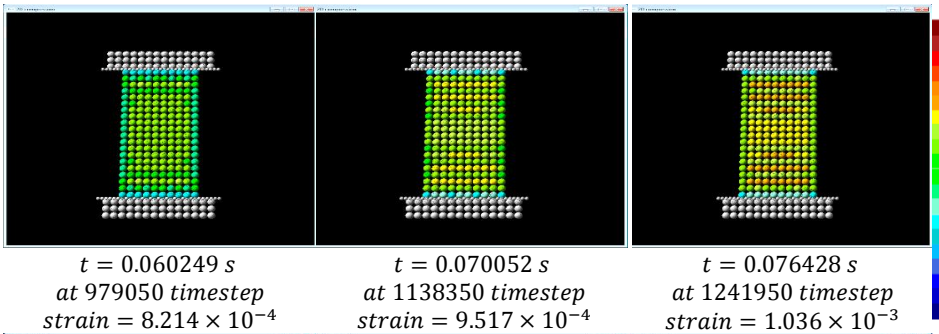
$t = 0.000062\ s$ *at* 1000 *timestep* $strain = 7.769 \times 10^{-7}$ | $t = 0.011200\ s$ *at* 182000 *timestep* $strain = 1.602 \times 10^{-4}$ | $t = 0.024092\ s$ *at* 391500 *timestep* $strain = 3.376 \times 10^{-4}$



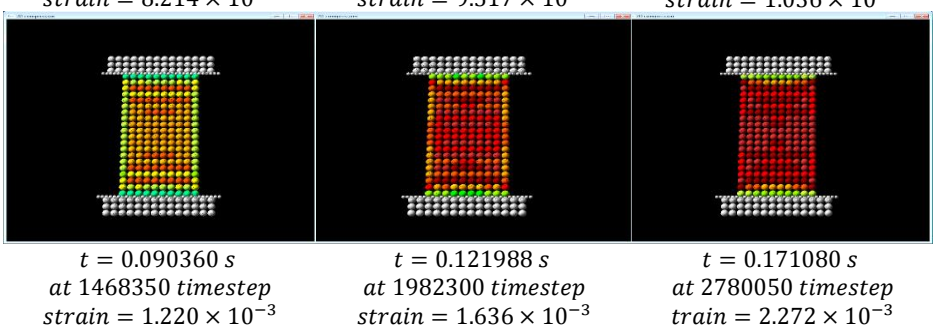
$t = 0.029468\ s$ *at* 478850 *timestep* $strain = 4.100 \times 10^{-4}$ | $t = 0.034782\ s$ *at* 565200 *timestep* $strain = 4.814 \times 10^{-4}$ | $t = 0.039631\ s$ *at* 644000 *timestep* $strain = 5.463 \times 10^{-4}$



$t = 0.044111\ s$ *at* 716800 *timestep* $strain = 6.062 \times 10^{-4}$ | $t = 0.049499\ s$ *at* 804350 *timestep* $strain = 6.782 \times 10^{-4}$ | $t = 0.052877\ s$ *at* 859250 *timestep* $strain = 7.232 \times 10^{-4}$



$t = 0.060249\ s$ *at* 979050 *timestep* $strain = 8.214 \times 10^{-4}$ | $t = 0.070052\ s$ *at* 1138350 *timestep* $strain = 9.517 \times 10^{-4}$ | $t = 0.076428\ s$ *at* 1241950 *timestep* $strain = 1.036 \times 10^{-3}$



$t = 0.090360\ s$ *at* 1468350 *timestep* $strain = 1.220 \times 10^{-3}$ | $t = 0.121988\ s$ *at* 1982300 *timestep* $strain = 1.636 \times 10^{-3}$ | $t = 0.171080\ s$ *at* 2780050 *timestep* $train = 2.272 \times 10^{-3}$

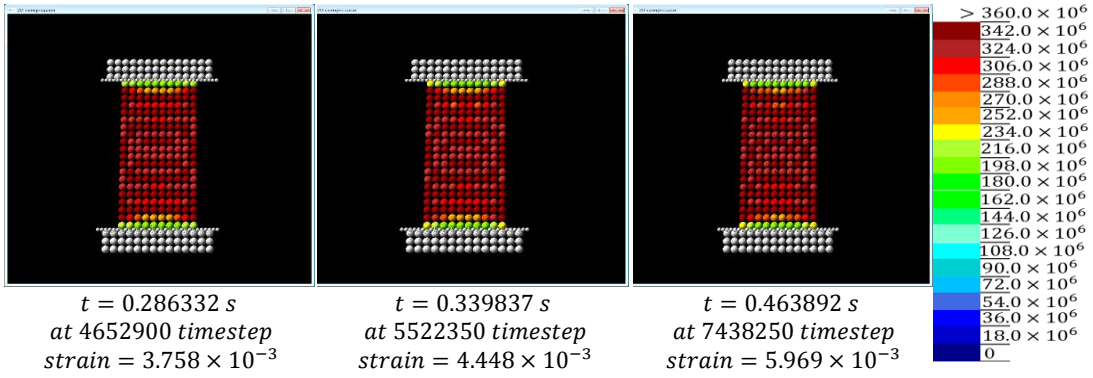


Figure 5.1: Vertical stress distribution at various time-steps for case 10.

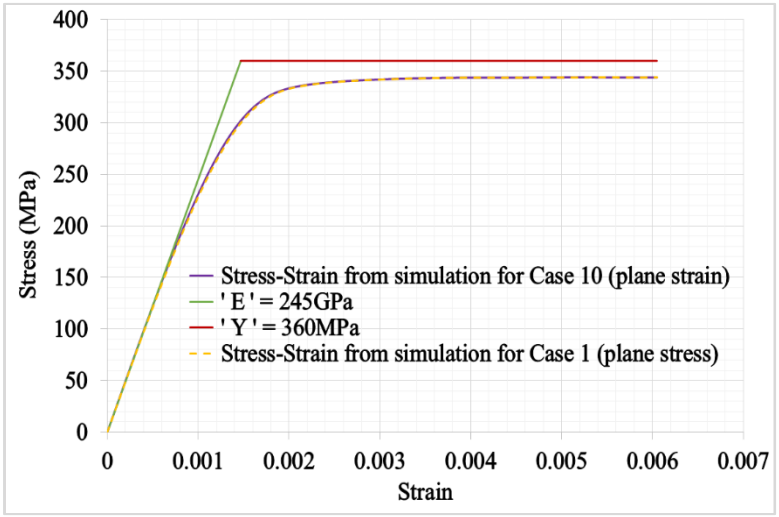


Figure 5.2: Comparison of plane strain and plane stress stress-strain curve for Beryllium alloy.

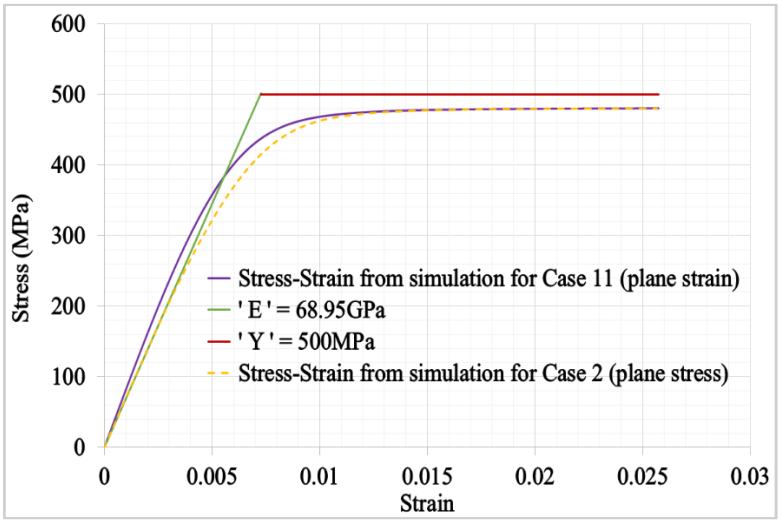
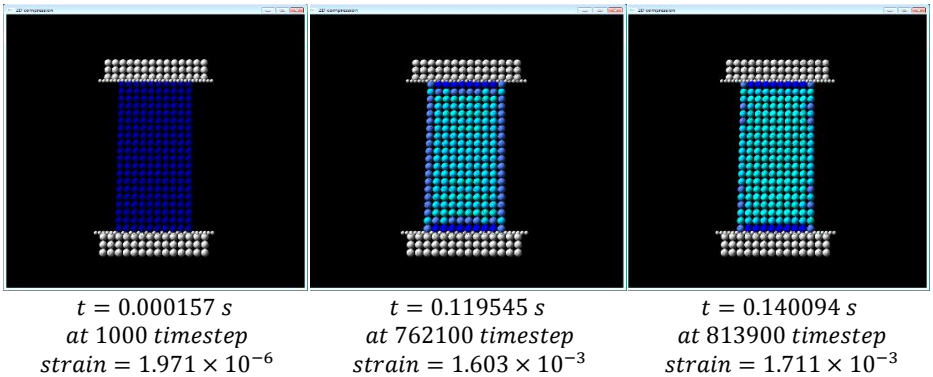
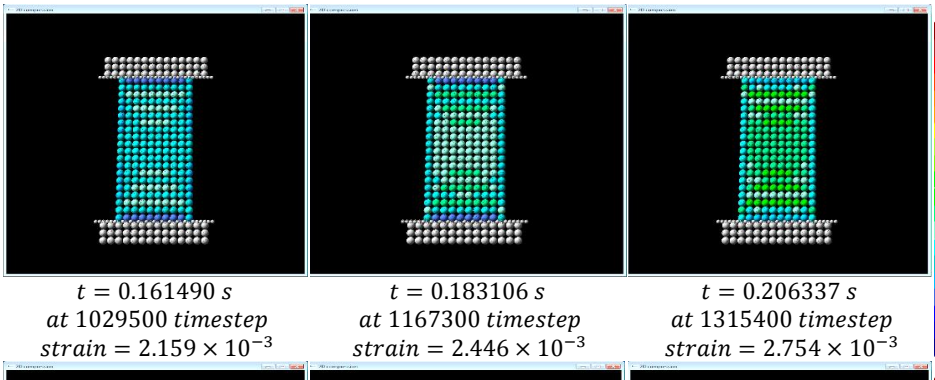


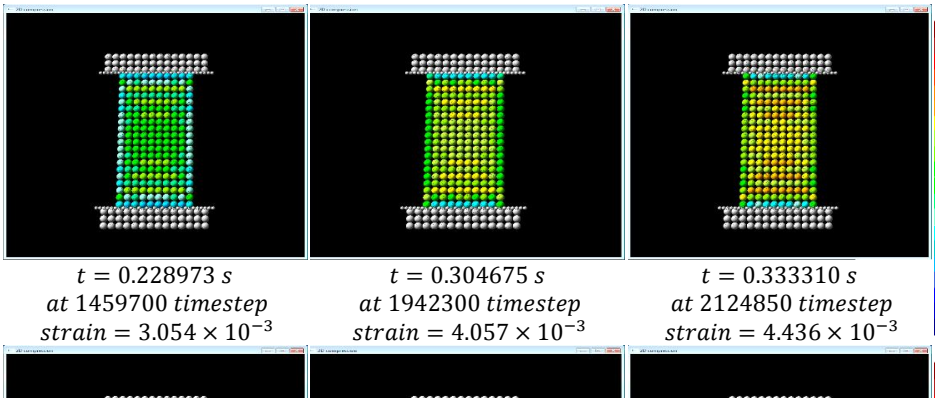
Figure 5.3: Comparison of plane strain and plane stress stress-strain curve for Aluminium alloy.



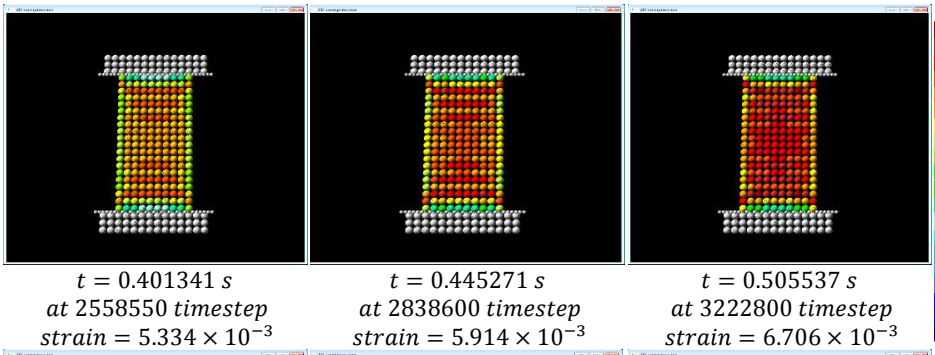
$t = 0.000157\ s$ at 1000 *timestep* $strain = 1.971 \times 10^{-6}$ | $t = 0.119545\ s$ at 762100 *timestep* $strain = 1.603 \times 10^{-3}$ | $t = 0.140094\ s$ at 813900 *timestep* $strain = 1.711 \times 10^{-3}$



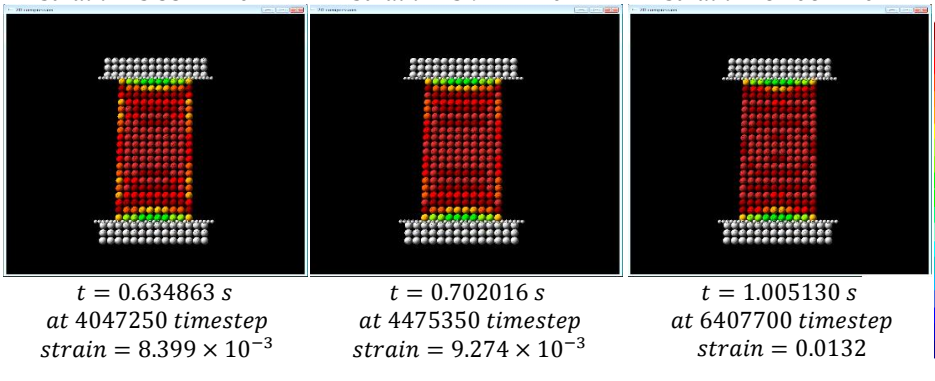
$t = 0.161490\ s$ at 1029500 *timestep* $strain = 2.159 \times 10^{-3}$ | $t = 0.183106\ s$ at 1167300 *timestep* $strain = 2.446 \times 10^{-3}$ | $t = 0.206337\ s$ at 1315400 *timestep* $strain = 2.754 \times 10^{-3}$



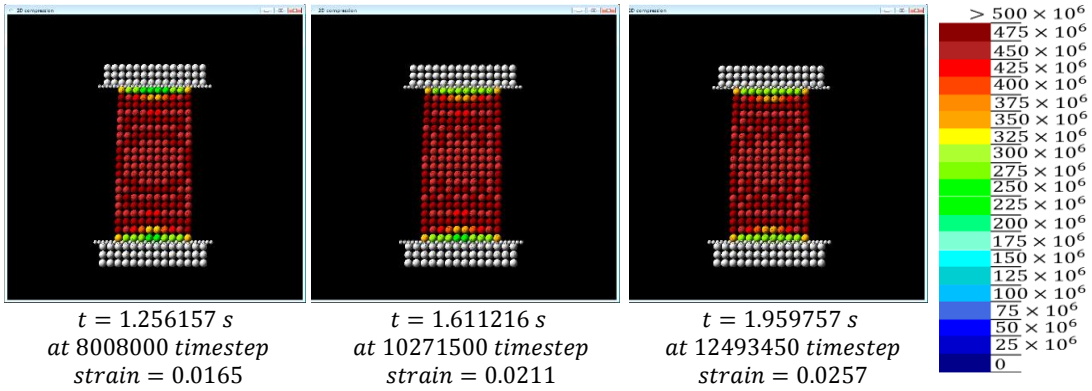
$t = 0.228973\ s$ at 1459700 *timestep* $strain = 3.054 \times 10^{-3}$ | $t = 0.304675\ s$ at 1942300 *timestep* $strain = 4.057 \times 10^{-3}$ | $t = 0.333310\ s$ at 2124850 *timestep* $strain = 4.436 \times 10^{-3}$



$t = 0.401341\ s$ at 2558550 *timestep* $strain = 5.334 \times 10^{-3}$ | $t = 0.445271\ s$ at 2838600 *timestep* $strain = 5.914 \times 10^{-3}$ | $t = 0.505537\ s$ at 3222800 *timestep* $strain = 6.706 \times 10^{-3}$



$t = 0.634863\ s$ at 4047250 *timestep* $strain = 8.399 \times 10^{-3}$ | $t = 0.702016\ s$ at 4475350 *timestep* $strain = 9.274 \times 10^{-3}$ | $t = 1.005130\ s$ at 6407700 *timestep* $strain = 0.0132$



$t = 1.256157\ s$ *at* 8008000 *timestep* $strain = 0.0165$

$t = 1.611216\ s$ *at* 10271500 *timestep* $strain = 0.0211$

$t = 1.959757\ s$ *at* 12493450 *timestep* $strain = 0.0257$

Figure 5.4: Vertical stress distribution at various time-steps for case 11.

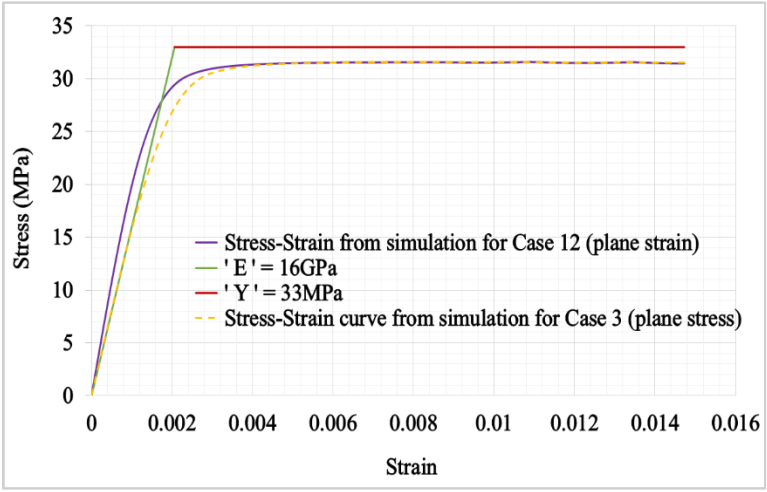
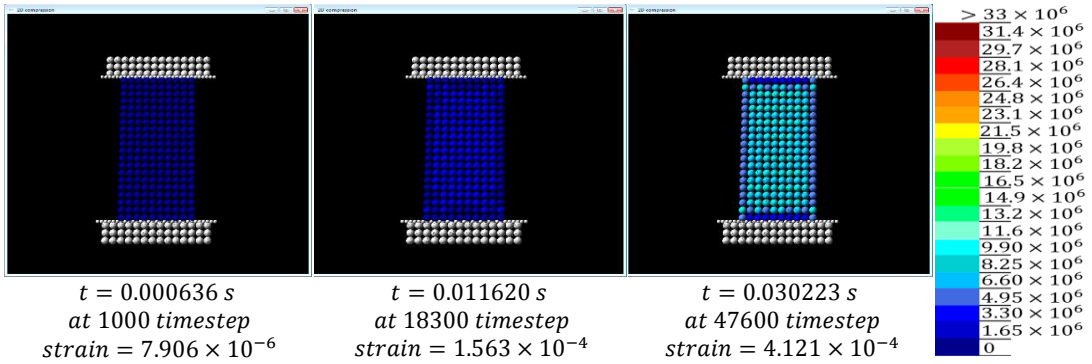


Figure 5.5: Comparison of plane strain and plane stress stress-strain curve for Lead alloy.



$t = 0.000636\ s$ *at* 1000 *timestep* $strain = 7.906 \times 10^{-6}$

$t = 0.011620\ s$ *at* 18300 *timestep* $strain = 1.563 \times 10^{-4}$

$t = 0.030223\ s$ *at* 47600 *timestep* $strain = 4.121 \times 10^{-4}$

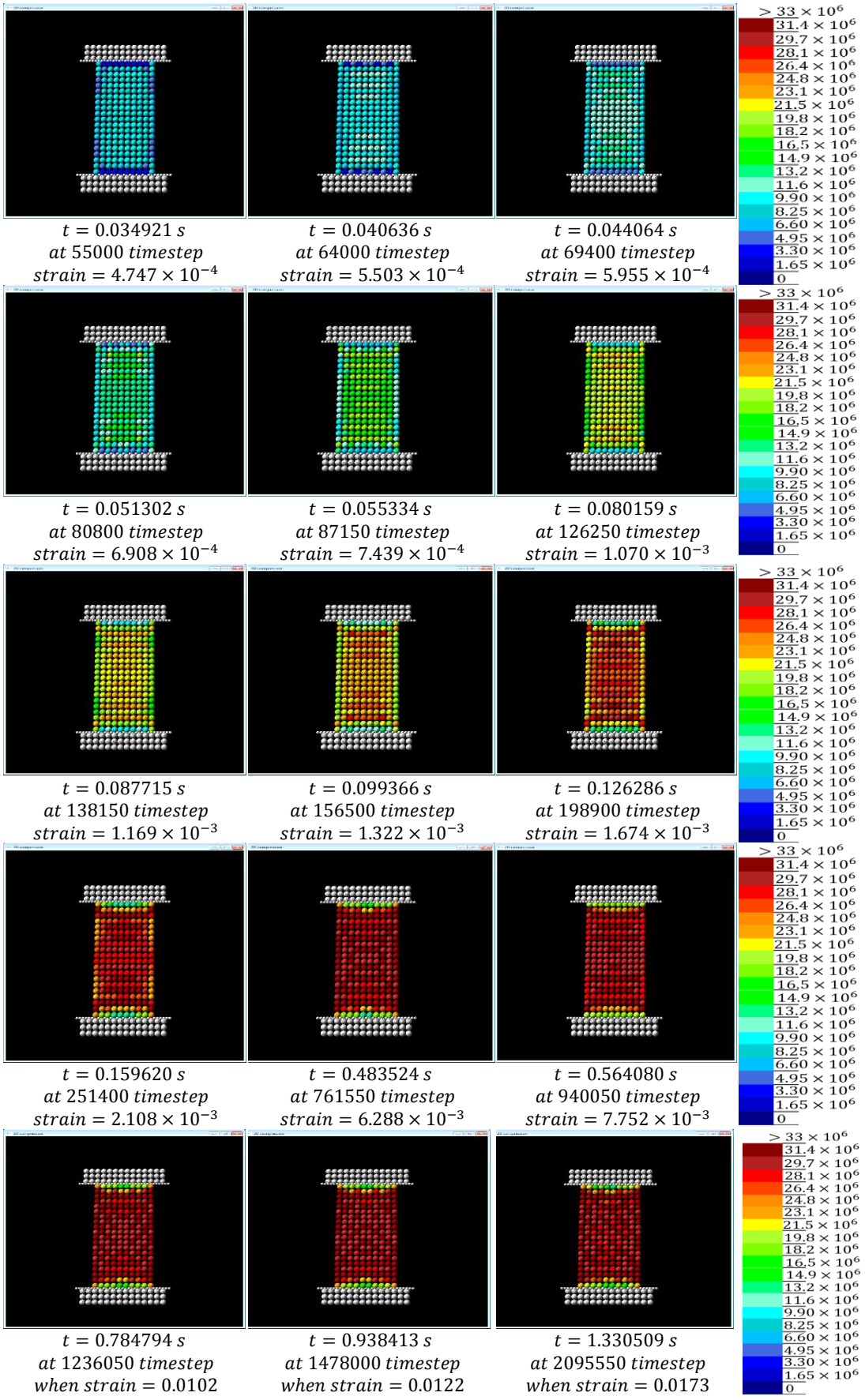


Figure 5.6: Vertical stress distribution at various time-steps for case 12.

5.5.2 Results obtained using Drucker-Prager constitutive model with non-associated flow rule

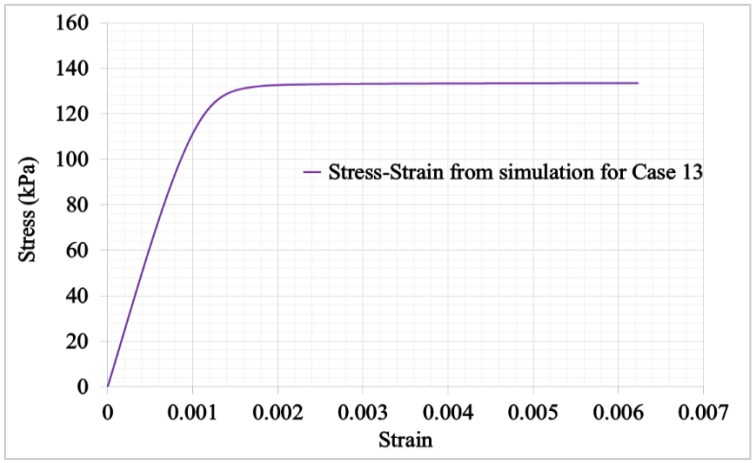


Figure 5.7: Average vertical stress-strain curve from simulation for case 13.

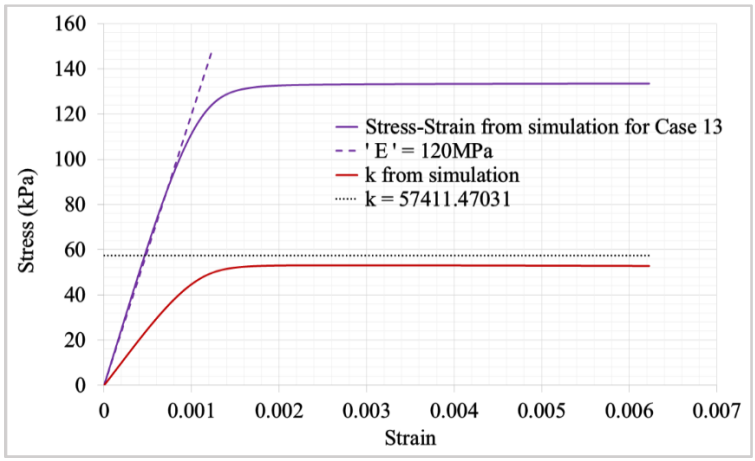


Figure 5.8: Verification of simulation result with analytical result for case 13.

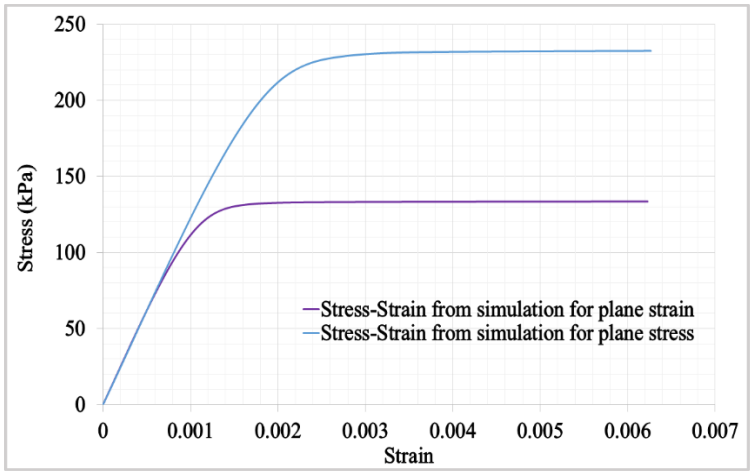
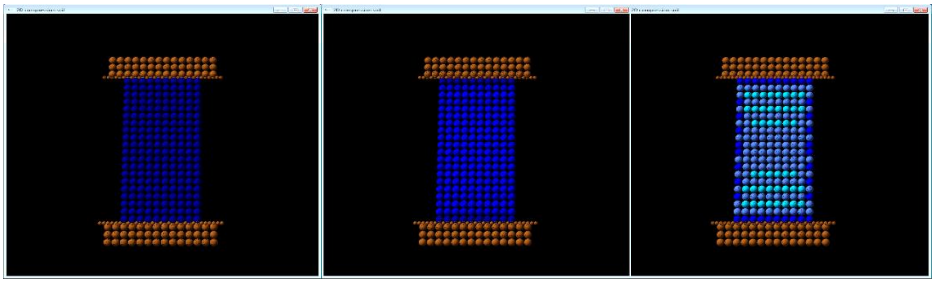


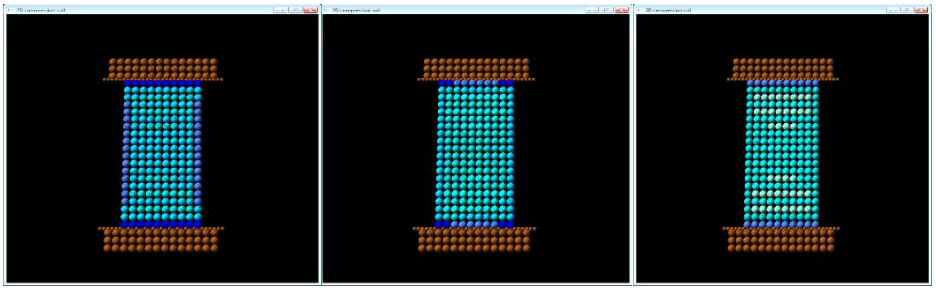
Figure 5.9: Comparison of plane strain and plane strain results for Soil with E=120MPa.



$t = 0.000138\ s$ $t = 0.011530\ s$ $t = 0.017983\ s$

at 1000 *timestep* *at* 83450 *timestep* *at* 130150 *timestep*

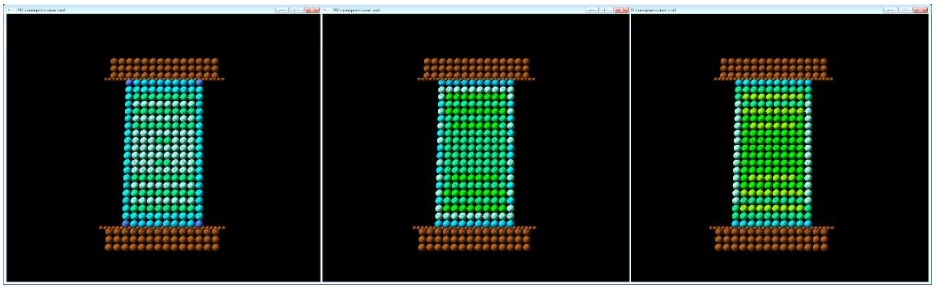
$strain = 1.743 \times 10^{-6}$ $strain = 1.530 \times 10^{-4}$ $strain = 2.388 \times 10^{-4}$



$t = 0.021354\ s$ $t = 0.024919\ s$ $t = 0.028587\ s$

at 154550 *timestep* *at* 180350 *timestep* *at* 206900 *timestep*

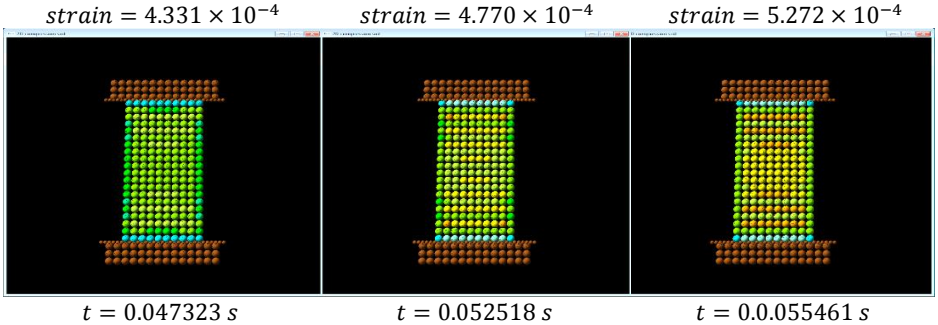
$strain = 2.836 \times 10^{-4}$ $strain = 3.311 \times 10^{-4}$ $strain = 3.799 \times 10^{-4}$



$t = 0.032587\ s$ $t = 0.035890\ s$ $t = 0.039662\ s$

at 235850 *timestep* *at* 259750 *timestep* *at* 287050 *timestep*

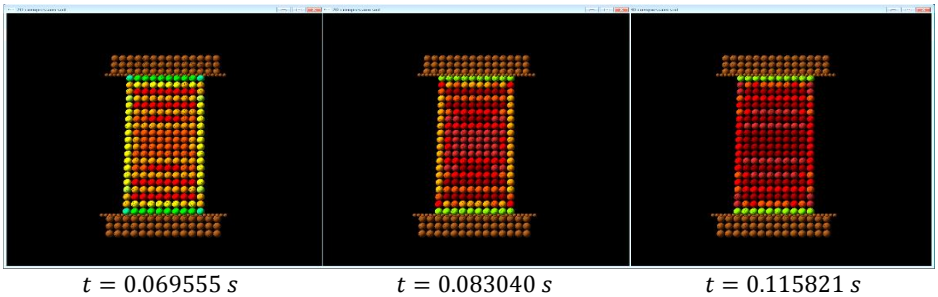
$strain = 4.331 \times 10^{-4}$ $strain = 4.770 \times 10^{-4}$ $strain = 5.272 \times 10^{-4}$



$t = 0.047323\ s$ $t = 0.052518\ s$ $t = 0.0.055461\ s$

at 342500 *timestep* *at* 380100 *timestep* *at* 401400 *timestep*

$strain = 6.291 \times 10^{-4}$ $strain = 6.981 \times 10^{-4}$ $strain = 7.372 \times 10^{-4}$



$t = 0.069555\ s$ $t = 0.083040\ s$ $t = 0.115821\ s$

at 503400 *timestep* *at* 601000 *timestep* *at* 838250 *timestep*

$strain = 9.240 \times 10^{-4}$ $strain = 1.102 \times 10^{-3}$ $strain = 1.529 \times 10^{-3}$

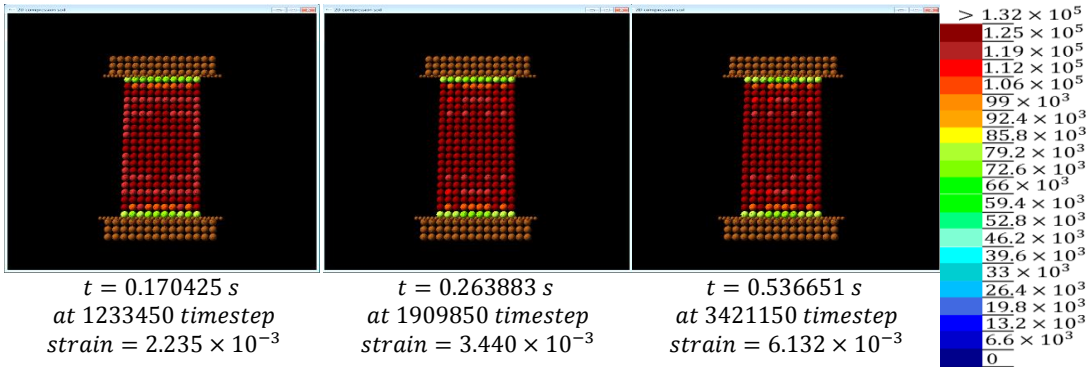


Figure 5.10: Vertical stress distribution at various time-steps for case 13.

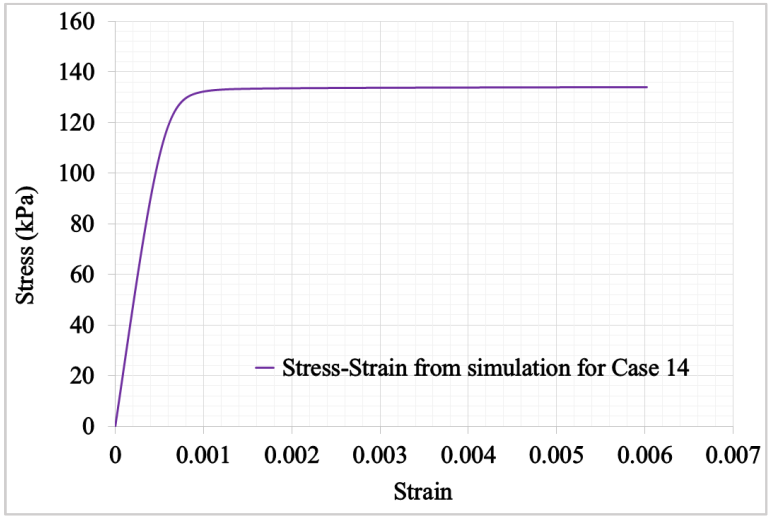


Figure 5.11: Average vertical stress-strain curve from simulation for case 14.

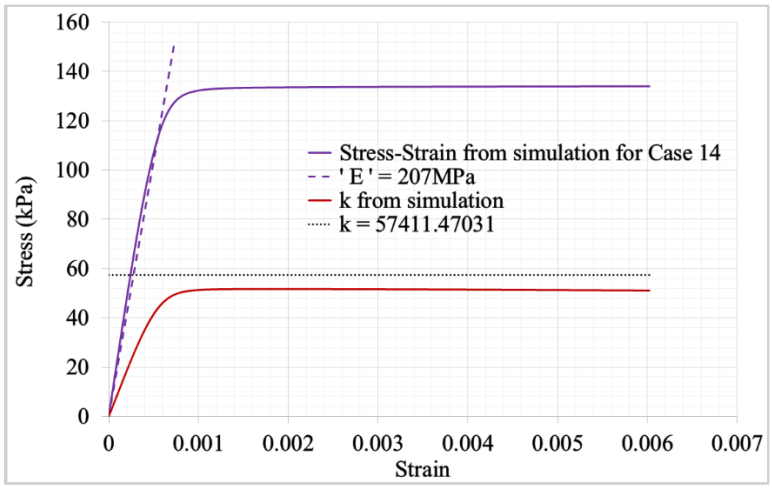


Figure 5.12: Verification of simulation result with analytical result for case 14.

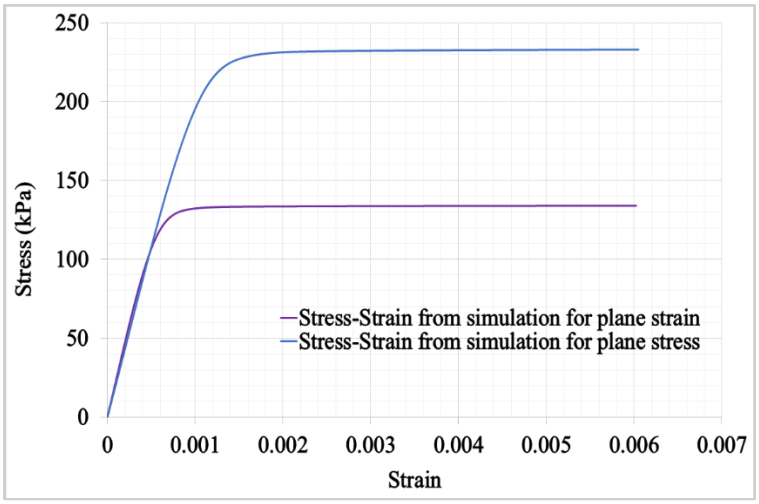
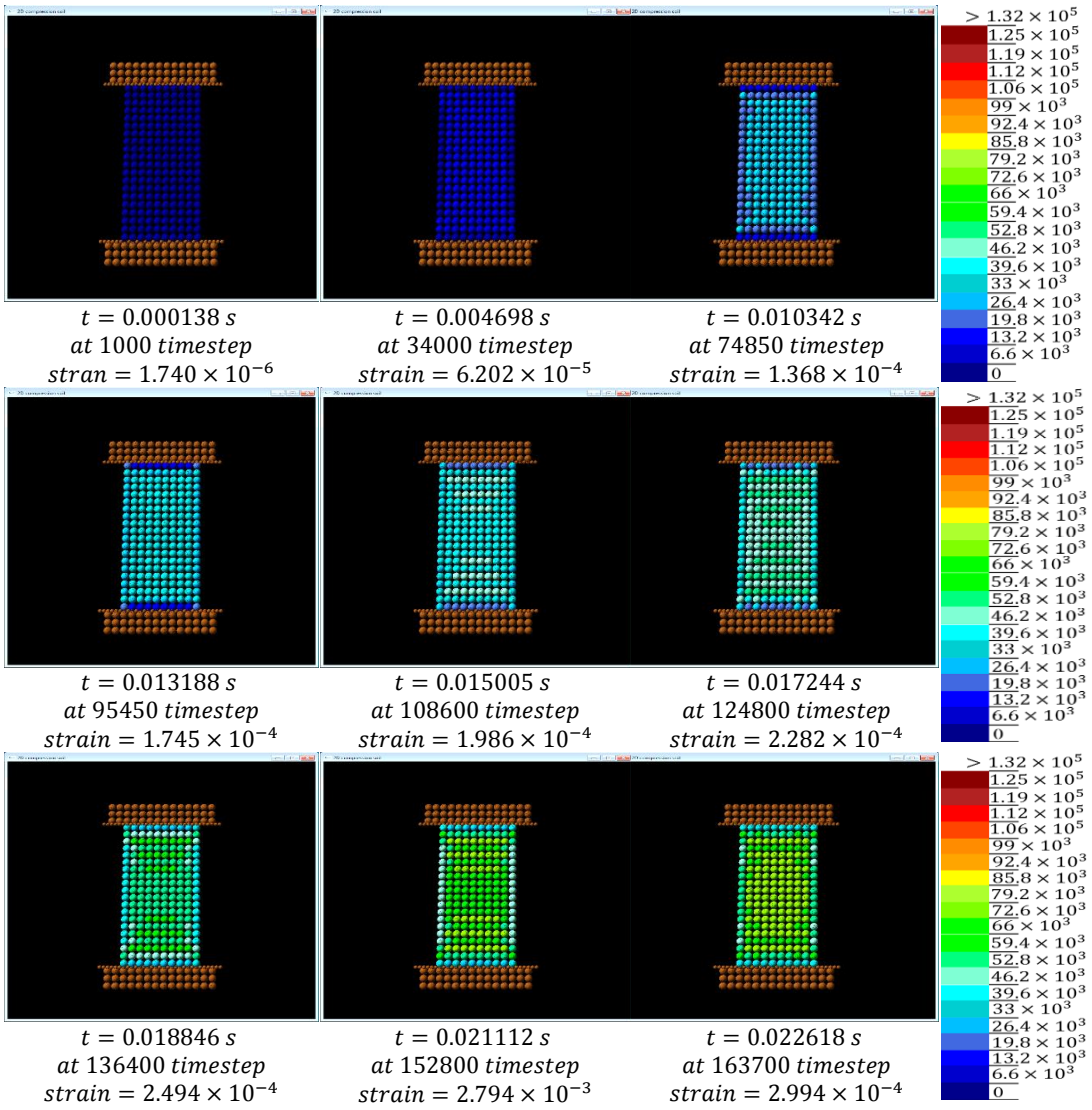


Figure 5.13: Comparison of plane strain and plane stress results for Soil with E=207MPa.



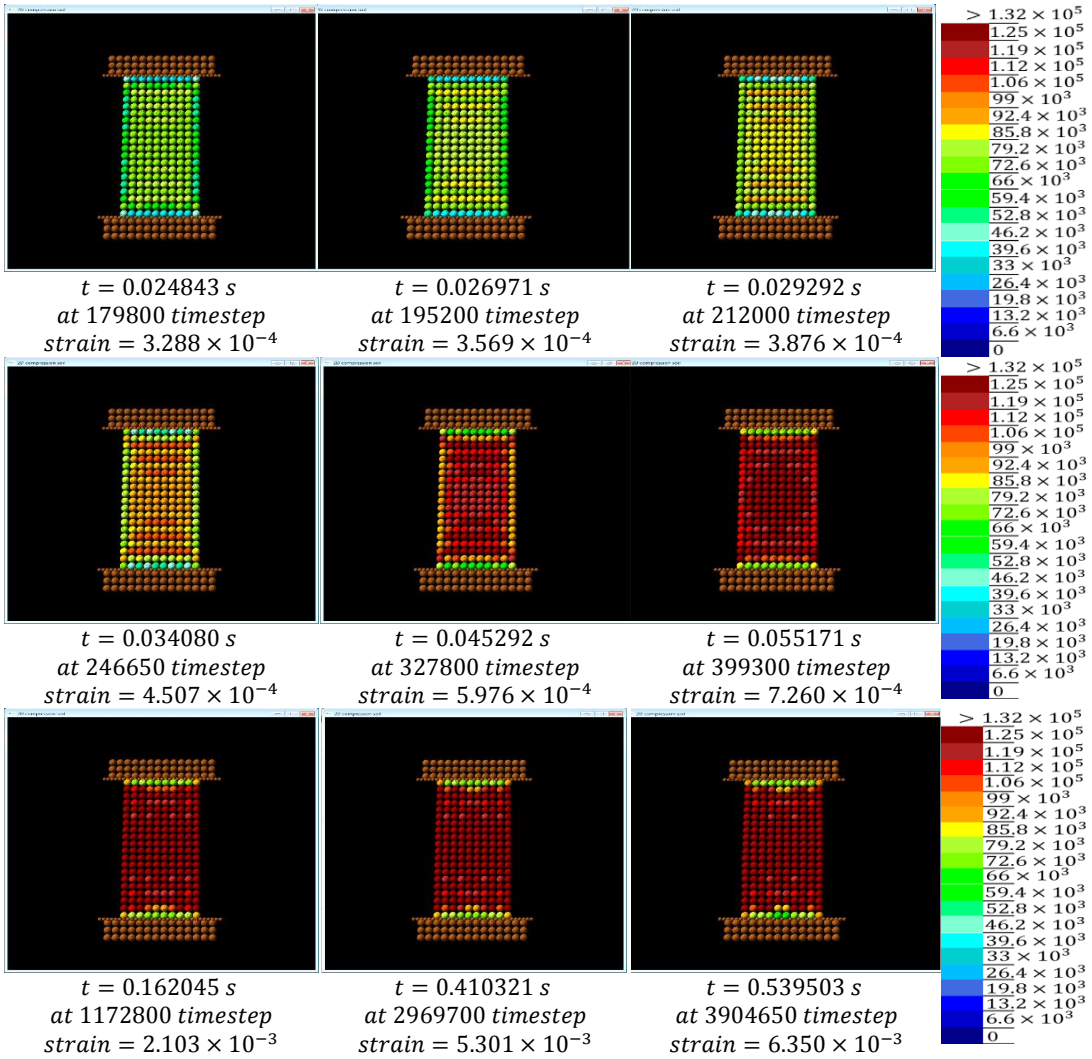


Figure 5.14: Vertical stress distribution at various time-steps for case 14.

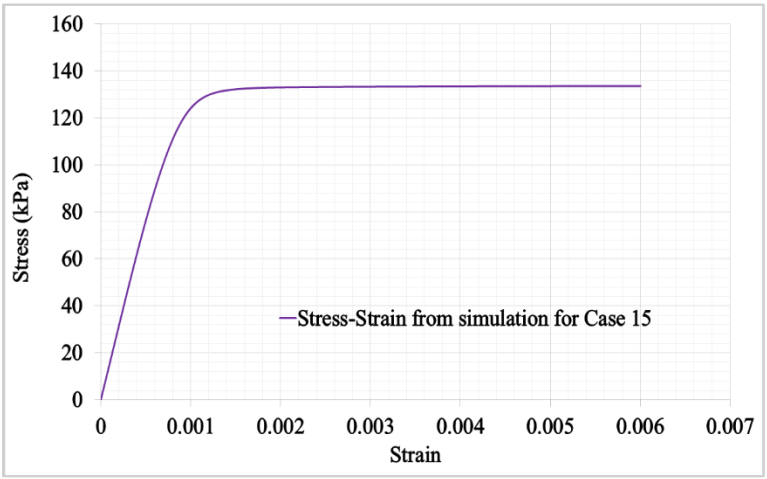


Figure 5.15: Average vertical stress-strain curve from simulation for case 15.

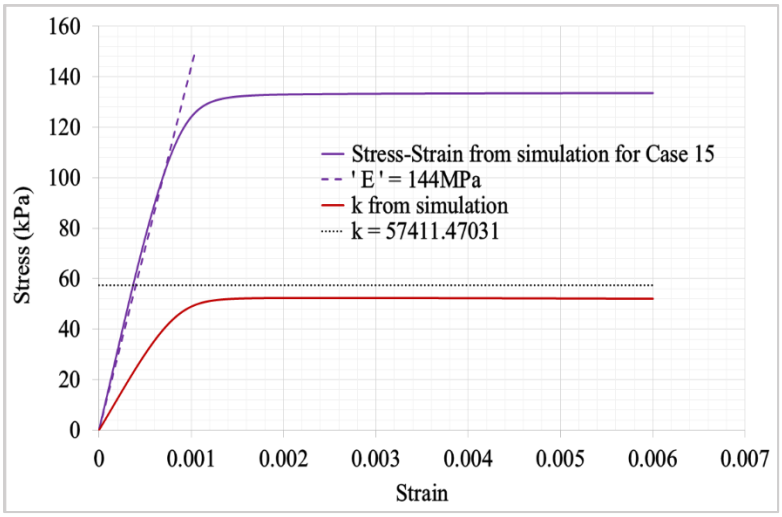


Figure 5.16: Verification of simulation result analytical results for case 15.

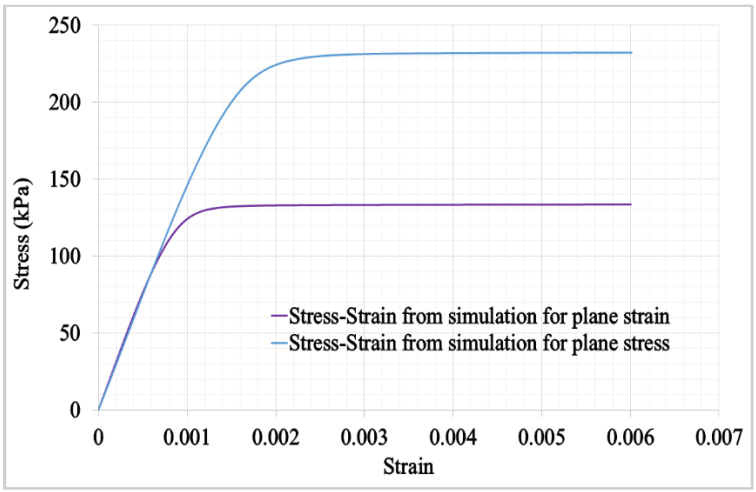
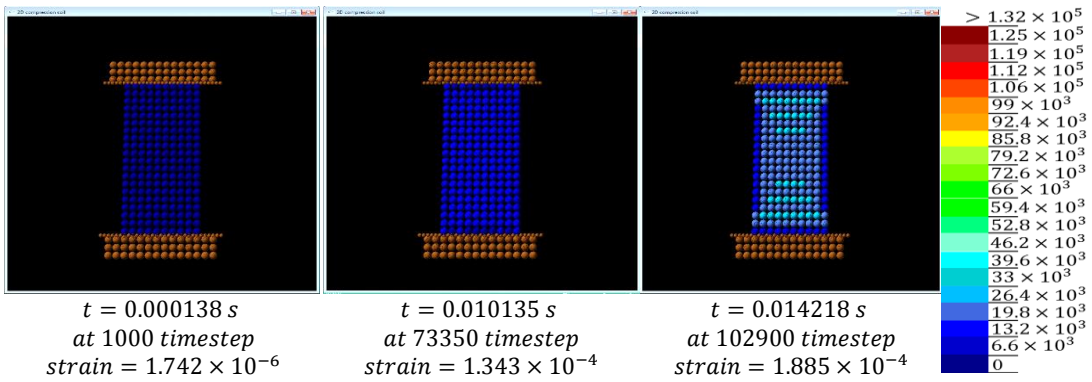


Figure 5.17: Comparison of plane strain and plane stress results for Soil with E=144MPa.



$t = 0.000138\ s$ $at\ 1000\ timestep$ $strain = 1.742 \times 10^{-6}$

$t = 0.010135\ s$ $at\ 73350\ timestep$ $strain = 1.343 \times 10^{-4}$

$t = 0.014218\ s$ $at\ 102900\ timestep$ $strain = 1.885 \times 10^{-4}$

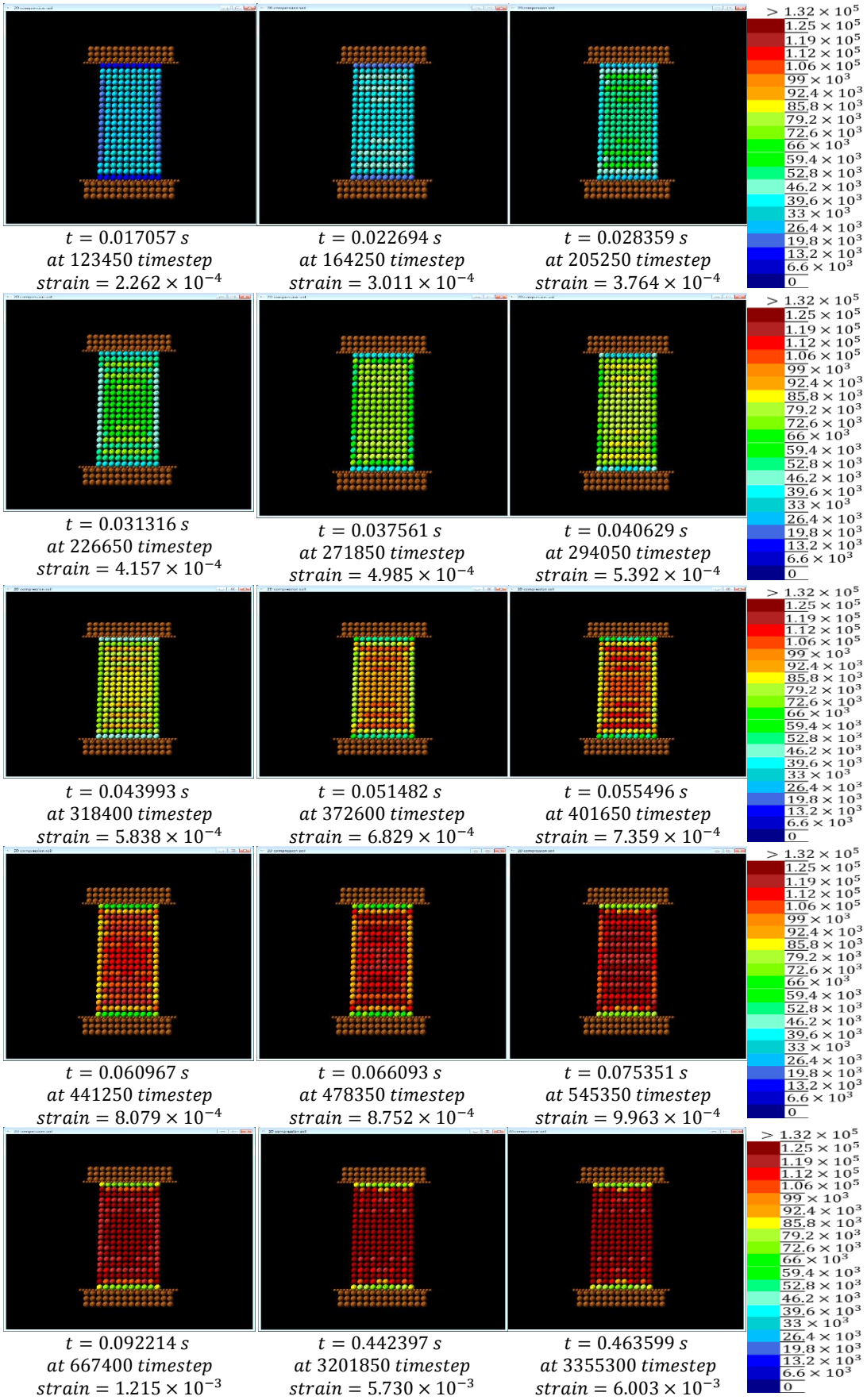


Figure 5.18: Vertical stress distribution at various time-steps for case 15.

5.5.3 Results obtained using Drucker-Prager constitutive model with associated flow rule

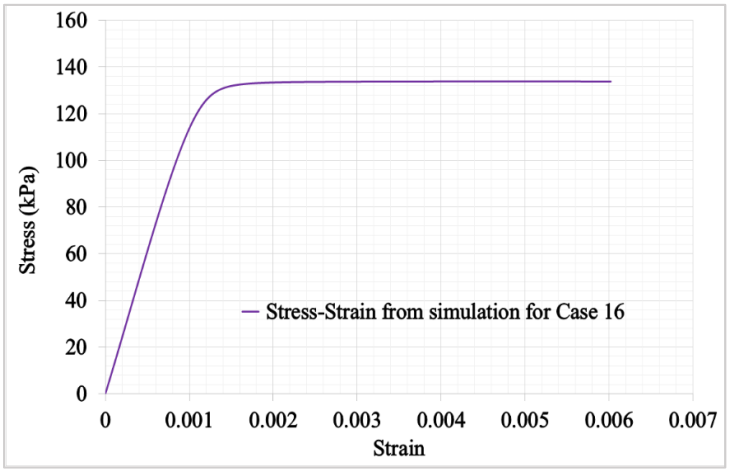


Figure 5.19: Average vertical stress-strain curve from simulation for case 16.

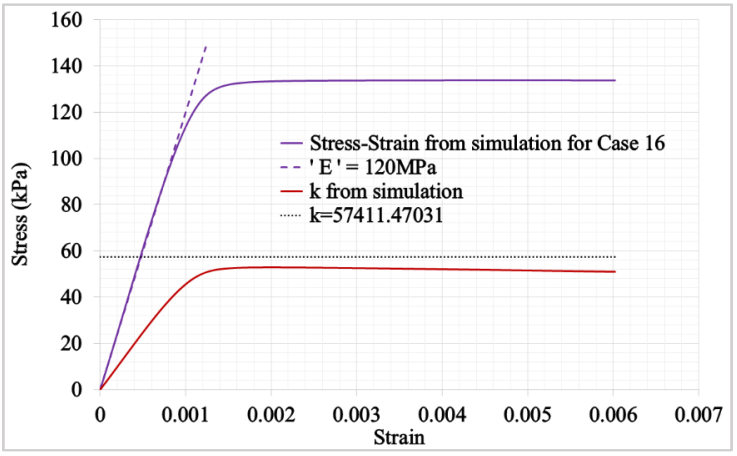


Figure 5.20: Verification of simulation result with analytical result for case 16.

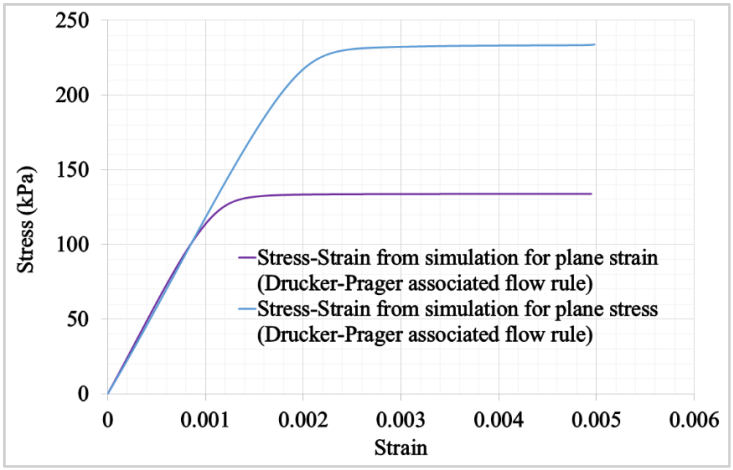
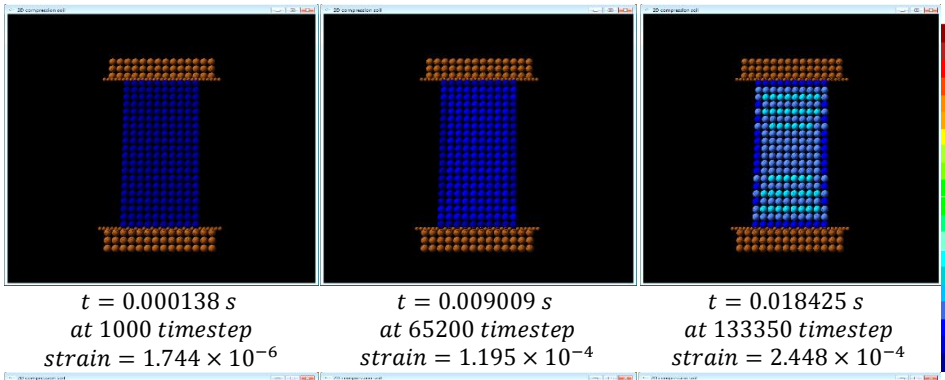
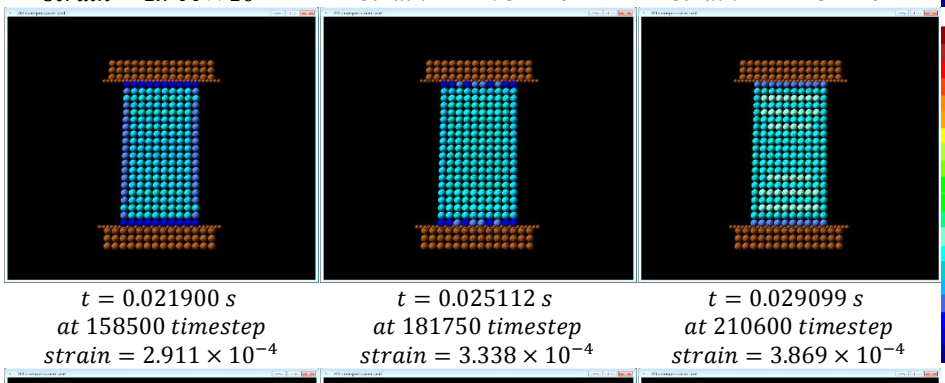


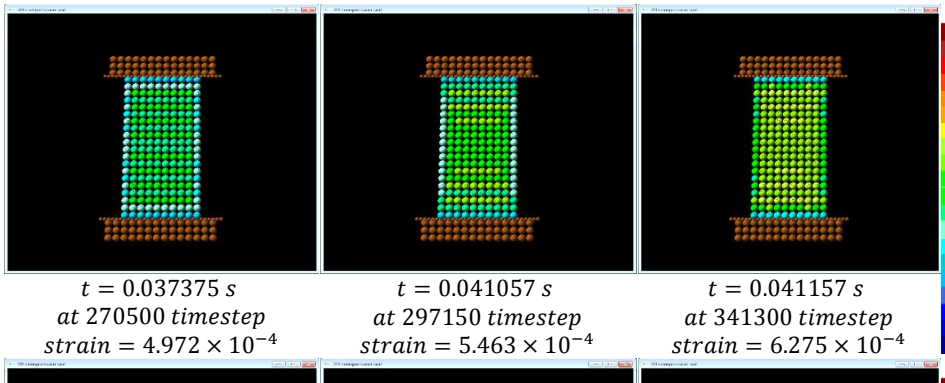
Figure 5.21: Comparison of plane strain and plane stress results for soil with E=120MPa.



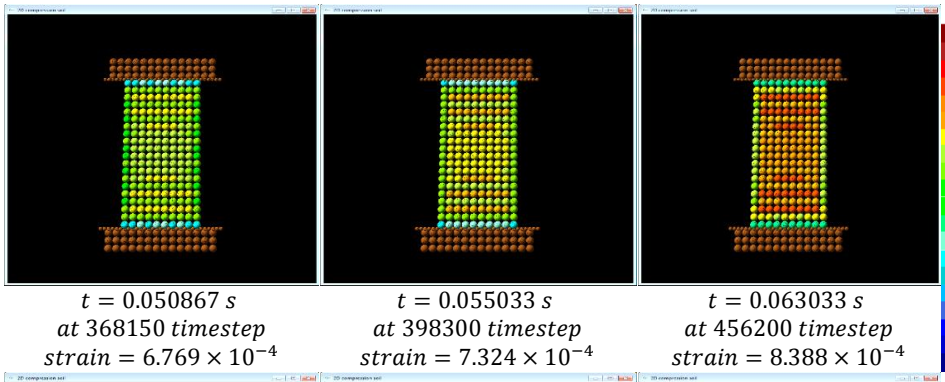
$t = 0.000138\ s$ $t = 0.009009\ s$ $t = 0.018425\ s$
at 1000 *timestep* *at* 65200 *timestep* *at* 133350 *timestep*
$strain = 1.744 \times 10^{-6}$ $strain = 1.195 \times 10^{-4}$ $strain = 2.448 \times 10^{-4}$



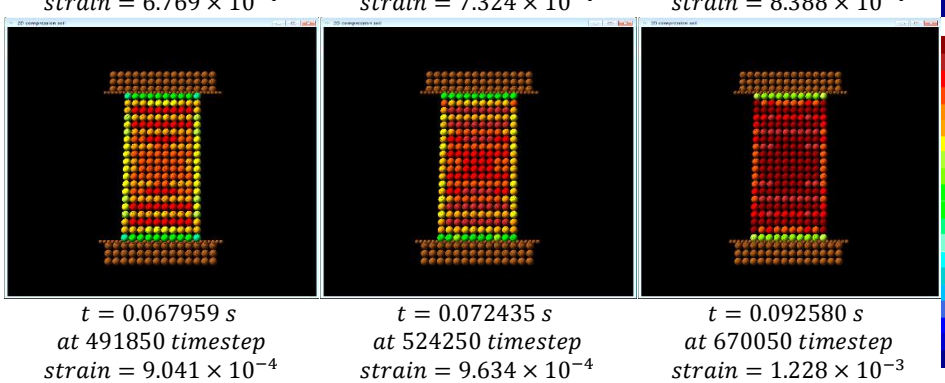
$t = 0.021900\ s$ $t = 0.025112\ s$ $t = 0.029099\ s$
at 158500 *timestep* *at* 181750 *timestep* *at* 210600 *timestep*
$strain = 2.911 \times 10^{-4}$ $strain = 3.338 \times 10^{-4}$ $strain = 3.869 \times 10^{-4}$



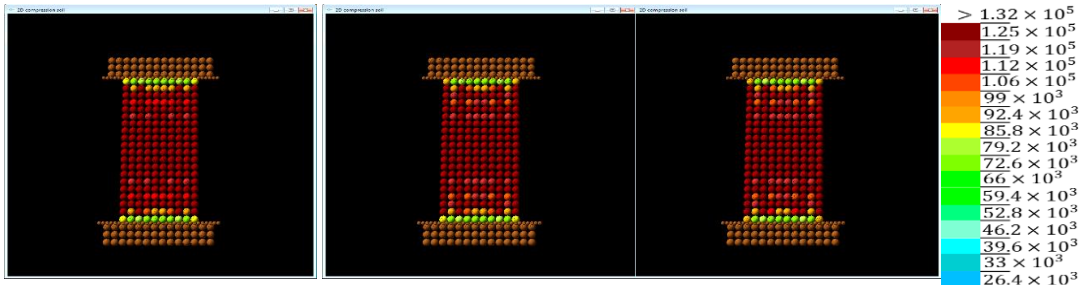
$t = 0.037375\ s$ $t = 0.041057\ s$ $t = 0.041157\ s$
at 270500 *timestep* *at* 297150 *timestep* *at* 341300 *timestep*
$strain = 4.972 \times 10^{-4}$ $strain = 5.463 \times 10^{-4}$ $strain = 6.275 \times 10^{-4}$



$t = 0.050867\ s$ $t = 0.055033\ s$ $t = 0.063033\ s$
at 368150 *timestep* *at* 398300 *timestep* *at* 456200 *timestep*
$strain = 6.769 \times 10^{-4}$ $strain = 7.324 \times 10^{-4}$ $strain = 8.388 \times 10^{-4}$



$t = 0.067959\ s$ $t = 0.072435\ s$ $t = 0.092580\ s$
at 491850 *timestep* *at* 524250 *timestep* *at* 670050 *timestep*
$strain = 9.041 \times 10^{-4}$ $strain = 9.634 \times 10^{-4}$ $strain = 1.228 \times 10^{-3}$



$t = 0.223993\ s$ at 1621150 *timestep* $strain = 2.922 \times 10^{-3}$

$t = 0.288159\ s$ at 2085550 *timestep* $strain = 3.745 \times 10^{-3}$

$t = 0.466086\ s$ at 3373300 *timestep* $srain = 6.020 \times 10^{-3}$

Figure 5.22: Vertical stress distribution at various time-steps for case 16.

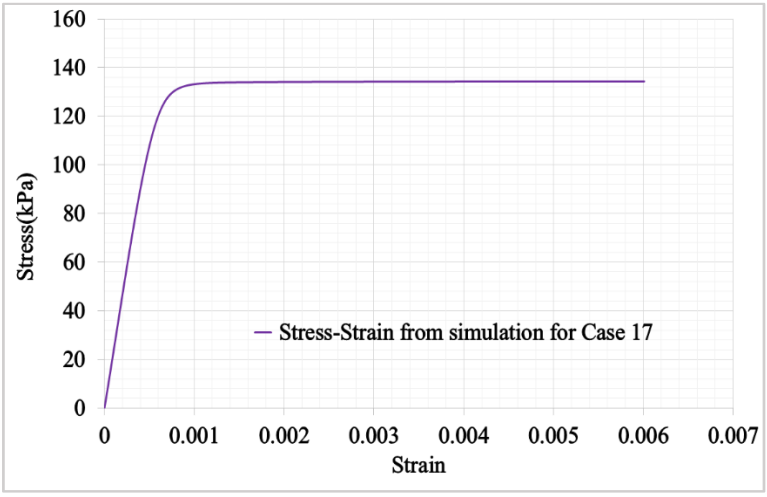


Figure 5.23: Average vertical stress-strain curve from simulation for case 17.

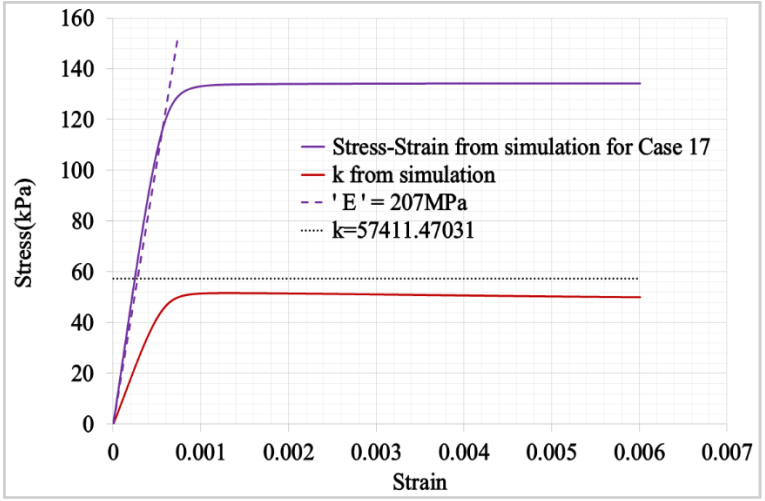


Figure 5.24: Verification of simulation result with analytical results for case 17.

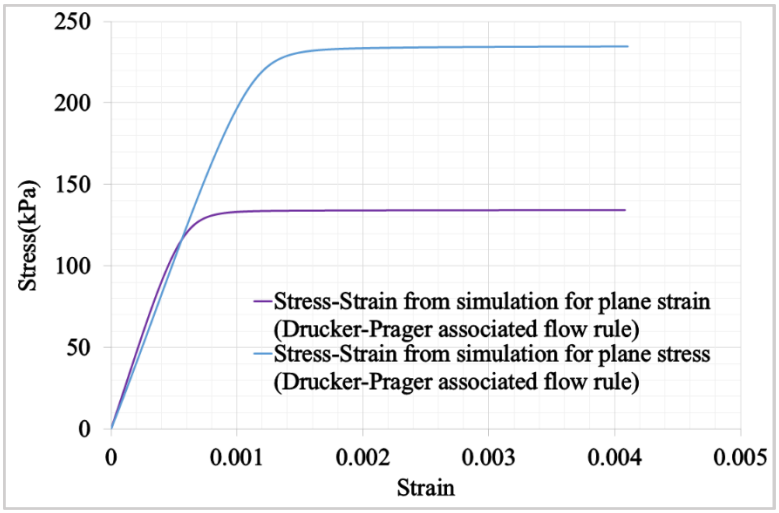
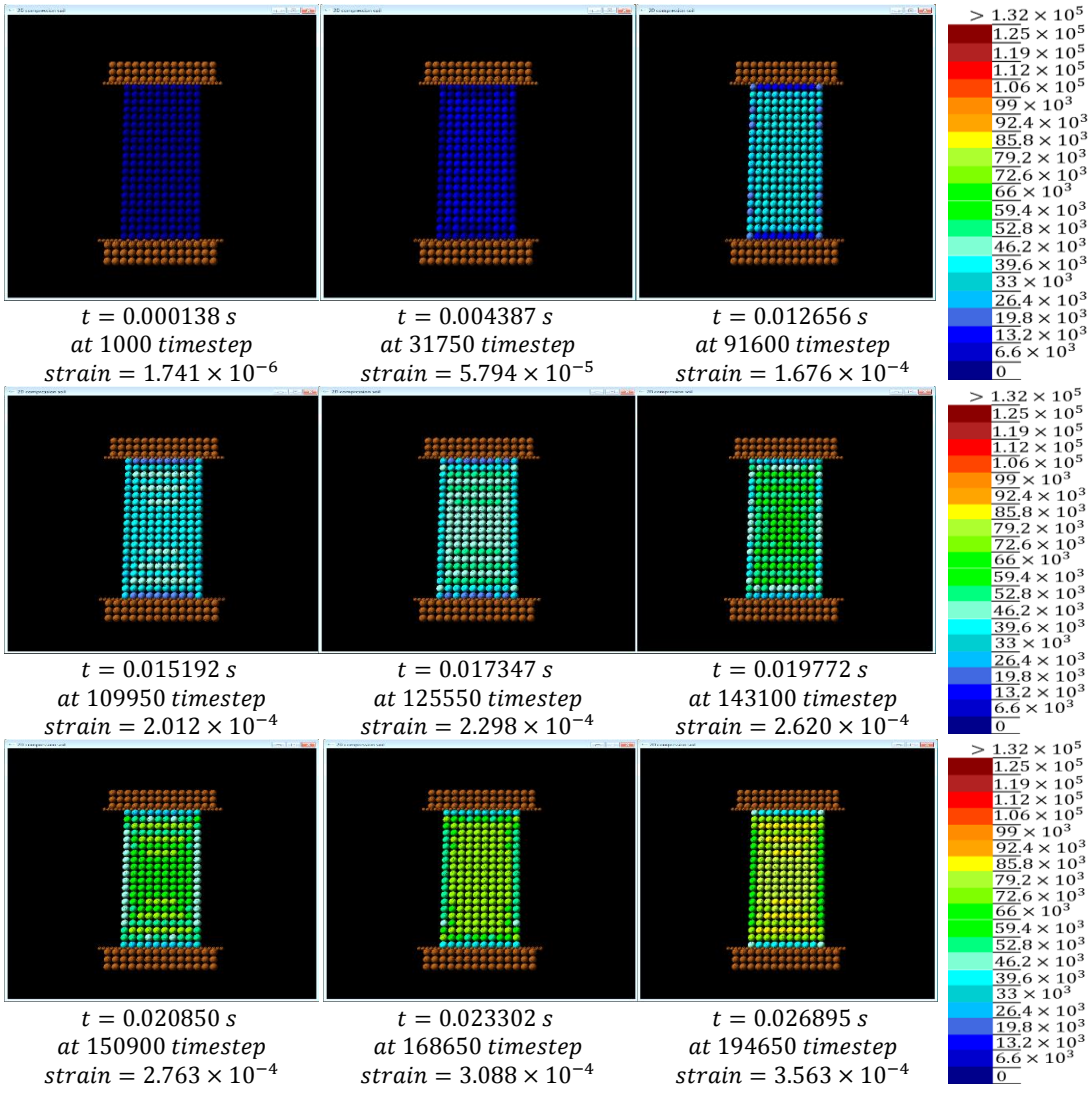


Figure 5.25: Comparison of plane strain and plane stress results for Soil with E=207MPa.



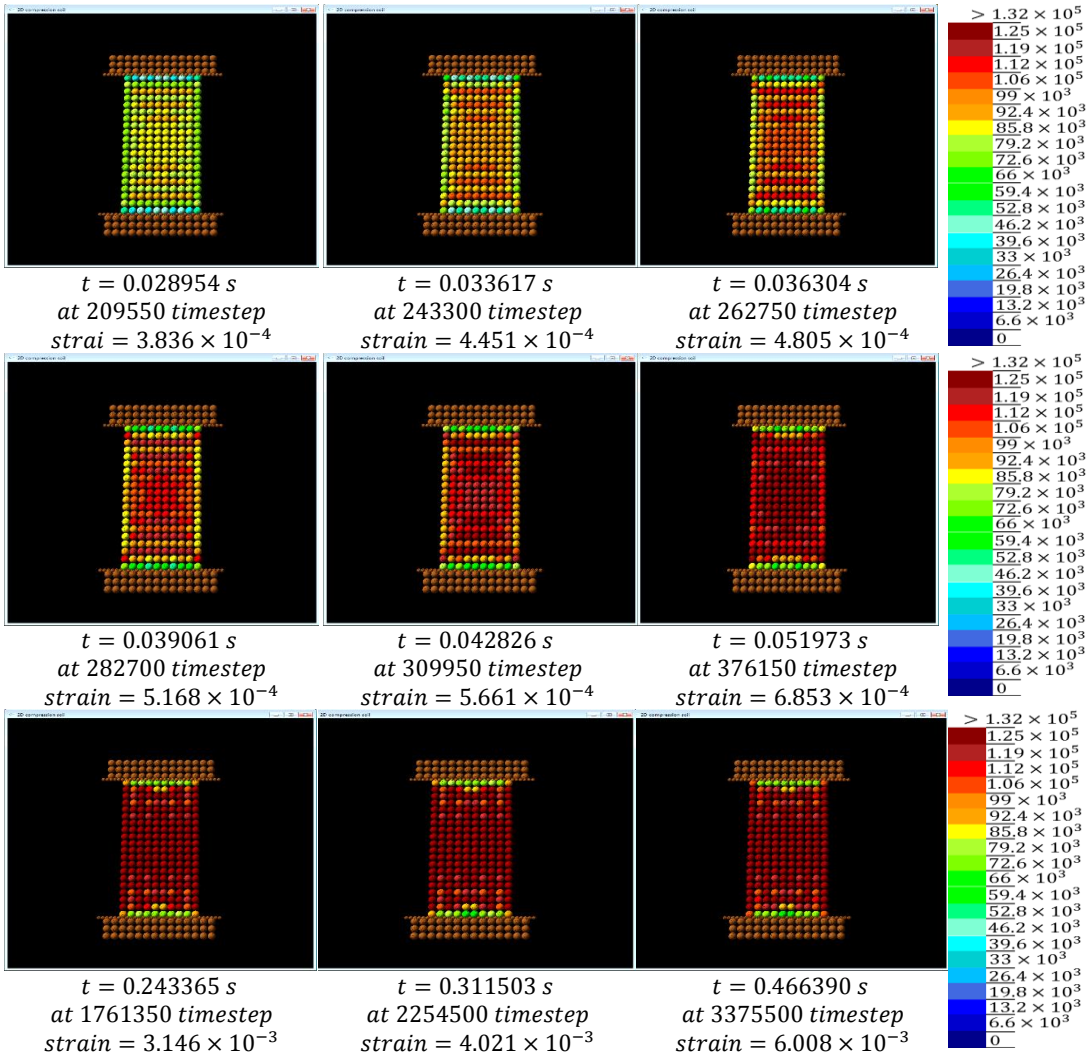


Figure 5.26: Vertical stress distribution at various time-steps for case 17.

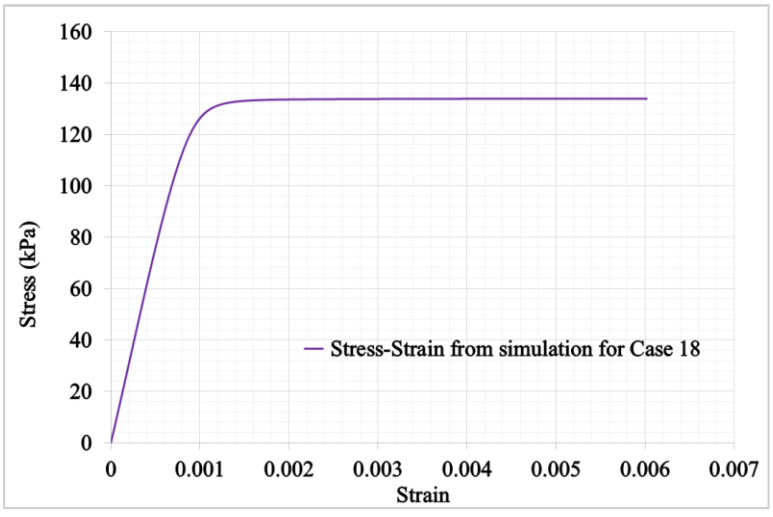


Figure 5.27: Average vertical stress-strain curve from simulation for case 18.

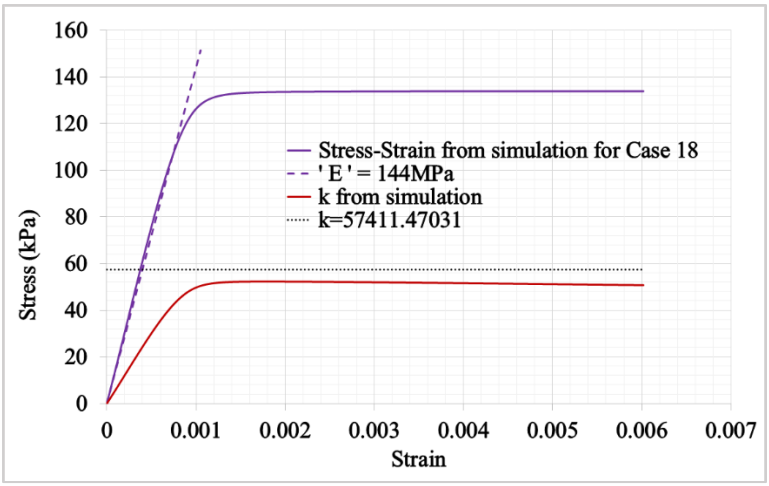


Figure 5.28: Verification of simulation result with analytical result for case 18.

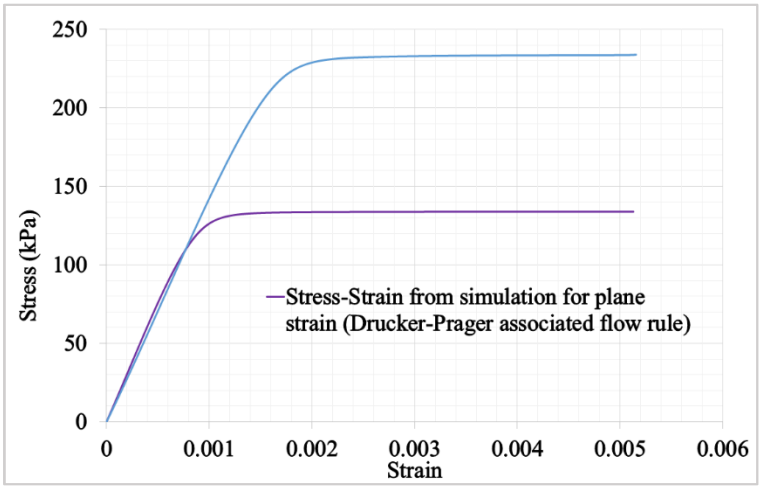
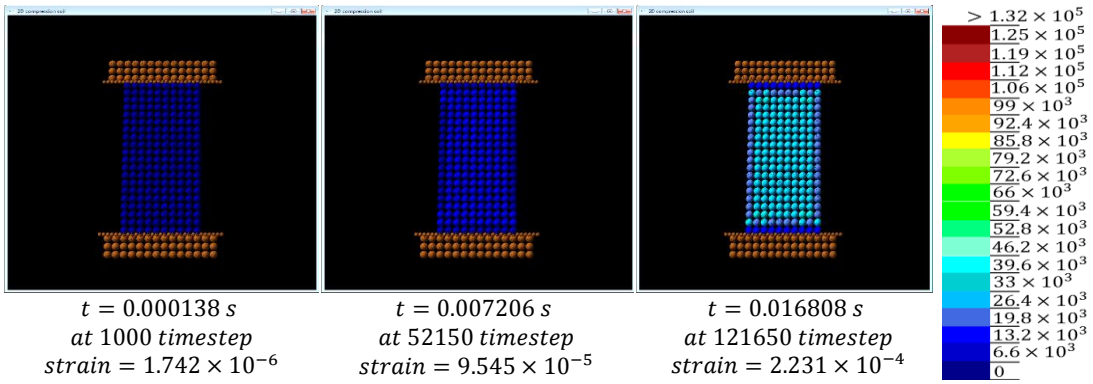


Figure 5.29: Comparison of plane strain and plane stress results for Soil with E=144MPa.



$t = 0.000138\ s$ $at\ 1000\ timestep$ $strain = 1.742 \times 10^{-6}$

$t = 0.007206\ s$ $at\ 52150\ timestep$ $strain = 9.545 \times 10^{-5}$

$t = 0.016808\ s$ $at\ 121650\ timestep$ $strain = 2.231 \times 10^{-4}$

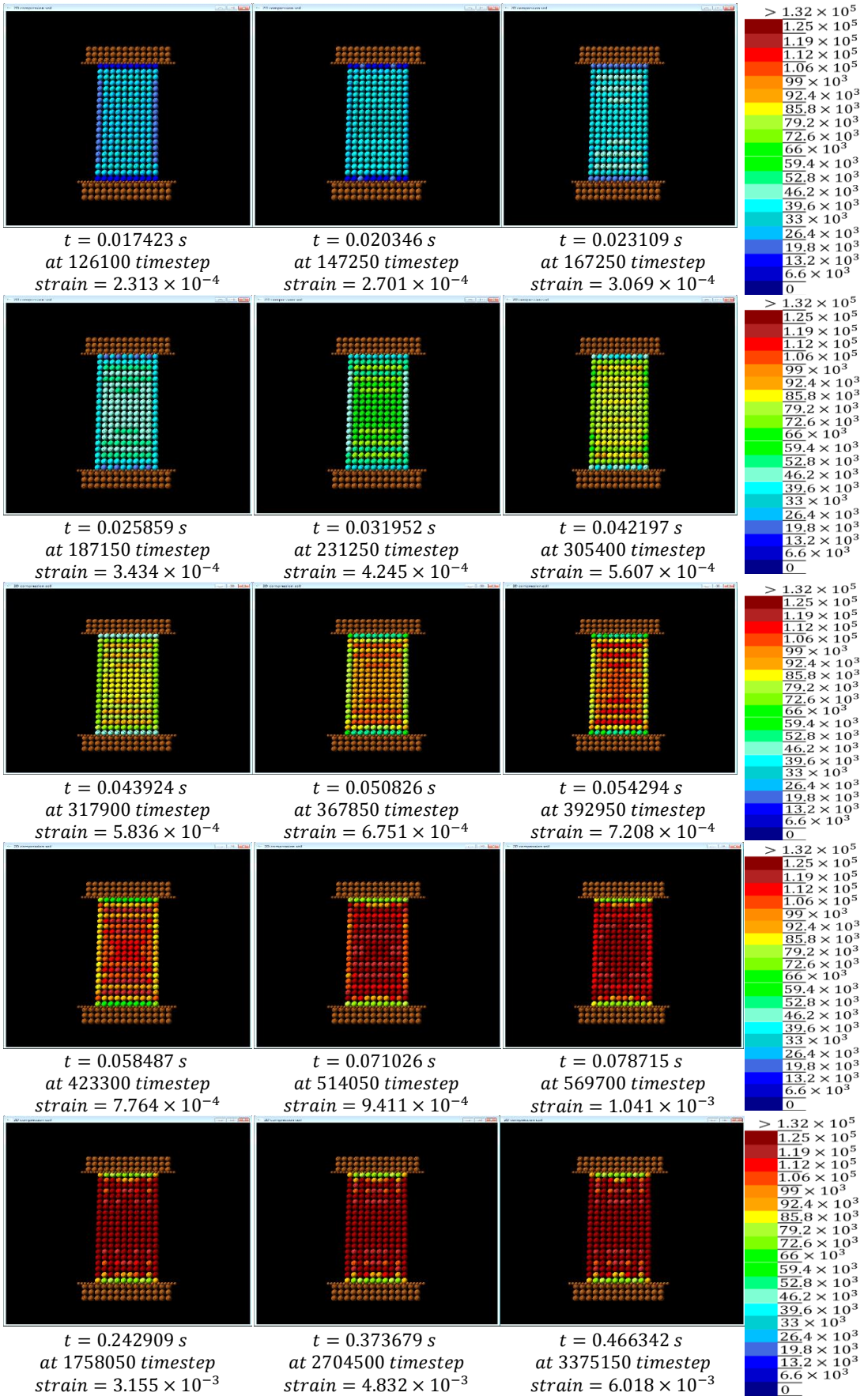


Figure 5.30: Vertical stress distribution at various time-steps for case 18.

5.5.4 Comparison between Drucker-Prager non-associated and associated flow rule

This section presents the comparison between the stress-strain responses obtained from Drucker-Prager SPH model with non-associated flow rule and the results from Drucker-Prager SPH model with associated flow rule. As such the comparison between cases 13-16, 14-17 and 15-18 are presented as follows:

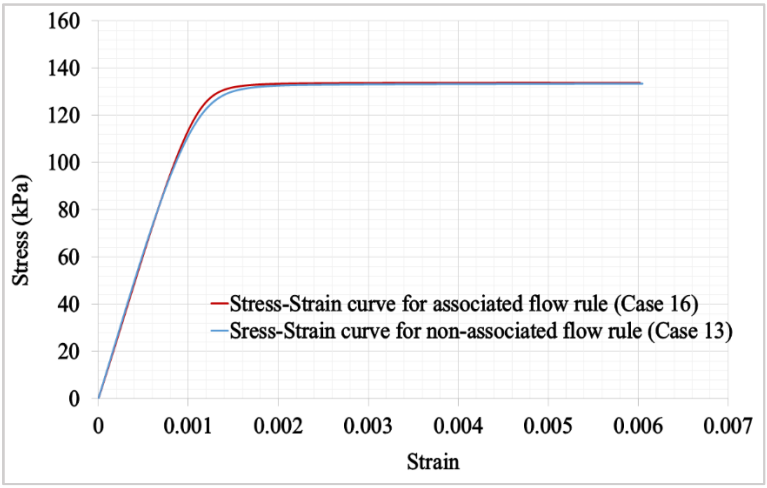


Figure 5.31: Comparison between associated and non-associated flow for soil with E=120MPa.

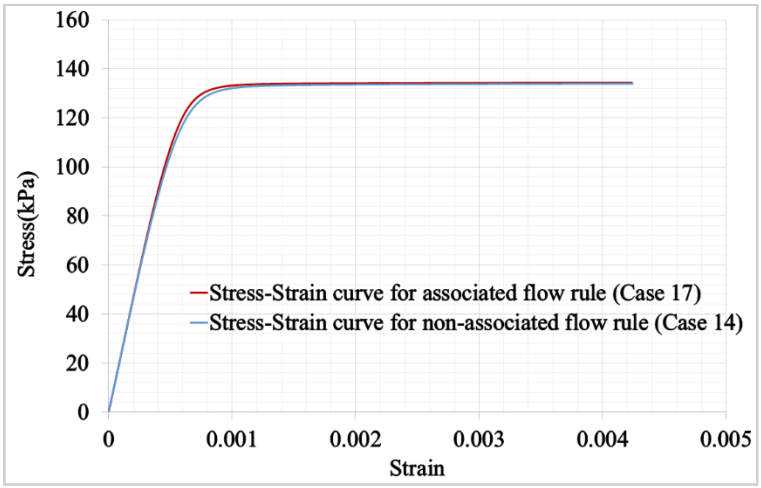


Figure 5.32: Comparison between associated and non-associated flow for soil with E=207MPa.

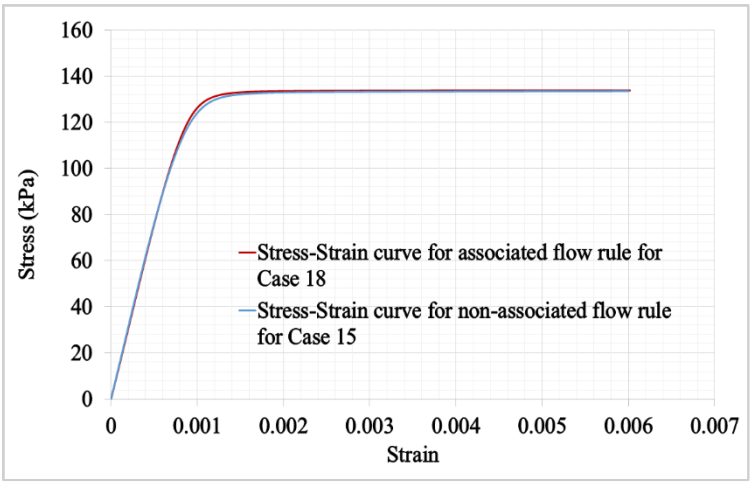


Figure 5.33: Comparison between associated and non-associated flow for soil with E=144MPa.

5.6 Discussion

Figures 5.2, 5.3, 5.5, 5.8, 5.12, 5.16, 5.20, 5.24 and 5.28 present the simulated results with analytical solutions for cases 10-18 respectively. It can be observed from the figures that the simulated stresses at elasticity correlate well with 'E' for all considered cases. This is proven by the achievement of accuracy levels greater than 94% as listed in Table 5.2. Furthermore, numerically obtained stresses at plasticity using the proposed von-Mises constitutive model agree well with 'Y' in Figures 5.2, 5.3 and 5.5 with greater than 95% of accuracy. For cases 10-12, the accuracy level of stresses at plasticity using the plane strain model is similar to the accuracy level obtained employing the plane stress model. However, as shown in Table 5.2, the plane-stress model well simulated the elasticity than the plane-strain model. Therefore, even though the developed plane-strain von-Mises elastic-perfectly plastic model provides

accurate solutions to sufficiency, the von-Mises elastic-perfectly plastic model for plane stress condition better simulated the scenario than the plane-strain model. This is further apparent from Figures 5.2, 5.3 and 5.5.

Table 5.2: Accuracy for plane strain models.

Case number	Constitutive Model	Figure Number	Accuracy with analytical solution for plane-strain		Accuracy with analytical solution for plane-stress	
			Elastic section	Plastic section	Elastic section	Plastic section
10	von-Mises	5.2	98.868%	95.507%	98.663%	95.512%
11	von-Mises	5.3	97.472%	96.006%	99.832%	95.729%
12	von-Mises	5.5	96.993%	95.515%	98.873%	95.636%
13	DP-non-ass	5.8	97.446%	92.247%	97.335%	92.340%
14	DP-non-ass	5.12	94.708%	90.163%	98.488%	90.229%
15	DP-non-ass	5.16	96.369%	91.256%	97.693%	91.233%
16	DP-ass	5.20	98.070%	91.875%	98.774%	93.452%
17	DP-ass	5.24	95.135%	90.049%	98.773%	92.423%
18	DP-ass	5.28	95.083%	90.899%	99.112%	92.023%

Similarly, 'k from simulation' for cases 13-18 using Drucker-Prager constitutive model correlate well with input value of k in Figures. 5.8, 5.12, 5.16, 5.20, 5.24, and 5.28 with accuracy greater than 90% as shown in Table 5.2. It can be observed from Table 5.2, the plane stress Drucker-Prager model provide better estimation of elasticity than the plane strain model. Furthermore, greater the Poisson's ratio, the larger the deviation of the plane strain model from the plane stress model in predicting the elastic behaviour of the material. This is evident in Figures 5.9, 5.13, 5.17,

5.21, 5.25 and 5.29. Even though both models were similar in predicting the plastic behaviour as shown in Table 5.2, plane-stress model simulated the scenario well due to its increased accuracy in predicting the elastic behaviour. Therefore, it is obvious that the proposed SPH models for plane stress condition are more accurate in predicting the stresses and strains in material under uniaxial compression than the plane-strain models.

Furthermore, graphical images were generated to acquire insight into vertical stress distribution in particles at various time steps. These are presented in Figures. 5.1, 5.4, 5.6, 5.10, 5.14, 5.18, 5.22, 5.26 and 5.30 for cases 10-18 respectively. This provide knowledge on the development of stresses of materials under compression and allows to match the individual images in Figures 5.1, 5.4, 5.6, 5.10, 5.14, 5.18, 5.22, 5.26, 5.30 with the corresponding strain values in Figures 5.2, 5.3, 5.5, 5.7, 5.11, 5.15, 5.19, 5.23, 5.27 respectively.

Moreover, Figures 5.31, 5.32 and 5.33 demonstrate the comparison between stress-strain plots achieved using Drucker-Prager associated flow rule and non-associated flow rule. It is obvious that the associated flow rule is much closer to the analytical solutions. This further clarifies that soil with cohesion is accurately modelled with means of associated flow rule than the non-associated flow rule.

All-in-all, the proposed elastic-perfectly plastic constitutive models for both von-Mises and Drucker-Prager yield criterion for plane strain condition well predicted the stress-strain behaviour of materials under uniaxial compression with greater than 90% of accuracy. Despite its

reduced accuracy in current application in comparison to the plane-stress models, the plane strain models are reliable engineering tools for the estimation of stresses and strains in plane strain structures.

5.7 Conclusion

A new approach has been proposed for the development of von-Mises and Drucker-Prager constitutive models under plane strain condition. The main feature of these plane strain models is their development in a complete two-dimensional SPH framework. This is ensured by deriving the elastic section of the constitutive equation with means of 2D Hooke's law and by employing two-dimensional formulas of failure criterion. Furthermore, unlike most of the SPH formulation in solid mechanics, hydrostatic pressure has been computed with means of constitutive equation. According to our knowledge, this combined approach has been performed for the first time in 2D SPH framework.

Simulated results using the proposed von-Mises SPH model agreed well with analytical solutions for all the considered materials comprising Poisson's ratio 0.12, 0.35 and 0.45. These selected values of Poisson's ratio ensured the capability of the developed model to accurately simulate any given material within the Poisson's ratio range 0-0.45. Similarly, developed Drucker-Prager SPH models for associated and non-associated flow rule successfully simulated the stress-strain response of materials comprising Poisson' ratio 0.15, 0.3 and 0.23. This allows the models'

applicability range to be extended to materials with Poisson's ratio within the range 0-0.3. Hence, the developed constitutive models embrace wider range of applications.

Moreover, in comparison to plane stress and plane strain models, plane stress models simulated the stresses and strains of materials with greater precision than the plane strain models. Even though the plane strain models are slightly less accurate than the plane stress models for current application, the results achieved have emphasized the ability of the proposed constitutive models in effectively simulating plane strain problems. Therefore, the developed models are promising tools for engineers to model plane strain scenarios in engineering applications. The models could be further examined on large deformation applications. As such, the following chapter presents the development of a SPH model comprising the proposed plane strain constitutive models to a complex scenario.

Chapter 6
Development of smooth particle hydrodynamics for the analysis of stresses around jack-in-pile

6.1 Introduction

The development of SPH model is presented in this chapter for simulating the soil stress field around jack-in pile. Maximum effort is made in the numerical model for reducing the simplified assumptions in previous studies. As such, by utilizing the proposed von-Mises constitutive model for plane strain condition, pile is represented as an elastic-perfectly plastic material and is modelled from the soil surface to the final penetration depth. The proposed Drucker-Prager constitutive model with non-associated flow rule for plane strain condition is employed for modelling the soil material during installation. In addition, soil-pile interaction is considered. The model is developed with the ability of providing graphical representation of both horizontal and vertical soil stress distribution at various instants of the simulation. Results acquired using the proposed SPH model are compared with previously published experimental results by Jardine et al. [15], [18] and numerically simulated results by Lorenzo et al. [28] for validation.

6.2 Experimental set up of jack-in pile installation

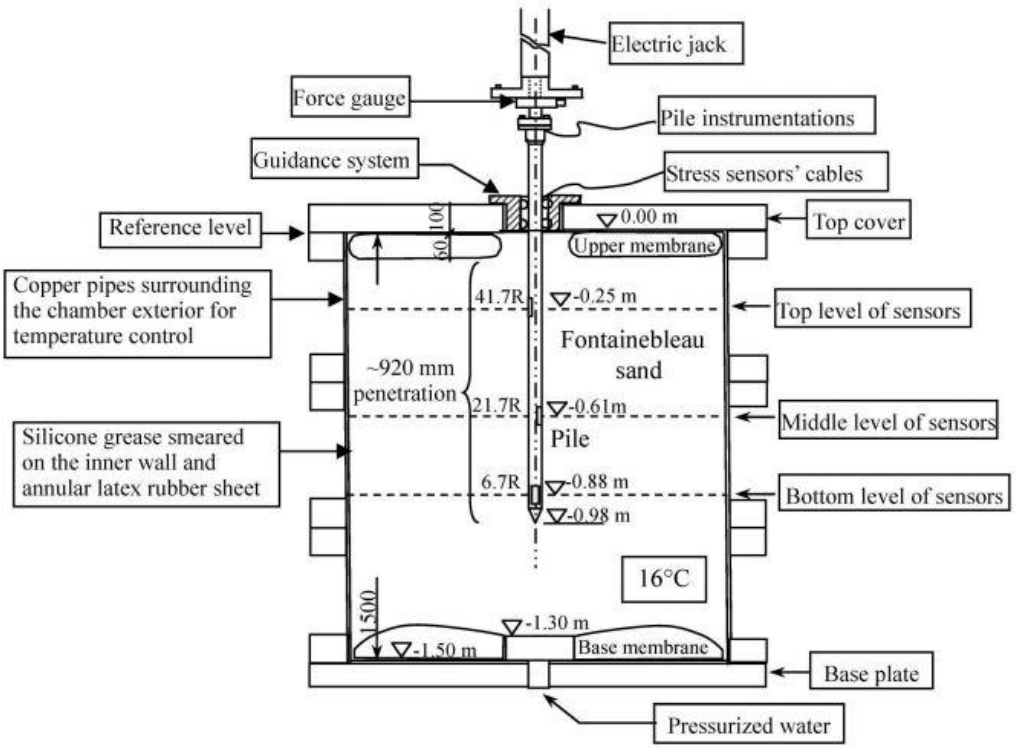


Figure 6.1: Experimental setup for measuring stresses in soil [15].

Jardine et al. [15] introduced an experimental method for acquiring reliable stress measurements within a calibration chamber. In the test, the calibration chamber with diameter 120cm and height 150cm was filled with sand deposit as illustrated in Figure 6.1. Pressurised membrane with diameter 50cm and thickness 6cm were placed between the surface of the sand and top cover to provide a surcharge pressure of 150kPa. A mini ICP stainless steel pile with diameter 3.6cm and length 140cm was jacked in for 92 cycles. Each cycle consisted a 1cm push and a pause where the pile was completely unloaded. The authors recorded radial stresses at point

55cm depth and 3.6cm distance from the pile axis at every push and pause as shown in Figure 6.2.

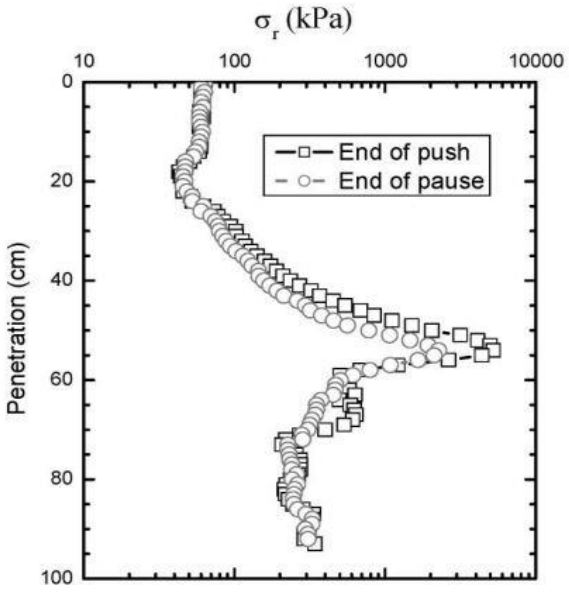


Figure 6.2: Radial stress at point 55cm depth and 3.6cm radial distance from the pile axis [15].

Furthermore, utilizing similar experimental setup, Jardine et al. [18] measured stresses at two additional points in the soil mass. Both horizontal and vertical stresses were recorded for points at radial distances 5.4cm and 14.4cm at a depth of 70cm from the soil surface. Figure 6.3a and b illustrate the vertical stress values obtained for both points at every push and pause respectively. Similarly, radial stresses recorded at both points are shown in Figure 6.4a and b for every push and pause respectively.

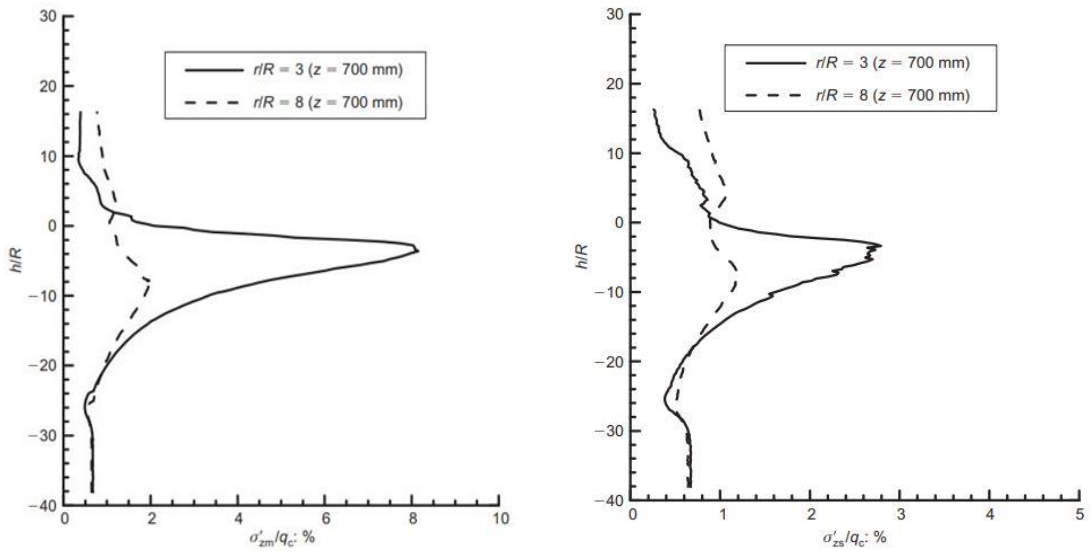


Figure 6.3: Vertical stress at end of: (a) push; (b) pause [18].

In present chapter, the SPH model is developed to numerically simulate the experimental values of stresses presented in Figures 6.2, 6.3a, 6.3b, 6.4a and 6.4b. This is performed to verify the developed SPH model to analyse stresses in soil around jack-in pile.

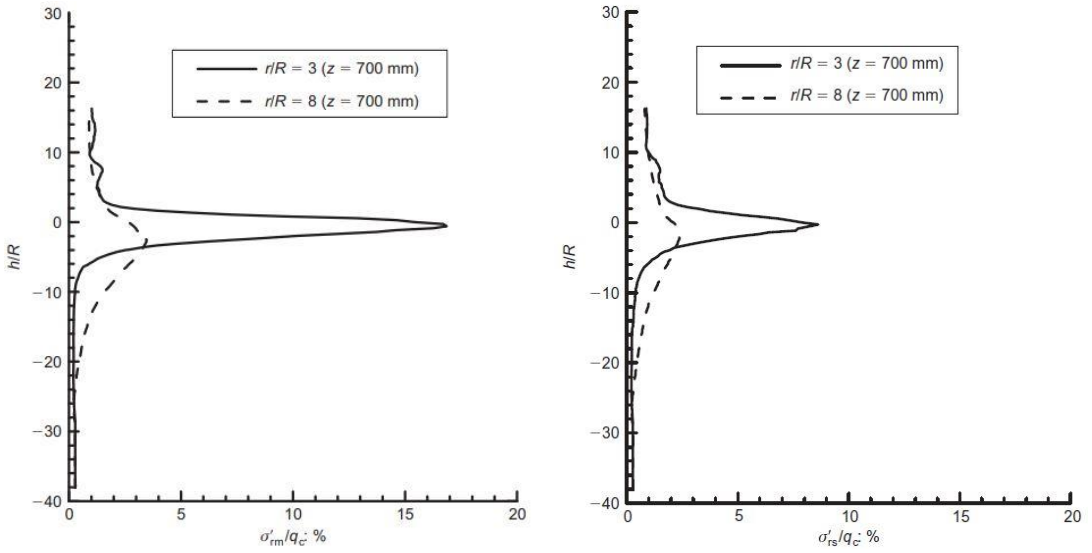


Figure 6.4: Radial stress at end of: (a) push; (b) pause [18].

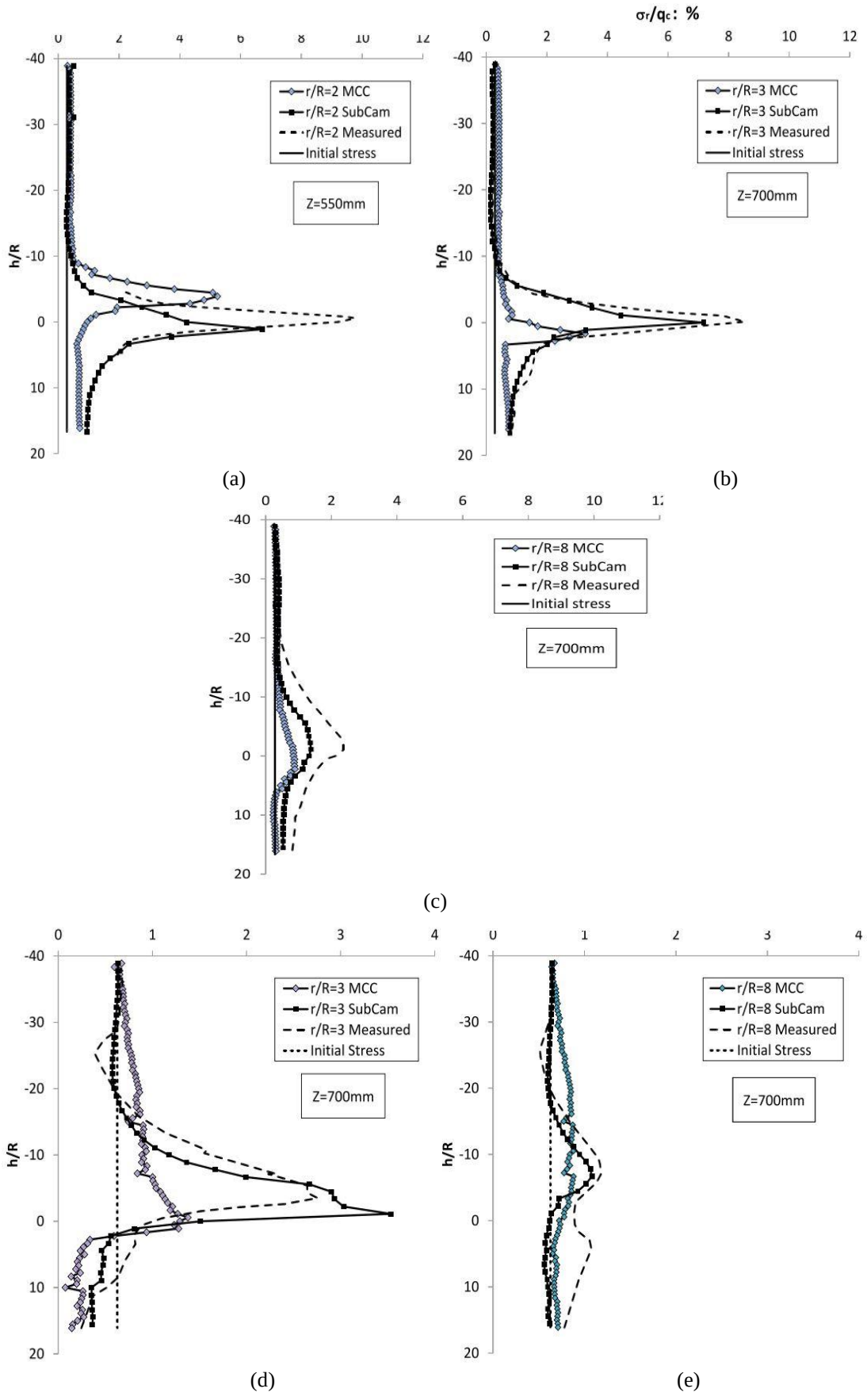


Figure 6.5: (a)-(c) horizontal stress; (d)-(e) vertical stress during jack-in pile installation [29].

Furthermore, Lorenzo et al. [28] assessed the capacity of Material Point Method (MPM) with means of MCC and SubCam constitutive models to numerically simulate the experimental results presented in Figures 6.2, 6.3 and 6.4. The numerical approach achieved similar trends as the experimental solutions. However, the values were far from the experimental results as shown in Figure 6.5. Nevertheless, among the constitutive models, SubCam better simulated the scenario.

Therefore, in addition to the SPH model's verification with experimental solutions, current chapter involves the comparison study between the proposed SPH model and MPM numerical model. As such, the numerically simulated results from SPH model are compared with the results obtained using MPM for points at r/R=2, 55cm depth and r/R=3, 70cm depth. This is performed to validate current model's capability in simulating the stresses in soil around jack-in pile in comparison to the MPM numerical model.

6.3 Numerical model for jack-in pile installation

The numerical simulation of jack-in pile installation is performed under plane strain condition. In summation, 2156 SPH particles are employed to model the scenario. As illustrated in Figure 6.6, 1360 and 39 particles are adopted to form the soil and pile respectively. 237 virtual particles are used to create chamber's boundary line. Jack-in motion is generated with means of the mass placed on the pile. This comprises 24 particles. 56 and 80

number of particles are employed to form the pressure membrane and top lid respectively. Finally, 360 particles are adopted to create the solid boundary to represent the chamber. Both the horizontal and vertical boundaries of the chamber were assumed fixed. The surcharge pressure (vertical stress) of 150kPa was applied to every particle of the membrane and horizontal stress of these particles were considered to be zero throughout the simulation.

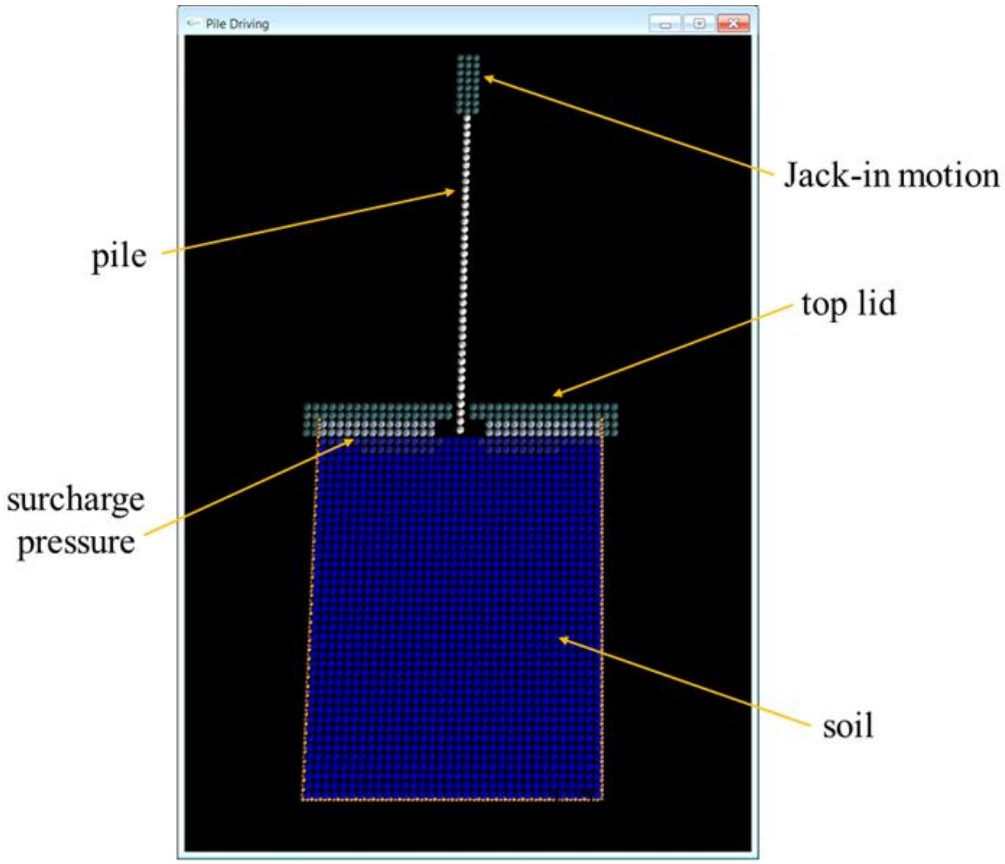


Figure 6.6: SPH particle arrangement for Jack-in pile installation.

Table 6.1 summarizes the mechanical properties of soil taken from Jardine et al. [15] and Lorenzo et al. [28]. The pile employed in the

experimental investigation of soil stresses around jack-in pile is of stainless steel material [15]. Therefore, for completing the parameters of the proposed model, the standard mechanical properties of grade 304 stainless steel are adopted in present study. Taking into consideration of the parameters listed in Table 6.1 in the numerical simulation, the pile is modelled from the soil surface to the final depth of 92cm. A constant vertical velocity of 10mm/sec is applied to the mass on top of the pile to induce jack-in motion. Every 1cm push is followed by a pause. The motion is repeated until the pile achieved its final depth of 92cm. The pile is assumed frictionless and initial stresses in soil were assumed to be zero.

Table 6.1: Material parameters for jack-in pile simulation.

Parameters	Soil	Pile
v	0.3	0.265
ρ	720 kg/m^3	8060 kg/m^3
ϕ	32.80	-
σ_y	-	205MPa
h	0.06	0.06

Figure 6.7 presents the SPH algorithm for modelling stresses in soil around jack-in pile. The algorithm begins with the initialization of every particle in the system. Subsequently, particles in the system searches neighbouring pairs. This is followed by the computation of field variables such as density, internal forces, artificial viscosity, external force, artificial

stress, stress and strain of particles. Thereafter, following the momentum calculation, physical properties are updated. If the updated values of stresses fall beyond the yield surfaces, the proposed tension cracking treatment and stress scaling back pressure are activated for eliminating the incorrect modelling of the physics. Finally, the updated particle positions, vertical and horizontal soil stress distributions are stored on data files and made visually available at every time-step using OpenGL. As shown in Figure 6.7, this loop is repeated until the final step of the simulation.

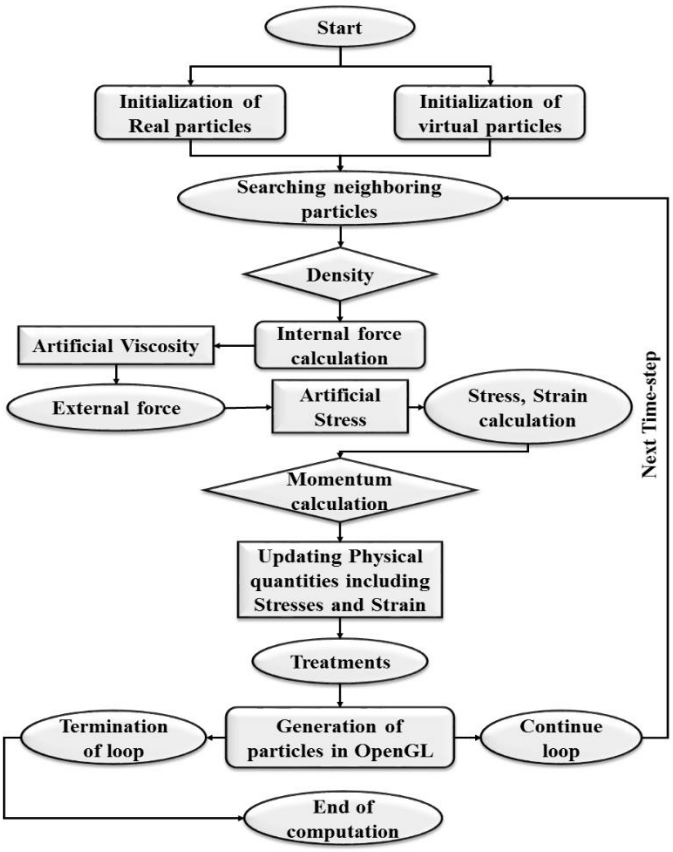


Figure 6.7: SPH algorithm for modelling jack-in pile installation.

SPH model comprising the algorithm in Figure 6.7 is developed from the SPH source code introduced by Liu and Liu. [77]. The model is developed using C++ language incorporating OpenCL and OpenGL programme codes. OpenCL is employed to parallelize the programme code for expediting the simulation and OpenGL is adopted for generating graphical images of the phenomenon. The developed programme is compiled and executed using command prompt in windows operating system. OpenGL window is updated at every time-step providing updates of soil stress distribution throughout the installation of jack-in pile. This feature provides the capability to the SPH model for delivering graphical images of soil stress distribution at various pile penetration depths. All-in-all the output of the proposed model involves horizontal, vertical stress measurements at selected points within the soil mass and visual images of horizontal and vertical soil stress distribution throughout the installation.

6.4 Development of SPH model to simulate jack-in pile installation

Governing equations employed to model jack-in pile installation is similar to the governing equations presented in Section 4.4 except for the momentum equation and plane stress constitutive models. Jack-in pile installation is modelled under plane strain condition. Hence, the plane strain constitutive models introduced in chapter 5 for both von-Mises and Drucker-Prager yield criterion with non-associated flow rule are employed

to model pile and soil respectively. As such, Eqs. (5.27) and (5.28) are employed instead of Eqs. (4.44) to (4.46). Furthermore, momentum equation for current application varies from Eq. (3.49) due to the adoption of artificial viscosity and artificial stress method explained in Section 6.4.1. Apart from above, the methods essential for the completion of the numerical model are included from Sections 6.4.2 to 6.4.4.

6.4.1 Problem during simulation and solving techniques

Problems in SPH such as unphysical oscillation, stresses falling beyond the yield surface were experienced during the modelling of uniaxial compression of materials in chapter 4. These problems were also encountered during the modelling of jack-in pile installation. However, by utilizing the proposed tension cracking treatment and stress-scaling back pressure from chapter 4, the problem of stresses falling outside the yield surface is eliminated. Furthermore, the problem of unphysical oscillation is solved by adopting artificial viscosity. Detail information on these solution techniques are included in chapter 4. However, a brief explanation on these methods is provided in Section 6.4.1.1.

Apart from above problems, particles forming clusters and particle penetration were observed during the simulation of jack-in pile installation. Such problems are eliminated through the employment of artificial stress method and Lennard-Jones form discussed in Sections 6.4.1.2 and 6.4.1.3 respectively.

6.4.1.1 Artificial viscosity and treatments

Artificial viscosity discussed in Section 4.5.1 is employed in the simulation of the complex scenario. The treatment is achieved by introducing artificial viscosity into the momentum equation which is defined by Eq. (4.49). The constants β_Π and α_Π are assumed to be 1 for current application. The values of c considered for pile and soil are 5794 m/s and 600 m/s respectively.

During the modelling of jack-in pile installation, values of stresses were found to lie outside the yield surface. It should be highlighted that the developed formulas of tension cracking treatment and stress scaling backpressure introduced in Section 4.5.2 are common for both plane stress and plane strain condition. As such, both tension cracking treatment and stress-scaling backpressure proposed in Section 4.5.2 for both von-Mises and Drucker-Prager criterion are employed for current application to eliminate the problem of stresses falling outside the yield surfaces.

6.4.1.2 Artificial stress method

Modelling of jack-in pile installation involved the problem of tensile instability. Although the problem did not appear within the soil mass or pile at the initial stage of the simulation, tensile instability became apparent in pile when the pile was driven into further depths as shown in Figure 6.8.

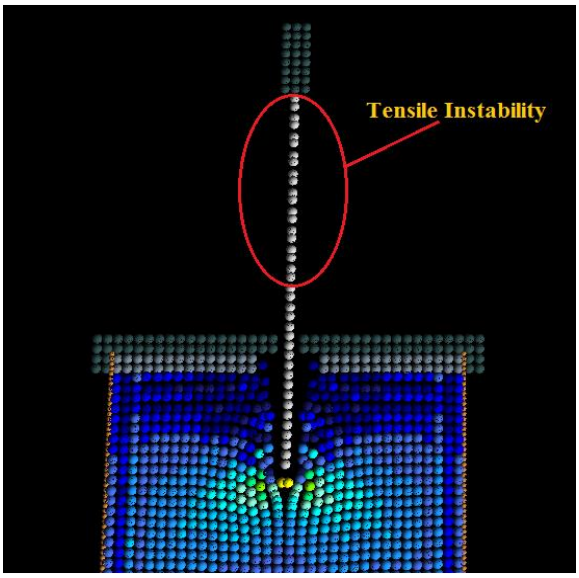


Figure 6.8: Tensile instability during jack-in pile installation.

Tensile instability is a generally encountered problem in SPH and occurs due to the rearrangement of particles into cluster formation. The behaviour affects the general flow of particles leading to imprecise solutions. Such instability is preventable through the employment of artificial stress method. The method was initially attended in-detail by Swegle et al. [157] for eliminating the tensile instability. Thereafter, many approaches have been introduced for solving the problem [126], [162]–[167]. Among the methods the most popular approach by Monaghan. [165] and Gray et al. [126] are employed in current application for treating the problem of tensile instability. This is achieved by involving the artificial stress term into the momentum equation as expressed by Eq. (6.1). The term functions when the separation of particles becomes lesser than the initial particle spacing. In such scenario, a repulsive force is generated in-between the particles for opposing the clumping behaviour.

$$\frac{Dv^{\alpha}}{Dt} = \sum_{j=1}^{N} m_j \left(\frac{\sigma_j^{\alpha\beta}}{\rho_j^2} + \frac{\sigma_i^{\alpha\beta}}{\rho_i^2} - \Pi_{ij}\delta^{\alpha\beta} + f_{ij}^{n}\left(R_i^{\alpha\beta} + R_j^{\alpha\beta}\right) \right) \frac{\partial W_{ij}}{\partial x_i^{\beta}} + F^{\alpha} \qquad (6.1)$$

where,

$$R_i^{xx} = cos^2\theta_i \acute{R}_i^{xx} + sin^2\theta_i \acute{R}_i^{yy}$$

$$R_i^{yy} = sin^2\theta_i \acute{R}_i^{xx} + cos^2\theta_i \acute{R}_i^{yy}$$

$$R_i^{xy} = sin\theta_i cos\theta_i \left(\acute{R}_i^{xx} - \acute{R}_i^{yy}\right)$$

$$\theta_i = \frac{1}{2} tan^{-1}\left(\frac{2\sigma_i^{xy}}{\sigma_i^{xx} - \sigma_i^{yy}}\right)$$

$\acute{R}_i^{yy}$

$$= \begin{cases} \varepsilon \dfrac{\acute{\sigma}_i^{yy}}{\rho_i^2} & if\, \acute{\sigma}_i^{yy} > 0 \\ 0 & else \end{cases} \quad replacing\ y\ by\ x\ leads\ to\ evaluation\ of\ \acute{R}_i^{xx}$$

$$\acute{\sigma}_i^{xx} = \sigma_i^{xx} cos^2\theta_i + 2\, sin\theta_i cos\theta_i \sigma_i^{xy} + sin^2\theta_i \sigma_i^{yy}$$

$$\acute{\sigma}_i^{yy} = \sigma_i^{xx} sin^2\theta_i - 2\, sin\theta_i cos\theta_i \sigma_i^{xy} + cos^2\theta_i \sigma_i^{yy}$$

$$f_{ij} = \frac{W_{ij}}{W(\Delta x, h)}$$

where θ_i is the angle of rotation. $\acute{\sigma}_i^{xx}$, $\acute{\sigma}_i^{yy}$ and $\acute{R}_i^{xx}$, $\acute{R}_i^{yy}$ are the stress and artificial stress components along principal coordinates. R_i^{xx} and R_i^{yy} represent the artificial stress components in original coordinates. Δx is initial particle spacing and h is the smoothing length which are assumed to be constant. The values of n and ε are considered to be 2.55 and 0.5 respectively.

6.4.1.3 Soil-pile interaction

As proposed by Bui et al. [87], the general SPH particle summation method is applied to the soil particles interacting with pile particles and vice-versa despite the differences in its properties. A coupling condition is employed at the interface between the pile and soil as:

$$v_s^{\alpha} = v_{pile}^{\alpha} \tag{6.2}$$

$$\sigma_s^{\alpha\beta} = \sigma_{pile}^{\alpha\beta}$$

However, during soil-pile interaction soil particles penetrating the pile particles became apparent as illustrated in Figure 6.9. As such, for eliminating this adverse behaviour, similar to Bui et al. [87], Lennard-Jones form is adopted [168]. The method provides a repulsive force to the soil particle preventing penetration when distance between the interacting pairs becomes lesser than the initial particle spacing r_0. This is expressed as:

$$F(r) = D\left(\left(\frac{r_0}{r_{ij}}\right)^{n_1} - \left(\frac{r_0}{r_{ij}}\right)^{n_2}\right)\frac{x_{ij}}{r_{ij}^2} \qquad r_{ij} < r_0 \tag{6.3}$$

where x_{ij} is the separation between interacting pairs, D is the problem dependent parameter which scales with the largest velocity. n_1 and n_2 are considered to be 4 and 2 respectively.

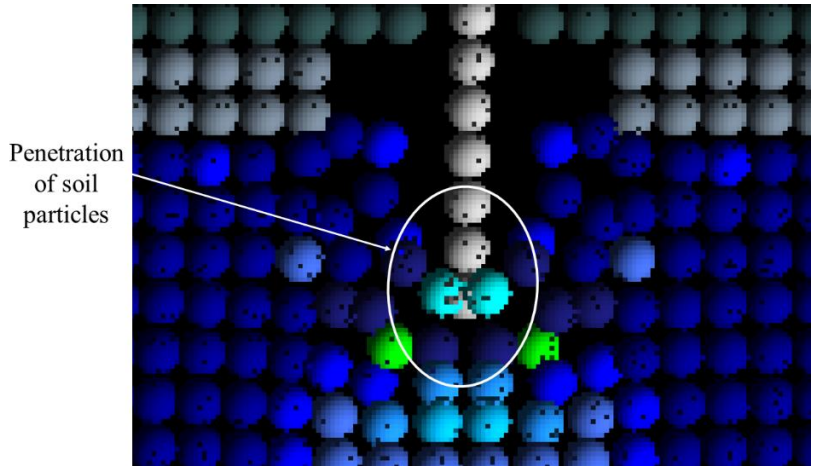


Figure 6.9: Soil particle penetrating through pile particle.

6.4.2 Method of stress computation

Both vertical and horizontal stresses at selected points within the soil mass are computed at every time-step of the simulation utilizing the expression:

$$\sigma_p^{\alpha\beta} = \frac{\sum_{\mathrm{PA}=1}^{N} \sigma_{PA}^{\alpha\beta}}{niac} \tag{6.4}$$

where, PA is the neighbouring particle within the smoothing length h, $niac$ is the total number of neighbouring pairs and $\sigma_p^{\alpha\beta}$ is the stress at a given point.

6.4.3 Boundary condition

As mentioned in Section 4.6, real particles near solid boundary lack neighbouring particles. Therefore, summation approach over the neighbourhood leads to inaccurate solutions [139]. Furthermore, particle

penetration through the boundary was experienced during the modelling of pile installation process. Therefore, the method introduced by Morris et al. [145] for no-slip boundary condition is employed to represent the solid boundary.

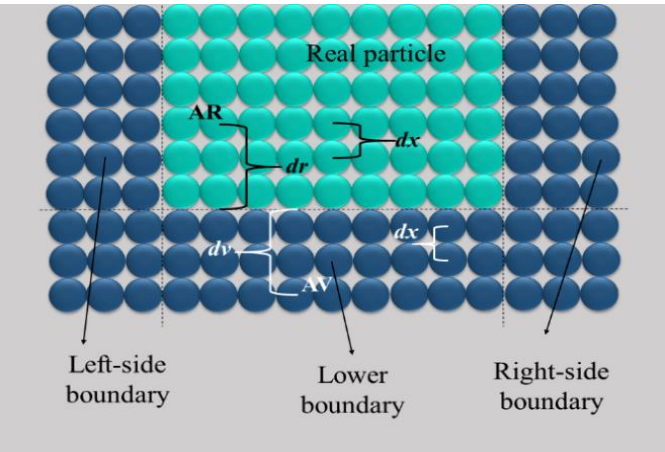


Figure 6.10: Solid boundary particles.

As illustrated in Figure 6.10, three rows of virtual particles are utilized to generate the lower, left and right-side of the solid boundaries. Dark blue represents the boundary particles and lighter shade represents the real particles. Boundary particles hold similar parameters as of real particles except for the stress tensor and velocity. The particles are spaced equally to the real particles. They contribute to the stress and velocity computation of real particles as stated by Morris et al. [145]. However, density of boundary particles is not evolved in present study.

Eqs. (4.71) to (4.73) are employed for no-slip boundary condition. β_{max} = 1.5 is adopted for current application. Furthermore, Morris et al. [145] treatment alone was insufficient for handling the boundary

condition. During the simulation of jack-in pile installation, penetration of particles was observed through the solid boundaries. Moreover, as mentioned in Section 4.6, it is essential to assign stress to solid boundary particles for the estimation of stress on real particles. As such, Eq. (4.74) proposed in Section 4.6 is adopted for preventing particle penetration through the assignment of stress on boundary particles.

6.4.4 Time integration

Leap-Frog method explained in Section 4.7 is adopted in the simulation of jack-in pile installation. As such Eqs. (4.75) to (4.79) are incorporated in the model for solving the SPH formulations.

6.5 Results and discussion

Figures 6.12a-b and 6.12c-d present the simulated radial stresses at specific points in the soil mass at the end of each push and pause respectively. The experimental values produced by Jardine et al. (2009, 2013b) are included in these figures. The numerical peak stresses shown in these figures using the proposed SPH model correlate well with the experimental peak stress proving 82-85% of accuracy as presented in Table 6.2. The proposed model simulates these peak values at depths closer to the experimental depths at which the peak stresses are experienced. This is proven through the achievement of accuracy levels greater than 98% as

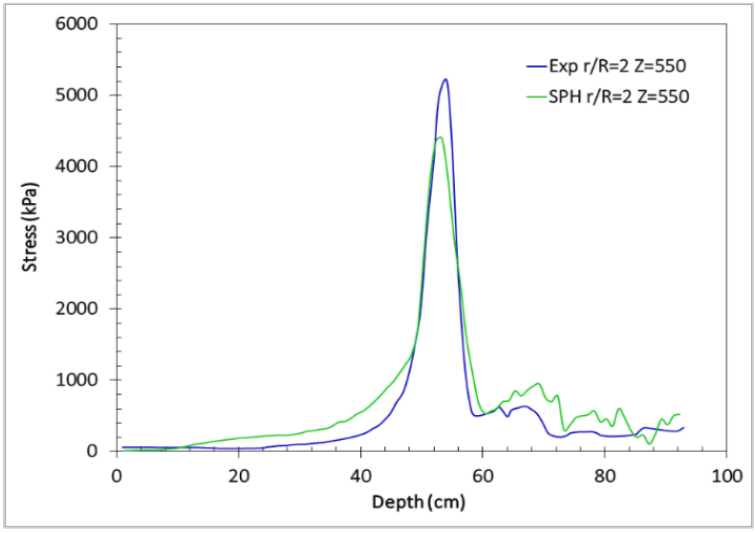
shown in Table 6.2. It can be observed from Figure 6.11 that the radial stress peak when the pile tip is slightly above the measuring point. Thereafter, the stress values decrease with pile penetration. The stresses obtained for r=2R is greater than those for r=3R, exposing the propensity of decrease in stresses with the increase in horizontal distance from the pile axis.

Table 6.2: Comparison between experiment and SPH results.

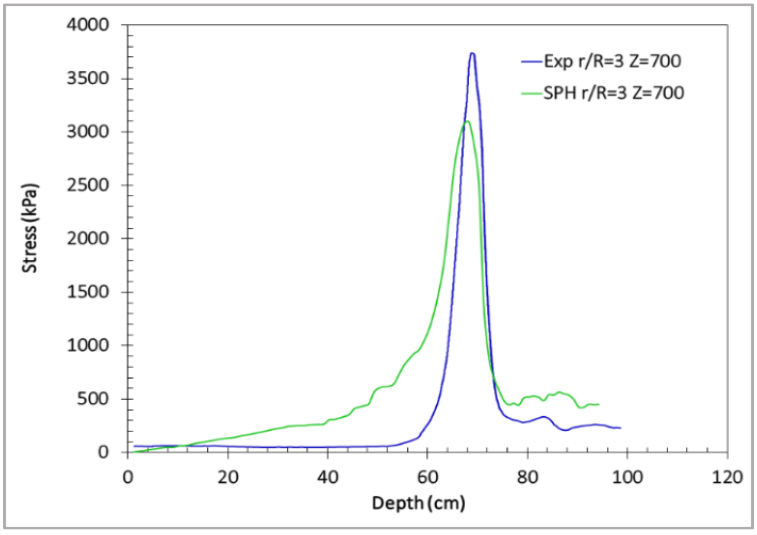
Stress point	At the end of	Figure No	Maximum Stress			Depth		
			Exp (kPa)	SPH (kPa)	Error (%)	Exp (cm)	SPH (cm)	Error (%)
r/R=2,Z=550	push	6.12a	5213.42	4394.23	15.7	54.1	53.3	1.5
r/R=3,Z=700	push	6.12b	3742.08	3095.19	17.3	68.9	68.3	0.9
r/R=2,Z=550	pause	6.12c	2275.85	1874.89	17.6	54.0	54.3	0.5
r/R=3,Z=700	pause	6.12d	1907.49	1574.37	17.5	69.6	70.3	1.0
r/R=3,Z=700	push	6.13a	1815.98	2094.37	15.3	63.5	64.3	1.3
r/R=3,Z=700	pause	6.13b	619.39	703.05	11.9	64.0	64.3	0.5

Figures 6.12a and 6.12b show vertical stresses at the end of each push and pause at a specific point in the soil mass. The measured values published by Jardine et al. [18] and simulated values using the proposed SPH model are presented. Similar to radial stresses, the vertical stress peaked just before passing the level of measuring sensor and over predicted the measured value by 15.3% at push and 11.9% at pause as illustrated in Table 6.2. The maximum value was observed at a depth of 64.3cm during

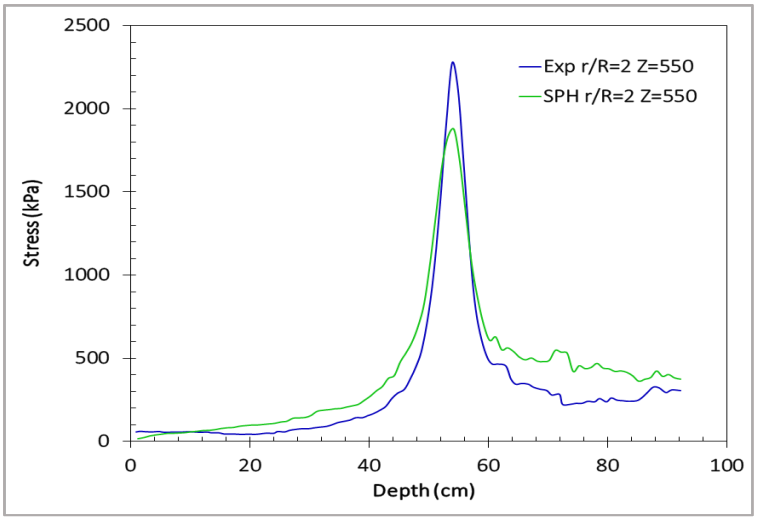
both push and pause with 1.3% and 0.5% of error from the respective measured values as presented in Table 6.2. Stress reduced as the penetration increased beyond the level of stress sensor. In average, the simulated results had similar trend as the measured graphs.



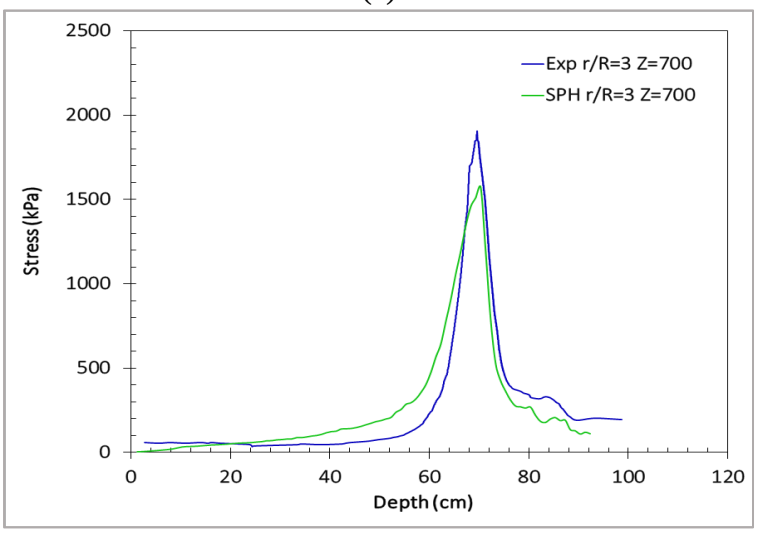
(a)



(b)



(c)



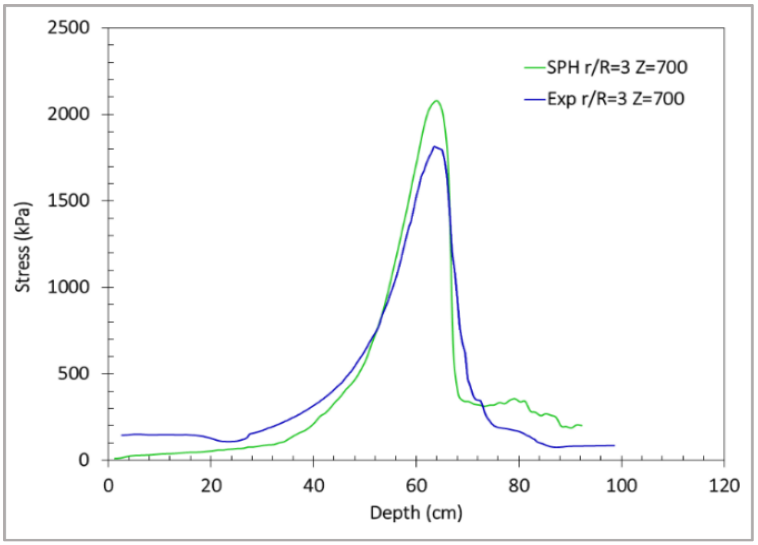
(d)

Figure 6.11: Radial stress during jack-in pile installation at the end of each: (a) push; (b) push; (c) pause; (d) pause.

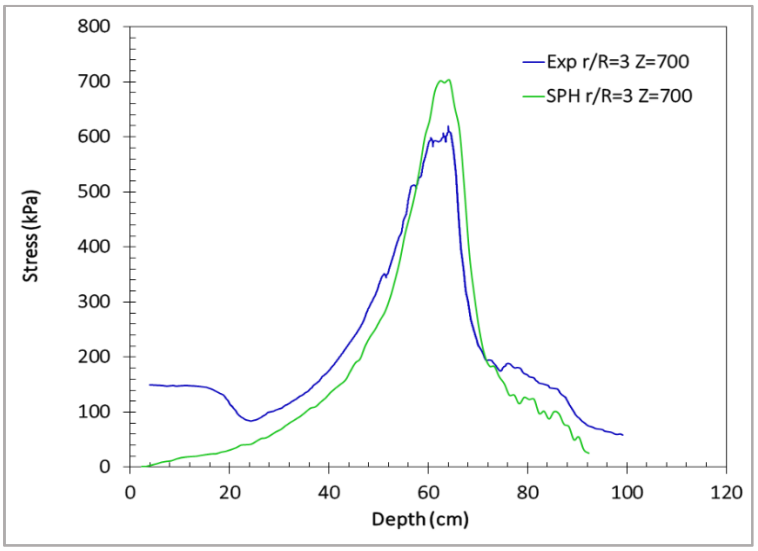
In consideration to the literature, the previous numerical models have provided visual images of stress distribution only at a certain depth of pile penetration. However, in present study, with means of OpenGL, visual images of both horizontal and vertical stress contours were obtained from start to finish at several depths of pile penetration as presented in Figures 6.14 and 6.15 respectively. It is apparent from Figure 6.14 that the highest values of radial stresses are experienced at the pile toe and spreads

in a bulb shape on either side of the pile. Stress contours increase with the increase of pile penetration. It can be observed that the stress distribution from in-situ test results published by Henke & Grabe. [21] varies from small scale centrifuge test results presented in this chapter. However, the stress distribution pattern matches the results provided for a centrifuge test involving the modelling of pile penetration by Dijkstra et al. [30]. The change in stress distribution from in-situ test to centrifuge test may be due to the boundary condition imposed by the chamber. When the horizontal stress approaches the boundary, the stress begins to distribute vertically from the concentrated area at the boundary. This allows distribution of horizontal stress to upper and lower regions as shown in Figure 6.13 at depths greater than 35cm. Therefore, due to the absence of chamber boundaries this scenario may not be experienced in the in-situ test results.

Similarly, Figure 6.14 presents vertical stress distribution at various depths of pile penetration. It is apparent that the highest values of vertical stresses are experienced at the pile toe. Vertical stresses spread in an arch shape towards downward direction. This is obvious from Figures 6.15a and 6.15b. However, as the vertical stress contour approaches the boundary, the arch pattern slightly varies due to boundary conditions. Pressurized membrane generated vertical stresses in soil on either side of the pile as shown in Figure 6.14f. Eventually it can be observed that the vertical stresses from pile and membrane combines and spread to remaining regions of the chamber.



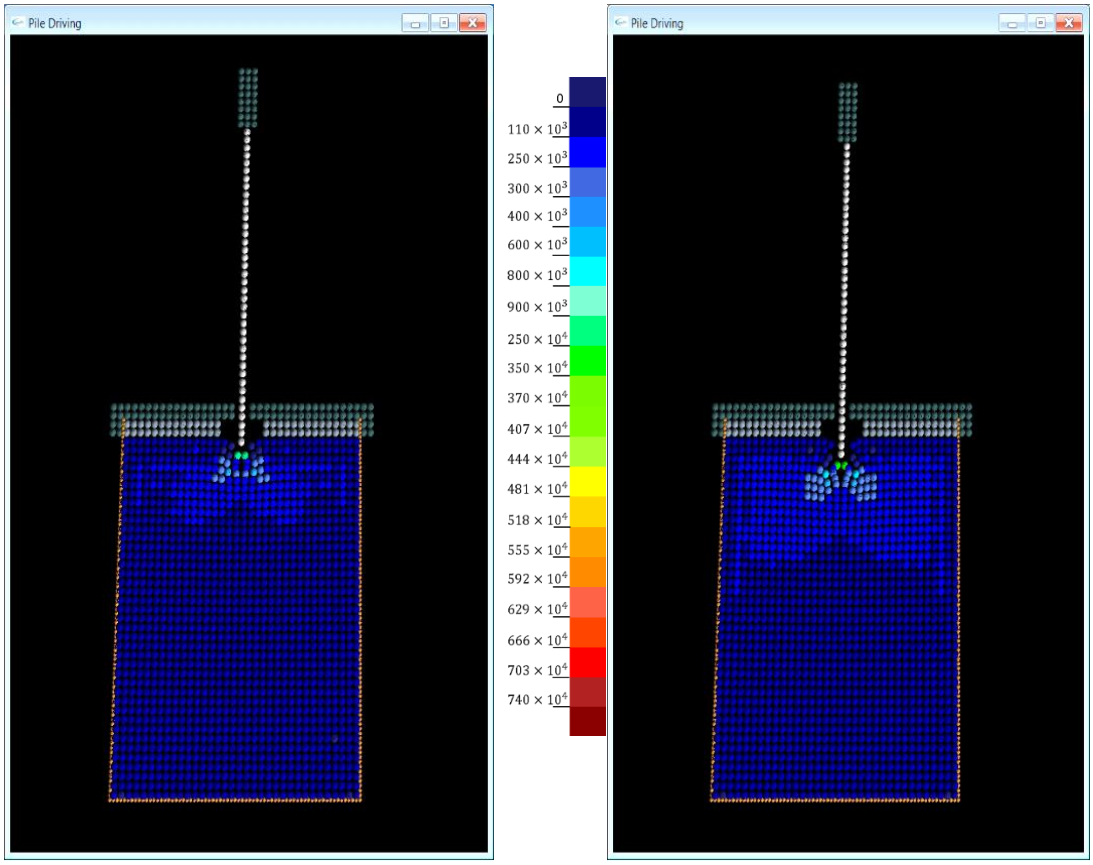
(a)



(b)

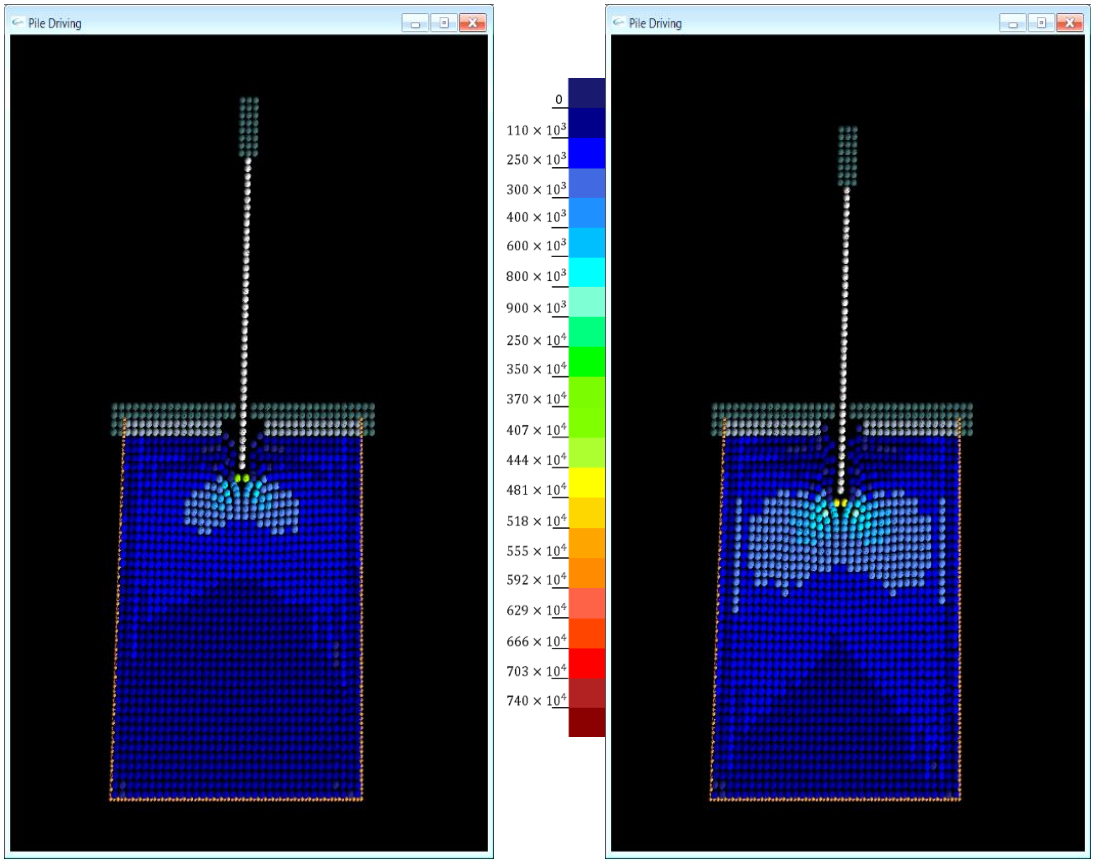
Figure 6.12: Vertical stress at the end of each: (a) push; (b) pause.

Furthermore, at penetration depths greater than 50cm in Figure 6.14, vertical stresses were noticed to spread from being near the pile toe to soil surrounding the pile shaft. Even though the deformation is not quantified in current study, it could be visualised in figures in-addition to the stress contours. Large deformation of soil around the vicinity of the pile can be observed. It is apparent from the figures that soil surrounding the pile is heavily disturbed.



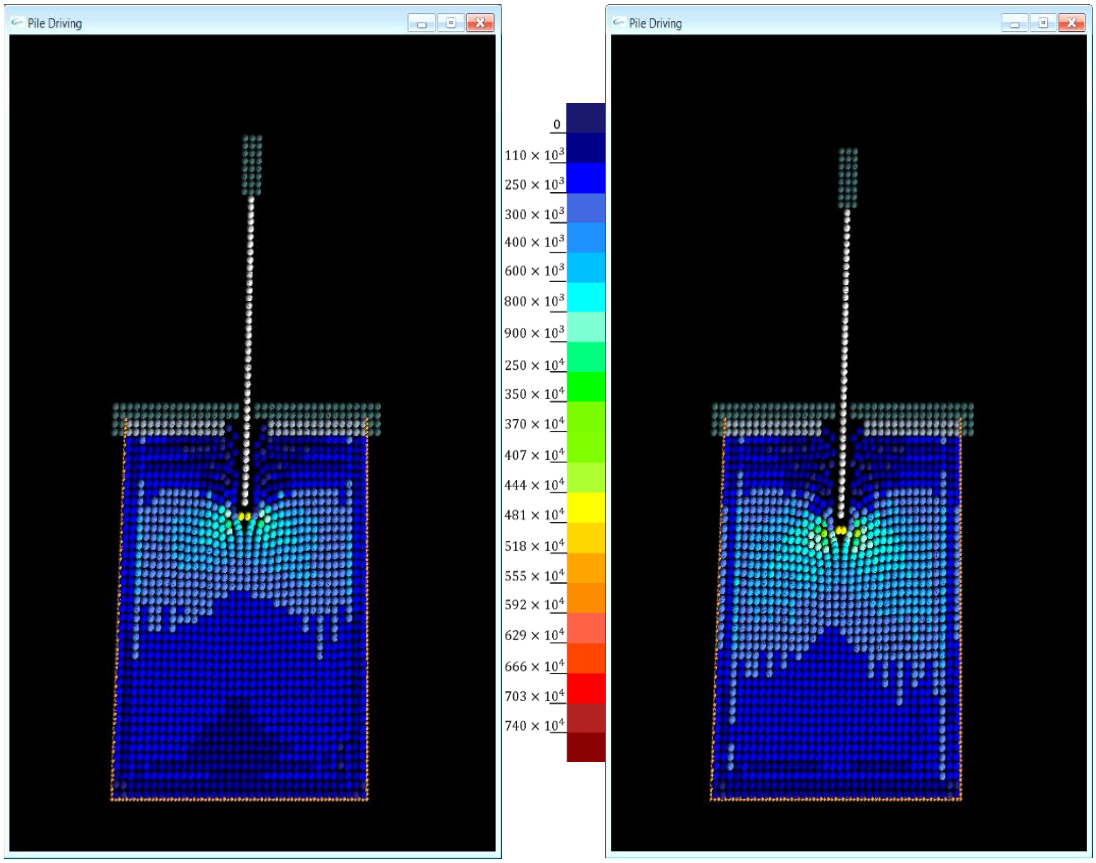
(a) Depth = 5cm; Time-step = 2419210

(b) Depth = 10cm; Time-step = 3592620



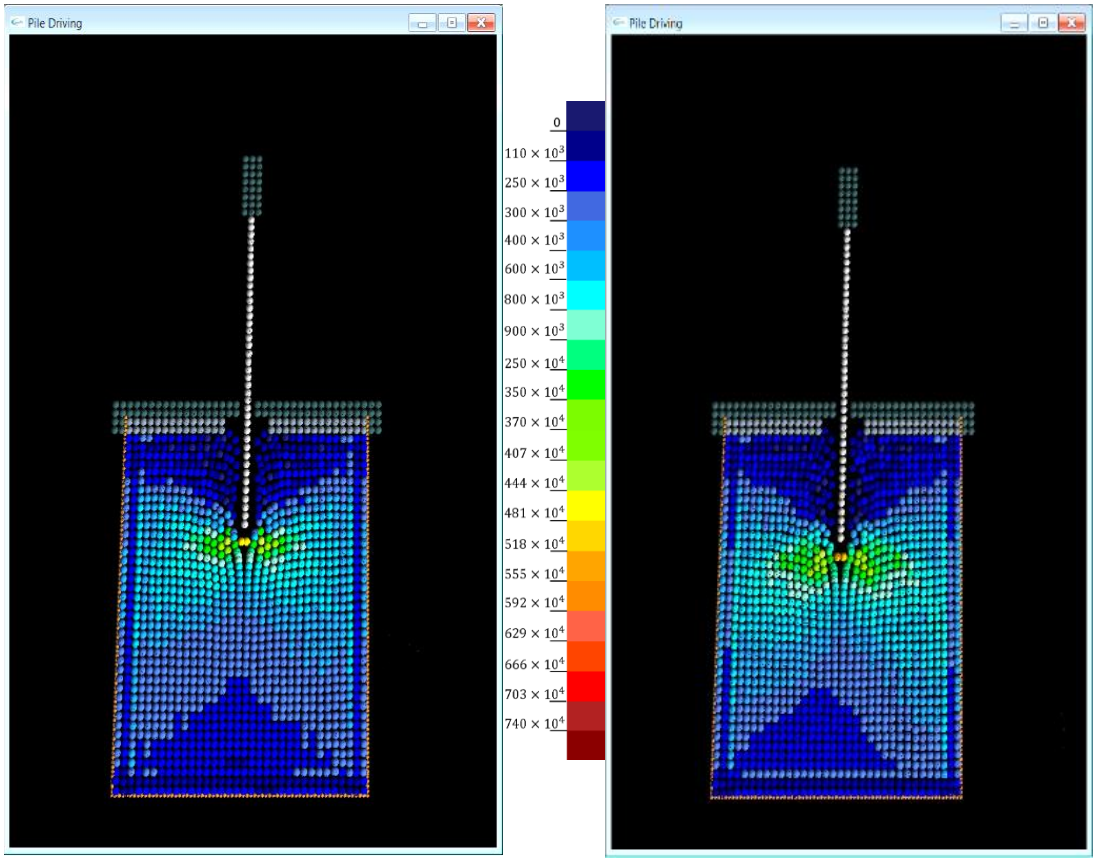
(c) Depth = 15cm; Time-step = 5407050

(d) Depth = 25cm; Time-step = 8029180



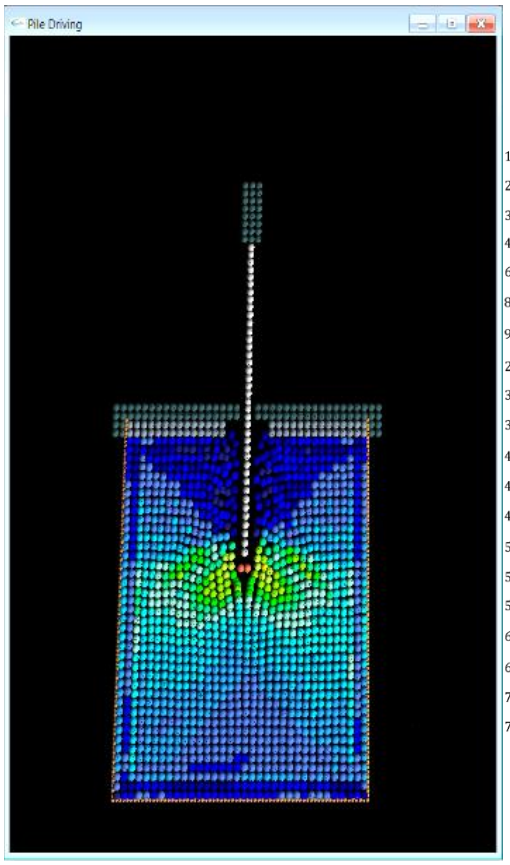
(e) Depth = 30cm; Time-step = 9889980

(f) Depth = 35cm; Time-step = 11951720

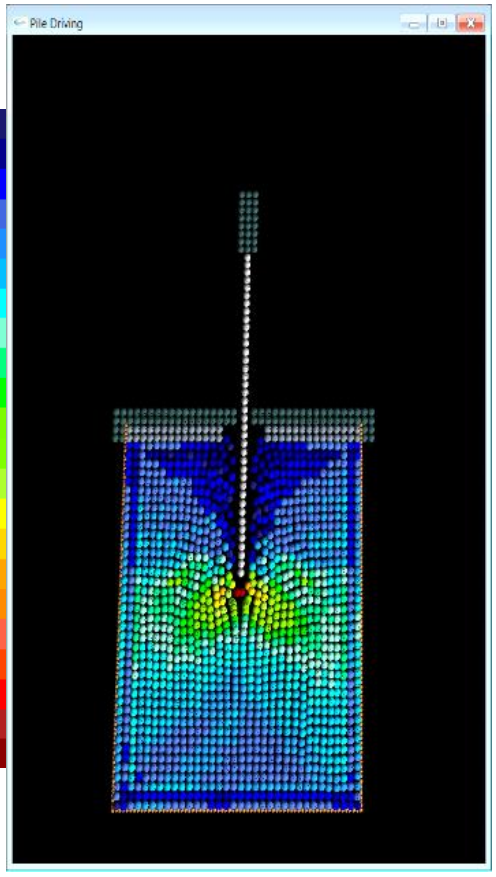


(g) Depth = 40cm; Time-step = 14087020

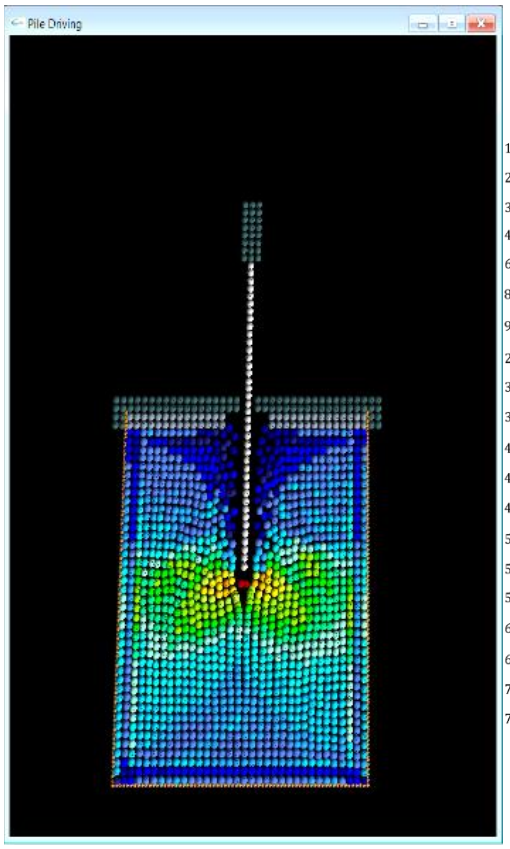
(h) Depth = 45cm; Time-step = 16559350



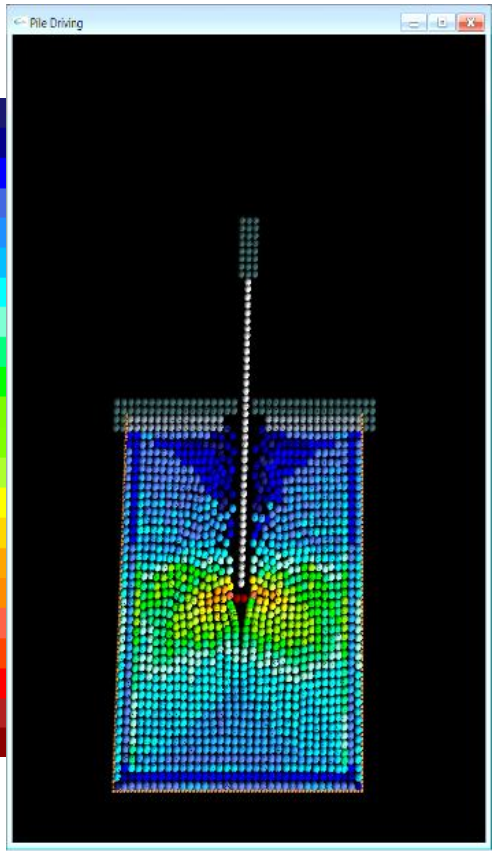
(i) Depth = 50cm; Time-step = 18655770



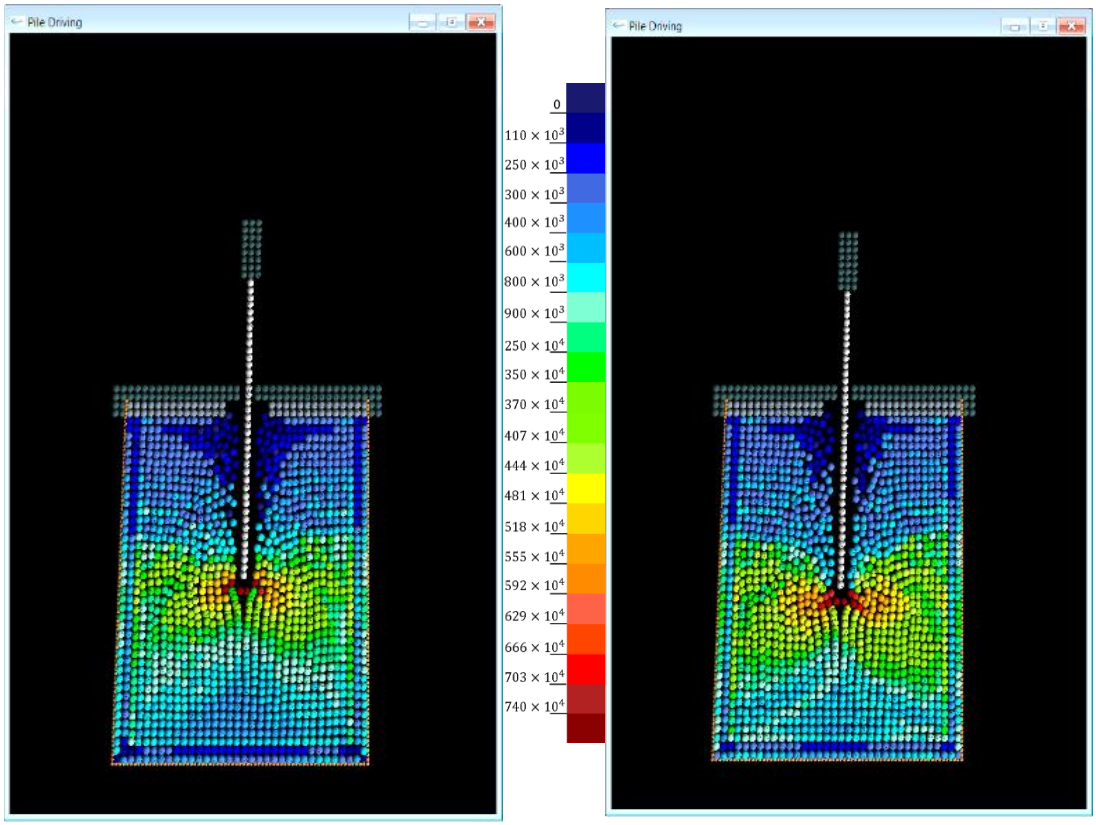
(j) Depth = 55cm; Time-step = 21038690



(k) Depth = 60cm; Time-step = 22575270

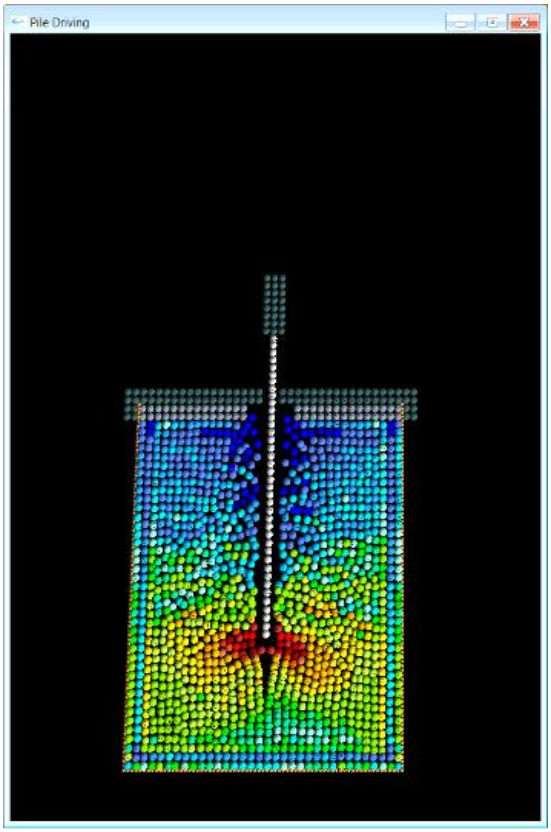


(l) Depth = 65cm; Time-step = 24270140



(m) Depth = 70cm; Time-step = 26447640

(n) Depth = 75cm; Time-step = 28741580



(o) Depth = 92cm; Time-step = 36193380

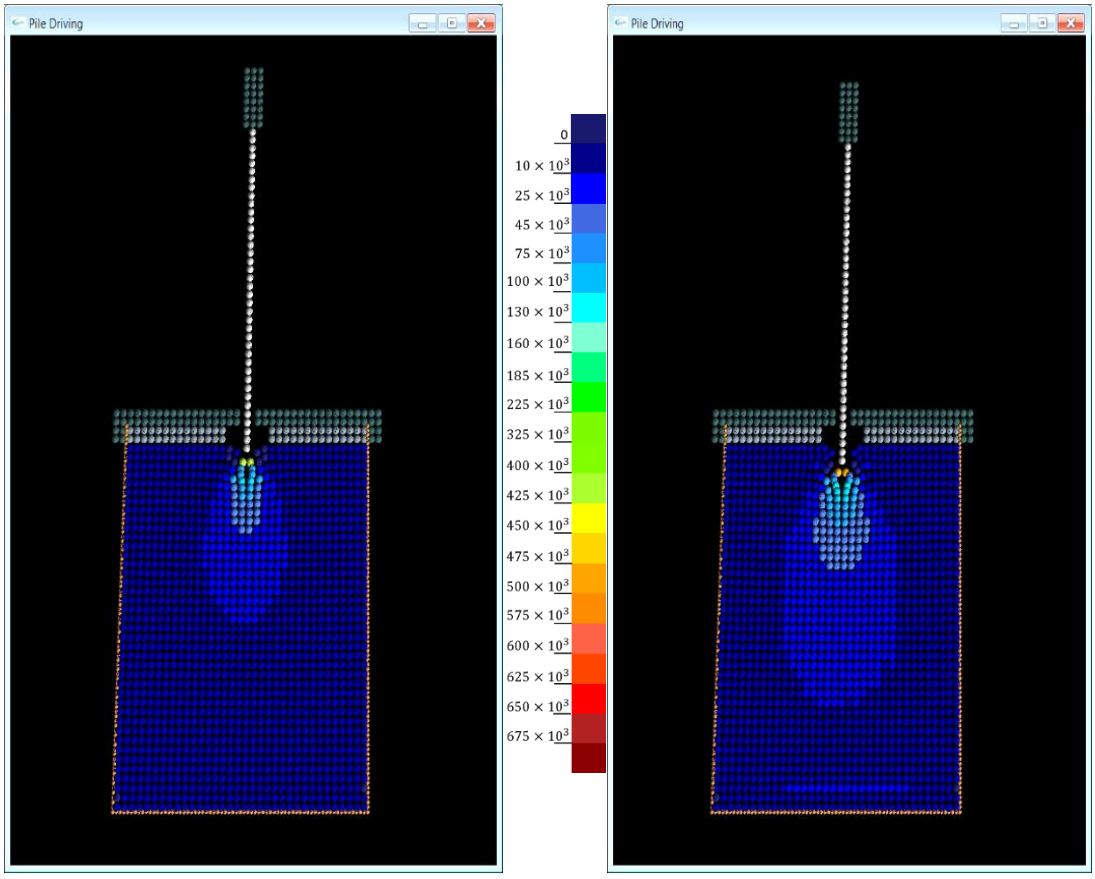
Figure 6.13: Horizontal stress distribution.

Figure 6.15 presents the comparison between the experimental values and numerical values obtained from SPH and MPM models. The MPM results presented by Lorenzo et al. [28] were compared to the measured values achieved at every pause of the pile installation process. Hence, the comparison study in present chapter is limited to horizontal and vertical stress plots achieved at every pause of the installation process. This is shown in Table 6.3.

Table 6.3: Comparison between experiment and MPM results.

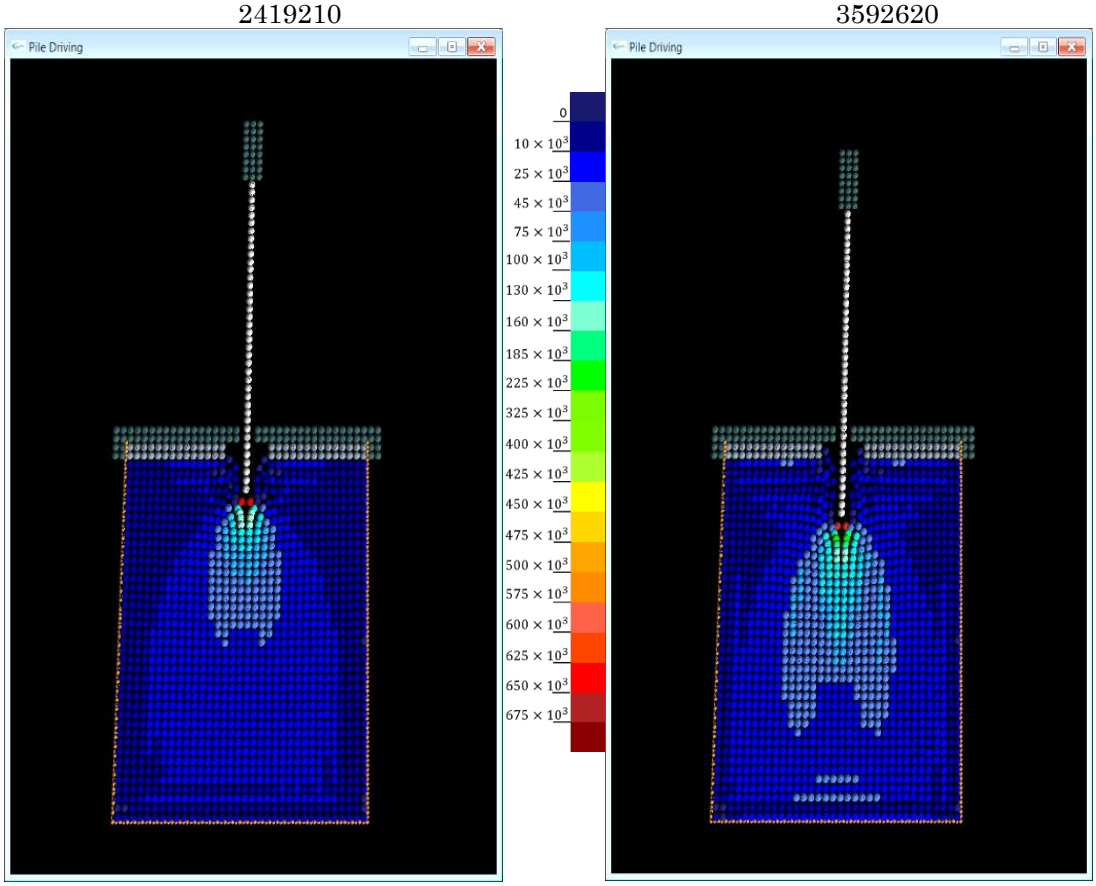
Stress point	At the end of	Figure No	Maximum Stress			Depth		
			Exp (kPa)	MPM (kPa)	Error (%)	Exp (cm)	MPM (cm)	Error (%)
r/R=2,Z=550	pause	6.15a	2275.9	1497.94	34.2	54.0	57.1	5.7
r/R=3,Z=700	pause	6.15b	1907.5	1595.11	16.4	69.6	70.0	0.6
r/R=3,Z=700	pause	6.15c	619.4	788.67	27.3	64.0	67.9	6.1

Figure 6.15a offers the horizontal stresses achieved for point at 55cm depth and 2R distance from the pile axis. SPH and MPM models simulated the maximum stress value with 17.6% and 34.2% error as presented in Table 6.2 and 6.3 respectively. Furthermore, SPH model simulated the maximum stress value at 54.3cm depth and MPM model simulated the value at a depth of 57.1cm. This proves an error of 0.5% for SPH model and 5.7% for MPM model. Hence, it is apparent that SPH model better predicted the horizontal stresses than MPM.



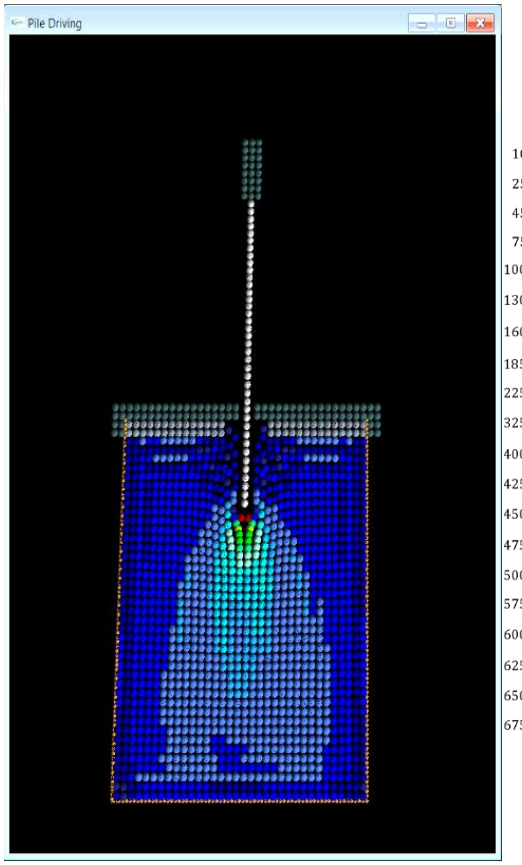
(a) Depth = 5cm; Time-step = 2419210

(b) Depth = 10cm; Time-step = 3592620

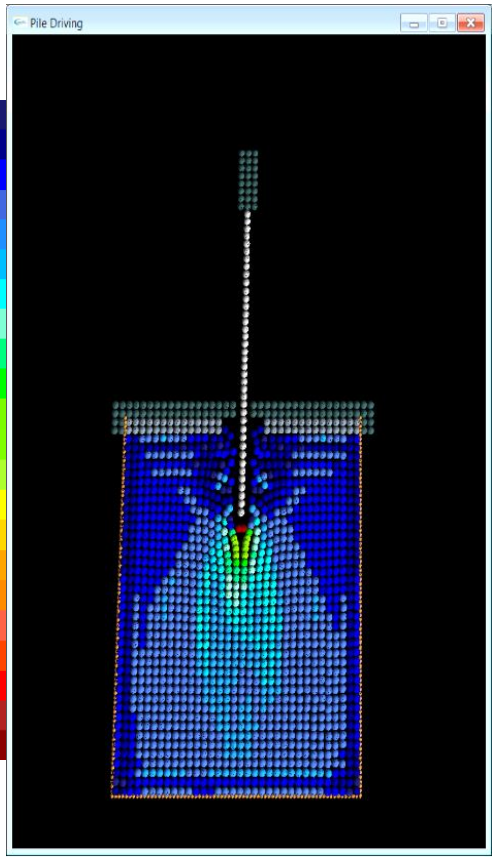


(c) Depth = 15cm; Time-step = 5407050

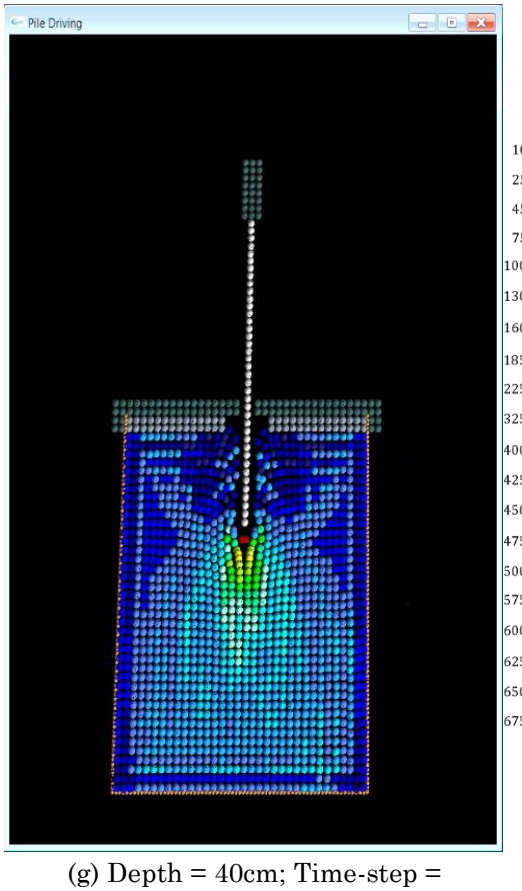
(d) Depth = 25cm; Time-step = 8029180



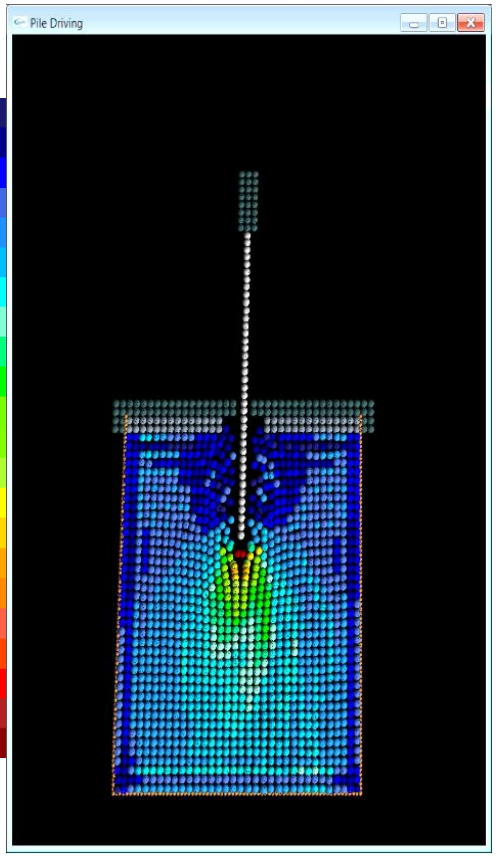
(e) Depth = 30cm; Time-step = 9889980



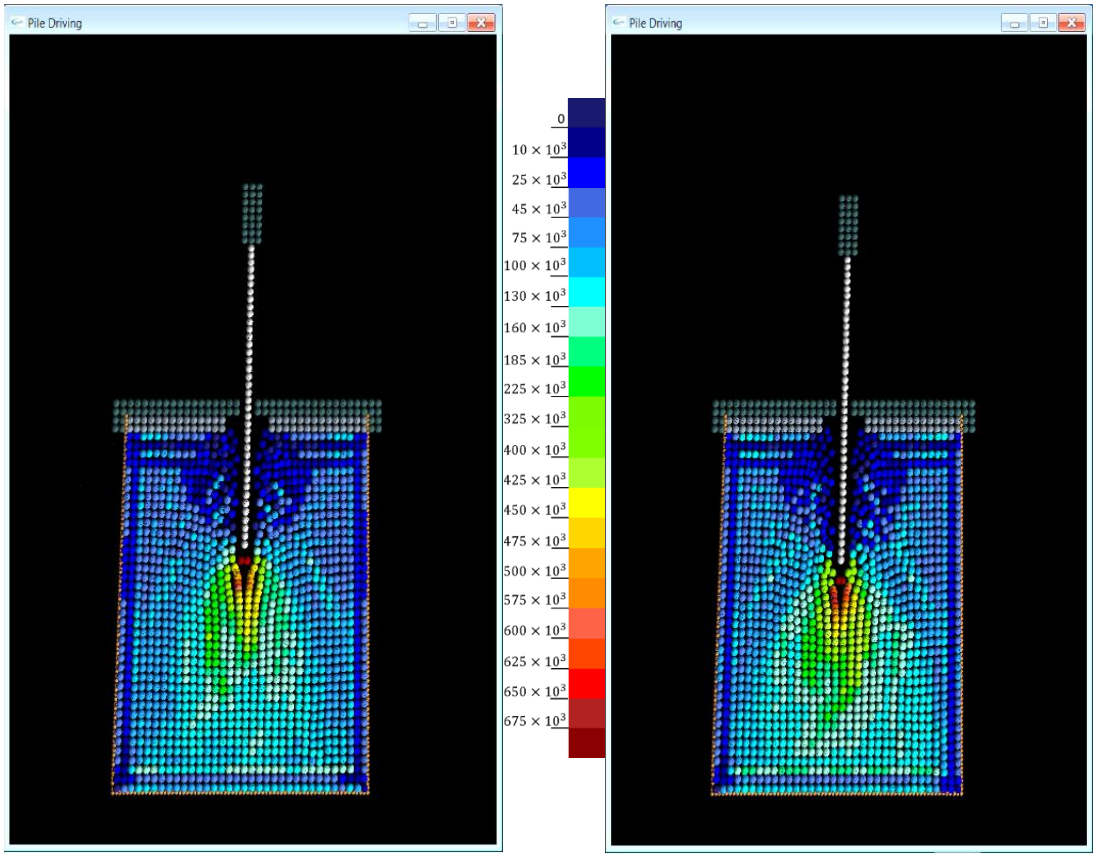
(f) Depth = 35cm; Time-step = 11951720



(g) Depth = 40cm; Time-step = 14087020

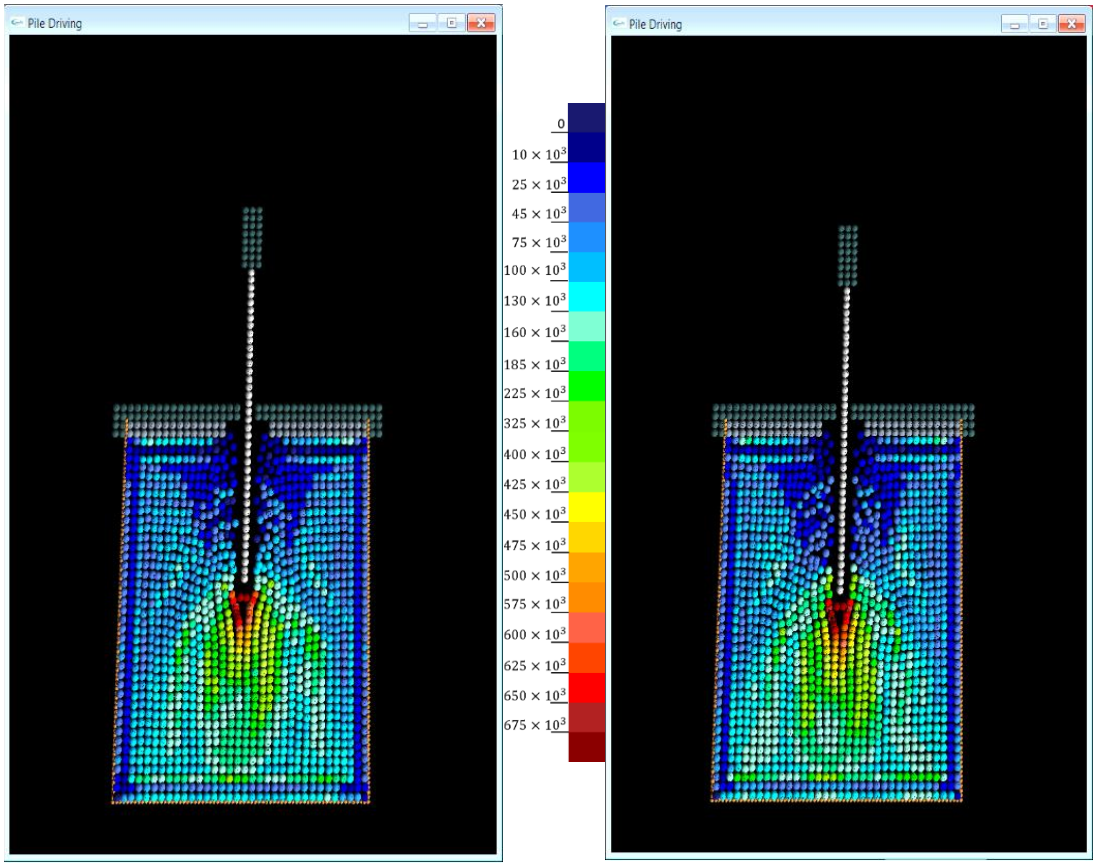


(h) Depth = 45cm; Time-step = 16559350



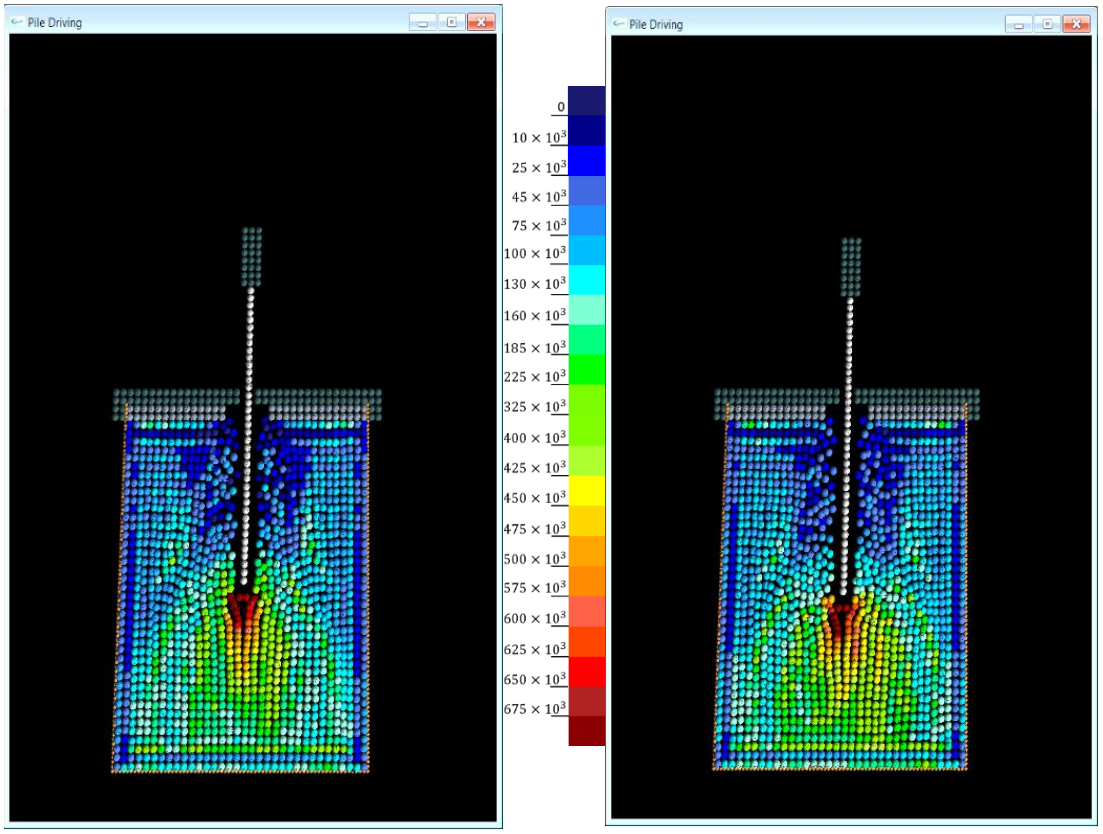
(i) Depth = 50cm; Time-step = 18655770

(j) Depth = 55cm; Time-step = 21038690



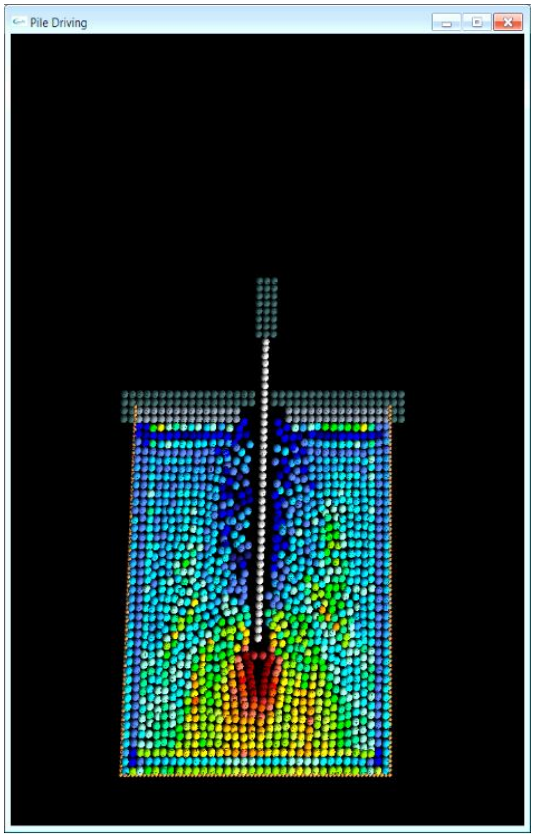
(k) Depth = 60cm; Time-step = 22575270

(l) Depth = 65cm; Time-step = 24270140



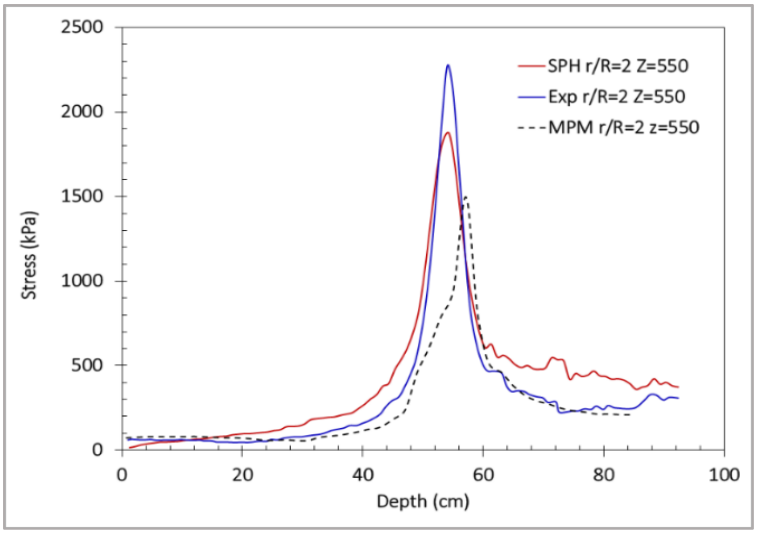
(m) Depth = 70cm; Time-step = 26447640

(n) Depth = 75cm; Time-step = 28741580

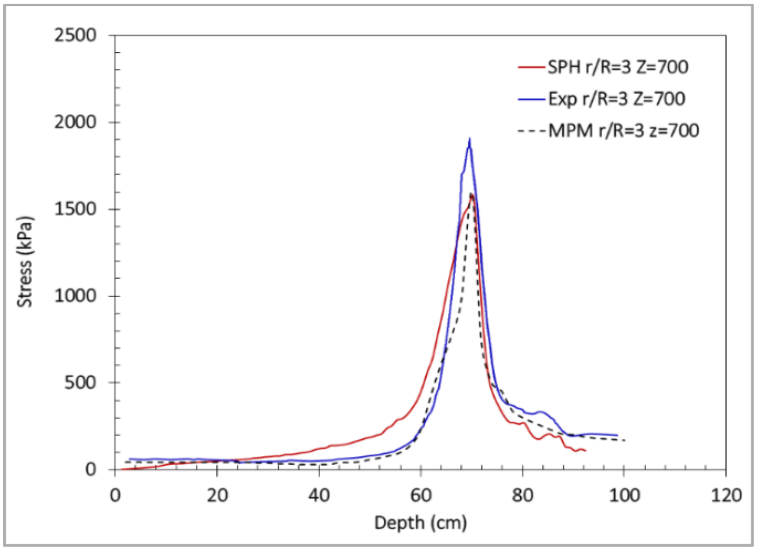


(o) Depth = 92cm; Time-step = 36193380

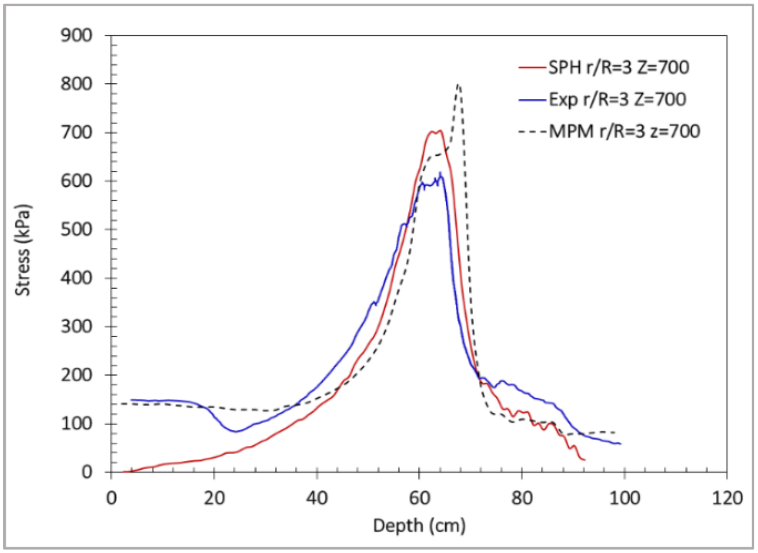
Figure 6.14: Vertical stress distribution.



(a)



(b)



(c)

Figure 6.15: SPH results with measured and MPM solutions.

Similarly, horizontal stresses for point at 70cm depth and 3R distance from the pile axis is presented in Figure 6.15b. SPH and MPM simulated the maximum stress with an error of 17.5% and 16.4% respectively. This shows that MPM better simulated the behaviour by a reduced error of 1.1% in comparison to the SPH model. However, due to the minor difference between the SPH and MPM values, it could be concluded that SPH and MPM are more or less similar in modelling the maximum stress for point at Z=700 and r=3R.

Figure 6.15c provides the vertical stresses at 70cm depth and 3R distance from the pile axis. The maximum stress value using the proposed SPH model was observed at a depth of 64.3cm with an error of 0.5% with the measured value. On the other hand, MPM simulated the maximum stress at a depth of 67.9cm with 6.1% error. Furthermore, SPH and MPM modelled the peak stress value with an error of 11.9% and 27.3% respectively. The significant difference in these errors prove that the SPH model better simulated the vertical stresses than the MPM model. Therefore, from above results it is apparent that the developed SPH model not only predicted the peak stresses well (with accuracy between 80%-88%) but also better simulated the scenario than MPM model.

6.6 Conclusion

The chapter has introduced SPH model for the investigation of soil stress field around jacking pile. To the best of our knowledge, the implementation

of SPH method to simulate jack-in pile installation has been attempted for the first time in literature. Unlike the numerical models in previous studies for jack-in pile installation, current SPH model contains the combined capability of modelling the pile as an elastic-perfectly plastic material from the soil surface along with the consideration of soil-pile interaction and to deliver graphical images of both horizontal and vertical soil stress distribution throughout the installation.

In the model, pile and soil are represented by the proposed two-dimensional von-Mises and Drucker-Prager constitutive models. Comprising the proposed constitutive models, the proposed SPH model successfully simulated the soil peak stresses with accuracy within the range 80%-88%. In addition, SPH better simulated the distribution of stresses than MPM approach. Apart from above, the ability of the model in providing continuous insights into both horizontal and vertical stress distributions extended the knowledge and understanding on the progress of soil stress contours with pile penetration. The above outcomes have emphasised the model's proficiency in modelling the complex scenario. Therefore, the SPH model is reliable and a promising numerical tool for modelling jack-in pile installation.

Chapter 7
Conclusion and future work

7.1 Conclusions

In current section, three conclusions are drawn addressing the objectives of present study in Chapter 1. The conclusions are presented as follows.

7.1.1 Development and validation of plane stress von-Mises and Drucker-Prager SPH constitutive models

The proposed von-Mises SPH model successfully simulated the stress-strain responses of three various pressure independent materials (metals) with greater than 95% of accuracy. Similarly, Drucker-Prager SPH models comprising either Drucker-Prager constitutive model with associated flow rule or non-associated flow rule simulated the stress-strain behaviour of three various pressure sensitive dilatant materials (soil) with greater than 90% of accuracy. Moreover, the results highlight that the proposed von-Mises SPH model is capable of accurately simulating internal stresses and strains of pressure in-sensitive materials within the Poisson's ratio 0-0.45. Similarly, Drucker-Prager SPH models with associated and non-associated flow rule are capable of modelling pressure sensitive dilatant materials

within the Poisson's ratio 0-0.3. This verifies that the developed constitutive models for plane stress condition introduced in present study contain a wider application range and therefore are promising numerical tools for engineers to investigate the internal stresses and strains of plane stress structures.

7.1.2 Development and validation of plane strain von-Mises and Drucker-Prager SPH constitutive models

The study introduced three plane strain constitutive models. The significant feature of these proposed models is their development in a complete two-dimensional SPH framework. The proposed constitutive models for von-Mises with associated flow rule and Drucker-Prager with non-associated and associated flow rules successfully simulated the internal stresses and strains of all considered materials with greater than 90% of accuracy. The materials considered under uniaxial compression using von-Mises and Drucker-Prager models are of Poisson's ratio 0.12, 0.35, 0.45 and 0.15, 0.3, 0.35 respectively. Therefore, similar to the plane stress constitutive models, the von-Mises and Drucker-Prager constitutive models proposed for plane strain condition on *xy* space are capable of accurately simulating the internal stresses and strains of many pressure independent materials with Poisson's ratio within the range 0-0.45 and pressure dependent dilatant materials with Poisson's ratio within the range 0-0.3 respectively. Hence, the developed constitutive models in

present study embrace a wider range of applications. Therefore, the developed plane strain constitutive models are promising tools for modelling plane strain scenarios in engineering applications.

7.1.3 Development and validation of SPH numerical model with reduced simplified assumptions for modelling jack-in pile installation

The developed SPH model introduced in present study simulates the soil stresses with accuracy within the range 80%-88% with previously published experimental results whereas the compared numerical model (MPM) simulated the peak stresses with accuracy between 65%-84%. This leaves the SPH numerical model to be a more reliable tool for engineers to analyse stresses in soil around jack-in pile. The model's unique ability of modelling pile as an elastic-perfectly plastic material from the soil surface considering soil-pile interaction and to present graphical images of the soil stress distributions throughout the installation makes it superior in modelling jack-in pile installation than many other numerical models in the literature.

7.2 Future work

Based on the accomplishments in this project, recommendations on future work are outlined in this section. Due to the mesh-free nature of the

method, future studies could be performed by applying the proposed plane stress constitutive models to complex scenarios involving large deformations. The proposed constitutive models for both plane stress and plane strain condition proved their capability in precisely modelling stresses and strains of various materials within a wide range of Poisson's ratio. As such, in future, the respective models could be utilized on numerous applications involving the modelling of pressure independent / dependent materials within the given range of Poisson's ratio.

SPH model proposed in current study for jack-in pile installation provided reliable soil stress estimations. However, the adoption of an elasto-plastic or elasto-viscous plastic constitutive model for soil material will further improve the precision in soil stress estimations. As such, the development of elasto-plastic or elasto-viscous plastic constitutive models could be considered in two-dimensional SPH framework for enhancing the performance of the existing model.

Furthermore, future studies could be carried out on increasing the accuracy of the existing model through the incorporation of skin friction. The proposed model disregards skin friction of the pile contributing to numerical inaccuracies. As such, further research can be performed on introducing SPH techniques for modelling the skin friction. Consideration of skin friction in the numerical model will not only contribute to greater precision of soil stress estimation but will also facilitate the investigation on shear stresses along pile shaft and pile bearing capacity. Therefore, further improvement of the proposed model considering the above factors

is believed to aid engineers for accurate estimation of pile bearing capacity. Moreover, due to the existing ability of the proposed model in generating graphical representation of the soil stress response during installation, further improvement of the existing model will certainly aid for enhancing the understanding of the physics involved in the phenomenon.

Bibliography

[1] M. A. El-Reedy, "Chapter 8 - Soil Investigation and Pile Design," in *Onshore Structural Design Calculations*, M. A. El-Reedy, Ed. Butterworth-Heinemann, 2017, pp. 345–385.

[2] B. M. Das, *Fundamentals of Geotechnical Engineering*. Thomson, 2005.

[3] U. Smoltczyk, *Geotechnical Engineering Handbook, Procedures*, vol. 2. John Wiley & Sons, 2003.

[4] R. D. Woods, *Dynamic effects of pile installations on adjacent structures*, no. Project 20-5 FY 1993. 1997.

[5] R. Sadek and others, *Micro-Tunneling Technology for Replacement Electric and Telecommunication Lines*. FriesenPress, 2014.

[6] C. Ovalles and C. E. Rechsteiner Jr, *Analytical Methods in Petroleum Upstream Applications*. CRC Press, 2015.

[7] S. Prakash and H. D. Sharma, *Pile foundations in engineering practice*. John Wiley & Sons, 1990.

[8] M. N. SOM and S. C. DAS, *Theory and practice of foundation design*. Phi Learning, 2003.

[9] L. Li, J. Li, D. Sun, and L. Zhang, "Time-dependent bearing capacity of a jacked pile: An analytical approach based on effective stress

method," *Ocean Eng.*, vol. 143, no. Supplement C, pp. 177–185, 2017.

[10] J. Dijkstra, W. Broere, and O. M. Heeres, "Numerical simulation of pile installation," *Comput. Geotech.*, vol. 38, no. 5, pp. 612–622, 2011.

[11] R. G. Esposito, R. Q. Velloso, E. do Amaral Vargas Jr, and B. R. Danziger, "Multi-scale sensitivity analysis of pile installation using DEM," *Comput. Part. Mech.*, vol. 5, no. 3, pp. 375–386, 2018.

[12] F. Burali d'Arezzo, S. Haigh, M. Talesnick, and Y. Ishihara, "Measuring horizontal stresses during jacked pile installation," *Proc. Inst. Civ. Eng. Eng.*, vol. 168, no. 4, pp. 306–318, 2015.

[13] T. Triantafyllidis, *Numerical Modelling of Construction Processes in Geotechnical Engineering for Urban Environment: Proceedings of the International Conference on Numerical Simulation of Construction Processes in Geotechnical Engineering for Urban Environment, 23-24 March 2*. CRC Press, 2006.

[14] J. Dijkstra, W. Broere, and A. F. van Tol, "Measurement of stress and strain development around a pile in a photoelastic granular material," in *Geomechanics and Geotechnics of Particulate Media: Proceedings of the International Symposium on Geomechanics and Geotechnics of Particulate Media, Ube, Japan, 12-14 September 2006*, 2006, p. 335.

[15] R. J. Jardine, B. Zhu, P. Foray, and C. P. Dalton, "Experimental arrangements for investigation of soil stresses developed around a displacement pile," *Soils Found.*, vol. 49, no. 5, pp. 661–673, 2009.

[16] B. Zhu, R. J. Jardine, and P. Foray, “The use of miniature soil stress measuring cells in laboratory applications involving stress reversals,” *Soils Found.*, vol. 49, no. 5, pp. 675–688, 2009.

[17] R. J. Jardine, B. T. Zhu, P. Foray, and Z. X. Yang, “Interpretation of stress measurements made around closed-ended displacement piles in sand,” *Géotechnique*, vol. 63, no. 8, p. 613, 2013.

[18] R. J. Jardine, B. T. Zhu, P. Foray, and Z. X. Yang, “Measurement of stresses around closed-ended displacement piles in sand,” *Géotechnique*, vol. 63, no. 1, p. 1, 2013.

[19] Y.-H. Wang and Z. Zhang, “An Innovative Experimental Setup for Characterizing Friction Fatigue during Cyclic Jacking of Piles in Dense Sand,” *Geotech. Test. J.*, vol. 42, no. 3, 2018.

[20] Y. Lu, Q. Wang, X. J. Li, H. Q. Sun, and X. Y. Wang, “Characterization of Soil Displacements During Press-in Pile Model Tests,” in *GeoShanghai International Conference*, 2018, pp. 550–556.

[21] S. Henke and J. Grabe, “Simulation of pile driving by 3-dimensional finite-element analysis,” in *Proceedings of 17th European Young Geotechnical Engineers’ Conference*, 2006, pp. 215–233.

[22] C. Zhang, Z. X. Yang, G. D. Nguyen, R. J. Jardine, and I. Einav, “Theoretical breakage mechanics and experimental assessment of stresses surrounding piles penetrating into dense silica sand,” *Géotechnique Lett.*, vol. 4, no. 1, pp. 11–16, 2014.

[23] D. Sheng, K. D. Eigenbrod, and P. Wriggers, “Finite element analysis

of pile installation using large-slip frictional contact," *Comput. Geotech.*, vol. 32, no. 1, pp. 17–26, 2005.

[24] J. Dijkstra, W. Broere, and A. F. Van Tol, "Numerical investigation into stress and strain development around a displacement pile in sand," *Numer. Methods Geotech. Eng.*, pp. 595–600, 2006.

[25] G. Qiu, S. Henke, and J. Grabe, "Application of a Coupled Eulerian–Lagrangian approach on geomechanical problems involving large deformations," *Comput. Geotech.*, vol. 38, no. 1, pp. 30–39, 2011.

[26] D. Sheng, P. Wriggers, and S. W. Sloan, "Improved numerical algorithms for frictional contact in pile penetration analysis," *Comput. Geotech.*, vol. 33, no. 6–7, pp. 341–354, 2006.

[27] N. T. V Phuong, A. F. van Tol, A. S. K. Elkadi, and A. Rohe, "Modelling of pile installation using the material point method (MPM)," *Numer. Methods Geotech. Eng.*, vol. 271, p. 276, 2014.

[28] R. Lorenzo, R. P. da Cunha, M. P. Cordão Neto, and J. A. Nairn, "Numerical simulation of installation of jacked piles in sand using material point method," *Can. Geotech. J.*, vol. 55, no. 1, pp. 131–146, 2017.

[29] S. Liu and J. Wang, "DEM investigation of stress field in sand during pile penetration," in *Advanced Materials, Structures and Mechanical Engineering: Proceedings of the International Conference on Advanced Materials, Structures and Mechanical Engineering, Incheon, South Korea, May 29-31, 2015*, 2016, p. 161.

[30] J. Dijkstra, W. Broere, and A. F. van Tol, “Eulerian simulation of the installation process of a displacement pile,” in *Contemporary topics in in situ testing, analysis, and reliability of foundations*, 2009, pp. 135–142.

[31] Y. Yang, L. Chen, X. Tang, H. Zheng, and Q. Liu, “A partition-of-unity based ‘FE-Meshfree’hexahedral element with continuous nodal stress,” *Comput. Struct.*, vol. 178, pp. 17–28, 2017.

[32] H. Nonoyama, S. Moriguchi, K. Sawada, and A. Yashima, “Slope stability analysis using smoothed particle hydrodynamics (SPH) method,” *Soils Found.*, vol. 55, no. 2, pp. 458–470, 2015.

[33] G.-R. Liu and S. S. Quek, *The finite element method: a practical course*. Butterworth-Heinemann, 2013.

[34] R. A. Gingold and J. J. Monaghan, “Smoothed particle hydrodynamics: theory and application to non-spherical stars,” *Mon. Not. R. Astron. Soc.*, vol. 181, no. 3, pp. 375–389, 1977.

[35] L. B. Lucy, “A numerical approach to the testing of the fission hypothesis,” *Astron. J.*, vol. 82, pp. 1013–1024, 1977.

[36] A. Colagrossi and M. Landrini, “Numerical simulation of interfacial flows by smoothed particle hydrodynamics,” *J. Comput. Phys.*, vol. 191, no. 2, pp. 448–475, 2003.

[37] R. Vacondio, B. D. Rogers, P. K. Stansby, and P. Mignosa, “SPH modeling of shallow flow with open boundaries for practical flood simulation,” *J. Hydraul. Eng.*, vol. 138, no. 6, pp. 530–541, 2011.

[38] S. Marrone, B. Bouscasse, A. Colagrossi, and M. Antuono, “Study of ship wave breaking patterns using 3D parallel SPH simulations,” *Comput. Fluids*, vol. 69, pp. 54–66, 2012.

[39] M. H. Patel, R. Vignjevic, and J. C. Campbell, “An SPH technique for evaluating the behaviour of ships in extreme ocean waves,” *Int. J. Marit. Eng.*, vol. 151, pp. 39–47, 2009.

[40] M. G. Korzani, S. A. Galindo-Torres, A. Scheuermann, and D. J. Williams, “Smoothed Particle Hydrodynamics for investigating hydraulic and mechanical behaviour of an embankment under action of flooding and overburden loads,” *Comput. Geotech.*, 2017.

[41] W. Benz and E. Asphaug, “Simulations of brittle solids using smooth particle hydrodynamics,” *Comput. Phys. Commun.*, vol. 87, no. 1–2, pp. 253–265, 1995.

[42] M. B. Liu and G. R. Liu, “Smoothed particle hydrodynamics (SPH): an overview and recent developments,” *Arch. Comput. methods Eng.*, vol. 17, no. 1, pp. 25–76, 2010.

[43] J. J. Monaghan, “Smoothed particle hydrodynamics,” *Reports Prog. Phys.*, vol. 68, no. 8, p. 1703, 2005.

[44] G. L. Vaughan, “The SPH equations for fluids,” *Int. J. Numer. Methods Eng.*, vol. 79, no. 11, pp. 1392–1418, 2009.

[45] A. Zhang, P. Sun, F. Ming, and A. Colagrossi, “Smoothed particle hydrodynamics and its applications in fluid-structure interactions,” *J. Hydrodyn. Ser. B*, vol. 29, no. 2, pp. 187–216, 2017.

[46] C. Wang, Y. Wang, C. Peng, and X. Meng, "Two-fluid smoothed particle hydrodynamics simulation of submerged granular column collapse," *Mech. Res. Commun.*, vol. 79, pp. 15–23, 2017.

[47] P. W. Cleary and J. J. Monaghan, "Conduction Modelling Using Smoothed Particle Hydrodynamics," *J. Comput. Phys.*, vol. 148, no. 1, pp. 227–264, 1999.

[48] L. D. Libersky and A. G. Petschek, "Smooth particle hydrodynamics with strength of materials," in *Advances in the free-Lagrange method including contributions on adaptive gridding and the smooth particle hydrodynamics method*, Springer, 1991, pp. 248–257.

[49] L. D. Libersky, A. G. Petschek, T. C. Carney, J. R. Hipp, and F. A. Allahdadi, "High strain Lagrangian hydrodynamics: a three-dimensional SPH code for dynamic material response," *J. Comput. Phys.*, vol. 109, no. 1, pp. 67–75, 1993.

[50] H. H. Bui, R. Fukagawa, and K. Sato, "Smoothed particle hydrodynamics for soil mechanics," *Proc. Numer. Methods Geotech. Eng. Graz*, pp. 275–281, 2006.

[51] H. H. Bui, R. Fukagawa, K. Sako, and S. Ohno, "Lagrangian meshfree particles method (SPH) for large deformation and failure flows of geomaterial using elastic--plastic soil constitutive model," *Int. J. Numer. Anal. Methods Geomech.*, vol. 32, no. 12, pp. 1537–1570, 2008.

[52] C. Peng, W. Wu, H. Yu, and C. Wang, "A SPH approach for large

deformation analysis with hypoplastic constitutive model," *Acta Geotech.*, vol. 10, no. 6, pp. 703–717, 2015.

[53] Y. An, Q. Wu, C. Shi, and Q. Liu, "Three-dimensional smoothed-particle hydrodynamics simulation of deformation characteristics in slope failure," *Geotechnique*, vol. 66, no. 8, pp. 670–680, 2016.

[54] H. Wu, J. Wang, C. Wang, and J. Hua Wang, "Soil-Water-Structure Interaction Algorithm in Smoothed Particle Hydrodynamics (SPH) with Application to Deep-Penetrating Problems," *Int. J. Comput. Methods*, 2018.

[55] E. Kermani and T. Qiu, "Simulation of Quasi-Static and Dynamic Collapses of Rectangular Granular Columns Using Smoothed Particle Hydrodynamics Method," *Int. J. Geomech.*, vol. 18, 2018.

[56] N. Hiraoka, A. Oya, H. H. Bui, P. Rajeev, and R. Fukagawa, "Seismic slope failure modelling using the mesh-free SPH method," *Int. J. GEOMATE*, vol. 5, no. 1, pp. 660–665, 2013.

[57] H. H. Bui, R. Fukagawa, K. Sako, and J. C. Wells, "Slope stability analysis and discontinuous slope failure simulation by elasto-plastic smoothed particle hydrodynamics (SPH)," *Geotechnique*, vol. 61, no. 7, pp. 565–574, 2011.

[58] K. Kovaleva and others, "The value of CRM systems and IoT-based solutions for future prospects in pile driving industry," 2017.

[59] R. Summary, "Piling Machine Market Size , Share | Industry Report , 2024 Piling Machine Market Analysis , By Product (Impact

Hammers , Vibratory Drivers , Rigs), By Method (Impact Driven , Drilled Percussive , Rotary Bored , Air Lift Reverse Circulation Drilling (," vol. 2024, pp. 1–4, 2017.

[60] M. Tomlinson and J. Woodward, *Pile design and construction practice*. CRC Press, 2014.

[61] M.-A. Allard, "Soil stress field around driven piles," 1989.

[62] A. D. Deeks and D. J. White, "Centrifuge modelling of jacked piles," *ICPMG '06, Hong Kong*, 2006.

[63] C. Viggiani, A. Mandolini, and G. Russo, *Piles and pile foundations*. CRC Press, 2014.

[64] R. A. Rajapakse, *Pile design and construction rules of thumb*. Butterworth-Heinemann, 2016.

[65] U. S. N. Oceanic and A. Administration, *Essential Fish Habitat Designation and Minimization of Adverse Impacts, Pacific Coast Groundfish Fishery Management Plan: Environmental Impact Statement*. 2005.

[66] M. R. A, E. A. V, and O. A. I, *Pile Construction Technology*. Bokförlaget Efron & Dotter AB, 2016.

[67] D. White, T. Finlay, M. Bolton, and G. Bearss, "Press-in piling: Ground vibration and noise during pile installation," in *Deep Foundations 2002: An International Perspective on Theory, Design, Construction, and Performance*, 2002, pp. 363–371.

[68] D. J. Rockhill, M. D. Bolton, and D. J. White, "Ground-borne

vibrations due to press-in piling operations," in *Proceedings of the British Geotechnical Association International Conference on Foundations, Dundee, Scotland*, 2003, pp. 2–5.

[69] D. J. White and B. M. Lehane, "Friction fatigue on displacement piles in sand," *Géotechnique*, vol. 54, no. 10, pp. 645–658, 2004.

[70] F. B. d'Arezzo, S. K. Haigh, and Y. Ishihara, "Modelling of jacked piles in centrifuge," in *ICPMG2014--Physical Modelling in Geotechnics: Proceedings of the 8th International Conference on Physical Modelling in Geotechnics*, 2014, vol. 2, pp. 807–812.

[71] L. S. Shong, H. S. Feng, and V. B. Chuan, "Pile capacity reduction of jack-in piles with empty prebored hole at meta-sedimentary formation in peninsular malaysia," 2014.

[72] C. Zhang, G. D. Nguyen, and I. Einav, "The end-bearing capacity of piles penetrating into crushable soils," *Géotechnique*, vol. 63, no. 5, p. 341, 2013.

[73] Z. X. Yang, R. J. Jardine, B. T. Zhu, and S. Rimoy, "Stresses developed around displacement piles penetration in sand," *J. Geotech. Geoenvironmental Eng.*, vol. 140, no. 3, p. 4013027, 2013.

[74] R. J. Jardine and Z. X. Yang, "Joint Research into the Behaviour of Driven Piles," in *Proceedings of China-Europe Conference on Geotechnical Engineering*, 2018, pp. 961–972.

[75] Y. M. Desai, Ti. Eldho, and A. H. Shah, *Finite element method with applications in engineering*. Pearson Education India, 2011.

[76] J. Geng, W. Yan, and W. Xu, *Application of the finite element method in implant dentistry*. Springer Science & Business Media, 2008.

[77] G.-R. Liu and M. B. Liu, *Smoothed particle hydrodynamics: a meshfree particle method*. World Scientific, 2003.

[78] X. Zhang, Z. Chen, and Y. Liu, *The material point method: a continuum-based particle method for extreme loading cases*. Academic Press, 2016.

[79] S. Ma and X. Zhang, "Material point method for impact and explosion problems," in *Computational Mechanics*, Springer, 2007, pp. 156–166.

[80] M. A. Homel and E. B. Herbold, "Field-gradient partitioning for fracture and frictional contact in the material point method," *Int. J. Numer. Methods Eng.*, vol. 109, no. 7, pp. 1013–1044, 2017.

[81] K. Soga, E. Alonso, A. Yerro, K. Kumar, and S. Bandara, "Trends in large-deformation analysis of landslide mass movements with particular emphasis on the material point method," *Géotechnique*, vol. 66, no. 3, pp. 248–273, 2015.

[82] T. Yun and H. Park, "Applicability Evaluation of Similarity Principle in Discrete Element Analysis," in *International Conference on Discrete Element Methods*, 2016, pp. 117–123.

[83] T. Zhao, "Introduction to Discrete Element Method," in *Coupled DEM-CFD Analyses of Landslide-Induced Debris Flows*, Singapore: Springer Singapore, 2017, pp. 25–45.

[84] J. J. Monaghan, "Smoothed particle hydrodynamics," *Annu. Rev. Astron. Astrophys.*, vol. 30, no. 1, pp. 543–574, 1992.

[85] J. J. Monaghan and J. C. Lattanzio, "A simulation of the collapse and fragmentation of cooling molecular clouds," *Astrophys. J.*, vol. 375, pp. 177–189, 1991.

[86] H. H. Bui, K. Sako, and R. Fukagawa, "Numerical simulation of soil–water interaction using smoothed particle hydrodynamics (SPH) method," *J. Terramechanics*, vol. 44, no. 5, pp. 339–346, 2007.

[87] H. H. Bui, K. Sako, R. Fukagawa, and J. C. Wells, "SPH-based numerical simulations for large deformation of geomaterial considering soil-structure interaction," in *The 12th International Conference of International Association for Computer Methods and Advances in Geomechanics (IACMAG)*, 2008, vol. 1, pp. 570–578.

[88] H. H. Bui, J. K. Kodikara, A. Bouazza, A. Haque, and P. G. Ranjith, "A novel computational approach for large deformation and post-failure analyses of segmental retaining wall systems," *Int. J. Numer. Anal. Methods Geomech.*, vol. 38, no. 13, pp. 1321–1340, 2014.

[89] Y. Huang and Z. Dai, "Large deformation and failure simulations for geo-disasters using smoothed particle hydrodynamics method," *Eng. Geol.*, vol. 168, pp. 86–97, 2014.

[90] J.-Y. Chen and F.-S. Lien, "Simulations for soil explosion and its effects on structures using SPH method," *Int. J. Impact Eng.*, vol. 112, pp. 41–51, 2018.

[91] K.-T. Tang, *Mathematical methods for engineers and scientists*, vol. 1. Springer, 2007.

[92] J. Stewart, *Calculus: Concepts and contexts*. Cengage Learning, 2009.

[93] L. Moubin and L. Gui-Rong, *Particle methods for multi-scale and multi-physics*. World Scientific, 2015.

[94] X. F. Yang, S. L. Peng, and M. B. Liu, "A new kernel function for SPH with applications to free surface flows," *Appl. Math. Model.*, vol. 38, no. 15, pp. 3822–3833, 2014.

[95] R. Ray, K. Deb, and A. Shaw, "Pseudo-Spring smoothed particle hydrodynamics (SPH) based computational model for slope failure," *Eng. Anal. Bound. Elem.*, vol. 101, pp. 139–148, 2019.

[96] M. R. I. Islam and C. Peng, "A Total Lagrangian SPH method for modelling damage and failure in solids," *Int. J. Mech. Sci.*, vol. 157–158, pp. 498–511, 2019.

[97] C. Pozrikidis, *Fluid dynamics: theory, computation, and numerical simulation*. Springer, 2016.

[98] W.-F. Chen and D.-J. Han, *Plasticity for structural engineers*. J. Ross Publishing, 2007.

[99] T. Gerya, *Introduction to numerical geodynamic modelling*. Cambridge University Press, 2009.

[100] M. Satake and J. T. Jenkins, *Micromechanics of Granular Materials: Proceedings of the US/Japan Seminar on the Micromechanics of*

Granular Materials, Sendai-Zao, Japan, October 26-30, 1987, vol. 20. Elsevier, 2013.

[101] S. Nemat-Nasser and M. Hori, *Micromechanics: overall properties of heterogeneous materials*, vol. 37. Elsevier, 2013.

[102] R. G. Park, *Foundations of Structural Geology*. Psychology Press, 1997.

[103] N. S. Ottosen and M. Ristinmaa, *The mechanics of constitutive modeling*. Elsevier, 2005.

[104] D. M. Wood, *Geotechnical modelling*. CRC press, 2014.

[105] Y. Prawoto, *Solid mechanics for materials engineers--Principles and Applications of Mesomechanics*. Lulu. com, 2013.

[106] Z. L. Liu, "Multiphysics in Porous Materials," in *Multiphysics in Porous Materials*, Springer, 2018, pp. 29–34.

[107] G. Ranjan and A. S. R. Rao, *Basic and applied soil mechanics*. New Age International, 2007.

[108] W.-F. Chen and E. M. Lui, *Handbook of structural engineering*. Crc Press, 2005.

[109] W.-F. Chen and X. L. Liu, *Limit analysis in soil mechanics*, vol. 52. Elsevier, 2012.

[110] X.-W. Gao and T. G. Davies, *Boundary element programming in mechanics*, vol. 1. Cambridge University Press, 2002.

[111] W.-F. Chen, *Plasticity in reinforced concrete*. J. Ross Publishing, 2007.

[112] H.-S. Yu, *Plasticity and geotechnics*, vol. 13. Springer Science & Business Media, 2007.

[113] L. A. Lubbers, M. Van Hecke, and C. Coulais, "Journal of the Mechanics and Physics of Solids A nonlinear beam model to describe the postbuckling of wide neo-Hookean beams," vol. 106, pp. 191–206, 2017.

[114] R. M. J. Groh and A. Tessler, "Computationally efficient beam elements for accurate stresses in sandwich laminates and laminated composites with delaminations," *Comput. Methods Appl. Mech. Eng.*, vol. 320, no. Supplement C, pp. 369–395, 2017.

[115] S. Bharath and S. N. Nv, "Structural Analysis of Aileron Panel using Finite Element Method," *IOSR*, vol. 16, pp. 2320–2334, 2016.

[116] J. Gere, *Mechanics of Materials (with CD-ROM and InfoTrac)*. Cengage Learning, 2003.

[117] G. M. Boyd, *Brittle Fracture in Steel Structures*, Kindle Edi. 2016.

[118] V. K. Devendiran, R. K. Sandeep, K. Kannan, and K. R. Rajagopal, "A thermodynamically consistent constitutive equation for describing the response exhibited by several alloys and the study of a meaningful physical problem," *Int. J. Solids Struct.*, vol. 108, pp. 1–10, 2017.

[119] Y. Yamada, N. Yoshimura, and T. Sakurai, "Plastic stress-strain matrix and its application for the solution of elastic-plastic problems by the finite element method," *Int. J. Mech. Sci.*, vol. 10, no. 5, pp.

343–354, 1968.

[120] P. V Marcal and I. P. King, “Elastic-plastic analysis of two-dimensional stress systems by the finite element method,” *Int. J. Mech. Sci.*, vol. 9, no. 3, pp. 143–155, 1967.

[121] F. Yoshida, T. Uemori, and K. Fujiwara, “Elastic--plastic behavior of steel sheets under in-plane cyclic tension--compression at large strain,” *Int. J. Plast.*, vol. 18, no. 5, pp. 633–659, 2002.

[122] L. Feng, Y. Kang, G. Zhang, and S. Wang, “Mechanism-based strain gradient Drucker--Prager elastoplasticity for pressure-sensitive materials,” *Int. J. Solids Struct.*, vol. 47, no. 20, pp. 2693–2705, 2010.

[123] C. K. H. Dharan, B. S. Kang, and I. Finnie, “Some Solutions That Are Useful in Fracture Prediction,” in *Finnie’s Notes on Fracture Mechanics*, Springer, 2016, pp. 63–94.

[124] G R Liu and Nguyen Thoi Thrung, *Smoothed Finite Element Methods*. CRC Press, 2010.

[125] P. W. Randles and L. D. Libersky, “Smoothed Particle Hydrodynamics: Some recent improvements and applications,” *Comput. Methods Appl. Mech. Eng.*, vol. 139, no. 1, pp. 375–408, 1996.

[126] J. P. Gray, J. J. Monaghan, and R. P. Swift, “SPH elastic dynamics,” *Comput. Methods Appl. Mech. Eng.*, vol. 190, no. 49, pp. 6641–6662, 2001.

[127] J. P. Gray and J. J. Monaghan, “Numerical modelling of stress fields

and fracture around magma chambers," *J. Volcanol. Geotherm. Res.*, vol. 135, no. 3, pp. 259–283, 2004.

[128] R. Das and P. W. Cleary, "Effect of rock shapes on brittle fracture using Smoothed Particle Hydrodynamics," *Theor. Appl. Fract. Mech.*, vol. 53, no. 1, pp. 47–60, 2010.

[129] E. A. Patiño, R. Reyes, D. A. Garc'\ia, A. F. Sarmiento, J. M. Arroyo, and D. A. Garzon, "Implementation of the smoothed particle hydrodynamics method to solve plastic deformation in metals," *Blucher Mech. Eng. Proc.*, vol. 1, no. 1, pp. 4593–4606, 2012.

[130] T. Douillet-Grellier, B. D. Jones, R. Pramanik, K. Pan, A. Albaiz, and J. R. Williams, "Mixed-mode fracture modeling with smoothed particle hydrodynamics," *Comput. Geotech.*, vol. 79, pp. 73–85, 2016.

[131] T. Douillet-Grellier, R. Pramanik, K. Pan, A. Albaiz, B. D. Jones, and J. R. Williams, "Development of stress boundary conditions in smoothed particle hydrodynamics (SPH) for the modeling of solids deformation," *Comput. Part. Mech.*, vol. 4, no. 4, pp. 451–471, 2017.

[132] S. A. Berggren, D. Lukkassen, A. Meidell, and L. Simula, "Some methods for calculating stiffness properties of periodic structures," *Appl. Math.*, vol. 48, no. 2, pp. 97–110, 2003.

[133] B. Cambou, H. Magoariec, and N.-S. Nguyen, *Granular Materials at Meso-scale: Towards a Change of Scale Approach*. Elsevier, 2016.

[134] F. A. Leckie and D. J. Bello, *Strength and stiffness of engineering systems*. Springer Science & Business Media, 2009.

[135] R. Brighenti and A. Carpinteri, “A unified stress-based approach to assess failure in solids and liquids,” in *Giornata IGF Forni di Sopra (UD) 2011*, 2011.

[136] A. S. Khan and S. Huang, *Continuum theory of plasticity*. John Wiley & Sons, 1995.

[137] J. VonNeumann and R. D. Richtmyer, “A method for the numerical calculation of hydrodynamic shocks,” *J. Appl. Phys.*, vol. 21, no. 3, pp. 232–237, 1950.

[138] J. J. Monaghan and R. A. Gingold, “Shock simulation by the particle method SPH,” *J. Comput. Phys.*, vol. 52, no. 2, pp. 374–389, 1983.

[139] J. J. Monaghan and H. Pongracic, “Artificial viscosity for particle methods,” *Appl. Numer. Math.*, vol. 1, no. 3, pp. 187–194, 1985.

[140] P. Wróblewski, K. Boryczko, and M. Kope, “Modeling incompressible fluids by means of the SPH method: Surface tension and viscosity,” *Comput. Sci. 2008*, pp. 600–609, 2008.

[141] A. Shaw and D. Roy, “Stabilized SPH-based simulations of impact dynamics using acceleration-corrected artificial viscosity,” *Int. J. Impact Eng.*, vol. 48, pp. 98–106, 2012.

[142] Z. Mao, G. R. Liu, and X. Dong, “A comprehensive study on the parameters setting in smoothed particle hydrodynamics (SPH) method applied to hydrodynamics problems,” *Comput. Geotech.*, vol. 92, pp. 77–95, 2017.

[143] T. Heck, B. Smeets, S. Vanmaercke, P. Bhattacharya, T. Odenthal,

H. Ramon, H. Van Oosterwyck, and P. Van Liedekerke, "Modeling extracellular matrix viscoelasticity using smoothed particle hydrodynamics with improved boundary treatment," *Comput. Methods Appl. Mech. Eng.*, vol. 322, pp. 515–540, 2017.

[144] H. Takeda, S. M. Miyama, and M. Sekiya, "Numerical simulation of viscous flow by smoothed particle hydrodynamics," *Prog. Theor. Phys.*, vol. 92, no. 5, pp. 939–960, 1994.

[145] J. P. Morris, P. J. Fox, and Y. Zhu, "Modeling low Reynolds number incompressible flows using SPH," *J. Comput. Phys.*, vol. 136, no. 1, pp. 214–226, 1997.

[146] T. Douillet-Grellier, R. Pramanik, K. Pan, A. Albaiz, B. D. Jones, and J. R. Williams, "Development of stress boundary conditions in smoothed particle hydrodynamics (SPH) for the modeling of solids deformation," *Comput. Part. Mech.*, pp. 1–21, 2016.

[147] J. J. Monaghan, "On the problem of penetration in particle methods," *J. Comput. Phys.*, vol. 82, no. 1, pp. 1–15, 1989.

[148] D. S. P. Rao, *Introduction to Strength of Materials*. Universities Press, 2002.

[149] R. F. Gibson, *Principles of composite material mechanics*. CRC press, 2016.

[150] T. Kobayashi, *Strength and toughness of materials*. Springer Science & Business Media, 2012.

[151] R. O. Davis and A. P. S. Selvadurai, *Plasticity and geomechanics*.

Cambridge University Press, 2005.

[152] E. Cicek, E. Guler, and T. Yetimoglu, “Stress Distribution below a Continuous Footing on Geotextile-Reinforced Soil,” *Int. J. Geomech.*, vol. 18, no. 3, p. 6018005, 2018.

[153] P. Ni, G. Mei, Y. Zhao, and H. Chen, “Plane strain evaluation of stress paths for supported excavations under lateral loading and unloading,” *Soils Found.*, p. , 2018.

[154] M. Saberi, C.-D. Annan, and J.-M. Konrad, “Numerical Analysis of Concrete Faced Rockfill Dams Considering the Effect of Face Slab-Cushion Layer Interaction,” *Can. Geotech. J.*, no. ja, 2018.

[155] P. Li, F. Wang, and Q. Fang, “Undrained analysis of ground reaction curves for deep tunnels in saturated ground considering the effect of ground reinforcement,” *Tunn. Undergr. Sp. Technol.*, vol. 71, pp. 579–590, 2018.

[156] F. Tschuchnigg and H. F. Schweiger, “Embankment prediction and back analysis by means of 2D and 3D finite element analyses,” *Comput. Geotech.*, vol. 93, pp. 104–114, 2018.

[157] J. W. Swegle, D. L. Hicks, and S. W. Attaway, “Smoothed Particle Hydrodynamics Stability Analysis,” *J. Comput. Phys.*, vol. 116, no. 1, pp. 123–134, 1995.

[158] H.-H. Lee, *Finite Element Simulations with ANSYS Workbench 18*. SDC publications, 2018.

[159] H.-H. Lee, *Mechanics of Materials Labs with SOLIDWORKS*

Simulation 2015. SDC Publications, 2015.

[160] M. Ostoja-Starzewski, *Microstructural randomness and scaling in mechanics of materials*. CRC Press, 2007.

[161] J. A. Epaarachchi and G. C. Kahandawa, *Structural health monitoring technologies and next-generation smart composite structures*. CRC Press, 2016.

[162] C. T. Dyka and R. P. Ingel, "An approach for tension instability in smoothed particle hydrodynamics (SPH)," *Comput. Struct.*, vol. 57, no. 4, pp. 573–580, 1995.

[163] G. R. Johnson and S. R. Beissel, "Normalized smoothing functions for SPH impact computations," *Int. J. Numer. Methods Eng.*, vol. 39, no. 16, pp. 2725–2741, 1996.

[164] J. K. Chen, J. E. Beraun, and T. C. Carney, "A corrective smoothed particle method for boundary value problems in heat conduction," *Int. J. Numer. Methods Eng.*, vol. 46, no. 2, pp. 231–252, 1999.

[165] J. J. Monaghan, "SPH without a Tensile Instability," *J. Comput. Phys.*, vol. 159, no. 2, pp. 290–311, 2000.

[166] P. W. Randles and L. D. Libersky, "Normalized SPH with stress points," *Int. J. Numer. Methods Eng.*, vol. 48, no. 10, pp. 1445–1462, 2000.

[167] L. D. G. Sigalotti and H. López, "Adaptive kernel estimation and SPH tensile instability," *Comput. Math. with Appl.*, vol. 55, no. 1, pp. 23–50, 2008.

[168] J. J. Monaghan, “Simulating Free Surface Flows with SPH,” *J. Comput. Phys.*, vol. 110, no. 2, pp. 399–406, 1994.